BOOSTING CO_2 ELECTROREDUCTION VIA MEMBRANE ELECTRODE ASSEMBLIES WITH INCREASED CO_2 CONVERSION RATES AND SELECTIVITY TOWARDS CO

by

FATMA ISMAIL, B.Sc., M.Sc.

A Thesis Submitted to the School of Graduate Studies in Partial Fulfilment of the Requirement of the Degree of Doctor of Philosophy in Chemical Engineering

McMaster University ©

McMaster University, DOCTOR OF PHILOSOPHY (2023), Hamilton, Ontario, Canada
(Chemical Engineering)

TITLE: Boosting CO_2 Electroreduction via Membrane Electrode Assemblies with Increased CO_2 Conversion Rates and Selectivity Towards CO
AUTHOR: Fatma Ismail
SUPERVISOR: Professor Drew Higgins
NUMBER OF PAGES: xxiii, 185

Lay Abstract

This PhD thesis aims to develop and implement a sustainable technology that tackles increased CO_2 emissions in the atmosphere and mitigates the greenhouse effect on climate change. The approach of this thesis focuses on developing efficient catalyst designs for CO_2 electroreduction (CO_2R) to CO as a beneficial chemical feedstock, and then pursues the practical implementation of these catalysts in an industrially relative reactor design in the form of a membrane electrode assembly (MEA)-type electrolyzer. This study selected atomically dispersed metal-doped nitrogen-carbon (M–N–C) and intermetallic carbide electrocatalysts as promising materials for CO_2R. Among different precursors, metal-organic frameworks (MOFs) have been employed to synthesize the desired electrocatalysts due to their unique geometric structure and high surface area. On a fundamental level, our findings demonstrated that all MOF-derived catalysts have exhibited high selectivity towards CO during CO_2R. However, the conversion rates were governed by the nature of the active sites and the implemented electrochemical systems.

Abstract

To combat the escalating environmental challenges and alleviate the current energy crisis, CO_2 conversion to fuels and chemical feedstocks provides a reliable approach to mitigate the devastating impact of greenhouse emissions on climate change. CO_2 conversion/reduction could be carried out by several methods; however, the electrochemical CO_2 reduction (CO_2R) approach has coupled several advantages. For instance, CO_2R occurs in near-ambient reaction conditions and could be driven through the employment of renewable energy resources (wind or solar) to generate electricity. However, this reaction has a large energy barrier which requires a catalyst to facilitate its pathway. In this context, various catalyst designs were developed and investigated during the last decades, such as heterogenous (metal and metal oxide) and homogenous (organic molecules) catalysts. A new class of materials – atomically dispersed metal nitrogen–doped carbon support (M–N–C)– has emerged recently and showed remarkable enhancement for CO_2R compared to the state-of-the-art. In particular, Ni–N–C catalysts have demonstrated an improved selectivity toward CO production compared to precious metal catalysts. Researchers have postulated this superior performance to the high atomic utilization (theoretically 100%) of the metal sites under reaction conditions and the enhanced electronic properties. In addition, intermetallic carbides have been included as a promising class of catalysts for CO_2R due to their unique physical and chemical characteristics. These catalysts could be synthesized using different precursors; among them, MOFs are currently one of the most promising platforms that generate several catalyst designs. It was demonstrated that MOF's unique characteristics, such as high surface area and porosity, would be transitioned to the derived catalysts.

In this thesis, two MOF architectures (ZIF-8 and MOF-74) were initially selected to be employed as precursors for deriving atomically dispersed Ni–N–C catalysts. Both MOF-derived

catalysts were evaluated for CO_2R using a customized electrochemical cell (E-cell) with a 3–electrode configuration. The derived Ni–N–C catalysts using ZIF-8 and MOF-74 have achieved enhanced CO selectivity with Faradaic efficiencies (FE) > 90% at less negative applied potentials, –0.68 and –0.76 V vs RHE, respectively. Further, various synthetic conditions were explored in these studies, such as the role of the Ni content and the pyrolysis temperature on the resulted catalyst structure, and the electrocatalytic performance during CO_2 electrolysis.

Subsequently, one of the MOF topologies – ZIF-8 – was further utilized to develop other designs of electrocatalysts by introducing different synthetic conditions. This has resulted in generating various moieties that are able to produce CO during CO_2R. For example, one derived catalyst design consists of homogenously distributed atomically dispersed dual Ni–Zn–N_X/C sites. Whereas the other design demonstrated a heterogenous structure of Ni_3ZnC-based particles anchored on atomically dispersed dual Ni–Zn–N_X/C sites. Both electrocatalyst designs were integrated into a gas diffusion electrode (GDE) and evaluated for CO_2R using an MEA-based electrolyzer. Our findings revealed that the co-existence of Ni_3ZnC particles and dual Ni–Zn–N_X/C active sites in a heterogenous structure has boosted the electrocatalytic activity towards CO production, achieving near unity CO FE at 448 mA/cm^2 at an overall cell voltage of 3.1 V. Aside from the electrocatalytic performance, the nature of active sites in the developed catalyst designs has been studied using *in-situ* and *ex-situ* X-ray absorption spectroscopy. Other analytical techniques such as transmission electron microscopy (TEM), energy dispersive spectroscopy (EDS), powder X-ray diffraction (PXRD), and X-ray photoelectron spectroscopy (XPS) have also been used to identify the catalysts' composition and morphology.

Acknowledgment

At the outset, I would like to thank my Lord Allah, The Almighty, for His grace, care, provision, and bounties. It was Him Who provided me with the strength to carry on this endeavor. I owe everything to Him and ask Him to continue to support and bless me with His mercy.

When I first met professor Drew Higgins while he was outlining the expectations from a Ph.D. student and his role as a supervisor, he said “my job is to enable you to become an independent researcher in a healthy and safe environment and to be a happy human being”. I realized how fortunate I was to get accepted in his lab. Early in my Ph.D. journey, Drew was confident in my capabilities and showed a great deal of flexibility when I proposed a scientific hypothesis and allowed me to apply it independently. He also helped me develop my critical thinking to troubleshoot any challenges I may have faced. In addition, Drew recommended me to work as a part-time researcher at Canada Center of Electron Microscopy during the first year of my Ph.D., which is an exceptional opportunity that exposed me to various scientific approaches. Drew has also shown incredible support during the Covid-19 pandemic when schools were shut down. He permitted me to bring my daughter to the office while I was working in the lab to keep up with my Ph.D. progress. On top of that, he was also and (still is) very welcoming to her with a nice smile/conversation every single time he meets her. Aside from his insightful guidelines throughout my Ph.D. on the academic side, I learned so much from Drew about communication, empathy, leadership, respect, trust, and credibility. He has been accommodating every time I asked for advice pertaining to my personal or professional life, which he provided amicably. Towards the end of my Ph.D. thesis chapter, when I was looking for jobs, Drew shared his experience in this regard with me, which assisted me to secure a research position before graduation. By pursuing a Ph.D. in Drew’s Lab, I was able to collaborate with huge industrial partners such as Suncor, also, I had the opportunity to carry out insightful science experimentation in the Canadian Light Source facility. I am forever grateful to Drew and for the privilege to do my degree under his supervision, for every single piece of advice, for helping me build scientific collaborations, for each recommendation letter he provided, for the healthy and safe lab environment he built throughout the four years, for selecting exceptional students from all over the world and establishing this amazing research group full of brilliant researchers, for welcoming my daughter, Nourine (deeply grateful), for enabling me to be an independent researcher, and for the incredible support I received

throughout this journey. I will endeavor to transfer this outstanding experience and all values I learned to my future colleagues and mentees.

I am also very grateful to my committee members, Dr. Nabil Bassim and Dr.Charles De Lannoy, for their insightful scientific guidelines and the continuous support they provided along the PhD journey. Dr.Charles and Dr.Nabil have always provided very constructive feedback regarding my progress, their feedback has assisted me to outline and answer some scientific questions, filling the gap in knowledge and defining research hypotheses. I am very fortunate to get the opportunity of being supervised by such great scientists in the field.

Special thanks go to one of the most brilliant brains I have ever met, the great beam time scientist, Dr. Ning Chen who has provided me with on-site and virtual support for my XAS measurements. Dr. Ning has also helped me to acquire both experimental and theoretical XAS knowledge, despite data fitting being very challenging and consuming a long time. Dr. Ning also assisted me in doing data fitting in a very short time frame. I am very grateful for working with such a great, supportive, and collaborative scientist!

I express my sincere thanks to the great scientist professor Adam Hitchcock, for his valuable guidelines in performing XAS measurements, interpreting the obtained data, and providing critical feedback that assisted me to figure out some relative challenges.

I would be remiss if I do not extend special thanks to our Suncor partners, Dr. Michael Fefer and Yuichi Terazono for the amazing opportunity to work closely with them on a very important research project.

To Mom (Eman) and Dad (Mostafa), I still remember the final day of my undergraduate studies in my hometown/Egypt, when I felt a mixture of excitement, nervousness, curiosity, and even fear. On that day, I had a memorable conversation with you when I asked to move out of my small hometown to the capital city to explore academic opportunities. I remember how incredibly supportive you were, despite the very conservative traditions that do not encourage women to pursue their careers. I owe, not only this Ph.D. and my work, but every single achievement I accomplished in my whole life to them. I thank you wholeheartedly, Mom and Dad, for everything

you did for me, for the trust I received, for believing in me, for the love and care you showered me with, and for prioritizing my career and dreams over the amazing and warm family companionship. I tried my best during the whole journey to make you proud and I hope that I have succeeded!

To Nourine, my precious one and only, I know that you might not be able to understand how I am really grateful to your lovely companionship throughout my life. You will read these lines after several years and know how you were an incredibly supportive and lovely daughter. You spent many days and nights during the covid pandemic with me on campus while I was working in the lab. You were just sitting on your iPad waiting for me. Despite being often bored, you never failed to brighten my day with your pure and innocent laugh once I asked "Hey Nourine, are you Okay?" You have given me all the love that I badly needed, without which my life would have been extremely difficult. Thank you so much, my Nourine! I hope one day you'll be proud of your mom.

To my sister Nada, and brothers, Ahmed and Abdelrahman, thanks a million for the motivation, and support you blessed me with. Above all, thanks for believing in me. I am very grateful for your companionship throughout my life.

Right before getting my undergraduate degree, when I started looking for research jobs, I met Professor Mohamed Ibrahim Zaki who guided me at the beginning of my research journey to select a specific approach and recommended me for a job position. I thank you a lot, Professor Mohamed. I owe my career achievements to your valuable guidelines, and I am also very grateful for all the advice you gave me. This could have not been achieved without your continuous support!

I would like to express my gratitude to Dr. Moustafa Khalaf, Dr. Mona Bakr and Dr. Nageh Allam who guided and supported me at the beginning of my academic career. Thank you very much, dear respectable professors.

In addition, I am very thankful to my colleagues and teammates, more specifically, Ahmed Abdellah who has supported and collaborated with me during the Ph.D. Through his outstanding skills in microscopic imaging, he enabled me to obtain amazing and bright TEM/EDS images which we published in two manuscripts. Besides, he also provided unforgettable support during the toughest times in my life. Ahmed is not just a brilliant teammate; he is a life-long friend. Many thanks to Ahmed, and more collaborations and publications to come!

Many thanks to one of the very exceptional team members, Wajdi Alnoush who spent many nights at CLS performing the *in-situ and ex-situ* XAS measurements along with his fruitful insights on one of my Ph.D. projects. I am also grateful for his overall support including data processing and fitting.

Also, I am very glad to have worked closely with many smart brains in the lab including my dear colleagues, Shunquan, Chunyang, Ecem, Kora, Navid, Storm, Shayan, Alejandra, Thomas, Arjun, Sudheesh, and Ricardo.

I would express my sincere gratitude to my best friends, Dr.Kholoud Nagy, Dr.Walaa Ramadan, Nagat Elrefaei, and Kholoud Abousalem. I can imagine how tough my life would be without your lovely and supportive companionship throughout the whole journey, there are no words that can ever express how I am grateful for everything you provided, you're a mercy from my Lord, thanks so much, my dear friends.

Table of Contents

List of Figures

Chapter | 2

List of Tables

Chapter | 3

List of Abbreviations and Symbols

CO_2R	Carbon Dioxide Reduction
MOF	Metal Organic Frameworks
ZIF-8	Zeolitic Imidazole Framework
MEA	Membrane Electrode Assembly
E-Cell	Electrochemical Cell
M–N–C	Metal–doped Nitrogen and Carbon
Ni–N–C	Nickel–doped Nitrogen and Carbon
CO	Carbon Monoxide
FE	Faradaic Efficiency
DFT	Density Function Theory
XAS	X-Ray Absorption Spectroscopy
PXRD	Powder X-Ray Diffraction
XPS	X-Ray Photoelectron Spectroscopy
TEM	Transmission Electron Microscopy
SEM	Scanning Electron Microscopy
RHE	Reversible Hydrogen Electrode
HER	Hydrogen Evolution Reaction
OER	Oxygen Evolution Reaction
Ni_3ZnC	Nickel Zinc Carbide
GDE	Gas Diffusion Electrode
GDL	Gas Diffusion Layer
2D	Two Dimension

EDS	Energy Dispersive Spectroscopy
M–N–C	Metal Doped Nitrogen and Carbon
Ni–N-C	Ni Doped Nitrogen and Carbon
SMAs	Single Metal Atoms
HNO_3	Nitric Acid
HCl	Hydrochloric Acid
$KHCO_3$	Potassium Bicarbonate
IPA	Isopropanol
D.I Water	Deionized Water
3D	Three Dimension
CB	Carbon Black
CNTs	Carbon Nanotubes
NPs	Nanoparticles
EXAFS	Extended X-ray Absorption Fine Structure
HAADF	high-angle annular dark-field
STEM	Scanning Transmission Electron Microscopy
ALD	Atomic Layer Deposition
EIS	Electrochemical Impedance Spectroscopy
PCET	proton-coupled electron transfer
TW	Tera Watts
GT	Gigatons
IPCC	Intergovernmental Panel on Climate Change
IEA	International Energy Agency

HCOOH	Formic Acid
CH_4	Methane
C_2H_5OH	Ethanol
mM	Millimoles
mA	Milliamperes
e^-	Electrons
H^+	Protons
C_2H_4	Ethylene
V	Volts
E°	Standard Potential
NaOH	Sodium Hydroxide

Declaration of Academic Achievements

Chapter 3 is featured as a published article in *ACS Applied Energy Materials* entitled (Impact of Nickel Content on the Structure and Electrochemical CO_2 Reduction Performance of Nickel–Nitrogen–Carbon Catalysts Derived from Zeolitic Imidazolate Frameworks). Authors: ***Fatma Ismail***, Ahmed Abdellah, Hye-jin Lee, Veeranmaril Sudheeshkumar, Wajdi Alnoush, Drew C. Higgins, ACS Appl. Energy Mater. 2022, 5, 430−439. In this paper, Fatma Ismail and Drew Higgins designed the whole study, Ahmed Abdellah performed TEM imaging and EELS mapping, Hye-jin Lee proofread the manuscript, Veeranmaril Sudheeshkumar helped in XPS fitting, and Wajdi Alnoush revised the manuscript. Fatma Ismail has conducted the remainder of the experimental work along with writing the entire manuscript with the revisions from the co-authors.

Chapter 4 outlines a published paper in *ACS Applied Energy Materials* entitled (Atomically Isolated Nickel–Nitrogen–Carbon Electrocatalysts Derived by the Utilization of Mg^{2+} ions as Spacers in Bimetallic Ni/Mg–Metal–Organic Framework Precursors for Boosting the Electroreduction of CO_2). Authors: ***Fatma Ismail***, Ahmed Abdellah, V. Sudheeshkumar, Amirhossein Rakhsha, Weifeng Chen, Ning Chen, and Drew C. Higgins*, ACS Appl. Energy Mater. 2022, 5, 9408−9417). In this article, Fatma Ismail and Drew Higgins have designed the whole study, Ahmed Abdellah helped in doing TEM imaging and EDS mapping, V. Sudheeshkumar, helped in XAS and XPS fitting, Amirhossein Rakhsha carried out some electrochemical measurements, Weifeng Chen and Ning Chen and has performed XAS measurements at the Canadian Light Source. Fatma Ismail has conducted the remainder of the experimental work along with writing the entire manuscript with the revisions from the co-authors.

Chapter 5 shows a research manuscript under Drew's review entitled (Unravelling the Nature of Active Sites in Metal-Organic Framework-derived Heterogenous Electrocatalysts for Boosting the Electroreduction of CO_2 to CO at Industrially Relevant Current Densities). Authors: ***Fatma Ismail***, Wajdi Alnoush, Ahmed Abdellah, Shunquan Tan, Kholoud Abousalem, Amirhossein Rakhsha, Ning Chen, Drew C. Higgins*– under review. In this manuscript, Fatma Ismail and Drew Higgins designed the whole study, Wajdi Alnoush helped with *in-situ* and *ex-situ* XAS measurements, Ahmed Abdellah performed TEM/EDS mapping, Shunquan Tan helped in MEA system optimization, Kholoud Abousalem helped in performing ECSA measurements, Amirhossein Rakhsha conducted SEM imaging, Ning Chen provided on-site technical support at CLS while performing *in-situ* XAS measurements and assisted in data fitting. Fatma Ismail has conducted the remainder of the experimental work along with writing the entire manuscript with the revisions from the co-authors.

1 Chapter | Introduction

1.1 Motivation

Establishing sustainable energy resources on a global scale while maintaining and preserving the environment has become one of the most imperative challenges for humanity today.[1, 2] According to the recent reports issued by the International Energy Agency (IEA), in 2013, the global energy demand reached 18 TW with the majority percent (~64%) coming from fossil fuel resources. With the rapid increase in the world's population and the excess industrialization processes, this demand is anticipated to face a further increase up to 24 or 26 TW in 2040.[3] This has raised significant concerns related to energy supplies and climate change resulting from the grand reliance on fossil fuels. Therefore, various attempts have been devoted to diversifying our energy sources by transitioning to renewable energy supplies. For instance, hydroelectric power, wind, and solar, have been utilized to minimize our dependence on fossil fuels. Despite the fact that combining both solar and wind energy sources can surpass the current world demand for electricity by 10000-fold, the intrinsic intermittency restricts their further development.[4] The Intergovernmental Panel on Climate Change (IPCC) claimed that a significant amount of carbon dioxide (CO_2) –one of the major greenhouse gases– must be removed from the atmosphere each year – at least 5~10 gigatons – in the latter half of this century.

CO_2 removal or emissions reduction could be achieved through different approaches, including the development and implementation of viable technologies/materials for CO_2 capture and sequestration, CO_2 reduction into beneficial feedstocks, and replacing fossil fuels with alternative renewable energy resources.[5] Of note, most materials produced via electrochemical CO_2 conversion are being generated from fossil fuels at a lower cost. This increases the desire towards developing economically competitive systems.[6] Initially, CO_2R was driven through

various methodologies, that includes thermochemical and photoelectrochemical approach; however, the electrochemical CO_2 reduction (E–CO_2R) has been widely investigated. This reaction has distinct advantages, such as the near ambient reaction conditions and the possibility of governing the reaction thermodynamics. However, it suffers from a large energy barrier, which requires the development of efficient electrocatalysts. Several catalyst structures have been designed to reduce CO_2 to different valuable products, namely methane (CH_4), ethanol (C_2H_5OH), ethylene (C_2H_4), formic acid (HCOOH), and carbon monoxide (CO).[7] Most of these products were obtained in aqueous CO_2R systems where a liquid electrolyte solubilized with reactant CO_2 molecules was used. This resulted in obtaining low current densities/reaction rates due to the low solubility (34 mM) of CO_2 gas molecules in the aqueous solutions. To enable the electrochemical CO_2R in aqueous media to be economically competitive, a current density regime of 300 mA/cm^2 is required, which is far from most of the obtained current densities to date (tens of mA/cm^2).[8] To tackle CO_2 mass transport restraints, scientists have explored the gas-phase electrochemical CO_2R technology. A key component of this technology is a gas diffusion electrode (GDE).[9-11] In this electrode, a gas diffusion layer (GDL) is used as a porous hydrophobic substrate where the catalyst is deposited, resulting in a shortening of the CO_2 diffusion path significantly. GDE technology has also imparted the opportunity to optimize the E–CO_2R reaction conditions, such as the utilization of alkaline solutions as electrolytes, which could significantly affect the reaction catalytic performance.[12] Developing a new catalyst design for GDEs is one of the key aspects of GDEs technology. In this context, various catalyst designs have been employed, that includes 2D thin films and 3D nano-structured materials. The overall performance of the integrated catalyst layer is influenced by different parameters such as the morphology and composition of the developed

electrocatalysts. Therefore, exploring and developing an efficient catalyst structure for the gas-phase E–CO_2R is required, along with their integration into GDEs and ultimately CO_2R reactors.

1.2 Thesis Structure

In this thesis, ***Chapter 2*** is divided into two parts. The first part outlines a detailed introduction to the fundamentals of E–CO_2R, including reaction mechanisms that occur on the cathodic and anodic sides, E–CO_2R-based systems (e.g., liquid and gas phase E-CO_2R), the different electrochemical cell configurations (e.g., flow cells and MEAs), and various catalyst compositions/morphologies that are used for E–CO_2R. The second part discusses the M–N–C catalyst development, including synthetic approaches, CO_2R mechanisms on M–N_X/C sites, and HER suppression mechanism.

In ***Chapter 3***, ZIF-8 precursor was used as a platform to prepare single Ni–N_X/C sites for CO_2R. A systematic study to optimize the Ni content inside the derived catalysts has been conducted. Different Ni^{2+}: Zn^{2+} atomic ratios were evaluated, which include 0.5:1, 1:1, 2:1, and 3:1. All prepared catalysts were characterized using various techniques such as TEM, EELS, SEM, and PXRD to obtain detailed insights on the morphology and composition of the generated active sites. Our findings revealed that low Ni content enabled the formation of single Ni–N_X/C sites (e.g. 0.5:1 and 1:1 Ni^{2+}:Zn^{2+} atomic ratios). Whilst the high Ni concentration led to the formation of Ni-based nano/microparticles. The electrochemical performance of the developed catalysts was investigated using a customized 3–electrode cell configuration. Lower Ni^{2+}: Zn^{2+} ratios exhibited

better selectivity towards CO production whereby 0.5:1 Ni^{2+}: Zn^{2+} ratio achieved ca. 99% CO FE at –0.68 V vs RHE.

In ***Chapter 4***, another MOF topology of Ni-Mg-MOF-74 was employed as a precursor for generating atomically dispersed Ni–N_X/C sites. Most of the currently used MOFs are constructed from N-containing building blocks which restrict the employment of MOF precursors to the N-containing compositions. Therefore, N-doped MOF has been recently explored to impart other MOF architectures along with N-based ones. However, increasing the active site concentration while retaining the separation of metal moieties is challenging. Therefore, metal ion spacers of Mg^{2+} in a bi-metallic NiMg-MOF-74 were used to prevent the agglomeration of Ni single moieties to Ni particles. Additionally, during the synthesis, urea molecules were used to impregnate N in the derived catalyst structure. Our results revealed that the role of Mg^{2+} as separators is vital in increasing the distance between the Ni sites in the parent structure, leading to the successful production of Ni single sites. In contrast, a structure of Ni-based particles immobilized in carbon nanotubes (CNTs) was evolved while using Mg-free Ni-MOF-74. Further, the influence of thermal treatment conditions as key reaction parameters on the derived structure was investigated. Our findings showed that high pyrolysis temperatures (e.g., 900°C) have promoted the formation of Ni–N_X/C, while using lower temperatures (e.g., 700°C) has generated Ni nano/microparticles. The developed Ni–N–C electrode was evaluated for CO_2R; revealing high CO selectivity that achieved ca. 90% FE and -4.2 mA/cm^2 at -0.76 V vs RHE.

In Chapter 5 one of the MOF topologies – ZIF-8 – was further utilized to develop other designs of electrocatalysts by introducing different synthetic conditions. This resulted in generating various active site moieties that can produce CO during CO_2R. For example, one derived catalyst consists of homogenously distributed atomically dispersed dual Ni–Zn–N_X/C

sites. Whereas the other catalyst design demonstrated a heterogenous structure of Ni_3ZnC-based particles and atomically dispersed dual Ni–Zn–N_X/C sites. Both electrocatalyst designs were integrated into a gas diffusion electrode (GDE) and evaluated for CO_2R using an MEA-based electrolyzer. Our findings revealed that the co-existence of Ni_3ZnC and atomically dispersed dual Ni–Zn–N_X/C active sites in a heterogenous structure has boosted the electrocatalytic activity towards CO production, achieving near unity CO FE at 448 mA/cm^2 by using 3.1 cell voltage. Along with the unique electrocatalytic performance, the nature of the active sites in the developed catalyst designs has been explored using *in-situ* and *ex-situ* X-ray absorption spectroscopy. Other analytical techniques such as transmission electron microscopy (TEM), energy dispersive spectroscopy (EDS), powder X-ray diffraction (PXRD), and X-ray photoelectron spectroscopy (XPS) have been utilized to identify structure compositions and morphology.

In Chapter 6 The obtained insights and results from the performed studies in this thesis are summarized along with the outlook.

References

1. Shen, L.; Luo, M.; Liu, Y.; Liang, R.; Jing, F.; Wu, L., Noble-metal-free MoS2 co-catalyst decorated UiO-66/CdS hybrids for efficient photocatalytic H2 production. Applied Catalysis B: Environmental 2015, 166, 445-453.

2. Wolter, B.; Pullen, M. G.; Baudisch, M.; Sclafani, M.; Hemmer, M.; Senftleben, A.; Schröter, C. D.; Ullrich, J.; Moshammer, R.; Biegert, J., Strong-field physics with mid-IR fields. Physical Review X 2015, 5 (2), 021034.

3. (International Energy Agency, "World Energy Outlook

4. Hepburn, C.; Adlen, E.; Beddington, J.; Carter, E. A.; Fuss, S.; Mac Dowell, N.; Minx, J. C.; Smith, P.; Williams, C. K., The technological and economic prospects for CO 2 utilization and removal. Nature 2019, 575 (7781), 87-97.

5. De Luna, P.; Hahn, C.; Higgins, D.; Jaffer, S. A.; Jaramillo, T. F.; Sargent, E. H., What would it take for renewably powered electrosynthesis to displace petrochemical processes? Science 2019, 364 (6438).

6. Kibria, M. G.; Edwards, J. P.; Gabardo, C. M.; Dinh, C. T.; Seifitokaldani, A.; Sinton, D.; Sargent, E. H., Electrochemical CO2 reduction into chemical feedstocks: from mechanistic electrocatalysis models to system design. Advanced Materials 2019, 31 (31), 1807166.

7. Nitopi, S.; Bertheussen, E.; Scott, S. B.; Liu, X.; Engstfeld, A. K.; Horch, S.; Seger, B.; Stephens, I. E.; Chan, K.; Hahn, C., Progress and perspectives of electrochemical CO2 reduction on copper in aqueous electrolyte. Chemical reviews 2019, 119 (12), 7610-7672.

8. Ross, M. B.; De Luna, P.; Li, Y.; Dinh, C.-T.; Kim, D.; Yang, P.; Sargent, E. H., Designing materials for electrochemical carbon dioxide recycling. Nature Catalysis 2019, 2 (8), 648-658.

9. Weekes, D. M.; Salvatore, D. A.; Reyes, A.; Huang, A.; Berlinguette, C. P., Electrolytic CO2 reduction in a flow cell. Accounts of chemical research 2018, 51 (4), 910-918.

10. Dinh, C.-T.; Burdyny, T.; Kibria, M. G.; Seifitokaldani, A.; Gabardo, C. M.; De Arquer, F. P. G.; Kiani, A.; Edwards, J. P.; De Luna, P.; Bushuyev, O. S., CO2 electroreduction to ethylene via hydroxide-mediated copper catalysis at an abrupt interface. Science 2018, 360 (6390), 783-787.

11. Higgins, D.; Hahn, C.; Xiang, C.; Jaramillo, T.; Weber, A., Gas-diffusion electrodes for carbon dioxide reduction: a new paradigm. ACS Energy Lett 4: 317–324. 2019.

12. Seifitokaldani, A.; Gabardo, C. M.; Burdyny, T.; Dinh, C.-T.; Edwards, J. P.; Kibria, M. G.; Bushuyev, O. S.; Kelley, S. O.; Sinton, D.; Sargent, E. H., Hydronium-induced switching between CO2 electroreduction pathways. Journal of the American Chemical Society 2018, 140 (11), 3833-3837.

2 Chapter | Fundamentals of Electrochemical CO_2 Reduction

The performance of the electrochemical CO_2R system is defined by different metrics involving the operational costs of the overall reaction. These metrics include current density, Faradaic efficiency, energy efficiency, and stability. The current density defines the reaction rate for the electrochemical CO_2R, whereby high current density systems are required to decrease capital costs, that mostly affects the system stability and reduces energy efficiency due to the presence of a large ohmic drop. The Faradaic efficiency (i.e., reaction selectivity) reflects the current percentage required to generate a specific product over the total consumed current. Reactions with high Faradaic efficiency require fewer separation procedures compared to low Faradaic efficiency-based systems and consequently decrease the required overall current for a specific production rate. The ratio of the energy stored in specific products related to the total input energy is defined as the energy efficiency which is directly related to the total cell voltage. Systems with high energy efficiency rates are desirable to lower electricity–related costs. To enhance the energy efficiency of a given CO_2R system, the total cell voltage (including anode and cathode overpotential, thermodynamic cell voltage, mass transport and ohmic potential drop) is needed to be reduced. The difference between the thermodynamic reversible potentials of the anodic and cathodic reactions is defined as thermodynamic cell voltage. Additionally, stability is a crucial parameter to characterize an electrochemical CO_2R system due to its direct relation to the replacement and maintenance expenses.

2.1 Cathodic reactions

The negative terminal of the CO_2R system is defined as the cathode where an electrocatalyst is deposited and CO_2 gas molecules are converted/reduced with the interaction of protons (H^+) or water molecules and electrons (e^-). Several products/chemicals could be generated

based on the number of protons/electrons transferred as illustrated in equations 1–7, alongside their thermodynamic reversible potentials:

$$CO_2 + 2H^+ + 2e^- \rightarrow CO + H_2O \qquad E = -0.11\,V\ vs\ RHE \quad (1)$$

$$CO_2 + 2H^+ + 2e^- \rightarrow HCOOH \qquad E = -0.21\,V\ vs\ RHE \quad (2)$$

$$CO_2 + 4H^+ + 4e^- \rightarrow HCHO + H_2O \qquad E = -0.10\,V\ vs\ RHE \quad (3)$$

$$CO_2 + 6H^+ + 6e^- \rightarrow CH_3OH + H_2O \qquad E = 0.3\ V\ vs\ RHE \quad (4)$$

$$CO_2 + 8H^+ + 8e^- \rightarrow CH_4 + 2H_2O \qquad E = 0.17\,V\ vs\ RHE \quad (5)$$

$$CO_2 + 12H^+ + 12e^- \rightarrow C_2H_4 + 4H_2O \qquad E = 0.07\,V\ vs\ RHE \quad (6)$$

$$CO_2 + 12H^+ + 12e^- \rightarrow C_2H_5OH + 3H_2O \qquad E = 0.09\,V\ vs\ RHE \quad (7)$$

As depicted in **Figure 2.1**, initially, *HCOO or *COOH intermediates are formed on the catalyst surface by the adsorption and activation of CO_2 molecules on the cathode. This generally results in the reduction of *COOH to *CO adsorbed on the catalyst surface or *HCOO to formic acid. *CO species has two different possibilities, either the desorption from the catalyst surface to form CO if it weakly anchored on the catalyst surface or the reduction to hydrocarbon materials if it strongly attached to the surface. This reduction has two main pathways, one of them leads to the generation of methane and methanol via a series of proton-coupled electron transfers, and the other involves the formation of *CO dimers followed by hydrogenation to produce C_{2+} products (e.g., ethanol and ethylene). The fact that CO_2R has several reaction pathways is being one of the largest

shortcomings in controlling product selectivity. Scientists and engineers paid extensive efforts to design new electrocatalysts that can tune the adsorption energies of the intermediates.[1-4]

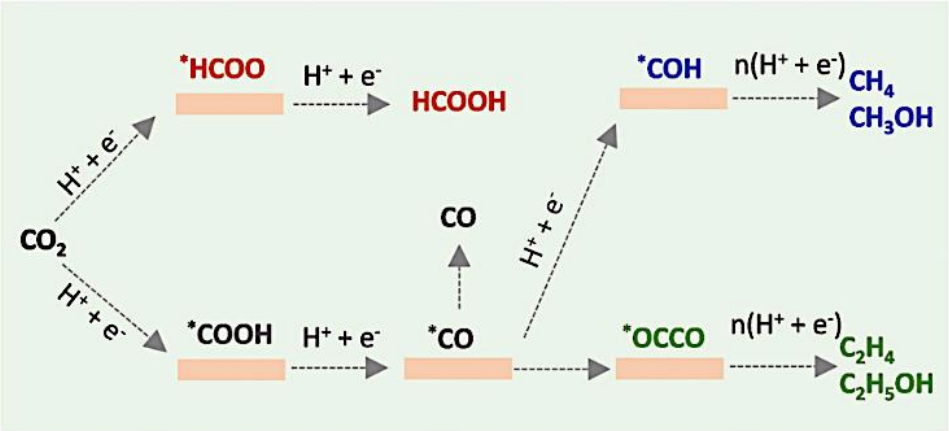

Figure 2-1 Different reaction pathways for the electrochemical CO_2R products. Reproduced with permission from ref.[4]

2.2 Anodic reactions

The reaction that occurs on the positive terminal of the electrochemical CO_2R system is typically the anodic water oxidation (oxygen evolution reaction) reaction **(Figure 2.2)**. This reaction generates the electrons that migrate towards the cathodic electrode to react with the CO_2 molecules and reduce them to other products. While the anodic reactions do not affect the CO_2R selectivity, however, the overall energy efficiency could be reduced as a result of increasing the overall cell voltage due to slow reaction kinetics at the anodic side.

$$2H_2O \rightarrow O_2 + 4H^+ + 4e^- \quad E^\circ = 1.23\,V\ vs\ RHE \quad (8)$$

Different materials are being used such as metal and metal oxides as catalysts to facilitate the oxidation reaction and minimize the activation energy barrier. Oxygen evolution reaction (OER) could be categorized into three main classes depending on the reaction environment, including acidic, neutral, and alkaline OER. [5-9]

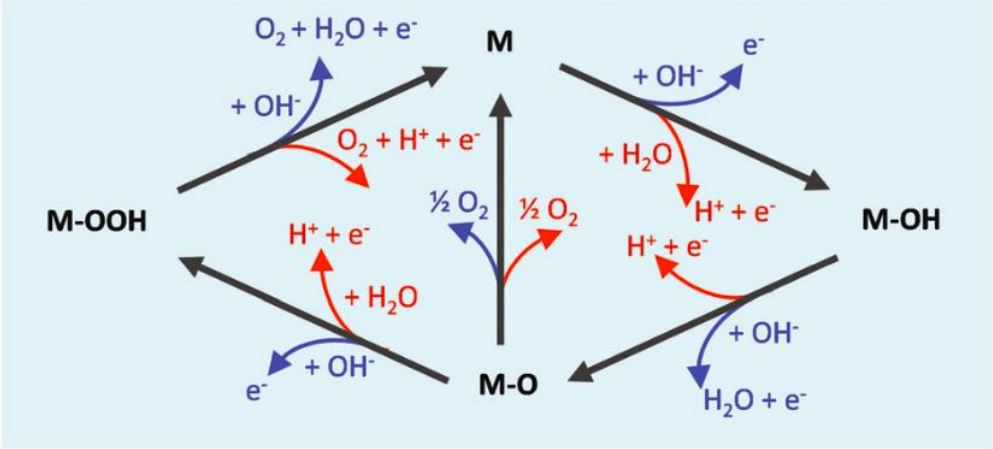

Figure 2-2 Schematic diagram of the reaction pathways of the oxygen evolution reaction in acidic and neutral media (red arrows) and in alkaline media (blue arrows) (M: metal). Reproduced with permission from ref.[4]

2.3 Electrolyte Membrane

The main role of the membranes is to allow the ionic exchange while separating the anode and cathode electrodes. A typical membrane basically contains side chains that have fixed ionic sites tethered with a polymer backbone as revealed in **Figure 2.3**. Effective membranes should have high chemical stability and ionic conductivity. In the meantime, the electrochemical CO_2R systems are using the same membranes developed for fuel cells and water electrolyzers. Nevertheless, the existence of several metal cations and carbonate anions makes the ionic transfer more difficult compared to water electrolysis, also, the electrochemical CO_2R produces various

liquid and gaseous products which may have a negative impact on the membrane performance. Currently, the electrochemical CO_2R community mainly uses three different types of membranes, which includes anion exchange membranes which transfer anions such as OH^-, cation exchange membranes that transport cations like H^+, and bi-polar membranes that are able to transfer both anions and cations.[9-12]

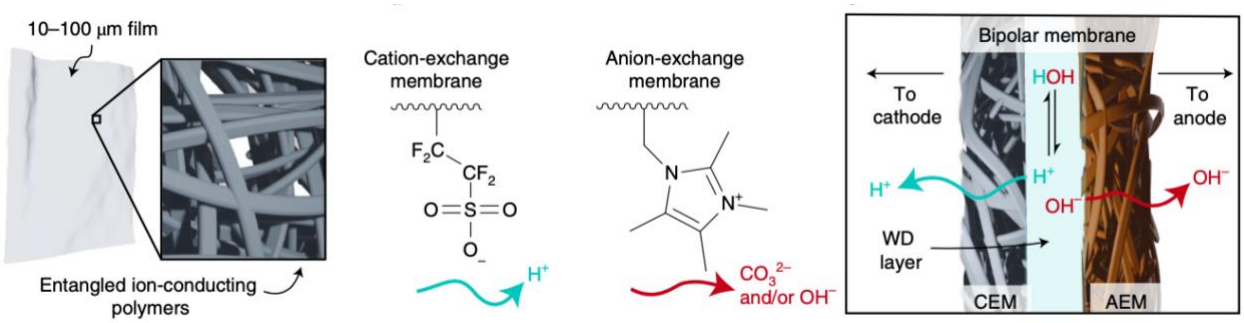

Figure 2-3 Schematic diagram illustrates of the polymer structure used for membranes. Reproduced with permission from ref.[13]

2.4 Electrochemical CO_2 conversion in Liquid Electrolytes

Intensive progress has been devoted to investigating electrochemical CO_2R in a liquid environment, in which CO_2 gas is dissolved in an aqueous electrolyte such as potassium bicarbonate and reduced over a catalyst surface. The exceptional synergistic interplay between theoretical and experimental research toward aqueous-phase CO_2R resulted in a better understanding of the influence of pH,[14] electrolyte ions,[15, 16] mass transport,[17] pressure,[18] and temperature on the obtained activity and selectivity. Therefore, the catalyst design approach has been widely guided by the developed activity descriptors and mechanistic insight into the reaction pathways, leading to searching for novel and efficient electrocatalysts with increased activity and selectivity for CO_2R.[19-21] Recently, a comprehensive overview of these investigations was provided in a published study.[22] Furthermore, an enhancement of these efforts is anticipated as a

result of utilizing machine learning processes for catalyst discovery.[23] Even though the previously mentioned studies have been crucial for providing deeper insights of CO_2R, their findings were dependent upon conventional aqueous-phase carbon dioxide reduction reactors constructed for fundamental analyses. However, these reactors are restricted with practical limitations which need addressing. It is worth noting that poor CO_2 solubility (ca. 34 mM) in aqueous electrolytes and the acid/base buffer (CO /HCO^{-}/CO^{-2}) equilibria resulted in major issues in terms of achieving enhanced performance and improved efficiency. Designs operating by delivering CO_2 to the cathode in the vapour phase can help overcome such challenges.[24] Gas-diffusion electrodes (GDEs) can overcome those challenges by utilizing a porous catalytic layer in parallel with diffusion media which contribute to fast reactant transport. GDEs have been implemented in other electrochemical energy-conversion devices including fuel cells and electrolysers, whereby their structure has been enhanced for high current density and low transport losses. Still, further strategies are necessary to address the selectivity and activity considerations for CO_2R, thus, avoiding the need for economically demanding downstream separations.[25] Two types of electrolyte can be used; either the aqueous environment or an ion-conducting polymer which form a catalyst/liquid or catalyst/polymer electrolyte interfaces, respectively.

2.5 Gas-phase electrochemical CO_2 conversion

The electrochemical CO_2R systems were developed using almost the same fuel cells and water electrolyzer configurations including an anode, a cathode, and a membrane. The reduction of CO_2 gas molecules is being occurred at the cathode while water oxidation is mostly the anode reaction where O_2 and protons are generated. To prevent the migration of products and balance the ionic charge, an ionic exchange membrane is being used to separate the cathode and anode chambers. The performance of the electrochemical CO_2R systems is mainly relying on the

products and reactants diffusion in the overall system, reaction kinetics on anode and cathode chambers, and the ion transfer through the membrane and the electrolyte.

2.6 Electrochemical cell designs

There are two main cell designs of the gas-phase CO_2R electrolyzer, including membrane electrode assembly (MEA) and flow cell. Both configurations have the same design except only one difference that the MEA design does not contain a liquid electrolyte flow on the cathodic side.

2.6.1 Flow cells

The flow-cell configuration for the electrochemical CO_2R has different components, including electrolyte chambers, cathode and anode current collectors, gas diffusion electrodes, and membranes as shown in **Figure 2.4A**. Cathodic and anodic sides are often gas diffusion electrodes while both chambers have in and out gas flow. Anolyte and catholyte compartments are being divided by an ionic exchange membrane. Generally, the current collector is pressed against the cathodic GDE back side while the other side is against the ionic exchange membrane. For the anodic side, to decrease the ohmic drop, the catalyst is placed very close to the membrane. During the CO_2R reaction, a flow of an electrolyte is pumped into the cathodic side while a continuous CO_2 gas flow is fed in both chambers. The liquid products migrate to the electrolyte and the gaseous phase products diffuse back through the GDE. Essentially, the role of the electrolyte on the cathodic side is to optimize the reaction environment and enhance the efficiency of CO_2 conversion. Also, two main parameters, including the identity of the ions and pH, have a strong influence on the cathodic reactions. As it was demonstrated that the adsorption of OH^- ions on or close to metal catalysts reduces the energy barrier for CO_2 reduction into ethylene while suppressing the competing hydrogen evolution reaction (HER). Also, both NaOH and KOH have

high ionic conductivity compared to $KHCO_3$ – neutral pH electrolyte – which boosts the system overall energy efficiency and decreases the ohmic losses. In a recent study, it was demonstrated that increasing KOH electrolyte concentration has significantly reduced the CO_2R onset potential. While by using 1 M and 10 M KOH as electrolytes for CO_2R reaction on a Cu catalyst, the onset potentials of CO_2 reduction to ethylene were almost –0.46 and –0.16 V vs RHE respectively. Also, both ethylene and carbon monoxide have low potentials as a result of high OH^- concentration which consequently raises the energy conversion efficiency to produce ethylene. Despite the alkaline systems showing promising selectivity and current densities in CO_2R reactions, however, the electrolyte regeneration procedures that resulted from the carbonate formation are still challenging towards achieving high energy efficiency.[26-29] Although the presence of liquid electrolytes is important for controlling the reaction environment, however, the possibility of electrolyte penetration into the GDE could reduce the system stability. Flooding could significantly reduce CO_2 diffusion to the catalyst which consequently lowers the overall performance of the CO_2R system. Also, the liquid electrolyte increases the total cell voltages at high current densities due to increasing the overall cell resistance. Nevertheless, flow cell configuration remains a competitive platform to investigate the electrochemical CO_2R at the industrial level.

2.6.2 Membrane electrode assembly (MEA) cell design

In MEA cell configuration (**Figure 2.4B**), a membrane is sandwiched between an anodic catalyst and cathodic GDE with eliminating the electrolyte between both electrodes, which generally results in reducing the ohmic resistance. In this design, a vapour phase of water reactant is provided to the cathodic side, avoiding the need to pump a flow of electrolytes. The absence of liquid electrolytes in this cell design assists in minimizing the GDE flooding and consequently enhances the system's stability. Also, the catalyst stability could be maintained by preventing the

impurities derived from the liquid electrolyte. Liquid products in MEA cells exit the reactor with the water vapour and gas products, in contrast to flow cells where liquid products enter the catholyte. By condensing the gas mixture outlet in MEAs, a higher concentration of liquid products could be obtained. In the electrochemical CO_2R electrolyzer, both energy efficiency and product separation procedures are affected by the diffusion of the molecules and the migration of the ions. That provides the flexible architecture of MEA with a high potential to fine-tune these processes by the reconfiguration of the membranes. For instance, the use of a combination of multiple membranes along with a solid polymer electrolyte instead of using only one membrane type. Xia et al. have developed an MEA design whereby an anode is contacted with a cation exchange membrane and a GDE is pressed against an anionic exchange membrane, while a solid electrolyte is used to separate both the cathode and anode. During CO_2R, the metal cations migrate from the anode to the solid electrolyte while the anionic species migrate in the opposite direction from the cathode. This configuration was able to produce pure products over 100 hours, showing a high potential towards industrial applications.[8, 9] MEA cell design has the same configuration as the commercially available polymer electrolyte membrane fuel cells, giving them great potential towards the implementation of industrial technologies. However, various design aspects of MEA should be optimized as the fuel cell chemistry is different from the electrochemical CO_2R. For instance, in MEA cells, additional separation procedures are required to re-use CO_2 because at the anode side of MEA, a mixture of O_2 and CO_2 are produced, that is ascribed to the formation of carbonate ions that migrate towards the anode to react with the protons and form CO_2. Also, a product crossover could occur through the membrane due to the high liquid product concertation, which likely might dilute the anolyte products and increase the possibility of re-oxidation back to CO_2 at the anodic side. Besides, membrane stability could be negatively affected by the high

concentrations of the produced alcohols. Additional considerations might be needed for designing an electrode for MEA because of the absence of liquid electrolytes significantly influences the local environment during CO_2 electroreduction. In MEA, the ionic transfer between the cathode and anode is governed by the electrode-membrane interface. Achieving close contact between both of them is critical for high ion transport. Two different approaches are being used to enable this contact, including hot-pressing to the membrane after catalyst deposition on GDL, and catalyst direct deposition on the membrane. While both methodologies are being efficient for fuel cell MEA, however, the first approach provides better flexibility in catalyst design and consequently widely used in the electrochemical CO_2R community. Unlike the fuel cell community which focuses on maximizing the catalyst surface area, the overall efficiency, selectivity, and activity of the electrochemical CO_2R are mainly relying on catalyst layer morphology.[30]

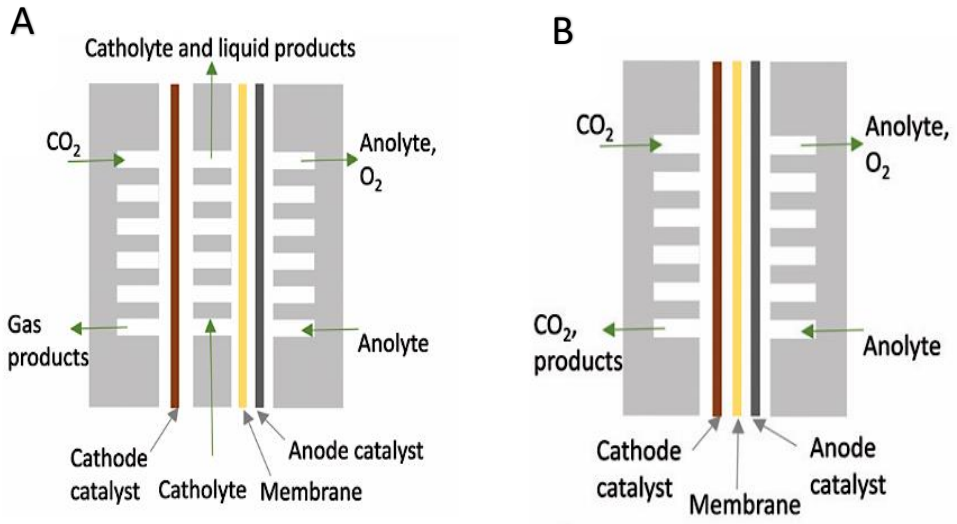

Figure 2-4 (A) Flow cell configuration and (B) Schematic diagram of a zero-gap cell (MEA), Reproduced with permission from ref [31].

2.7 Metrics of merit

Various key metrics are used to assess the performance of CO_2 electrolyzers (flow cells and MEA). The architecture of the electrolyzer and catalyst design impact all these metrics.

2.7.1 Current density

As mentioned earlier here, during CO_2 electroreduction, the current density (j) reflects the reaction rate and could be quantified using the following equation:

$$j = \frac{I}{A} \quad (9)$$

Where I is the total current passed and A is the electrode geometric area, normalizing the current density to the actual electrode area –which includes the roughness factor– is also used to obtain further mechanistic insights. The current density is directly associated to the operating volage, utilizing high voltages is required to achieve high current densities. In contrast, applying low voltages would yield low current density values and high capital costs.

2.7.2 Voltage

The driving force of the reaction is described by the operating voltage, and depends on the cell configuration, it could be expressed as a full cell voltage (e.g., MEA) or an overpotential /potential (half cell reactions e.g., H-cells). The difference in value between the thermodynamic voltage and the required voltage to achieve high current densities is known as the overpotential. This difference should be small values to reduce the applied electrical requirements and it could be calculated through the following equation:

$$\boldsymbol{\eta = |E_{Applied} - E^{\circ}|} \quad (10)$$

E° represents the thermodynamically calculated voltage and $E_{Applied}$ depicts the applied cell voltage. In a half-cell configuration, it is essential to compare both $E_{Applied}$ and E° to a reference electrode. Also, compensated iR overpotentials are commonly reported to compare different electrocatalytic reactions with different ohmic losses. To calculate the iR-corrected overpotentials, Electrochemical Impedance Spectroscopy (EIS) is used to quantify the resistance source in the cell. A full cell voltage can use the term of overpotential whereby the difference between the thermodynamic voltages of the anode and cathode is the thermodynamic cell voltage $\boldsymbol{E^{\circ}}$:

$$E^{\circ}_{Cell} = E^{\circ}_{Cathode} - E^{\circ}_{Anode} \quad (11)$$

When cell voltages expressed in negative values, this is an indication of the non-spontaneously nature of the reaction.

2.7.3 Faradaic Efficiency *(FE)*

The reaction selectivity during CO_2 reduction is commonly reported using the term of Faradaic Efficiency (FE) which could be calculated for each product using the following equation:

$$FE_i = \frac{I_i}{I} = \frac{z_i n_i F}{I} \quad (12)$$

Whereby I_i represents the partial current consumed in a specific gas/liquid-phase product i, and the number of transferred electrons for each molecule represented by z_i, F is Faraday's constant, n_i is the generation rate (in moles) of each product, and I is the total current passed throughout the reaction.

2.7.4 Energy Efficiency *(EE)*

The energy efficiency correlates the minimum electricity required for driving the reaction and the amount of the actual electrical energy consumed; the following equation indicates how to calculate EE values for the full-cell configuration:

$$EE_i = FE_i \times \frac{E^{\circ}_{Cell}}{E_{Applied}} \qquad (13)$$

Energy efficiency could be also calculated for multiple products by sum of each *EE* values for these products. For the half-cell configuration, *EE* values could be obtained via the iR corrected anode and cathode voltages without overpotential. However, calculating the full cell uncompensated *EE* is essential to consider all loss sources in the CO_2 electrolyzer (e.g., membrane and electrolyte).

2.7.5 Stability

In CO_2 conversion technology, the stability of CO_2 electrolyzer is a key factor in determining the related downtime, maintenance, and replacement costs. Most of the developed CO_2 electrolyzers maintain their efficiency for less than 100 hours, in contrast, commercially available water electrolyzers display a stable operation up to 20,000 hours without deterioration. Scientists have recently paid an extensive attention to the stability of CO_2 electrolysis, however, producing a clear descriptor for maintaining high efficiency of CO_2 electrolyzers for long durations is still under investigation.

2.7.6 Voltage Losses in CO_2 Electrolysis

The development of efficient and stable CO_2 electrolysis technology could be enhanced by identifying the sources of voltage deficiency during the reaction. As CO_2 could be reduced to a number of different hydrocarbons and chemicals whereby the reaction pathways of these products

are very competitive, mass transport and kinetic can significantly influence the reaction compared to the traditional fuel cell electrolyzer. To deconvolute voltage losses in CO_2 electrolyzer with multiple competitive reaction pathways, post processing models have been applied to avoid model re-computation of individual reactions. A power-loss method is applied to identify the mass transport and kinetic losses of each reaction. In this case, to calculate the thermodynamic cell voltage U^O, the change of free energy of each product should be considered as follows:

$$U^O = E^O_{Anode} - E^O_{Cathode} = E^O_{SHE} - \sum_m FE_m E^O_m \qquad (14)$$

Whereby, FE_m is the Faradaic efficiency of (m) reaction, E^O_m represents the standard reaction potential of (m) reaction. The voltage losses of CO_2 electrolyzer could be indicated by a polarization curve as follows:

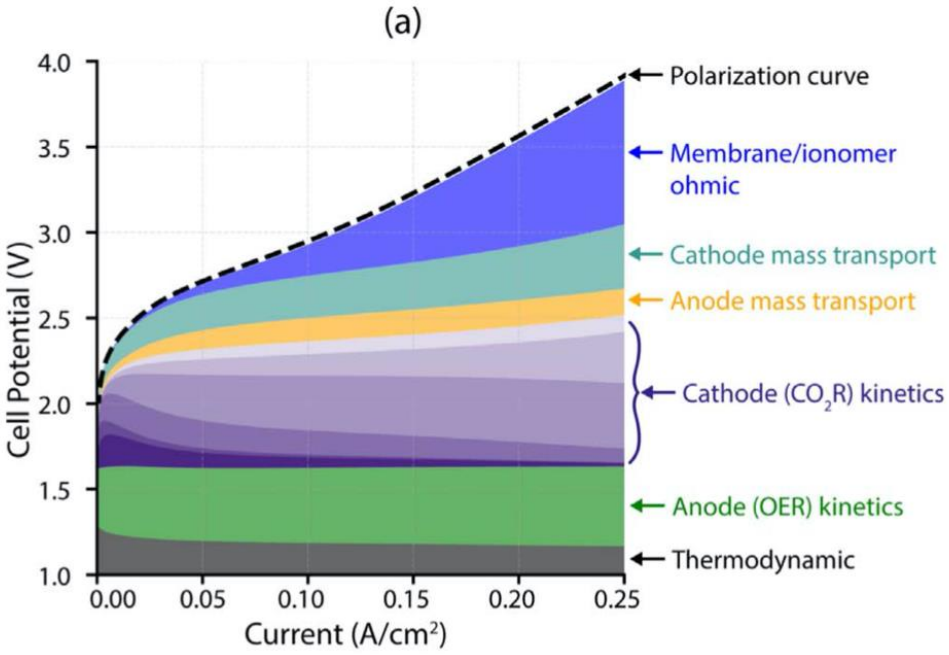

The voltage breakdown of a CO_2 electrolyzer.

Generally, a polarization curve of an electrochemical reaction (CO_2R as an example) depicts the relationship between the applied potential and current density, and commonly used to investigate the limiting key parameters that influences the overall reaction. As shown in the previous Figure, A polarization curve illustrates the performance limitation during the reaction that includes the onset potential, anode and cathode kinetics, ohmic drop and mass transport. To measure a polarization curve, a three-electrode system should be utilized, that involves working, counter, and reference electrodes. An electrolyte (mostly potassium bicarbonate) is degassed carefully prior use to eliminate any dissolved oxygen and a range of potential is applied to the working electrode while the obtained current density is measured. To plot a polarization curve, a wide range of applied potential should be used and plotted vs the corresponding current densities. Using this curve, the onset potential which defined as the minimum potential needed to drive the reaction, and the overpotential which is the excess potential needed to obtain a specific current density, could be identified. Further, information about anode and cathode kinetics, ohmic drop, and mass transport could be obtained from the polarization curve.[32] In a recent study, Kentaro et al. has developed a 5-electrode technique to identify the voltage drop in a zero-gap MEA-based CO_2 electrolyzer which comprises two quasi-reference wires in addition to the traditional cell components. Their findings demonstrated that the major source of overpotential (almost 720 mV loss at 600 mA/cm^2) is associated with the interface between the cathode layer and membrane. The authors claimed that coating the catalyst layer directly onto the membrane has reduced the voltage loss to 80 mV at 600 mA/cm^2.[33] These findings emphasize the importance of identifying the voltage loss sources for the rational development of efficient CO_2 electrolyzers.

2.8 Catalyst layer

2.8.1 Local environment "CO_2 gradient and pH" in the catalyst layer

The local environment in the electrochemical CO_2R is significantly influenced by operating at high current densities, that includes CO_2 concentration and pH in the catalyst layer.[34] The structure and morphology of the active catalyst particles largely govern the performance of the catalyst layer where catalyst particles could exist in three different structures including 3-dimensional nanostructures, 2-dimensional thin films, and 3-dimensional nanoparticles. Initially, CO_2 molecules react with H^+ or water during the electrochemical CO_2R to generate the desired products and OH^- as a by-product. The presence of high OH^- concentration generally leads to increasing the local pH and the formation of carbonate and bicarbonate ions, which significantly reduces the overall performance of the CO_2R system. The operating current density and nature of the electrolyte are mostly governing the OH^- concentration inside the catalyst layer. The neutralization of these OH^- could be achieved using a strong buffering electrolyte. Nevertheless, with a further increase in the current density, the concentration of the OH^- species significantly increases when using an alkaline electrolyte. Also, it was demonstrated by modelling results that, when a current density of 750 mA/cm^2 in 1M KOH electrolyte is used, the concentration of OH^- species is increased by an order of magnitude which decays the CO_2 concentration in the catalyst layer.[34, 35]

2.8.2 Nanostructured 3-D and 2-D Catalysts

Catalysts with 3D nanostructures could be formed in different structures such as nanoparticles, nanoneedles, wires, or dendrites. This class of electrocatalysts has a high electrical conductivity and surface area. Also, it has an increased electric field effect associated with the

presence of a sharp tip such as in nanoneedles. Nanostructured catalysts are generally prepared by an electroplating approach where a conductive substrate is used, and metallic ions are reduced into metallic atoms on the surface of the cathode.[36] For instance, $HAuCl_4$ is mostly used to produce Au nanoneedles, in this reaction, Au^0 is being obtained by the reduction of Au^{3+} during the electrodeposition. Optimizing the conditions of the synthesis such as electrolyte composition, applied potential, and deposition time can control the obtained catalyst morphology. For example, the nucleation is enhanced significantly with applying high negative potentials, and with applying high current densities, dendritic morphologies are mostly formed due to the quick consumption of the metal ions. In contrast, the nanostructures are efficiently grown in all directions at low applied potentials and demonstrate more isotropic characteristics.[37] Besides Au nanoneedles, dendrite architectures of various metals such as Ag and Zn could be prepared using the electrodeposition approach.[38] By applying a negative potential at a high growth rate, macroporous dendrite structures could be obtained as using these reaction conditions enhances the hydrogen evolution reaction where H_2gas bubbles act as a platform for the generation of macroporous structures.[39] Alloy nanostructured catalysts could be prepared using a co-deposition methodology. Generally, adjusting the deposition rates and precursor concentration can influence achieving the targeted morphologies and compositions.

Catalysts of the 2D structure are often a layer with an average thickness of 10-500 nm grown over the GDL. Through 2D architecture, both selectivity and activity are boosted due to the presence of a uniform local environment and CO_2 concentration.[40-42] Physical deposition methods such as atomic layer deposition (ALD) and evaporation deposition are commonly the fabrication approaches to prepare 2D active materials for the electrochemical CO_2R. These methodologies afford a strong interaction between catalyst and substrate owing to the direct growth of the active

materials on the substrate which results in highly stable CO_2R systems. Also, various materials such as metals, metal sulfides, and metal oxides could be deposited successfully using the same techniques while different catalyst compositions could be obtained through sequential deposition methods. Post-treatment techniques such as surface reconstruction and ionic exchange can be combined with the physical deposition ones for further optimization of catalyst morphology. Generally, the co-deposition approach is often used to prepare 2D catalysts with multi-component layers.[43, 44] For instance, Cu–Ag thin-film alloys could be prepared using sputtering deposition over a PTFE gas diffusion layer with achieving 70 to 90% Cu concentration inside the fabricated alloy. Using this approach and Cu-Ag composition, ethanol Faradaic efficiency of 41% was obtained at 250 mA/cm^2 current density, that's relatively higher than the ethanol selectivity of a pure Cu substrate (29%). In another study, a thermal co-deposition approach was used to deposit Cu-Al alloy on GDL which showed high ethylene Faradaic efficiency (80%) at 400 mA/cm^2 current density. While physical deposition approaches to prepare 2D catalysts exhibited good selectivity and selectivity in CO_2R, however, galvanic exchange approach has been recently used to fabricate 2D alloy catalysts over solid electrodes. Using this method, the composition optimization could be tuned by a galvanic exchange procedure which is considered a promising approach to produce high selective and active electrocatalysts for gas-phase CO_2R.[8, 45, 46]

2.8.3 Single Metal Atom Catalysts

Single metal atom catalysts (SMA) are newly emerged electrocatalysts that comprise isolated metal atoms dispersed on a substrate, with negligible interaction between the atoms. These catalysts are commonly used in electrocatalytic CO_2 reduction applications and are often immobilized on carbon-based materials such as graphene, carbon nanotubes, and amorphous carbon.[47-49] These carbonaceous supports demonstrate high electrical conductivity, which enables facile electron transport and large surface areas that enhance the electrocatalytic activity (**Figure 2.5**). Further, carbon-based substrates have low reactivity towards hydrogen evolution reactions, making them ideal candidates for electrocatalytic CO_2 reduction. Ni, Co, Fe, Cu, and Zn are mostly the employed metals in CO_2R, these metals have a weak binding energy on the carbon support. Therefore, to stabilize these metal atoms, they are often bonded to defect sites or different heteroatoms anchored on the carbon support, such as N, O, P, and S.

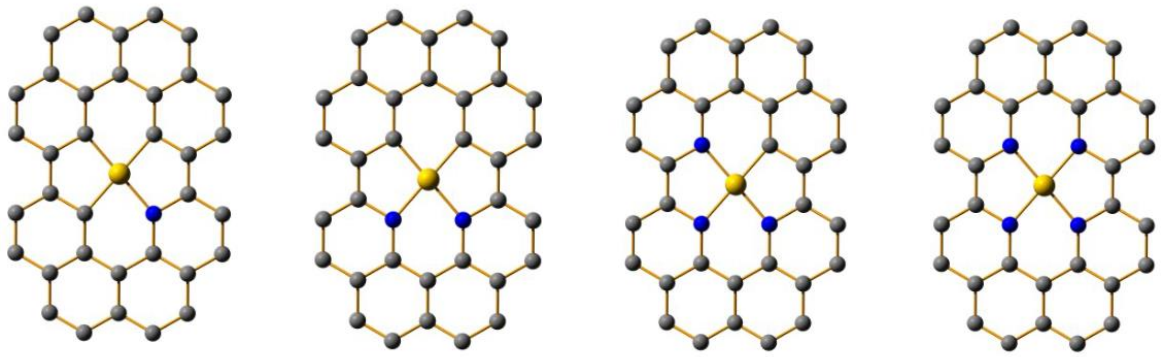

Figure 2-5 Different coordination configurations of SMAs on the support. Grey balls represent carbon atoms, yellow balls are SMAs, and blue balls are coordination elements. Reproduced with permission from ref.[50]

Metal atom coordination with the surface has a considerable effect on the overall performance of SMA catalysts. This coordination assists in inhibiting the agglomeration of the metal atoms and alters the geometric structure and electronic properties of the generated active sites. For instance, the metal atom interaction with CO_2 molecules and key intermediates might be adjusted by the electron-donating influence of heteroatoms on the carbonaceous support. Additionally, the symmetry (symmetric vs asymmetric) and position (in-plane vs out-of-plane) of the metal atom on the substrate can also impact its catalytic activity. Thus, fine-tuning the metal-support interaction could lead to a considerable improvement in the obtained catalytic performance of SMA electrocatalysts.[50]

The coordination number of SMAs and the nature of atoms surrounding the metal site play an imperative role in determining their electrochemical reactivity as they are typically undercoordinated materials, which makes them electrochemically active catalysts. Recent studies have reported that lowering the coordination number of the metal site was demonstrated in most cases to increase the interaction between CO_2 molecules and the metal sites;[51] however, the coordination number also affects the stability of SMA sites dispersed in the carbonaceous support. DFT calculations have revealed that a coordination number of 4 is optimal for stabilizing late transition SMAs such as Ni, Fe, and Co in a configuration of N-doped graphene. It was also speculated that the utilization of ligands to tune the energy required for CO_2 binding and the energy level of *d*-orbitals can also improve the activity of SMAs.[52]

2.8.3.1 Synthetic approaches of SMAs

The fabrication of SMA electrocatalysts for CO_2 electroreduction involves using a conductive carbon-based substrate to deposit metal atoms and coordination elements. Various

strategies are followed to produce atomically dispersed metal sites, such as physical deposition, electrochemical deposition, as well as wet-chemistry pyrolysis. The preparation of this class of materials comprises multiple synthetic steps, including preparing the carbon support and impregnation of the active sites and coordination elements. SMAs synthetic procedures could be categorized into three main approaches: (I) SMAs impregnation on a modified carbonaceous substrate, where the coordination elements and SMAs are deposited in separate procedures; (II) Co-impregnation of coordination elements and SMAs on a carbonaceous substrate, whereby these sites are generated in one process simultaneously; and (III) One-pot preparation method of SMAs and carbon substrate in a one-step procedure.[50]

2.8.3.2 SMAs impregnation in a modified carbonaceous support

This synthetic route involves two different steps starting with the synthesis of carbon substrate doped with coordination elements such as N, S, or O, subsequently, metal atoms are impregnated on the formed skeleton in the second step. Through this approach, fine-tuning of the catalyst composition and structure could be achieved by controlling the carbon support, coordination elements, and active metal sites separately. Either a post-treatment route or direct synthesis could be used to prepare carbon substrates doped with coordination elements. For instance, chemical vapour deposition is being employed using H_2 to synthesize N-doped graphene structure, where methane (CH_4) and ammonia (NH_3) are utilized as sources of carbon and nitrogen, respectively. Following this procedure, a major configuration of graphitic-N is formed with minor species of pyridinic-N and pyrrolic-N reported. Generally, nitrogen and carbon sources play an essential role in the composition and structure of the formed modified carbon substrate. A pure pyridinic-N configuration has been obtained by Luo et al.[53] by employing H_2, ethylene, and ammonia gas and achieved 16wt% of N-content in the developed structure. This wt% is much higher than most of

the recently reported wt% of N-graphene supports. Wang et al. have used poly(methylmethacrylate) and imidazole ($C_3H_4N_2$) as carbon and nitrogen source, respectively in modulating the structure of N-doped graphene structure to obtain pyrrolic-N configuration. Modulating N-configuration could be also achieved by the post-treatment approach, whereas N-atoms are impregnated in prepared carbon support.[54] To introduce N-sites to a carbon skeleton, there are three different procedures, which includes nitrogen plasma[55], nitrogen ion implantation[56], ammonia exposure[57]. Metal deposition on carbon substrate could be achieved using different routes such as photochemical reduction, thermal treatment, physical deposition, and mechanical ball-milling.

For example, atomic layer deposition (ALD) is a commonly used approach that is being employed for metal deposition in N-doped graphene. Stambula et al.[58] have controlled the formation of Pt-SMAs via ALD up to 100 cycles without the agglomeration of the SMAs to nanoparticles after 100 cycles, a significant number of Pt-based particles were observed after 100 ALD cycles due to the agglomeration of the formed SMAs to Pt-particles. Despite the wide ability of the ALD technique to impregnate metal sites into N-doped graphene structures, and produce SMAs catalysts, however, its applicability of it in large-scale synthesis is restricted, that prevent its further employment of it at the industrial level. The photochemical reduction method, whereas ultraviolet light is used to reduce the metal ion, is another effective procedure for the metal deposition into modified graphene support. N-doped carbon impregnated with Pt single sites have been developed by Liu et al using a photochemical solid phase procedure with a well-controlled configuration and without forming Pt particles. In this approach, Pt adsorption onto the carbon support has been performed by dispersing the N-doped carbon substrate in a Pt-precursor solution. Subsequently, the Pt-doped carbon substrate was illuminated by ultraviolet light to generate Pt-

SMAs whereby the Pt wt% was 3.8%.[59] The ball milling technique is inducing chemical bonding and reconstructs the material surface by transferring the kinetic energy generated from a high-speed ball to the surface of the material. For instance, Fe-SMAs electrocatalysts have been prepared by ball milling a mixture of N-doped graphene and iron phthalocyanine with a metal loading of 4 wt%. This approach has been further applied to prepare other transition metal SMAs such as Co, Mn, Cu, and Ni.[60] On the other hand, the chemical deposition method mainly relies on the chemical reduction or thermal treatment of metal cations impregnated in a modified carbon support. Various SMA electrocatalysts have been developed with controlling the metal loading using a chemical deposition approach, such as Ni, Mn, Co, and Cu **(Figure 2.6a).**[61]

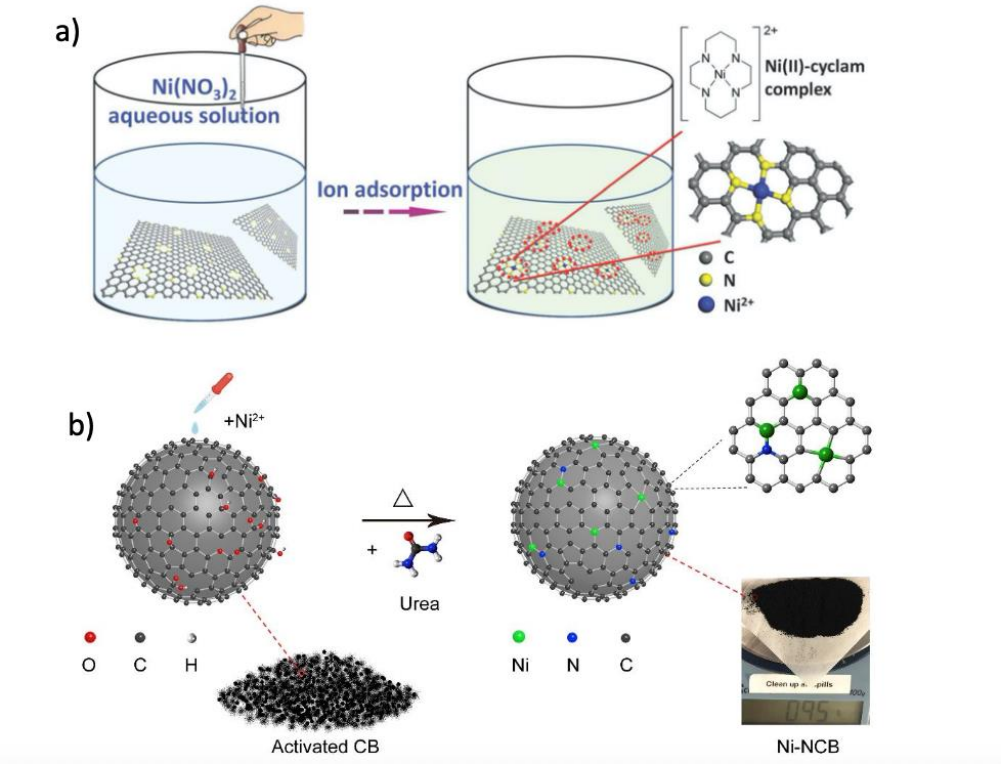

Figure 2-6 a) Schematic illustration of immobilized transition metal ions on N-doped graphene via ion adsorption. The inset compares the structure of Ni^{2+}@NG and Ni(II)-cyclam of Ni and N on activated carbon black (CB) to Ni SMA catalysts, (b) co-deposition of Ni and N on activated carbon black (CB) to Ni SMA catalysts. Reproduced with permission from references[50].

Following this approach, and in a single process, both coordination elements and metal sites are generated on the carbon substrate. This route uses a predeposition method to one of the precursors on the carbon substrate, subsequently, microwave radiation or pyrolysis process is conducted in the presence of the other precursors, and eventually, both metal and coordination elements are incorporated into the matrix. Zheng et al.[62] have developed Ni SMAs by the predeposition of Ni cations on a commercially available carbon black support, followed by a pyrolysis step of Ni-doped carbon black in the presence of urea as an N-source **(Figure 2.6b)**. Zhao and co-workers have prepared a series of transition metal SMAs such as Ni, Mn, Fe, Co, Pt, Cu, and Mo by depositing the metal sites on glucose support, careful grinding in the presence of Melamine as N-precursor, and pyrolyzing the mixture at 800°C. The co-impregnation method also could be performed using gas precursors such as hydrogen sulfide and ammonia as reported by Tour et al, whereas Co-SMAs-doped N-graphene was successfully prepared.[63]

2.8.3.3 One-pot preparation method of SMAs

In this synthetic approach, carbon support, coordination elements, and metal precursors are thermally treated at elevated temperatures to generate SMAs. Metal-organic frameworks (MOFs) – a crystalline class of materials that demonstrates the tunable chemical structure and high surface area – are being extensively employed as a precursor to synthesize SMAs. MOFs exhibit unique properties such as the ability to precisely control the metal deposition and the presence of an organic ligand that could act as a precursor for both carbon and nitrogen.[64] MOF-like structure carbon skeletons are generated by the thermal decomposition of MOFs at high temperatures. The produced MOF-like structure was found to exhibit most of MOF's features such as extended surface area and porosity.[65, 66] Under a pyrolysis environment, MOF metal ions/clusters were found

to migrate along the formed carbon skeleton and attach to the surface defects such as S and N to produce SMAs. Different key factors are influencing producing SMAs using MOF precursors, that includes the metal ion concentration, metal type, N-species, and MOF pores. Pyrolysis conditions such as temperature, ramp, and atmosphere also have an impact on this synthetic procedure. Zitolo et al have done the first attempt at producing SMAs via MOF structure. Their synthesis comprises two synthetic steps, first is a ball milling of a mixture of 1,10 phenanthroline, Zeolitic imidazole framework (ZIF-8), and Fe^{2+} acetate in a zirconium oxide crucible, followed by thermal treatment of the resulting composite at 1050°C under inert atmosphere.[67] Another route has been reported by Jiao et al,[68] whereas a mixed ligands of Fe-tetrakis (4-carboxyphenyl) porphyrin (Fe-TCPP) and H_2-TCPP to produce Fe SMAs. Optimizing the Fe concentration was achieved by changing the ratio of Fe-TCPP and H_2-TCPP **(Figure 2.7a)**. An additional strategy was provided by Chen et al[69] who have explored the ionic exchange between Zn^{2+} sites and Ni^{2+} at elevated temperatures when using ZIF-8 impregnated with Ni ions as a precursor **(Figure 2.7c)**, however, optimizing the Ni ions content during synthesis pathway is a significant factor, increasing the Ni content would result in forming Ni-based particles instead of SMAs.

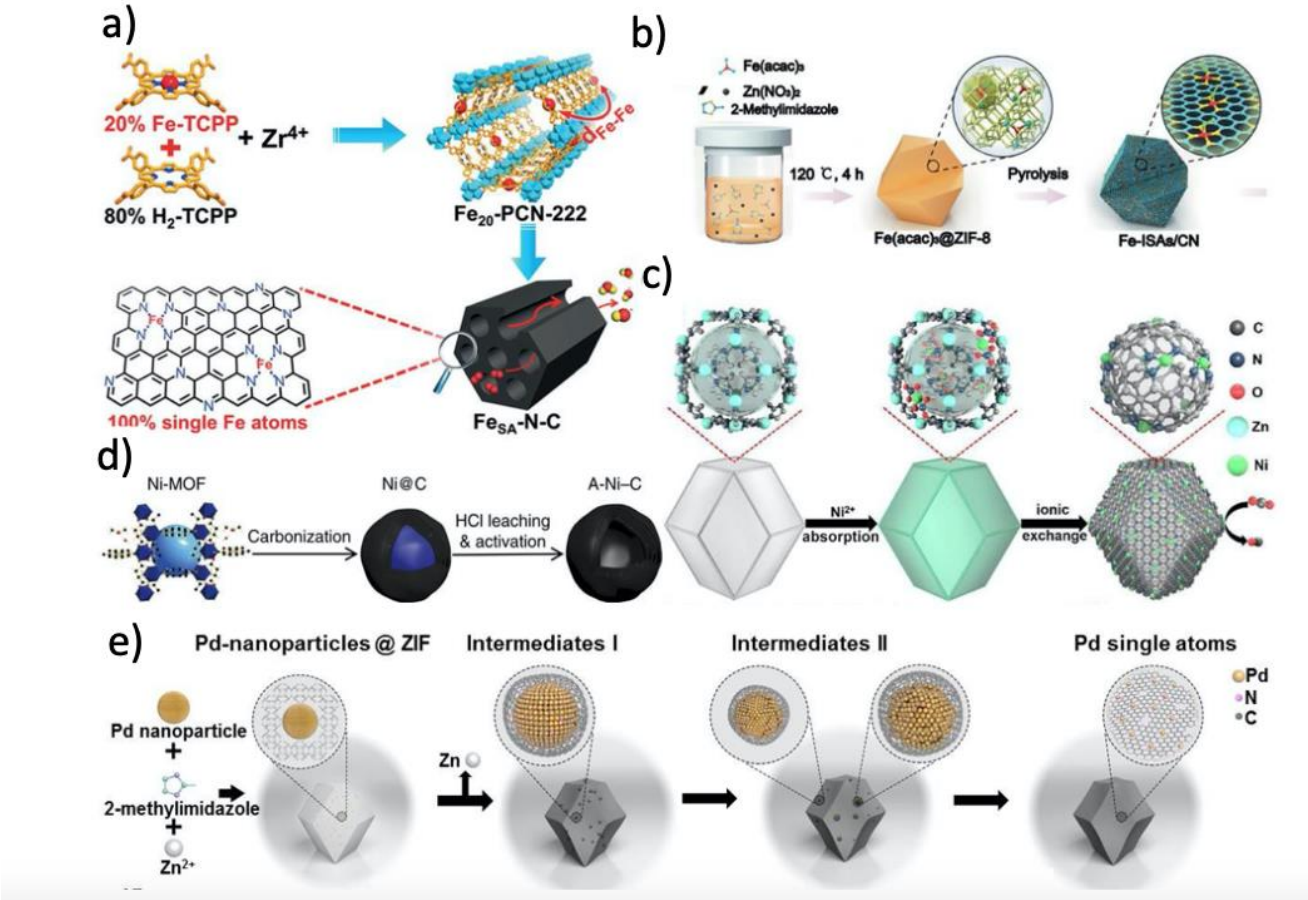

Figure 2-7 a) A schematic of Fe-SMAs/N-C electrocatalyst synthesized using a mixed-ligand method, b) An illustration of Fe-SMAs/MOF-NCs formation through the co-pyrolysis of cage-encapsulated precursor. (c) Ni-SMAs/MOF-NCs formation scheme illustrating the ionic exchange; d) Schematic representation of the electrochemical activation process of preparing the Ni-SMAs/MOF-NCs. (e) Demonstration of the Pd NPs transformation to single atoms and characterization measurements of atomically dispersed Pd. Reproduced with permission from ref [50].

Optimizing the pyrolysis conditions is crucial in producing MOF-based SMAs. Recent studies have revealed that thermal treatment of M-ZIF-8 where (M: Au, Pd, Pt) resulted in the transformation of metal-based nano/micro-particles to single atoms as illustrated in **Figure 2.7e**. This transformation was explained in three main mechanistic steps, initially, the metal nano/microparticle's diameter increases gradually at elevated temperature (900°C) which led to reducing the nano/microparticle number due to the coexistence of atomization and sintering. With

raising the temperature to 1000°C, the rate of either atomization or sintering rapidly increases, whereby these metallic nano/microparticles are supposed to disappear/vaporize at such elevated temperatures, followed by the diffusion of the mobile M-atoms through the MOF skeleton and associated to the N-defects existed in the carbon structure to form SMAs. Another approach to produce SMAs is through the electrochemical activation[70] as shown in **Figure 2.7d**, however, this methodology has not been investigated by other researchers to date.

2.8.4 Structure-performance relationship of SMA in CO_2R

The nature of the coordination elements and active sites are the two key factors that impact the behaviour of single-metal atom electrocatalysts in CO_2 electroreduction.

2.8.4.1 Impact of the nature of active sites

Product selectivity during CO_2R relies mainly on the characteristics of the active sites. Commonly, the structure of the SMAs is identified as a metal atom coordinated to 4 pyridinic-N from the carbon skeleton.

Ni-single atoms electrocatalysts in CO_2R

One of the most investigated SMAs in CO_2R is Ni-based SMAs whereas the major product is carbon monoxide (CO). Initially, Lie et al [71] investigated exclusive Ni-pyridinic-N_4 sites for CO_2R as shown in **Figure 2.8a**. They confirmed the presence of single Ni sites by extended X-ray absorption fine structure (EXAFS) measurements and tried to visualize them using high-angle annular dark-field STEM (HAADF-STEM) images (**Figure 2.8b**). The group claimed that HER was suppressed significantly which is contrary to Ni-based nano/microparticles behaviour that favours HER over CO_2R. They also carried out DFT calculations to obtain more insights into their developed materials. Their findings revealed a more positive value of the thermodynamic

potentials for carbon dioxide reduction and H_2 evolution ($UL(CO_2) - UL(H_2)$) on $Ni{-}N_4{-}C$, suggesting a suppression of the competitive HER and high catalytic performance for CO_2 conversion to CO. They also found that $Ni{-}N_4{-}C$ favors *COOH formation which enhances the production of CO (**Figure 2.8c**). They verified their prediction experimentally and obtained near unity CO production at 28.6 mA/cm^2 at -0.81V vs RHE, which is better than the state-of-the-art catalysts such as Ag and Au using the same electrochemical setup. [72, 73] Bi et al. and Cheng et al. have developed Ni^{2+}@NG and Ni^{2+} on N-doped carbon nanotubes SMAs for CO_2R, respectively.[74, 75] They also obtained very high selectivity towards CO production. Both studies have significantly different Ni loading in the developed catalysts, Cheng et al. have 20 ± 4 wt% Ni content while Bi et al. content is less than 1 wt%. Surprisingly, both catalysts have similar activities, suggesting that some of the generated Ni-SMAs were not catalytically active for CO_2R. Ni-SMAs demonstrate improved catalytic activity towards CO production compared to pristine carbon materials due to the lower interfacial charge-transfer resistance of Ni-SMAs as illustrated in **Figure 2.8d**, which significantly enhances the kinetics of CO_2 electroreduction. Generally, most of the developed Ni-based SMAs electrocatalysts display stable Faradaic efficiencies and current densities for up to 10 hours without the observing aggregation of Ni-SMAs to Ni-nano/microparticles. It also worth mentioning that Ni^{2+} sites showed better selectivity towards CO during CO_2R compared to Fe^{2+}

and Co^{2+} metal sites. This phenomenon was linked to the strong binding between the Co^{2+} and Fe^{2+} metal sites, and CO molecules, resulting in surface poisoning and favouring HER.

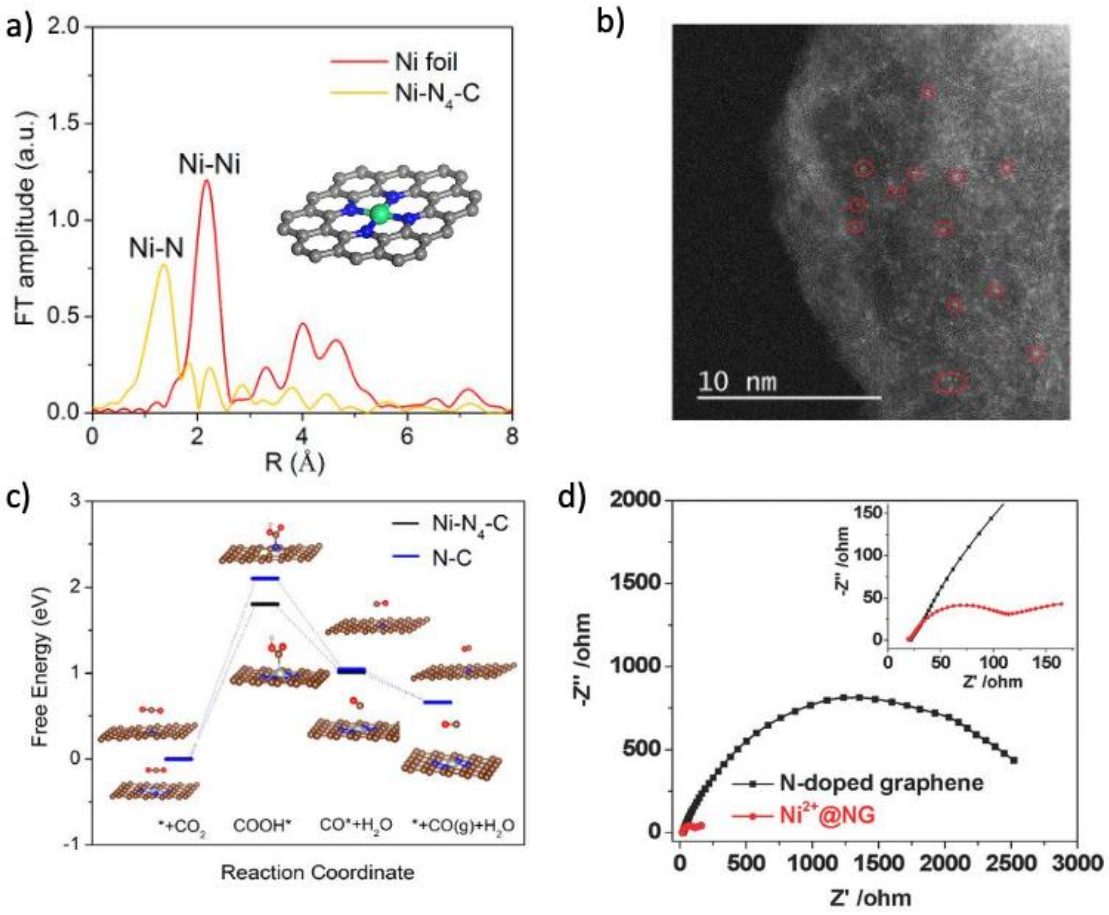

Figure 2-8 a) Ni K-edge EXAFS measurements of Ni–N_4–C (inset is their proposed structure); b) Ni−N_4−C HAADF-STEM image; c) Ni−N_4−C and N−C free energy diagram of CO_2 reduction calculated by DFT. d) Comparison of Nyquist plots of Ni^{2+}@NG and N-doped graphene. Reproduced with permission from reference[50].

2.8.4.2 Impact of the N coordination environment

The local coordination environment displays a significant impact on the activity, selectivity, and stability of the developed electrocatalysts. While the configuration of M–N_4 with a pyridinic–N site is very common in most of the developed SMAs, however, other configurations such as M–N_4 with different types of N (graphitic or pyrrolic) and M–N_X–C_{4-X} have been

investigated. For instance, Ni-N_3C SMA electrocatalysts have been developed by Zhao et al and exhibited 71% of CO selectivity at a current density of 10.48mA/cm^2 at -1.0V vs RHE. These findings are significantly lower than those resulting from Ni-N_4 configuration, illustrating the impact of the coordination environment on the overall activity of the developed catalysts in CO_2R.[76] Furthermore, researchers started to examine the impact of other N-types on the catalyst performance during CO_2R. They found that M-pyrrolic-N_4 coordination exhibits improved selectivity towards C_{2+} products compared to producing CO over M-pyridinic-N_4.

2.8.5 Reaction Mechanism of CO_2R on SMAs

Generally, extensive efforts have been exerted to investigate the CO_2 electroreduction mechanism by either computational DFT[77-80] methods or *in-situ* spectroscopic tools such as in-situ IR and Raman.[81-84] However, a distinct understanding of some mechanistic pathways and reaction intermediates is still required. The electroreduction of CO_2 to C_{2+} products has three possible bonding formations, which includes O–H, C–H hydrogenation, and C–C coupling which is considered the most critical step in this reaction. Several mechanisms have been hypothesized for the coupling of C–C, for instance, the formation of *OCCOH OR *OCCHO through the coupling of *CO with hydrogenated *CO such as *CHO or *COH. Other mechanisms also proposed such as *CO dimerization and the formation of *OCCO, generating *HOCCOH through the coupling o hydrogenated *CO, and the formation of *HCCH, *CC, and *H_2CCH_2 by the coupling of deoxygenated carbonaceous intermediates (*CH, *C, *CH_2). Despite the intensive research that has been done on investigating C–C coupling step, however, it is still the most debatable mechanistic step in CO_2R. On the contrary, hydrogenation steps including C–H and O–H formation have been well–proposed to two distinct mechanistic pathways.[85] The first mechanism suggested the presence of electrons and water molecules results in generating hydrogen (Eley-

Ridal mechanism). The other one proposed that the *H species adsorbed on the catalyst surface is the reactant (Langmuir-Hinshelwood mechanism). Following this mechanism, an increased number of active sites is required to provide *H, while in the Eley-Ridal mechanism, the electrolyte provides the hydrogen. CO_2 reduction mechanistic pathways are commonly divided into C_1 and C_{2+} products, C_1 pathway includes formate and CO pathways, while C_{2+} goes through C-C coupling of *CO species. In most studies, it was hypothesized that producing formate results through the formation of *HCOO intermediate, which bounds via oxygen atoms to the catalyst surface. Thus, targeting formate production demands the presence of two adjacent sites with the same intrinsic characteristics for oxygen desorption. However, this might be challenging for SMAs where the active site is only one single metal atom bonded to different coordination elements (N, S, or O), while for those SMAs that produce formate, it was proposed that the key intermediate *CHOO configuration is different on the surface from traditional electrocatalysts. Also, it was demonstrated that for the first step of hydrogenation, the source and availability of *H on regular catalyst surfaces are governed by the electrolyte pH. As the polarity of the O–H and C–H bond is different, it was found that the electrolyte H^+ protons are less favored than the surface hydrogen, which consequently limits the ability of SMAs to produce formate. 121 On the contrary, producing CO during CO_2R is regulated by the intermediate *COOH formed via the mechanism of a proton-coupled electron transfer (PCET),[86] these species are bounded to the surface of the catalyst through C atoms. Afterwards, *CO species are formed via further hydrogenation of *COOH intermediate, the adsorption energy of these species on the catalysts controls whether they will undergo further reduction or desorb from the catalyst surface and produce CO. The catalytic activity of different metal catalysts is associated with the energy of adsorption of *CO on the metal sites through the scaling relationships.[87] *CO species were found to have strong adsorption energy on Pt and Ni,

leading to poisoning the active sites and enhancing the HER over CO_2R. On the contrary, *CO species are weakly bounded to the Au and Ag surfaces which favors the CO_2R and suppress HER, also, there are some metals that have intermediate *CO adsorption energy such as Cu which enables it to undergo further reduction and form C_{2+} products. On the other hand, SMAs – which have an undercoordination nature, leading to significant changes in their electronic structures – exhibit different scaling relationships and adsorption energies compared to bulk metal catalysts. Further, the CO_2R reaction mechanism and reaction energies of SMAs are not similar to the traditional metallic catalysts, most probably because of their distinct electronic structure. This difference impacts the overall performance and the catalytic activity of the catalysts in CO_2R. For example, under CO_2R conditions, Pt, Fe, and Ni bulk metals revealed poor activity towards CO2R while favoring HER.[88] In contrast, HER is significantly suppressed when using SMAs derived from the same metals while CO and formate are generated. Further, metallic Cu is commonly employed for hydrocarbon production, however, it was demonstrated that Cu SMAs are favoring CO formation and inhibiting the generation of C_{2+} products.[89]

2.8.6 Suppression of hydrogen evolution reaction on SMAs

Under CO_2 reduction conditions, hydrogen evolution reaction is the competing reaction and is commonly derived by various metallic electrocatalysts such as Co, Fe, and Ni. However, the employment of SMAs in CO_2R has revealed significant suppression of the competing HER. Two different mechanistic pathways are proposed for HER, which include Volmer−Heyrovsky and Volmer−Tafel pathways.[90] Initially, a Volmer reaction of a proton is provided by the electrolyte and an electron is driven, followed by the formation of *H adsorbed on the catalyst surface. Secondly, either Tafel's or Heyrovsky's mechanisms are applicable to the next reaction steps. In Tafel, another PCET step proceeds whereby a solvated proton provided by the electrolyte

interacts with the adsorbed *H species on the catalyst surface to produce H_2(g). While in the Heyrovsky mechanism, a new *H is formed by an interaction of the proton and electron, followed by a coupling reaction of the two adsorbed *H species to generate H_2(g).

$$*H + H^+ + e^- \xrightarrow{\text{Heyrovsky}} H_2(g)$$

$$*H + H^+ + e^- \xrightarrow{\text{Tafel}} 2*H \longrightarrow H_2(g)$$

A report by Skuĺason et al.[91] studied the HER mechanism on several metallic electrocatalysts using DFT calculations, their findings demonstrated the favorability of the Tafel mechanism over the Heyrovsky pathway, they also found that Pt – as a case study – exhibited an activation energy value of 0.55 eV at zero applied bias for HER through Tafel reaction, while Heyrovsky pathway showed higher activation energy value of 1.03 eV as illustrated in **Figure 2.9a and b**, respectively.

Further, other metals such as. Ni, Cu, Pt, Co, and Au have been investigated and revealed similar behaviour of favoring the Tafel pathway over Heyrovsky for HER. In SMAs, the presence of two adjacent active sites is precluded, leading to the exclusion of the Tafel pathway and enabling only the Heyrovsky mechanism with the large activation energy barrier, that results in suppressing the HER on SMAs compared to bulk metallic catalysts. In the context of the CO_2R mechanism, the first hydrogenation step can follow either Tafel or Heyrovsky pathways to generate the *COOH intermediate, whereas the latter mechanism has more applicability on SMAs derived catalysts. A recent study has used computational measurements to assess a metallic Fe catalyst and a porphyrin-

like Fe single-atom catalyst for both mechanisms.[90] Their results showed that Volmer−Tafel is the leading mechanism of metallic Fe towards HER, while the Volmer−Heyrovsky mechanism was dominant to drive HER as shown in **Figure 2.10**, which consequently limited HER on porphyrin-like Fe single-atom catalyst.

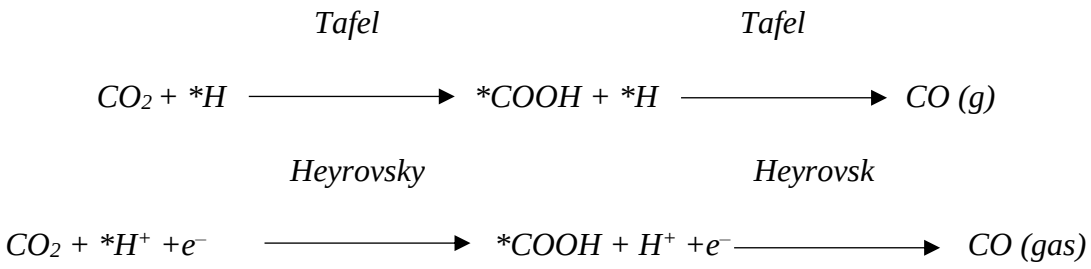

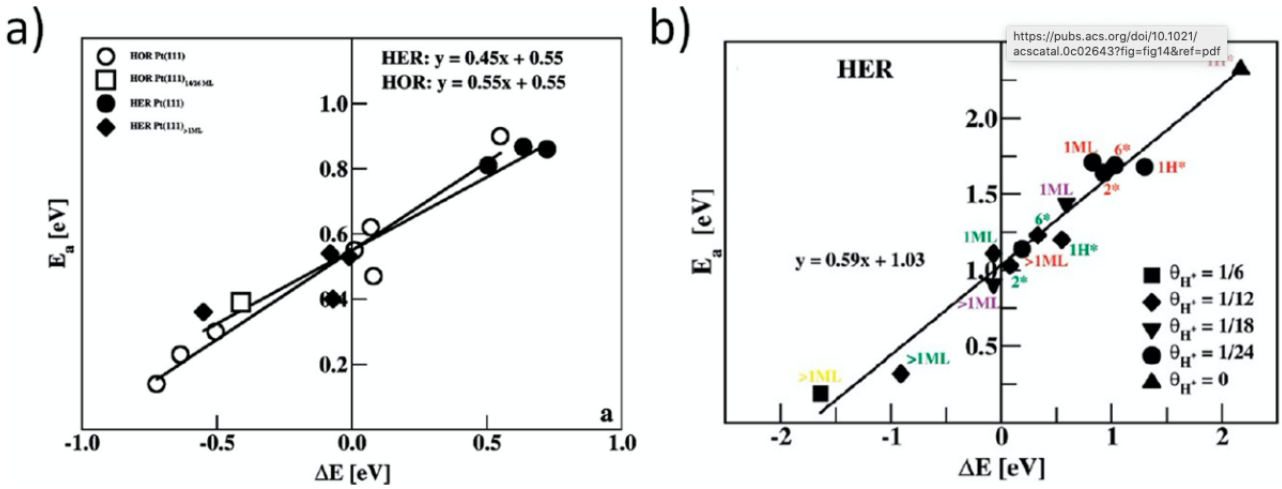

Figure 2-9 (a) HER activation barrier, Ea, on Pt(111) via the Tafel reaction as a function of the reaction energy, ΔE. X = 0.02. (b) HER activation barrier, E_a, on Pt(111) via the Heyrovsky reaction as a function of the reaction energy, ΔE. X = 0.15. Reproduced with permission from ref. [91]

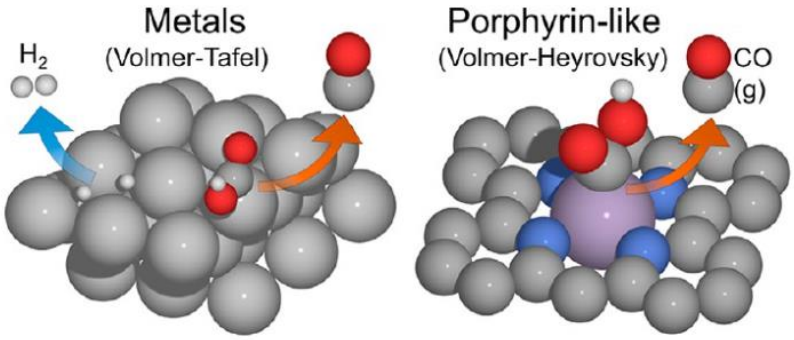

Figure 2-10 A schematic diagram illustrates the porphyrin-like structure (right) and the metal surface (left). Reproduced with permission from ref.[90]

References

1. Birdja, Y. Y.; Pérez-Gallent, E.; Figueiredo, M. C.; Göttle, A. J.; Calle-Vallejo, F.; Koper, M. T., Advances and challenges in understanding the electrocatalytic conversion of carbon dioxide to fuels. Nature Energy 2019, 4 (9), 732-745.

2. Gao, D.; Arán-Ais, R. M.; Jeon, H. S.; Cuenya, B. R., Rational catalyst and electrolyte design for CO_2 electroreduction towards multicarbon products. Nature Catalysis 2019, 2 (3), 198-210.

3. Singh, M. R.; Kwon, Y.; Lum, Y.; Ager III, J. W.; Bell, A. T., Hydrolysis of electrolyte cations enhances the electrochemical reduction of CO_2 over Ag and Cu. Journal of the American Chemical Society 2016, 138 (39), 13006-13012.

4. Nguyen, T. N.; Dinh, C.-T., Gas diffusion electrode design for electrochemical carbon dioxide reduction. Chemical Society Reviews 2020.

5. Seh, Z.; Kibsgaard, J.; Dickens, C.; Chorkendorff, I.; Norskov, J.; Jaramillo, T., Combining theory and experiment in electrocatalysis: Insights into materials design. Science 355, eaad4998. 2017.

6. Zhang, B.; Zheng, X.; Voznyy, O.; Comin, R.; Bajdich, M.; García-Melchor, M.; Han, L.; Xu, J.; Liu, M.; Zheng, L., Homogeneously dispersed multimetal oxygen-evolving catalysts. Science 2016, 352 (6283), 333-337.

7. Zheng, X.; Zhang, B.; De Luna, P.; Liang, Y.; Comin, R.; Voznyy, O.; Han, L.; De Arquer, F. P. G.; Liu, M.; Dinh, C.T., Theory-driven design of high-valence metal sites for water oxidation confirmed using in situ soft X-ray absorption. Nature chemistry 2018, 10(2),149.

8. Li, F.; Thevenon, A.; Rosas-Hernández, A.; Wang, Z.; Li, Y.; Gabardo, C. M.; Ozden, A.; Dinh, C. T.; Li, J.; Wang, Y., Molecular tuning of CO_2-to-ethylene conversion. Nature 2020, 577 (7791), 509-513.

9. Gabardo, C. M.; O'Brien, C. P.; Edwards, J. P.; McCallum, C.; Xu, Y.; Dinh, C.-T.; Li, J.; Sargent, E. H.; Sinton, D., Continuous carbon dioxide electroreduction to concentrated multi-carbon products using a membrane electrode assembly. Joule 2019, 3 (11), 2777-2791.

10. Weng, L.-C.; Bell, A. T.; Weber, A. Z., Towards membrane-electrode assembly systems for CO_2 reduction: a modeling study. Energy & Environmental Science 2019, 12 (6), 1950-1968.

11. Jouny, M.; Luc, W.; Jiao, F., High-rate electroreduction of carbon monoxide to multi-carbon products. Nature Catalysis 2018, 1 (10), 748-755.

12. Li, Y. C.; Zhou, D.; Yan, Z.; Gonçalves, R. H.; Salvatore, D. A.; Berlinguette, C. P.; Mallouk, T. E., Electrolysis of CO_2 to syngas in bipolar membrane-based electrochemical cells. ACS Energy Letters 2016, 1 (6), 1149-1153.

13. Wakerley, D.; Lamaison, S.; Wicks, J.; Clemens, A.; Feaster, J.; Corral, D.; Jaffer, S. A.; Sarkar, A.; Fontecave, M.; Duoss, E. B., Gas diffusion electrodes, reactor designs and key metrics of low-temperature CO2 electrolysers. Nature Energy 2022, 7 (2), 130-143.

14. Wang, L.; Nitopi, S. A.; Bertheussen, E.; Orazov, M.; Morales-Guio, C. G.; Liu, X.; Higgins, D. C.; Chan, K.; Nørskov, J. K.; Hahn, C., Electrochemical carbon monoxide reduction on polycrystalline copper: Effects of potential, pressure, and pH on selectivity toward multicarbon and oxygenated products. Acs Catalysis 2018, 8 (8), 7445-7454.

15. Hori, Y. i., Electrochemical CO_2 reduction on metal electrodes. In Modern aspects of electrochemistry, Springer: 2008; pp 89-189.

16. Resasco, J.; Chen, L. D.; Clark, E.; Tsai, C.; Hahn, C.; Jaramillo, T. F.; Chan, K.; Bell, A. T., Promoter effects of alkali metal cations on the electrochemical reduction of carbon dioxide. Journal of the American Chemical Society 2017, 139 (32), 11277-11287.

17. Singh, M. R.; Goodpaster, J. D.; Weber, A. Z.; Head-Gordon, M.; Bell, A. T., Mechanistic insights into electrochemical reduction of CO2 over Ag using density functional theory and transport models. Proceedings of the National Academy of Sciences 2017, 114 (42), E8812-E8821.

18. Hashiba, H.; Yotsuhashi, S.; Deguchi, M.; Yamada, Y., Systematic analysis of electrochemical CO_2 reduction with various reaction parameters using combinatorial reactors. ACS combinatorial science 2016, 18 (4), 203-208.

19. Clark, E. L.; Hahn, C.; Jaramillo, T. F.; Bell, A. T., Electrochemical CO_2 reduction over compressively strained CuAg surface alloys with enhanced multi-carbon oxygenate selectivity. Journal of the American Chemical Society 2017, 139 (44), 15848-15857.

20. Han, Z.; Kortlever, R.; Chen, H.-Y.; Peters, J. C.; Agapie, T., CO_2 reduction selective for $C\geq 2$ products on polycrystalline copper with N-substituted pyridinium additives. ACS central science 2017, 3 (8), 853-859.

21. Higgins, D.; Landers, A. T.; Ji, Y.; Nitopi, S.; Morales-Guio, C. G.; Wang, L.; Chan, K.; Hahn, C.; Jaramillo, T. F., Guiding electrochemical carbon dioxide reduction toward carbonyls using copper silver thin films with interphase miscibility. ACS Energy Letters 2018, 3 (12), 2947-2955.

22. Raciti, D.; Wang, C., Recent advances in CO_2 reduction electrocatalysis on copper. ACS Energy Letters 2018, 3 (7), 1545-1556.

23. Ulissi, Z. W.; Tang, M. T.; Xiao, J.; Liu, X.; Torelli, D. A.; Karamad, M.; Cummins, K.; Hahn, C.; Lewis, N. S.; Jaramillo, T. F., Machine-learning methods enable exhaustive searches for active bimetallic facets and reveal active site motifs for CO_2 reduction. Acs Catalysis 2017, 7 (10), 6600-6608.

24. Singh, M. R.; Clark, E. L.; Bell, A. T., Effects of electrolyte, catalyst, and membrane composition and operating conditions on the performance of solar-driven electrochemical reduction of carbon dioxide. Physical Chemistry Chemical Physics 2015, 17 (29), 18924-18936.

25. Greenblatt, J. B.; Miller, D. J.; Ager, J. W.; Houle, F. A.; Sharp, I. D., The technical and energetic challenges of separating (photo) electrochemical carbon dioxide reduction products. Joule 2018, 2 (3), 381-420.

26. De Arquer, F. P. G.; Dinh, C.-T.; Ozden, A.; Wicks, J.; McCallum, C.; Kirmani, A. R.; Nam, D.-H.; Gabardo, C.; Seifitokaldani, A.; Wang, X., CO_2 electrolysis to multicarbon products at activities greater than 1 A cm− 2. Science 2020, 367 (6478), 661-666.

27. Dinh, C.; Burdyny, T.; Kibria, M. G.; Sei, A., tokaldani, CM Gabardo, FP Garcıa de Arquer, A. Kiani, JP Edwards, P. De Luna, OS Bushuyev, C. Zou, R. Quintero-Bermudez, Y. Pang, D. Sinton and EH Sargent, Science 2018, 360, 783-787.

28. Gabardo, C.; Sei, A., tokaldani, JP Edwards, C.-T. Dinh, T. Burdyny, MG Kibria, CP O'Brien, EH Sargent and D. Sinton. Energy Environ. Sci 2018, 11, 2531-2539.

29. Dinh, C.-T.; García de Arquer, F. P.; Sinton, D.; Sargent, E. H., High rate, selective, and stable electroreduction of CO_2 to CO in basic and neutral media. ACS Energy Letters 2018, 3 (11), 2835-2840.

30. Xia, C.; Zhu, P.; Jiang, Q.; Pan, Y.; Liang, W.; Stavitski, E.; Alshareef, H. N.; Wang, H., Continuous production of pure liquid fuel solutions via electrocatalytic CO_2 reduction using solid-electrolyte devices. Nature Energy 2019, 4 (9), 776-785.

31. Nguyen, T. N.; Dinh, C.-T., Gas diffusion electrode design for electrochemical carbon dioxide reduction. Chemical Society Reviews 2020, 49 (21), 7488-7504.

32. Gerhardt, M. R.; Pant, L. M.; Bui, J. C.; Crothers, A. R.; Ehlinger, V. M.; Fornaciari, J. C.; Liu, J.; Weber, A. Z., Method—Practices and pitfalls in voltage breakdown analysis of electrochemical energy-conversion systems. Journal of the Electrochemical Society 2021, 168 (7), 074503.

33. Hansen, K. U.; Cherniack, L. H.; Jiao, F., Voltage Loss Diagnosis in CO_2 Electrolyzers Using Five-Electrode Technique. ACS Energy Letters 2022, 7 (12), 4504-4511.

34. Burdyny, T.; Smith, W. A., CO_2 reduction on gas-diffusion electrodes and why catalytic performance must be assessed at commercially-relevant conditions. Energy & Environmental Science 2019, 12 (5), 1442-1453.

35. Luo, M.; Wang, Z.; Li, Y. C.; Li, J.; Li, F.; Lum, Y.; Nam, D.-H.; Chen, B.; Wicks, J.; Xu, A., Hydroxide promotes carbon dioxide electroreduction to ethanol on copper via tuning of adsorbed hydrogen. Nature communications 2019, 10 (1), 1-7.

36. Liu, M.; Pang, Y.; Zhang, B.; De Luna, P.; Voznyy, O.; Xu, J.; Zheng, X.; Dinh, C. T.; Fan, F.; Cao, C., Enhanced electrocatalytic CO_2 reduction via field-induced reagent concentration. Nature 2016, 537 (7620), 382-386.

37. Saberi Safaei, T.; Mepham, A.; Zheng, X.; Pang, Y.; Dinh, C.-T.; Liu, M.; Sinton, D.; Kelley, S. O.; Sargent, E. H., High-density nanosharp microstructures enable efficient CO2 electroreduction. Nano letters 2016, 16 (11), 7224-7228.

38. Rosen, J.; Hutchings, G. S.; Lu, Q.; Forest, R. V.; Moore, A.; Jiao, F., Electrodeposited Zn dendrites with enhanced CO selectivity for electrocatalytic CO_2 reduction. Acs Catalysis 2015, 5 (8), 4586-4591.

39. Dutta, A.; Morstein, C. E.; Rahaman, M.; Cedeño López, A.; Broekmann, P., Beyond copper in CO_2 electrolysis: effective hydrocarbon production on silver-nanofoam catalysts. ACS Catalysis 2018, 8 (9), 8357-8368.

40. Dinh, C.-T.; Burdyny, T.; Kibria, M. G.; Seifitokaldani, A.; Gabardo, C. M.; García de Arquer, F. P.; Kiani, A.; Edwards, J. P.; De Luna, P.; Bushuyev, O. S., CO_2 electroreduction to ethylene via hydroxide-mediated copper catalysis at an abrupt interface. Science 2018, 360 (6390), 783-787.

41. Li, F.; Thevenon, A.; Rosas-Hernández, A.; Wang, Z.; Li, Y.; Gabardo, C. M.; Ozden, A.; Dinh, C. T.; Li, J.; Wang, Y., Molecular tuning of CO_2-to-ethylene conversion. Nature 2020, 577 (7791), 509-513.

42. Wang, X.; Wang, Z.; García de Arquer, F. P.; Dinh, C.-T.; Ozden, A.; Li, Y. C.; Nam, D.-H.; Li, J.; Liu, Y.-S.; Wicks, J., Efficient electrically powered CO_2-to-ethanol via suppression of deoxygenation. Nature Energy 2020, 5 (6), 478-486.

43. Li, Y. C.; Wang, Z.; Yuan, T.; Nam, D.-H.; Luo, M.; Wicks, J.; Chen, B.; Li, J.; Li, F.; De Arquer, F. P. G., Binding site diversity promotes CO_2 electroreduction to ethanol. Journal of the American Chemical Society 2019, 141 (21), 8584-8591.

44. Zhong, M.; Tran, K.; Min, Y.; Wang, C.; Wang, Z.; Dinh, C.-T.; De Luna, P.; Yu, Z.; Rasouli, A. S.; Brodersen, P., Accelerated discovery of CO_2 electrocatalysts using active machine learning. Nature 2020, 581 (7807), 178-183.

45. Dinh, C.-T.; Burdyny, T.; Kibria, M. G.; Seifitokaldani, A.; Gabardo, C. M.; De Arquer, F. P. G.; Kiani, A.; Edwards, J. P.; De Luna, P.; Bushuyev, O. S., CO_2 electroreduction to ethylene via hydroxide-mediated copper catalysis at an abrupt interface. Science 2018, 360 (6390), 783-787.

46. Wang, Y.; Wang, Z.; Dinh, C.-T.; Li, J.; Ozden, A.; Kibria, M. G.; Seifitokaldani, A.; Tan, C.-S.; Gabardo, C. M.; Luo, M., Catalyst synthesis under CO_2 electroreduction favours faceting and promotes renewable fuels electrosynthesis. Nature Catalysis 2020, 3 (2), 98-106.

47. Lu, X.-L.; Rong, X.; Zhang, C.; Lu, T.-B., Carbon-based single-atom catalysts for CO_2 electroreduction: progress and optimization strategies. Journal of Materials Chemistry A 2020, 8 (21), 10695-10708.

48. Lü, F.; Bao, H.; Mi, Y.; Liu, Y.; Sun, J.; Peng, X.; Qiu, Y.; Zhuo, L.; Liu, X.; Luo, J., Electrochemical CO_2 reduction: from nanoclusters to single atom catalysts. Sustainable Energy & Fuels 2020, 4 (3), 1012-1028.

49. Su, X.; Yang, X.-F.; Huang, Y.; Liu, B.; Zhang, T., Single-atom catalysis toward efficient CO_2 conversion to CO and formate products. Accounts of chemical research 2018, 52 (3), 656-664.

50. Nguyen, T. N.; Salehi, M.; Le, Q. V.; Seifitokaldani, A.; Dinh, C. T., Fundamentals of electrochemical CO_2 reduction on single-metal-atom catalysts. ACS Catalysis 2020, 10 (17), 10068-10095.

51. Wang, X.; Chen, Z.; Zhao, X.; Yao, T.; Chen, W.; You, R.; Zhao, C.; Wu, G.; Wang, J.; Huang, W., Regulation of coordination number over single Co sites: triggering the efficient electroreduction of CO_2. Angewandte Chemie 2018, 130 (7), 1962-1966.

52. Zhou, Y.; Gao, G.; Li, Y.; Chu, W.; Wang, L.-W., Transition-metal single atoms in nitrogen-doped graphenes as efficient active centers for water splitting: a theoretical study. Physical Chemistry Chemical Physics 2019, 21 (6), 3024-3032.

53. Luo, Z.; Lim, S.; Tian, Z.; Shang, J.; Lai, L.; MacDonald, B.; Fu, C.; Shen, Z.; Yu, T.; Lin, J., Pyridinic N doped graphene: synthesis, electronic structure, and electrocatalytic property. Journal of Materials Chemistry 2011, 21 (22), 8038-8044.

54. Wang, Z.; Chen, Y.; Li, P.; Zhou, J.; He, J.; Zhang, W.; Guo, Z.; Li, Y.; Dong, M., Modulation of N-bonding configurations and their influence on the electrical properties of nitrogen-doped graphene. RSC advances 2016, 6 (95), 92682-92687.

55. Iyer, G. R.; Wang, J.; Wells, G.; Bradley, M. P.; Borondics, F., Nanoscale imaging of freestanding nitrogen doped single layer graphene. Nanoscale 2015, 7 (6), 2289-2294.

56. Telychko, M.; Mutombo, P.; Ondracek, M.; Hapala, P.; Bocquet, F. C.; Kolorenc, J.; Vondracek, M.; Jelinek, P.; Svec, M., Achieving high-quality single-atom nitrogen doping of graphene/SiC (0001) by ion implantation and subsequent thermal stabilization. ACS nano 2014, 8 (7), 7318-7324.

57. Yazici, M. S.; Azder, M. A.; Salihoglu, O., CVD grown graphene as catalyst for acid electrolytes. International Journal of Hydrogen Energy 2018, 43 (23), 10710-10716.

58. Stambula, S.; Gauquelin, N.; Bugnet, M.; Gorantla, S.; Turner, S.; Sun, S.; Liu, J.; Zhang, G.; Sun, X.; Botton, G. A., Chemical structure of nitrogen-doped graphene with single platinum atoms and atomic clusters as a platform for the PEMFC electrode. The Journal of Physical Chemistry C 2014, 118 (8), 3890-3900.

59. Li, T.; Liu, J.; Song, Y.; Wang, F., Photochemical solid-phase synthesis of platinum single atoms on nitrogen-doped carbon with high loading as bifunctional catalysts for hydrogen evolution and oxygen reduction reactions. ACS catalysis 2018, 8 (9), 8450-8458.

60. Cui, X.; Xiao, J.; Wu, Y.; Du, P.; Si, R.; Yang, H.; Tian, H.; Li, J.; Zhang, W. H.; Deng, D., A graphene composite material with single cobalt active sites: a highly efficient counter electrode for dye-sensitized solar cells. Angewandte Chemie International Edition 2016, 55 (23), 6708-6712.

61. Huang, K.; Zhang, L.; Xu, T.; Wei, H.; Zhang, R.; Zhang, X.; Ge, B.; Lei, M.; Ma, J.-Y.; Liu, L.-M., − 60° C solution synthesis of atomically dispersed cobalt electrocatalyst with superior performance. Nature communications 2019, 10 (1), 606.

62. Lai, Q.; Zhao, Y.; Zhu, J.; Liang, Y.; He, J.; Chen, J., Directly anchoring highly dispersed copper sites on nitrogen-doped carbon for enhanced oxygen reduction electrocatalysis. ChemElectroChem 2018, 5 (14), 1822-1826.

63. Fei, H.; Dong, J.; Arellano-Jiménez, M. J.; Ye, G.; Dong Kim, N.; Samuel, E. L.; Peng, Z.; Zhu, Z.; Qin, F.; Bao, J., Atomic cobalt on nitrogen-doped graphene for hydrogen generation. Nature communications 2015, 6 (1), 1-8.

64. Zhou, H.-C.; Long, J. R.; Yaghi, O. M., Introduction to metal–organic frameworks. ACS Publications: 2012; Vol. 112, pp 673-674.

65. Liu, B.; Shioyama, H.; Akita, T.; Xu, Q., Metal-organic framework as a template for porous carbon synthesis. Journal of the American Chemical Society 2008, 130 (16), 5390-5391.

66. Jiang, H.-L.; Liu, B.; Lan, Y.-Q.; Kuratani, K.; Akita, T.; Shioyama, H.; Zong, F.; Xu, Q., From metal–organic framework to nanoporous carbon: toward a very high surface area and hydrogen uptake. Journal of the American Chemical Society 2011, 133 (31), 11854-11857.

67. Zitolo, A.; Goellner, V.; Armel, V.; Sougrati, M.-T.; Mineva, T.; Stievano, L.; Fonda, E.; Jaouen, F., Identification of catalytic sites for oxygen reduction in iron-and nitrogen-doped graphene materials. Nature materials 2015, 14 (9), 937-942.

68. Jiao, L.; Wan, G.; Zhang, R.; Zhou, H.; Yu, S. H.; Jiang, H. L., From metal–organic frameworks to single-atom Fe implanted N-doped porous carbons: efficient oxygen reduction in both alkaline and acidic media. Angewandte Chemie 2018, 130 (28), 8661-8665.

69. Chen, Y.; Ji, S.; Wang, Y.; Dong, J.; Chen, W.; Li, Z.; Shen, R.; Zheng, L.; Zhuang, Z.; Wang, D., Isolated single iron atoms anchored on N-doped porous carbon as an efficient electrocatalyst for the oxygen reduction reaction. Angewandte Chemie International Edition 2017, 56 (24), 6937-6941.

70. Fan, L.; Liu, P. F.; Yan, X.; Gu, L.; Yang, Z. Z.; Yang, H. G.; Qiu, S.; Yao, X., Atomically isolated nickel species anchored on graphitized carbon for efficient hydrogen evolution electrocatalysis. Nature communications 2016, 7 (1), 10667.

71. Li, X.; Bi, W.; Chen, M.; Sun, Y.; Ju, H.; Yan, W.; Zhu, J.; Wu, X.; Chu, W.; Wu, C., Exclusive Ni–N4 sites realize near-unity CO selectivity for electrochemical CO_2 reduction. Journal of the American Chemical Society 2017, 139 (42), 14889-14892.

72. Lu, Q.; Rosen, J.; Zhou, Y.; Hutchings, G. S.; Kimmel, Y. C.; Chen, J. G.; Jiao, F., A selective and efficient electrocatalyst for carbon dioxide reduction. Nature communications 2014, 5 (1), 3242.

73. Chen, Y.; Li, C. W.; Kanan, M. W., Aqueous CO_2 reduction at very low overpotential on oxide-derived Au nanoparticles. Journal of the American Chemical Society 2012, 134 (49), 19969-19972.

74. Bi, W.; Li, X.; You, R.; Chen, M.; Yuan, R.; Huang, W.; Wu, X.; Chu, W.; Wu, C.; Xie, Y., Surface immobilization of transition metal ions on nitrogen-doped graphene realizing high-efficient and selective CO_2 reduction. Advanced Materials 2018, 30 (18), 1706617.

75. Cheng, Y.; Zhao, S.; Johannessen, B.; Veder, J. P.; Saunders, M.; Rowles, M. R.; Cheng, M.; Liu, C.; Chisholm, M. F.; De Marco, R., Atomically dispersed transition metals on carbon nanotubes with ultrahigh loading for selective electrochemical carbon dioxide reduction. Advanced Materials 2018, 30 (13), 1706287.

76. Zhao, C.; Dai, X.; Yao, T.; Chen, W.; Wang, X.; Wang, J.; Yang, J.; Wei, S.; Wu, Y.; Li, Y., Ionic exchange of metal–organic frameworks to access single nickel sites for efficient electroreduction of CO_2. Journal of the American Chemical Society 2017, 139 (24), 8078-8081.

77. Chen, J. G., Electrochemical CO_2 reduction via low-valent nickel single-atom catalyst. Joule 2018, 2 (4), 587-589.

78. Jeong, H.-Y.; Balamurugan, M.; Choutipalli, V. S. K.; Jeong, E.-s.; Subramanian, V.; Sim, U.; Nam, K. T., Achieving highly efficient CO_2 to CO electroreduction exceeding 300 mA cm^{-2} with single-atom nickel electrocatalysts. Journal of Materials Chemistry A 2019, 7 (17), 10651-10661.

79. Ju, W.; Bagger, A.; Hao, G.-P.; Varela, A. S.; Sinev, I.; Bon, V.; Roldan Cuenya, B.; Kaskel, S.; Rossmeisl, J.; Strasser, P., Understanding activity and selectivity of metal-nitrogen-doped carbon catalysts for electrochemical reduction of CO_2. Nature communications 2017, 8 (1), 944.

80. Pan, F.; Zhang, H.; Liu, Z.; Cullen, D.; Liu, K.; More, K.; Wu, G.; Wang, G.; Li, Y., Atomic-level active sites of efficient imidazolate framework-derived nickel catalysts for CO_2 reduction. Journal of Materials Chemistry A 2019, 7 (46), 26231-26237.

81. Baruch, M. F.; Pander III, J. E.; White, J. L.; Bocarsly, A. B., Mechanistic insights into the reduction of CO_2 on tin electrodes using in situ ATR-IR spectroscopy. Acs Catalysis 2015, 5 (5), 3148-3156.

82. Firet, N. J.; Smith, W. A., Probing the reaction mechanism of CO_2 electroreduction over Ag films via operando infrared spectroscopy. Acs Catalysis 2017, 7 (1), 606-612.

83. Gunathunge, C. M.; Li, X.; Li, J.; Hicks, R. P.; Ovalle, V. J.; Waegele, M. M., Spectroscopic observation of reversible surface reconstruction of copper electrodes under CO_2 reduction. The Journal of Physical Chemistry C 2017, 121 (22), 12337-12344.

84. Heyes, J.; Dunwell, M.; Xu, B., CO_2 reduction on Cu at low overpotentials with surface-enhanced in situ spectroscopy. The Journal of Physical Chemistry C 2016, 120 (31), 17334-17341.

85. Weinberg, W. H., Eley− Rideal surface chemistry: direct reactivity of gas phase atomic hydrogen with adsorbed species. Accounts of chemical research 1996, 29 (10), 479-487.

86. Huynh, M. H. V.; Meyer, T. J., Proton-coupled electron transfer. Chemical Reviews 2007, 107 (11), 5004-5064.

87. Shi, C.; Hansen, H. A.; Lausche, A. C.; Nørskov, J. K., Trends in electrochemical CO_2 reduction activity for open and close-packed metal surfaces. Physical Chemistry Chemical Physics 2014, 16 (10), 4720-4727.

88. Hori, Y.; Wakebe, H.; Tsukamoto, T.; Koga, O., Electrocatalytic process of CO selectivity in electrochemical reduction of CO_2 at metal electrodes in aqueous media. Electrochimica Acta 1994, 39 (11-12), 1833-1839.

89. Lin, R.; Guo, J.; Li, X.; Patel, P.; Seifitokaldani, A., Electrochemical reactors for CO_2 conversion. Catalysts 2020, 10 (5), 473.

90. Bagger, A.; Ju, W.; Varela, A. S.; Strasser, P.; Rossmeisl, J., Single site porphyrine-like structures advantages over metals for selective electrochemical CO_2 reduction. Catalysis Today 2017, 288, 74-78.

91. Skúlason, E.; Tripkovic, V.; Björketun, M. E.; Gudmundsdóttir, S.; Karlberg, G.; Rossmeisl, J.; Bligaard, T.; Jónsson, H.; Nørskov, J. K., Modeling the electrochemical hydrogen oxidation and evolution reactions on the basis of density functional theory calculations. The Journal of Physical Chemistry C 2010, 114 (42), 18182-18197.

3. Chapter | Impact of Nickel Content on the Structure and Electrochemical CO_2 Reduction Performance of Ni–N–C Catalysts

In this Chapter, a zeolitic imidazolate framework (ZIF-8) has been employed to derive Ni-N-C electrocatalysts. Initially, a systematic study has been performed to identify the role of the Ni content doped into the ZIF-8 substrate during synthesis on the structure and performance of the produced Ni-N-C materials for CO_2R. Our results demonstrated that, by increasing the Ni concentrations in the mixed mixture of ZIF-8 impregnated with Ni, Ni nano/microparticles were formed which directed the electrocatalytic selectivity towards HER. Whilst the formation of atomically dispersed Ni-N_x/C active sites has preferred the reduced Ni contents. Following this systematic study, a selectivity of CO of ca. 99% FE has been achieved at an applied potential of -0.68 V vs RHE. These findings have been published in *ACS applied energy materials* as illustrated in the following section.

The Impact of Nickel Content on the Structure and Electrochemical CO_2 Reduction Performance of Nickel-Nitrogen-Carbon Catalysts Derived from Zeolitic Imidazolate Frameworks

Fatma M. Ismail[a], Ahmed Abdellah[b], Hye-Jin Lee[c], V.Sudheeshkumar[d] Drew C. Higgins[e*]

Department of Chemical Engineering, McMaster University, Hamilton, Ontario L8S 4L7, Canada

[a]ismaif1@mcmaster.ca, [b]abdellaa@mcmaster.ca, [c]leeh114@mcmaster.ca, veeranms@mcmaster.ca, [e]higgid2@mcmaster.ca

Keywords: CO_2 reduction; metal-nitrogen-carbon; Ni single atoms; MOF-based electrocatalyst; Electrolysis.

3.1 Abstract

Electrochemical conversion of CO_2 affords a sustainable route to produce chemicals and fuels from renewable sources of electricity. Nickel-nitrogen-carbon (Ni-N-C) materials have shown promise in terms of activity and selectivity towards the electro-conversion of CO_2 into CO, a feedstock widely used in the chemical sector. Ni-N-C catalysts, postulated to be comprised of catalytically active atomically dispersed Ni-N_x/C sites, are commonly prepared by pyrolyzing a mixture of transition metal, nitrogen and carbon containing precursors. Herein, we use a zeolitic imidazolate frameworks (ZIF-8) — a subclass of MOF — as a platform for synthesizing Ni-N-C electrocatalysts. We systematically investigate the role of the Ni concentration impregnated into the ZIF-8 precursor structure during synthesis on the overall structure and performance of the resulting Ni-N-C catalysts for electrochemical CO_2 reduction. Our findings show that increased Ni contents in the catalyst precursor results in the formation of Ni-containing particles that increase the catalytic selectivity towards the competing hydrogen evolution reaction, whereas reduced Ni

contents preferentially forms atomically dispersed Ni-N_x/C active sites dispersed in heterogeneous carbon structures consisting of carbon nanotubes and carbonaceous particles. As an optimized concentration of Ni in the precursor mixture, we demonstrate a CO_2 reduction selectivity towards CO of ca. 99% Faradaic efficiency at an applied potential of –0.68 V vs the reversible hydrogen electrode

3.2 Introduction

Intense reliance on fossil fuels as the major global energy source has resulted in an unprecedented increase of carbon emissions and CO_2 concentration within the atmosphere. Consequently, serious temperature variations have been recorded leading to drastic weather patterns, along with habitat and agricultural land disturbances that are expected to get more precarious in the near future.[1, 2] Scientists and engineers are therefore devoting significant efforts to develop alternative and sustainable energy technologies and processes to reduce our dependence on fossil fuels.[3] One promising process under development is the conversion of carbon dioxide into fuels and chemicals,[3-6] which can be done by thermochemical, photochemical and electrochemical means. In particular, the electrochemical approach provides some advantages[7-16] in that renewable energy sources such as wind, solar or hydro can be used to produce the electricity that drives the conversion of CO_2 into valuable carbon-based fuel and chemical products. Additionally, the electrochemical CO_2 reduction (CO_2R) reaction can be conducted at near-ambient conditions,[17-19] circumventing the need for sophisticated or energy intensive plant designs.

Efficient CO_2R technologies rely on the availability of high performance and inexpensive catalysts — a lofty goal that researchers across the globe have been pursuing for several decades and with heightened interest over the past 5-10 years.[20, 21] In terms of CO_2R catalyst development,

there are several challenges that must be addressed. First, CO_2 molecules can be electrochemically reduced into many (15+) different carbon-based compounds, including hydrocarbons or oxygenated species. Therefore, catalyst material should ideally have high selectivity towards just one or a select few products to avoid the need for costly and energy intensive separation processes. The catalyst should also possess several key features, including high activity towards the product(s) of interest, along with long-term operational stability and low cost.[22] To this end, a variety of different nature-derived, [23-26] heterogenous,[3, 27] and homogenous molecular catalysts [28-30] have been explored for application towards CO_2R. Nature-derived and homogenous electrocatalysts can provide high selectivity along with (theoretically) 100% metal utilization. However, these electrocatalysts commonly require electron-transfer driven regeneration and would require separation from the formed CO_2R product(s). On the other hand, heterogeneous catalysts can provide high electronic conductivity and are immobilized on solid electrode structures, but developing heterogeneous catalysts with high selectivity towards one particular product has been a challenging endeavor. Atomically dispersed metal-nitrogen-doped carbon (M-N-C) electrocatalysts represent an interesting class of materials that can couple several of the advantages of both homogeneous and heterogeneous catalyst materials to achieve high selectivity with easy recovery and high stability.[31] Their hypothesized atomically dispersed $M\text{-}N_x/C$ structures that are analogous to metal-centered molecular catalysts can provide good activity and selectivity,[32, 33] and their active site structures are immobilized in a graphitic support that can provide facile electron transport and stability.

M-N-C electrocatalysts can be synthesized by straightforward processes that generally involves pyrolyzing a mixture of carbon, metal salt, and nitrogen containing precursors.[34-36] This type of catalyst rose to prominence in the fuel cell community with Fe-N-C being the most active

non-platinum group metal catalyst reported to date, with significant efforts devoted to identifying the catalytically active sites in these catalysts and developing structure-property-performance relationships.[31, 32, 37-39] In M-N-C electrocatalysts it is postulated that atomically dispersed active sites ($M\text{-}N_x/C$) are formed by metal-ion coordination with nitrogen-dopant atoms within a graphitic carbon architecture.[40-44] Leveraging this insight from the fuel cell community, researchers have investigated M-N-C catalysts for the electrochemical CO_2R with both theoretical and experimental approaches.[31] In an early investigation, Tripkovic et al.[45] computationally investigated various metal-centred M-N-C catalysts for their activity towards CO_2R. Their results demonstrated the promise of these materials towards the electrochemical CO_2R and indicated that the generated activity and selectivity is mainly depending on the metal center. Strasser et al.[46] investigated various types of metal centers in M-N-C catalysts (Mn, Fe, Co, Ni, Cu) for the CO_2R through computational and experimental methods. Their findings postulated that this class of materials consists of $M\text{-}N_x/C$ active site structures, and the identity of the active metal center impacts the binding energies with reactive species. These binding energies and the resulting reaction energetics were used to explain the CO_2R selectivity trends towards CO or H_2, and even the production of small amounts of CH_4.

Interest in M-N-C electrocatalysts for CO_2R has continued due to their promising electro-catalytic performance in addition to that fact that they can be synthesized from inexpensive, earth abundant precursor materials using relatively straightforward synthetic techniques. Although several M-N-C (where M=Fe, Co, Mn, Ni) catalysts have been investigated for CO_2R[31, 33, 47-52], Ni-N-C has been demonstrated as one of the most promising due to its superior selectivity and cost effectiveness. Atomically dispersed $Ni\text{-}N_x/C$ sites, in particular, were identified to be highly selective towards CO while inhibiting the competing hydrogen evolution reaction (HER).[46]

Among the different precursors used for the synthesis of Ni-N-C catalysts, metal organic frameworks (MOFs) are attractive as they have well-ordered structures and high surface area to volume ratios, while also being tunable in terms of pore size, metal-metal distances and the chemical structure of the connecting ligands.[53, 54]

Recently, studies have focused on the preparation of Ni-N-C catalysts using MOF precursors as a platform in the hope that the structural features of MOFs, including their high porosity and well-distributed species (including transition metal ions), could be translated to the resulting structure of Ni-N-C catalysts with high surface areas concentration of accessible atomically dispersed Ni-N_x/C sites. [55, 56] For instance, MOF-74 — a sub class of MOF with metal ion sites coordinated by 2,5 dihydroxy terephthalic acid — has been used to prepare Ni-N-C structures with a Faradaic efficiency towards CO of 98% at -0.8 V vs RHE.[57] Zeolitic imidazole framework (ZIF)-8, a subclass of MOFs generated from the self-assembly of Zn^{2+} with 2-methyimidazole has also been used as a precursor, whereby Ni^{2+} was included during the ZIF-8 self-assembly and reacted with the nitrogen/carbon in the imidazolate ligands during high temperature pyrolysis to form active sites resulting in a Faradaic efficiency of 95% towards CO at -0.54 V vs RHE.[56] Although ZIF-8 has successfully been used as a precursor to produce selective Ni-N-C electrocatalysts for CO_2R, the impact of impregnated Ni concentration on the structure of the Ni-N-C catalyst and resulting electrochemical CO_2R activity and selectivity is still under investigated.

In this report, we conducted a systematic study to understand the influence of Ni content used during synthesis of Ni-N-C catalysts from Zn^{2+} impregnated ZIF-8 precursors. We find that using relatively lower Ni contents during synthesis resulted in high activity and selectivity towards CO, likely due to the formation of atomically dispersed M-N_x/C sites within heterogeneous catalyst

structures consisting of carbon nanotubes and carbonaceous particles. Particularly, at the lowest Ni concentration investigated in this work, the resulting Ni-N-C catalyst exhibited a Faradaic efficiency of 99% towards CO at an electrode potential of -0.68 V vs RHE and current density of -1.6 mA/cm^2. At increased Ni contents, the formation of significant amounts of Ni-based particles were observed, concomitant with increasing catalytic selectivity towards the competing hydrogen evolution reaction. Nevertheless, in this research, we're monitoring the impact of the Ni content inside the developed Ni-N-C catalysts on the structure/property of the produced catalysts and consequently correlating this impact on the obtained CO_2R performance.

3.3 Materials & Methods

3.3.1 Materials

$Zn(NO_3)_2.6H_2O$, 2-methylimidazole, $Ni(NO_3)_2.6H_2O$, $KHCO_3$, a 5wt.% Nafion solution in isopropanol, isopropanol, methanol, n-hexane and graphite foil were purchased from Sigma Aldrich and used without further purification. Type 1 ultrapure water (< 10 ppb TOC; > 18 MΩ-cm) was used for all experiments.

3.3.2 Synthesis of Zeolitic Imidazolate Frameworks (ZIF-8)

0.558g of zinc nitrate hexahydrate was dissolved in 15mL of methanol until complete dissolution. Then, 0.616g of 2-methyl imidazole was dissolved in 15mL of methanol and was added to the previous solution. The whole mixture was kept under continuous stirring for 12 hours at 35 °C. The obtained white precipitate was washed and separated using centrifuge at 10,000 rpm for 20 minutes. The formed white paste was dried at 65 °C for 6 hours.

3.3.3 Synthesis of Ni-N-C catalysts

To prepare Ni-N-C catalysts, 100 mg of ZIF-8 was first completely dispersed in 10mL of n-hexane. Then, an aqueous solution of $Ni(NO_3)_2.6H_2O$ (50mg/0.5 mL) was injected into the ZIF-8 suspension to impregnate the ZIF-8 with the Ni salt precursor [Ni:Zn atomic ratio of (0.5:1)]. This mixture was kept under continuous stirring for 3 hours. The obtained green precipitate was separated by filtration, and the resulting light green paste was dried at 65 °C for 6 hours. The powder was then collected and pyrolyzed at 1000 °C for 2 hours in a tube furnace under constant Ar flow. Three additional Ni:Zn atomic ratios were prepared by injecting (100 mg/1 mL), (200 mg/2 mL), and (400 mg/4 mL) of an aqueous $Ni(NO_3)_2$ solution into the ZIF-8 suspension to achieve (1:1), (2:1) and (3:1) Ni:Zn atomic ratios in the precursors, respectively. These different Ni:Zn atomic ratios (0.5:1), (1:1), (2:1), and (3:1) will be referred here as a-Ni-N-C-, b-Ni-N-C, c-Ni-N-C, and d-Ni-N-C, respectively.

3.3.4 Material Characterization

To investigate the morphology and composition of the synthesized electrocatalysts, high resolution transmission electron microscopy (HRTEM), and high-angle annular dark-field scanning transmission electron microscopy (HAADF-STEM) imaging along with electron energy loss spectroscopy (EELS) mapping were carried out in the Canadian centre for electron microscopy (CCEM) using a FEI titan operating at 300 KeV. Powder X-ray diffraction (PXRD) analysis was performed at McMaster analytical X-ray diffraction facility (MAX), using Cu Kα radiation to investigate the crystallinity of the synthesized catalysts. X-ray photoelectron spectroscopy (XPS) measurements were conducted at biointerfaces institute (BI) at McMaster university using a PHI Quantera II scanning XPS microprobe to evaluate the near-surface chemical compositions and chemical bonding environments of the synthesized materials.

3.3.5 Electrode preparation

The pyrolyzed Ni-N-C black powder was carefully grinded by a mortar and pestle prior to use. A homogenous ink was prepared by dispersing 10 mg of the active materials in a 2 mL mixture of (3:1) isopropanol:water, along with the addition of 110 µL of a 5wt.% Nafion solution. Afterwards, the homogenous ink was drop-casted on a graphite foil and kept at 65 °C for 2 hours to dry.

3.3.6 Electrochemical Characterization

Investigating the electrochemical CO_2R activity and selectivity of the Ni-N-C catalysts was conducted using a custom-built two compartment electrochemical cell reported on previously[21] that was developed to evaluate the activity and selectivity of catalysts for CO_2R. A Selemion anion exchange membrane (Selemion AMV, AGC Inc.) was utilized to separate the anolyte and catholyte chambers in the electrochemical cell, whereby the anolyte and catholyte chambers were each filled with 9 mL 0.1 M $KHCO_3$. A mass flow control unit (MKS Instrument) was used to control the CO_2 flow to be 20 sccm through the catholyte during the course of the reaction. A Pt foil was used as the counter electrode and an Ag/AgCl connected to the catholyte chamber by a Luggin capillary was used as the reference electrode. A Biologic VSP-300 potentiostat was used to carry out all the electrochemical measurements and all potentials were measured vs Ag/AgCl and converted afterwards to RHE using the equation $V_{vs\ RHE} = V_{measured\ vs.\ Ag/AgCl} + 0.197 + 0.059*6.8$ (pH of electrolyte). In order to quantify the gaseous phase products, the effluent from the electrochemical cell was connected directly to the sample loop in gas chromatography unit (GC, supplier: SRI, model: 8610C in the Multi-Gas configuration #5), with 1 mL of the gas injected at various times throughout the course of the experiments.

3.4 Results & Discussion

Initially, ZIF-8 was synthesized according to previous reports[58] and exhibited a uniform rhombododecahedral crystal shape with an average of 150-200 nm size distribution **(Figure S1)**. The synthesis procedure and postulated structural transformations occurring during each step of Ni-N-C catalyst preparation are illustrated in **Figure 3.1** and **Figure S2**. Prior pyrolysis, the impregnation of Ni^{2+} ions into the porous structure of ZIF-8 has been derived by physical adsorption. During the pyrolysis of $Ni(NO_3)_2$ impregnated ZIF-8 at 1000 °C, the ZIF-8 structure decomposed and a certain degree of graphitization occurs, most likely consisting of nitrogen-doped carbon owing to the presence of nitrogen present in the imidazole linkers. These nitrogen-doped carbon sites have been proposed as likely anchoring sites for Ni^{2+} species to form atomically dispersed Ni-Nx/C active sites that are characteristic of M-N-C catalysts.[33, 46] Zn has a boiling point of ca. 910 °C mostly escape from the structure during pyrolysis, which has been demonstrated previously to result in porosity of the catalyst [59] and produce a structure with N-rich defects[60] that can likely anchor the nearby Ni^{2+} species. For Ni-N-C catalysts, the local coordination environment of the atomically dispersed Ni-N_x/C active sites has been under debate in the literature,[57, 61, 62] whereby in the Ni-N_x/C sites x could be 1, 2, 3 or 4 as shown in **Figure 3.1**. Ni-N-C catalysts with four different Ni:Zn atomic ratios as well as a Ni-free catalyst (pyrolyzed ZIF-8) were prepared and characterized using physical and chemical characterization techniques to understand the impact Ni loading had on the structure and properties.

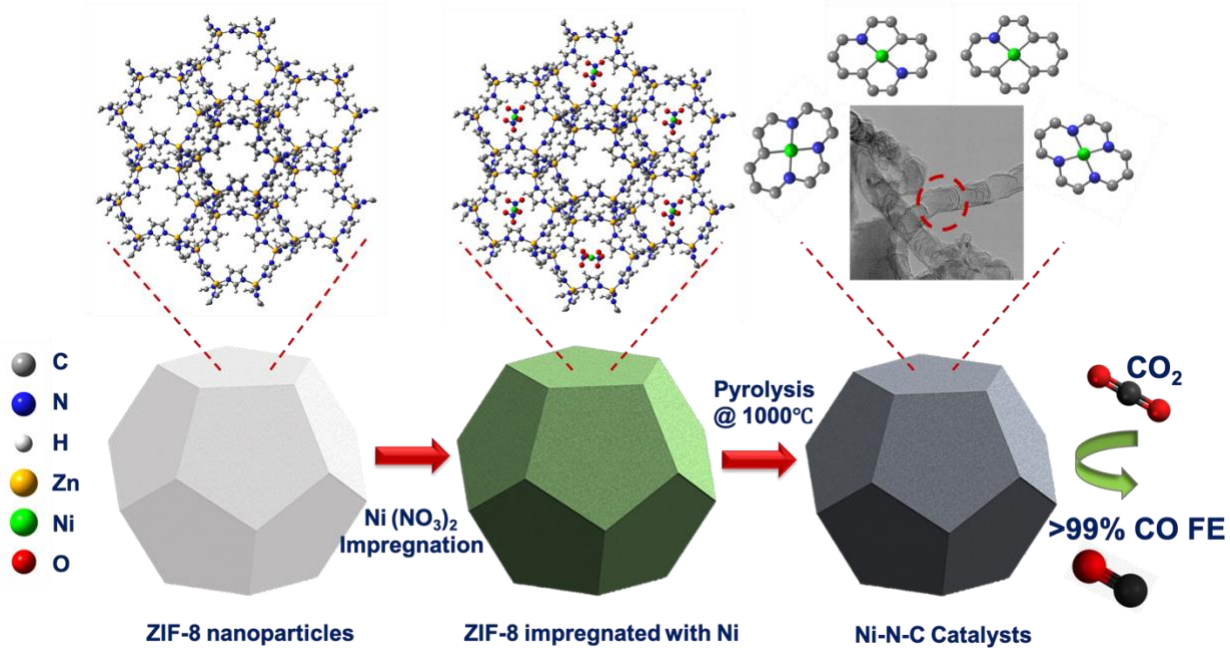

Figure 3-1 Schematic diagram illustrates the formation of Ni-N-C catalyst.

Figure 3.2a-h, and **Figure S3a-h** provide TEM images at a different magnification of Ni-N-C catalysts prepared with varying Ni:Zn atomic ratios, while **Figure S7** illustrates the EDS mapping of the same catalysts, alongside TEM images of Ni-free pyrolyzed ZIF-8 for comparison shown in **Figure 3.2j-k**. The Ni-N-C catalysts showed a heterogeneous distribution of structures consisting of both carbon nanotubes (CNTs), carbon-based particle structures with sizes ranging from ca. 100 nm to several micrometers, and dark Ni-based particles with diameters ranging from a few nm to ~100nm. The ability of Ni to catalyze the growth of CNTs [63] is the likely reason CNTs are observed in the Ni-N-C catalysts and not in the pyrolyzed ZIF-8. As the content of Ni in the catalyst precursors is increased a lower proportion of CNTs is observed in the final catalyst structure. The successful nucleation of CNTs relies not only on the Ni content, but also on other various factors including morphology, composition, crystal facets, and synthetic conditions.

Therefore, the impact of the progressive increase of Ni content in the developed atomically dispersed Ni-N-C catalysts has not demonstrated a similar enhancement of the formed of CNTs.[64-66]. In the a-Ni-N-C catalyst prepared with a Ni:Zn ratio of (0.5:1), very few Ni-based nanoparticles are observed distributed throughout the structure **(Figure 3.2b)**. With an increase in the Ni content used during catalyst synthesis, an increasing number and increased size of Ni-based nanoparticles were observed in the Ni-N-C catalyst structures. This could potentially be due to a saturation point being reached for the formation of atomically dispersed NiN_x/C active sites[47] and a propensity for Ni agglomeration at increased concentrations. HRTEM imaging **(Figure S4)** demonstrated that the Ni-based nanoparticles observed in the samples were covered by a thin graphitic layer, likely due to the ability of Ni to catalyze the formation of graphitic carbon structures.[47] The structure of the a-Ni-N-C catalyst imaged by STEM-HAADF is provided in **Figure 3.3a**, along with a higher resolution image in **Figure 3.3b**. The higher resolution image showed bright spots (indicated by arrows), indicating the presence of single atoms of an element with a higher Z-number than the carbon matrix. These spots are likely due to single Ni atoms dispersed throughout the catalyst structure, although detailed high resolution spectroscopic measurements (i.e., EELS) of this particular location would be necessary to confirm the identity of these single atoms as demonstrated previously,[33, 37] which requires advanced instrumentation and capabilities that are outside the scope of this work. However, STEM-EELS chemical imaging was done to characterize the atomic distributions of Ni, N and C within the catalyst structures **(Figure 3.3c)**, which demonstrated a homogeneous dispersion of all three elements, suggesting that Ni-species were distributed throughout the nitrogen-doped carbon framework of the a-Ni-N-C catalyst. Also, developing techniques to accurately quantify the number of surface accessible Ni-Nx/C catalysts in these types of catalysts remains a scientific opportunity.

PXRD measurements to investigate the crystalline features of the Ni-N-C catalysts (b-Ni-N-C, c-Ni-N-C, and d-Ni-N-C) are presented in **Figure 3.3d**. The PXRD spectra of the ZIF-8 precursor showed several peaks with a spectral pattern consistent with those reported previously for ZIF-8 materials.[67] No additional PXRD peaks appeared after mixing the Ni^{2+} ions with the ZIF-8 structure, which indicates the Ni^{2+} ions were simply impregnated into the ZIF-8 and did not cause any structural changes. For the Ni-N-C catalysts prepared with different Ni:Zn atomic ratios, no significant diffraction peaks were observed for b-Ni-N-C. This indicates that the Ni species present during synthesis did not coalesce into enough crystalline structures for detection by PXRD, and potentially indicates the Ni species instead formed atomically dispersed Ni ions integrated in N-C structure after a complete decomposition of the ZIF-8 crystalline structure. In contrast, crystalline diffraction peaks at 45.6°, 54.2°, and 75.8° were observed when higher Ni contents were used during synthesis (c-Ni-N-C and d-Ni-N-C). These peaks are assigned to Ni(111), Ni(200), and Ni(220), respectively, with no peak shifts observed that would be indicative of Ni alloying with Zn as illustrated in **Figure S6**. This difference in the PXRD patterns support the results from TEM in that higher Ni contents used during Ni-N-C synthesis led to an increased number of Ni particles formed in the catalyst structure.

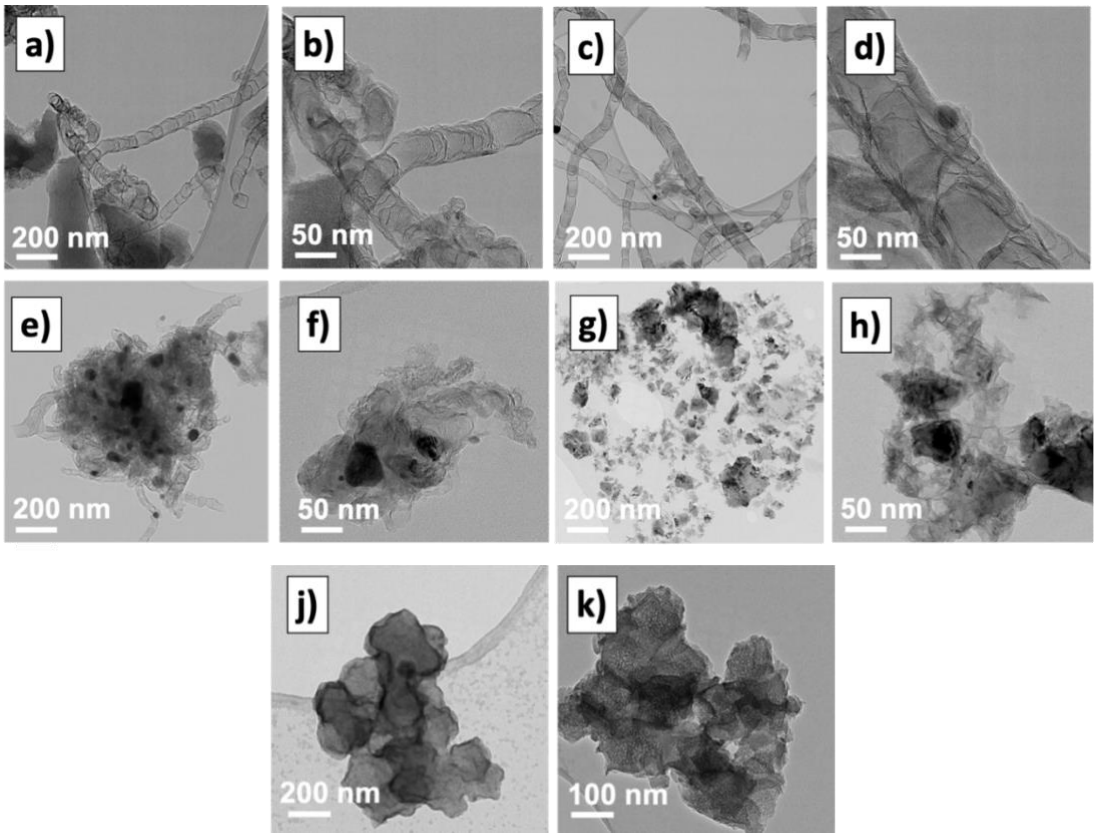

Figure 3-2 TEM images of Ni-N-C catalysts with different contents of Ni used during synthesis. (a,b) a-Ni-N-C, (c,d) b-Ni-N-C, (e,f) c-Ni-N-C, (g,h) d-Ni-N-C, (j,k) Ni-free pyrolyzed ZIF-8.

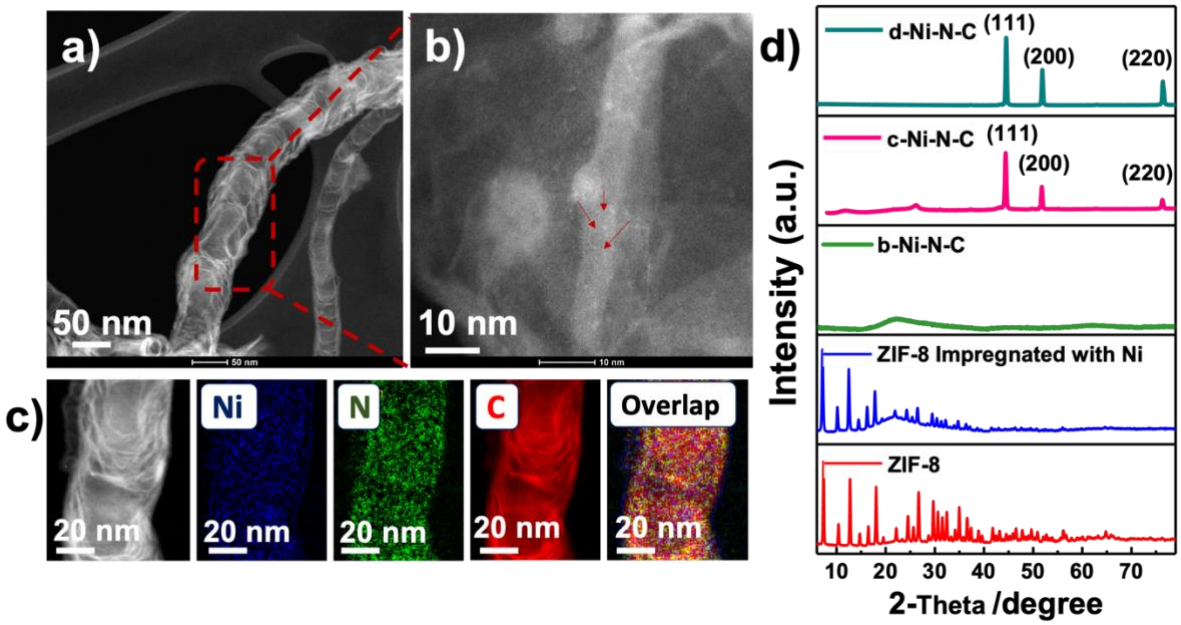

Figure 3-3 (a,b) HAADF-STEM images of a-Ni-N-C catalyst, whereby the bright spots marked with red arrows are likely single Ni atoms. (c) EELS mapping shows the homogenous distribution of the Ni, N and C throughout the a-Ni-N-C catalyst. (d) PXRD of ZIF-8, ZIF-8 impregnated with $Ni(NO_3)_2$, and Ni-N-C catalysts prepared with different Ni contents.

Brunauer−Emmett−Teller (BET) measurements were carried out on b-Ni-N-C and ZIF-8 as shown in **Figure S5**. The measured specific surface area of the b-Ni-N-C catalyst was 136 m^2/g, exhibiting a substantial decrease in specific surface area compared to ZIF-8 (1430 m^2/g) that was used as the platform for catalyst synthesis. These results arise due to the structural changes that occur during the pyrolysis of $Ni(NO_3)_2$ impregnated ZIF-8 templates, including the formation of CNT, carbonaceous structures and Ni-based nanoparticles as observed by TEM and PXRD analysis.

X-ray photoelectron spectroscopy (XPS) measurements were conducted on the four different ratios. By XPS, the near surface composition of the developed Ni-N-C catalysts was found to be ca. 70at% carbon, 16at% nitrogen, 6 at% oxygen, 3.5 at% Zn and less than 1at% Ni. The high-resolution N 1s spectra shown in **Figure 3.4** indicates five different peaks centered as pyridinic-N at 398.7 eV, pyrrolic-N at 400.2 eV, graphitic-N at 401.5 eV, oxidized-N at 403.2 eV, and Ni–N at 399.3 eV.[68, 69] Several reports have discussed the role of N-configurations on the obtained electrochemical activity and selectivity of CO_2R, for instance, Li et al. ascribed the remarkably high CO selectivity of a developed Ni@N-C catalyst to the presence of $Ni\text{-}N_4$ moieties compared to other Ni motifs that reveals relatively lower catalytic activity[70]. In contrast, Yang et al. have studied the activity of $Ni\text{-}N_3$ and $Ni\text{-}N_4$ using DFT calculations. Their findings demonstrate that $Ni\text{-}N_3$ sites are more active than $Ni\text{-}N_4$[71], opening the debate on the Ni moiety nature of this class of materials. In this research, owing to the ambiguity in fitting XPS peaks and the fact that peaks can shift due to surrounding environments, it is hard to deconvolute exactly what nitrogen dopants are impacting activity. Therefore, to identify the local coordination

environment of the atomically dispersed Ni sites, Extended X-ray Absorption Fine Structure (EXAFS) measurements will be carried out in the next stage of this research. The Ni 2p XPS spectra were deconvoluted into multiple peaks which are shown in **Figure 3.5**. The peak at 852.9 eV corresponds to the $2p_{3/2}$ of metallic Ni. A major peak was dominated at 854.9 eV which is a higher energy than that for Ni^0 (852 eV) and lower than that of Ni^{2+} (856 eV), indicating that Ni species are likely to be in low valent state. As the Ni loading increases, metallic character of the developed Ni-N-C catalysts increases. C 1s shows two peaks with binding energy at 285.0 eV and 286.3 eV, which can be assigned to C-C sp^2 and C-N/O respectively **(Figure S8)**. To quantify the Ni content in all Ni-N-C catalysts, inductively coupled plasma (ICP) measurements were carried out. The obtained results are summarized in **Table S2** and demonstrated 6.8% of the lowest Ni ratio (a-Ni-N-C).

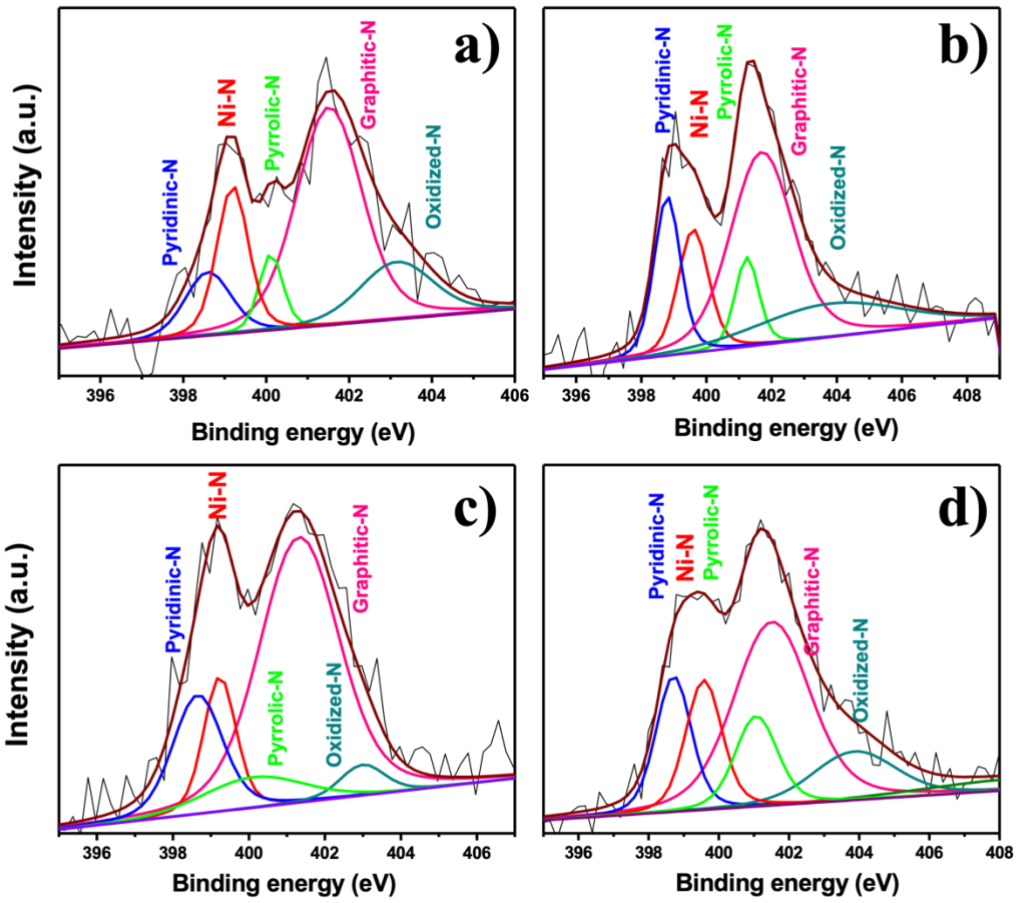

Figure 3-4 N 1s XPS spectra of a) a-Ni-N-C b) b-Ni-N-C c) c-Ni-N-C d) d-Ni-N-C catalysts.

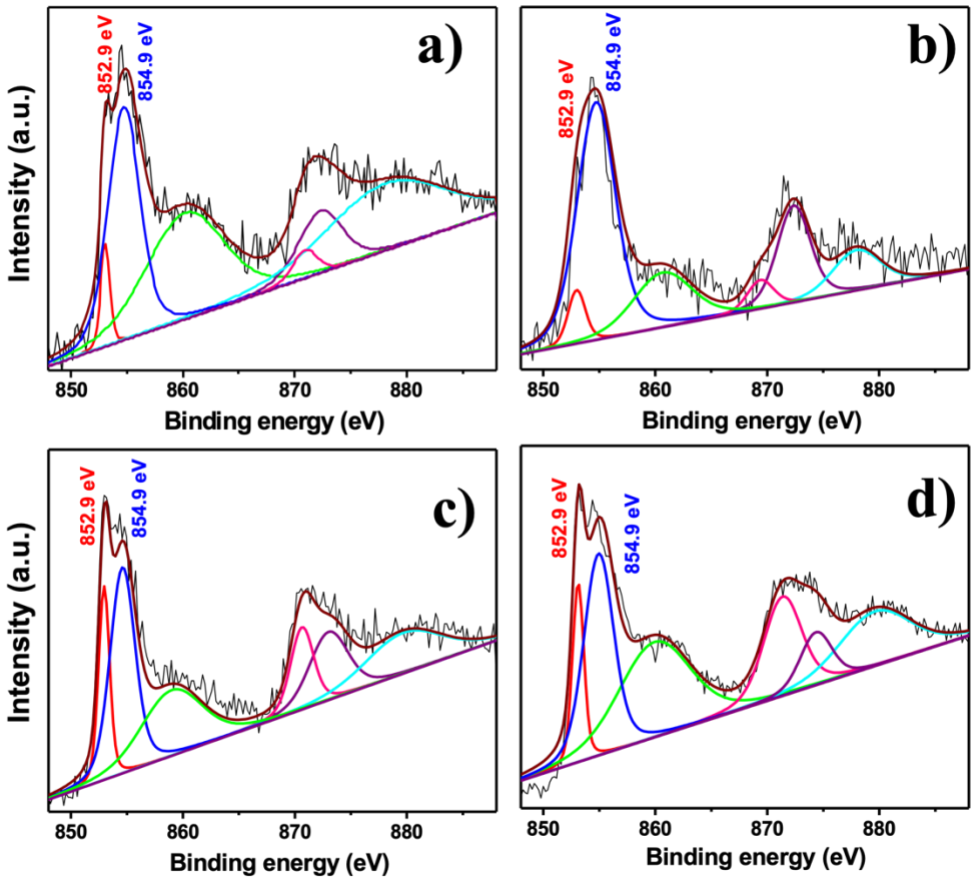

Figure 3-5 Ni 2p XPS spectra of a) a-Ni-N-C b) b-Ni-N-C c) c-Ni-N-C d) d-Ni-N-C catalysts.

The electrochemical CO_2R performance of the Ni-N-C catalysts synthesized with varying Ni contents was tested at different electrode potentials in CO_2 saturated 0.1M $KHCO_3$, with the results shown in **Figure 3.6**. CO_2R testing indicated that the Ni-N-C catalysts electrochemically produced CO and H_2. The potential window range employed in these measurements was -0.68 V vs RHE to -1.05 V vs RHE, which is the most appropriate potential window for CO_2R. The Faradaic efficiencies of each catalyst towards CO are shown in **Figure 3.6a**, which illustrates that at low Ni contents used during synthesis (a-Ni-N-C and b-Ni-N-C) that near unity (99%)

selectivity towards CO for a-Ni-N-C and 96 % selectivity towards CO for b-Ni-N-C were obtained at -0.68 V vs RHE. Despite the presence of some metallic Ni particles in b-Ni-N-C sample, we speculate that the high selectivity towards CO for both samples is likely due to the successful generation of atomically dispersed Ni-N_x/C sites that have been shown as active and selective towards CO.[33] The presence of Ni during catalyst synthesis has been demonstrated as essential for catalytic selectivity towards CO by testing a pyrolyzed (Ni-free) ZIF-8 as a comparison. Pyrolyzed ZIF-8 with zero Ni content shows very little CO_2R activity and (<5%) Faradaic efficiency towards CO at all of the electrochemical potentials investigated **(Figure S9-a and 9-b)**, suggesting that Zn does not play a significant role in the CO_2R activity of Ni-N-C and that Ni is essential for achieving selectivity towards CO. Furthermore, no evidence of Zn alloying with Ni was observed in the catalyst, further indicating Zn does not have a significant impact on the observed catalysis. When higher Ni contents were used during Ni-N-C synthesis, a significantly lower Faradaic efficiency towards CO of 69% was observed for c-Ni-N-C at -0.68 V vs RHE, with partial current densities towards CO for all catalysts shown in **Figure S9-c**. We attribute this to the formation of metallic Ni particles in the catalyst structure as indicated by TEM and PXRD. While c-Ni-N-C likely contains Ni-N_x/C sites that are responsible for the production of CO that is observed, metallic Ni is known to produce H_2 under CO_2R conditions [18] and are likely responsible for the increase in Faradaic efficiency towards H_2 that is observed **(Figure 3.6b)**. Although HRTEM indicated that many of the Ni particles observed in the catalyst are covered by a graphitic shell that would presumably limit electrolyte/reactant access, it is likely that not all of the Ni particles are completely coated, giving rise to the decrease in CO selectivity observed. This hypothesis is supported by electrochemical CO_2R testing results for d-Ni-N-C, which was synthesized using the highest Ni content. d-Ni-N-C showed very limited (<10%) Faradaic efficiency towards CO,

producing almost exclusively H_2 through the competing hydrogen evolution reaction. We attribute this to the significant content of Ni particles observed in this catalyst sample. These trends observed during electrochemical CO_2R testing are shown in **Figure 3.6d**, which depicts the correlation between the content of Ni used during Ni-N-C catalyst synthesis and the selectivity towards CO or H_2 at -0.68 V vs RHE. For a-Ni-N-C, b-Ni-N-C and c-Ni-N-C the Faradaic efficiency towards CO was found to steadily decrease **(Figure 3.6a)** while the Faradaic efficiency towards H_2 increased **(Figure 3.6b)** with more negative electrode potentials. This is consistent with a previous report whereby the selectivity towards CO for Ni-N-C catalysts reached a maximum at ca. -0.7 V vs RHE,[46] and this shift in selectivity is likely due to shifting reaction energetics towards the CO_2R and competing hydrogen evolution reaction. To investigate the impact of acid leaching on the electrochemical CO_2R performance of the developed c-Ni-N-C and d-Ni-N-C catalysts which comprise a large portion of Ni-based particles, both samples have been immersed in 1M nitric acid at room temperature for two hours, followed by careful washing with Millipore water. The electrochemical CO_2R performance of both samples were improved to achieve CO selectivity of 81% at -0.88 V vs RHE and 65% at -1.03 V vs RHE for c-Ni-N-C and d-Ni-N-C respectively as illustrated in **Figure S10**. Nevertheless, the obtained CO_2R performance after acid wash is still poorer than a-Ni-N-C and b-Ni-N-C catalysts which contain mainly atomically dispersed Ni sites. Further investigations have been devoted by testing a very low Ni content in (0.25:1) Ni:Zn atomic ratio referred as e-Ni-N-C, however, a maximum Faradaic efficiency of 84% towards CO at -0.88 V vs RHE was obtained **(Figure S11)**, emphasizing that reducing the Ni content less than (0.5:1) ratio has likely decreased the number of available active sites for CO_2R and indicating that the optimum Ni:Zn atomic ratio is likely around (0.5:1).The obtained Faradaic efficiency of the formed gas products was ca.100% at most of the applied

potentials, which demonstrates that the selectivity of the developed atomically dispersed Ni-N-C catalysts is mainly towards the generation of gas phase products. Evaluating the stability of the developed Ni-N-C catalysts will be performed in the next steps of this research using membrane electrode assembly electrolyzer. With promising CO_2R activity and selectivity shown for Ni-N-C catalysts in this work, integrating these well-performing materials into high current density electrochemical devices will be necessary for developing competitive industrial-scale electrochemical systems for CO_2R.

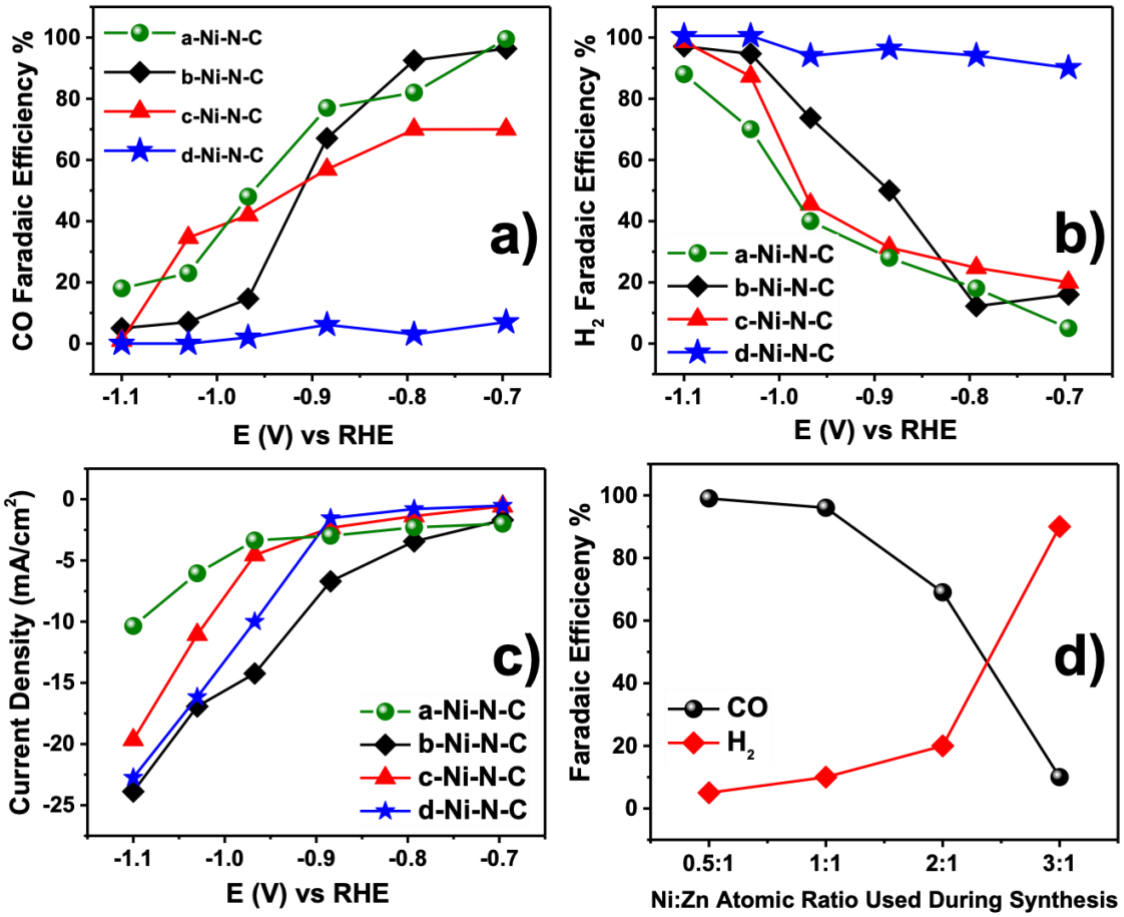

Figure 3-6 The electrochemical performance of the as-synthesized Ni-N-C catalysts, a) the obtained CO FE %, b) the obtained H_2 FE %, c) current density (mA/cm^2) at different potentials, and d) correlation between Ni:Zn atomic ratio and the produced CO and H_2 at -0.68 V vs RHE.

3.5 Conclusion

In summary, the influence of the Ni content inside a series of Ni-N-C electrocatalysts derived from Ni^{2+} impregnated ZIF-8 precursors on the structure and electrochemical activity and selectivity for CO_2R has been investigated. It was found that increasing the Ni concentration used during synthesis resulted in the formation of Ni-based particles in the Ni-N-C that shifted selectivity towards HER rather than CO_2R, consequently decreasing the selectivity towards CO. However, by decreasing the Ni concentration used during synthesis, the generated Ni-N-C catalyst were able to achieve a CO Faradaic efficiency of ~99% at -0.68 V vs RHE and a current density of -1.6 mA/cm^2. The catalyst consisted of a heterogeneous structure, including carbon nanotube and carbonaceous particles likely consisting of atomically dispersed Ni-N_x/C sites that provided the CO_2R activity. The role of Zn species in the catalyst structure was determined to be negligible based on comparison evaluation of Ni-free pyrolyzed ZIF-8 materials.

3.6 Supporting Information

SEM, TEM, graphic illustrations, XPS, XRD, BET, EDS, ICP, and electrocatalytic performances are included in the supporting information file.

Acknowledgments

This research was supported by the Department of Chemical Engineering at McMaster University and the National Research Council of Canada (NRC) Materials for Clean Fuels Challenge Program. Electron microscopy measurements were performed at the Canadian Centre for Electron Microscopy (CCEM). X-ray photoelectron spectroscopy was carried out at the Biointerfaces Institute (BI). X-ray diffraction analysis was performed at McMaster Analytical X-ray Diffraction Facility (MAX).

3.7 References

1. Agency, U. S. E. P., Climate Change Indicators in the United States, 2012. United States Environmental Protection Agency: 2012.

2. Arakawa, H.; Aresta, M.; Armor, J. N.; Barteau, M. A.; Beckman, E. J.; Bell, A. T.; Bercaw, J. E.; Creutz, C.; Dinjus, E.; Dixon, D. A., Catalysis research of relevance to carbon management: progress, challenges, and opportunities. Chemical Reviews 2001, 101 (4), 953-996.

3. Seh, Z. W.; Kibsgaard, J.; Dickens, C. F.; Chorkendorff, I.; Nørskov, J. K.; Jaramillo, T. F., Combining theory and experiment in electrocatalysis: Insights into materials design. Science 2017, 355 (6321).

4. Zhang, H.; Xu, H.; Li, Y.; Su, Y., Octahedral core–shell bimetallic catalysts M@ UIO-67 (M= Pt–Pd nanoparticles, Pt–Pd nanocages): metallic nanocages that enhanced CO2 conversion. Applied Materials Today 2020, 19, 100609.

5. Cárdenas-Arenas, A.; Quindimil, A.; Davó-Quiñonero, A.; Bailón-García, E.; Lozano-Castello, D.; De-La-Torre, U.; Pereda-Ayo, B.; González-Marcos, J. A.; González-Velasco, J. R.; Bueno-López, A., Design of active sites in Ni/CeO_2 catalysts for the methanation of CO_2: tailoring the Ni-CeO_2 contact. Applied Materials Today 2020, 19, 100591.

6. Liu, S.; Pang, F.; Zhang, Q.; Guo, R.; Wang, Z.; Wang, Y.; Zhang, W.; Ou, J., Stable nanoporous Sn/SnO_2 composites for efficient electroreduction of CO_2 to formate over wide potential range. Applied Materials Today 2018, 13, 135-143.

7. Lewis, N. S.; Nocera, D. G., Powering the planet: Chemical challenges in solar energy utilization. Proceedings of the National Academy of Sciences 2006, 103 (43), 15729-15735.

8. Chen, Z.; Jaramillo, T. F.; Deutsch, T. G.; Kleiman-Shwarsctein, A.; Forman, A. J.; Gaillard, N.; Garland, R.; Takanabe, K.; Heske, C.; Sunkara, M., Accelerating materials development for photoelectrochemical hydrogen production: Standards for methods, definitions, and reporting protocols. Journal of Materials Research 2010, 25 (1), 3-16.

9. De Klerk, A., Fischer–Tropsch facilities at a glance. Fischer–Tropsch Refining 2011, 1-20.

10. De Luna, P.; Hahn, C.; Higgins, D.; Jaffer, S. A.; Jaramillo, T. F.; Sargent, E. H., What would it take for renewably powered electrosynthesis to displace petrochemical processes? Science 2019, 364 (6438).

11. Back, S.; Kim, J.-H.; Kim, Y.-T.; Jung, Y., Bifunctional interface of Au and Cu for improved CO_2 electroreduction. ACS applied materials & interfaces 2016, 8 (35), 23022-23027.

12. Zhao, K.; Liu, Y.; Quan, X.; Chen, S.; Yu, H., CO_2 electroreduction at low overpotential on oxide-derived Cu/carbons fabricated from metal organic framework. ACS applied materials & interfaces 2017, 9 (6), 5302-5311.

13. Chen, H.; Handoko, A. D.; Xiao, J.; Feng, X.; Fan, Y.; Wang, T.; Legut, D.; Seh, Z. W.; Zhang, Q., Catalytic effect on CO_2 electroreduction by hydroxyl-terminated two-dimensional MXenes. ACS applied materials & interfaces 2019, 11 (40), 36571-36579.

14. Daiyan, R.; Chen, R.; Kumar, P.; Bedford, N. M.; Qu, J.; Cairney, J. M.; Lu, X.; Amal, R., Tunable syngas production through CO_2 electroreduction on cobalt–carbon composite electrocatalyst. ACS applied materials & interfaces 2020, 12 (8), 9307-9315.

15. Mascaretti, L.; Niorettini, A.; Bricchi, B. R.; Ghidelli, M.; Naldoni, A.; Caramori, S.; Li Bassi, A.; Berardi, S., Syngas evolution from CO_2 electroreduction by porous au nanostructures. ACS applied energy materials 2020, 3 (5), 4658-4668.

16. He, B.; Jia, L.; Cui, Y.; Zhou, W.; Sun, J.; Xu, J.; Wang, Q.; Zhao, L., $SnSe_2$ nanorods on carbon cloth as a highly selective, active, and flexible electrocatalyst for electrochemical reduction of CO_2 into formate. ACS Applied Energy Materials 2019, 2 (10), 7655-7662.

17. Gattrell, M.; Gupta, N.; Co, A., Electrochemical reduction of CO_2 to hydrocarbons to store renewable electrical energy and upgrade biogas. Energy Conversion and Management 2007, 48 (4), 1255-1265.

18. Kuhl, K. P.; Hatsukade, T.; Cave, E. R.; Abram, D. N.; Kibsgaard, J.; Jaramillo, T. F., Electrocatalytic conversion of carbon dioxide to methane and methanol on transition metal surfaces. Journal of the American Chemical Society 2014, 136 (40), 14107-14113.

19. Kou, Z.; Li, X.; Wang, T.; Ma, Y.; Zang, W.; Nie, G.; Wang, J., Fundamentals, On-Going Advances and Challenges of Electrochemical Carbon Dioxide Reduction. Electrochemical Energy Reviews 2021, 1-30.

20. Hori, Y. i., Electrochemical CO_2 reduction on metal electrodes. In Modern aspects of electrochemistry, Springer: 2008; pp 89-189.

21. Kuhl, K. P.; Cave, E. R.; Abram, D. N.; Jaramillo, T. F., New insights into the electrochemical reduction of carbon dioxide on metallic copper surfaces. Energy & Environmental Science 2012, 5 (5), 7050-7059.

22. Diercks, C. S.; Liu, Y.; Cordova, K. E.; Yaghi, O. M., The role of reticular chemistry in the design of CO_2 reduction catalysts. Nature materials 2018, 17 (4), 301-307.

23. Concepcion, J. J.; House, R. L.; Papanikolas, J. M.; Meyer, T. J., Chemical approaches to artificial photosynthesis. Proceedings of the National Academy of Sciences 2012, 109 (39), 15560-15564.

24. Liu, C.; Colón, B. C.; Ziesack, M.; Silver, P. A.; Nocera, D. G., Water splitting–biosynthetic system with CO_2 reduction efficiencies exceeding photosynthesis. Science 2016, 352 (6290), 1210-1213.

25. Sakimoto, K. K.; Wong, A. B.; Yang, P., Self-photosensitization of nonphotosynthetic bacteria for solar-to-chemical production. Science 2016, 351 (6268), 74-77.

26. Higgins, D.; Landers, A. T.; Ji, Y.; Nitopi, S.; Morales-Guio, C. G.; Wang, L.; Chan, K.; Hahn, C.; Jaramillo, T. F., Guiding electrochemical carbon dioxide reduction toward carbonyls using copper silver thin films with interphase miscibility. ACS Energy Letters 2018, 3 (12), 2947-2955.

27. White, J. L.; Baruch, M. F.; Pander III, J. E.; Hu, Y.; Fortmeyer, I. C.; Park, J. E.; Zhang, T.; Liao, K.; Gu, J.; Yan, Y., Light-driven heterogeneous reduction of carbon dioxide: photocatalysts and photoelectrodes. Chemical reviews 2015, 115 (23), 12888-12935.

28. Morris, A. J.; Meyer, G. J.; Fujita, E., Molecular approaches to the photocatalytic reduction of carbon dioxide for solar fuels. Accounts of chemical research 2009, 42 (12), 1983-1994.

29. Costentin, C.; Passard, G.; Robert, M.; Savéant, J.-M., Ultraefficient homogeneous catalyst for the CO_2-to-CO electrochemical conversion. Proceedings of the National Academy of Sciences 2014, 111 (42), 14990-14994.

30. Rajeshwar, K.; Thomas, A.; Janáky, C., Photocatalytic activity of inorganic semiconductor surfaces: myths, hype, and reality. ACS Publications: 2015.

31. Shi, Q.; Hwang, S.; Yang, H.; Ismail, F.; Su, D.; Higgins, D.; Wu, G., Supported and coordinated single metal site electrocatalysts. Materials Today 2020.

32. Chen, Z.; Higgins, D.; Yu, A.; Zhang, L.; Zhang, J., A review on non-precious metal electrocatalysts for PEM fuel cells. Energy & Environmental Science 2011, 4 (9), 3167-3192.

33. Koshy, D. M.; Landers, A. T.; Cullen, D. A.; Ievlev, A. V.; Meyer III, H. M.; Hahn, C.; Bao, Z.; Jaramillo, T. F., Direct Characterization of Atomically Dispersed Catalysts: Nitrogen-Coordinated Ni Sites in Carbon-Based Materials for CO_2 Electroreduction. Advanced Energy Materials 2020, 10 (39), 2001836.

34. Wu, G.; More, K. L.; Johnston, C. M.; Zelenay, P., High-performance electrocatalysts for oxygen reduction derived from polyaniline, iron, and cobalt. Science 2011, 332 (6028), 443-447.

35. Choi, J.-Y.; Hsu, R. S.; Chen, Z., Highly active porous carbon-supported nonprecious metal− N electrocatalyst for oxygen reduction reaction in PEM fuel cells. The Journal of Physical Chemistry C 2010, 114 (17), 8048-8053.

36. Johnson, D.; Qiao, Z.; Djire, A., Progress and Challenges of Carbon Dioxide Reduction Reaction on Transition Metal Based Electrocatalysts. ACS Applied Energy Materials 2021, 4 (9), 8661-8684.

37. Chung, H. T.; Cullen, D. A.; Higgins, D.; Sneed, B. T.; Holby, E. F.; More, K. L.; Zelenay, P., Direct atomic-level insight into the active sites of a high-performance PGM-free ORR catalyst. Science 2017, 357 (6350), 479-484.

38. Kramm, U. I.; Herranz, J.; Larouche, N.; Arruda, T. M.; Lefevre, M.; Jaouen, F.; Bogdanoff, P.; Fiechter, S.; Abs-Wurmbach, I.; Mukerjee, S., Structure of the catalytic sites in

Fe/N/C-catalysts for O_2-reduction in PEM fuel cells. Physical Chemistry Chemical Physics 2012, 14 (33), 11673-11688.

39. Jaouen, F.; Proietti, E.; Lefèvre, M.; Chenitz, R.; Dodelet, J.-P.; Wu, G.; Chung, H. T.; Johnston, C. M.; Zelenay, P., Recent advances in non-precious metal catalysis for oxygen-reduction reaction in polymer electrolyte fuel cells. Energy & Environmental Science 2011, 4 (1), 114-130.

40. Tylus, U.; Jia, Q.; Strickland, K.; Ramaswamy, N.; Serov, A.; Atanassov, P.; Mukerjee, S., Elucidating oxygen reduction active sites in pyrolyzed metal–nitrogen coordinated non-precious-metal electrocatalyst systems. The Journal of Physical Chemistry C 2014, 118 (17), 8999-9008.

41. Lefèvre, M.; Dodelet, J.; Bertrand, P., Molecular oxygen reduction in PEM fuel cells: evidence for the simultaneous presence of two active sites in Fe-based catalysts. The Journal of Physical Chemistry B 2002, 106 (34), 8705-8713.

42. Lefevre, M.; Dodelet, J.; Bertrand, P., Molecular oxygen reduction in PEM fuel cell conditions: ToF-SIMS analysis of Co-based electrocatalysts. The Journal of Physical Chemistry B 2005, 109 (35), 16718-16724.

43. Li, J.; Sougrati, M. T.; Zitolo, A.; Ablett, J. M.; Oğuz, I. C.; Mineva, T.; Matanovic, I.; Atanassov, P.; Huang, Y.; Zenyuk, I., Identification of durable and non-durable FeNx sites in Fe–N–C materials for proton exchange membrane fuel cells. Nature Catalysis 2021, 4 (1), 10-19.

44. Wang, Y.; Su, H.; He, Y.; Li, L.; Zhu, S.; Shen, H.; Xie, P.; Fu, X.; Zhou, G.; Feng, C., Advanced electrocatalysts with single-metal-atom active sites. Chemical reviews 2020, 120 (21), 12217-12314.

45. Tripkovic, V.; Vanin, M.; Karamad, M.; Björketun, M. r. E.; Jacobsen, K. W.; Thygesen, K. S.; Rossmeisl, J., Electrochemical CO_2 and CO reduction on metal-functionalized porphyrin-like graphene. The Journal of Physical Chemistry C 2013, 117 (18), 9187-9195.

46. Ju, W.; Bagger, A.; Hao, G.-P.; Varela, A. S.; Sinev, I.; Bon, V.; Cuenya, B. R.; Kaskel, S.; Rossmeisl, J.; Strasser, P., Understanding activity and selectivity of metal-nitrogen-doped carbon catalysts for electrochemical reduction of CO_2. Nature communications 2017, 8 (1), 1-9.

47. Koshy, D. M.; Chen, S.; Lee, D. U.; Stevens, M. B.; Abdellah, A. M.; Dull, S. M.; Chen, G.; Nordlund, D.; Gallo, A.; Hahn, C., Understanding the origin of highly selective CO2 electroreduction to CO on Ni, N-doped carbon catalysts. Angewandte Chemie 2020, 132 (10), 4072-4079.

48. Cheng, Y.; Yang, S.; Jiang, S. P.; Wang, S., Supported single atoms as new class of catalysts for electrochemical reduction of carbon dioxide. Small Methods 2019, 3 (9), 1800440.

49. Qin, X.; Zhu, S.; Xiao, F.; Zhang, L.; Shao, M., Active sites on heterogeneous single-iron-atom electrocatalysts in CO_2 reduction reaction. ACS Energy Letters 2019, 4 (7), 1778-1783.

50. Vijay, S.; Gauthier, J. A.; Heenen, H. H.; Bukas, V. J.; Kristoffersen, H. H.; Chan, K., Dipole-Field Interactions Determine the CO_2 Reduction Activity of 2D Fe–N–C Single-Atom Catalysts. ACS Catalysis 2020, 10 (14), 7826-7835.

51. Koshy, D.; Nathan, S.; Asundi, A.; Abdellah, A.; Dull, S.; Cullen, D.; Higgins, D.; Bao, Z.; Bent, S.; Jaramillo, T., Bridging thermal catalysis and electrocatalysis: Catalyzing CO_2 conversion with carbon-based materials. Angewandte Chemie International Edition 2021.

52. Zhu, H.-L.; Zheng, Y.-Q.; Shui, M., Synergistic interaction of nitrogen-doped carbon nanorod array anchored with cobalt phthalocyanine for electrochemical reduction of CO_2. ACS Applied Energy Materials 2020, 3 (4), 3893-3901.

53. Ghanbari, T.; Abnisa, F.; Daud, W. M. A. W., A review on production of metal organic frameworks (MOF) for CO_2 adsorption. Science of The Total Environment 2020, 707, 135090.

54. Diercks, C. S.; Yaghi, O. M., The atom, the molecule, and the covalent organic framework. Science 2017, 355 (6328).

55. Zhao, C.; Dai, X.; Yao, T.; Chen, W.; Wang, X.; Wang, J.; Yang, J.; Wei, S.; Wu, Y.; Li, Y., Ionic exchange of metal–organic frameworks to access single nickel sites for efficient electroreduction of CO_2. Journal of the American Chemical Society 2017, 139 (24), 8078-8081.

56. Ma, Z.; Wu, D.; Han, X.; Wang, H.; Zhang, L.; Gao, Z.; Xu, F.; Jiang, K., Ultrasonic assisted synthesis of Zn-Ni bi-metal MOFs for interconnected Ni-NC materials with enhanced electrochemical reduction of CO_2. Journal of CO_2 Utilization 2019, 32, 251-258.

57. Gong, Y. N.; Jiao, L.; Qian, Y.; Pan, C. Y.; Zheng, L.; Cai, X.; Liu, B.; Yu, S. H.; Jiang, H. L., Regulating the Coordination Environment of MOF-Templated Single-Atom Nickel Electrocatalysts for Boosting CO_2 Reduction. Angewandte Chemie International Edition 2020, 59 (7), 2705-2709.

58. Huang, X. C.; Lin, Y. Y.; Zhang, J. P.; Chen, X. M., Ligand-directed strategy for zeolite-type metal–organic frameworks: zinc (II) imidazolates with unusual zeolitic topologies. Angewandte Chemie International Edition 2006, 45 (10), 1557-1559.

59. Proietti, E.; Jaouen, F.; Lefèvre, M.; Larouche, N.; Tian, J.; Herranz, J.; Dodelet, J.-P., Iron-based cathode catalyst with enhanced power density in polymer electrolyte membrane fuel cells. Nature communications 2011, 2 (1), 1-9.

60. Yin, P.; Yao, T.; Wu, Y.; Zheng, L.; Lin, Y.; Liu, W.; Ju, H.; Zhu, J.; Hong, X.; Deng, Z. J. A. C., Single cobalt atoms with precise N-coordination as superior oxygen reduction reaction catalysts. 2016, 128 (36), 10958-10963.

61. Fan, Q.; Hou, P.; Choi, C.; Wu, T. S.; Hong, S.; Li, F.; Soo, Y. L.; Kang, P.; Jung, Y.; Sun, Z., Activation of Ni particles into single Ni–N atoms for efficient electrochemical reduction of CO_2. Advanced Energy Materials 2020, 10 (5), 1903068.

62. Wang, Z.-L.; Choi, J.; Xu, M.; Hao, X.; Zhang, H.; Jiang, Z.; Zuo, M.; Kim, J.; Zhou, W.; Meng, X., Optimizing electron densities of Ni-NC complexes by hybrid coordination for efficient electrocatalytic CO_2 reduction. ChemSusChem 2020, 13 (5), 929-937.

63. Sengupta, J.; Jacob, C., The effect of Fe and Ni catalysts on the growth of multiwalled carbon nanotubes using chemical vapor deposition. Journal of Nanoparticle Research 2010, 12 (2), 457-465.

64. Dupuis, A.-C., The catalyst in the CCVD of carbon nanotubes—a review. Progress in materials science 2005, 50 (8), 929-961.

65. Rao, R.; Sharma, R.; Abild-Pedersen, F.; Nørskov, J. K.; Harutyunyan, A. R., Insights into carbon nanotube nucleation: Cap formation governed by catalyst interfacial step flow. Scientific reports 2014, 4 (1), 1-6.

66. Chen, M.; Zhao, G.; Shao, L.-L.; Yuan, Z.-Y.; Jing, Q.-S.; Huang, K.-J.; Huang, Z.-Y.; Zhao, X.-H.; Zou, G.-D., Controlled synthesis of nickel encapsulated into nitrogen-doped carbon nanotubes with covalent bonded interfaces: the structural and electronic modulation strategy for an efficient electrocatalyst in dye-sensitized solar cells. Chemistry of Materials 2017, 29 (22), 9680-9694.

67. Shekhah, O.; Eddaoudi, M., The liquid phase epitaxy method for the construction of oriented ZIF-8 thin films with controlled growth on functionalized surfaces. Chemical Communications 2013, 49 (86), 10079-10081.

68. Sun, C.; Zhang, Y.; Wang, P.; Yang, Y.; Wang, Y.; Xu, J.; Wang, Y.; William, W. Y., Synthesis of nitrogen and sulfur co-doped carbon dots from garlic for selective detection of Fe^{3+}. Nanoscale research letters 2016, 11 (1), 1-9.

69. Yang, H. B.; Hung, S.-F.; Liu, S.; Yuan, K.; Miao, S.; Zhang, L.; Huang, X.; Wang, H.-Y.; Cai, W.; Chen, R., Atomically dispersed Ni (I) as the active site for electrochemical CO_2 reduction. Nature energy 2018, 3 (2), 140-147.

70. Li, X.; Bi, W.; Chen, M.; Sun, Y.; Ju, H.; Yan, W.; Zhu, J.; Wu, X.; Chu, W.; Wu, C., Exclusive Ni–N4 sites realize near-unity CO selectivity for electrochemical CO_2 reduction. Journal of the American Chemical Society 2017, 139 (42), 14889-14892.

71. Yang, J.; Qiu, Z.; Zhao, C.; Wei, W.; Chen, W.; Li, Z.; Qu, Y.; Dong, J.; Luo, J.; Li, Z., In situ thermal atomization to convert supported nickel nanoparticles into surface-bound nickel single-atom catalysts. Angewandte Chemie International Edition 2018, 57 (43), 14095-14100.

The Impact of Nickel Content on the Structure and Electrochemical CO_2 Reduction Performance of Nickel-Nitrogen-Carbon Catalysts Derived from Zeolitic Imidazolate Frameworks

Fatma M. Ismail[a], Ahmed Abdellah[b], Hye-jin Lee[c], V.Sudheeshkumar[d], Drew C. Higgins[e*]

Department of Chemical Engineering, McMaster University, Hamilton, Ontario L8S 4L7, Canada.

[a]ismaif1@mcmaster.ca, [b]abdellaa@mcmaster.ca, [c]leeh114@mcmaster.ca, [d]veeranms@mcmaster.ca, [e]higgid2@mcmaster.ca

3.8 Supporting Information

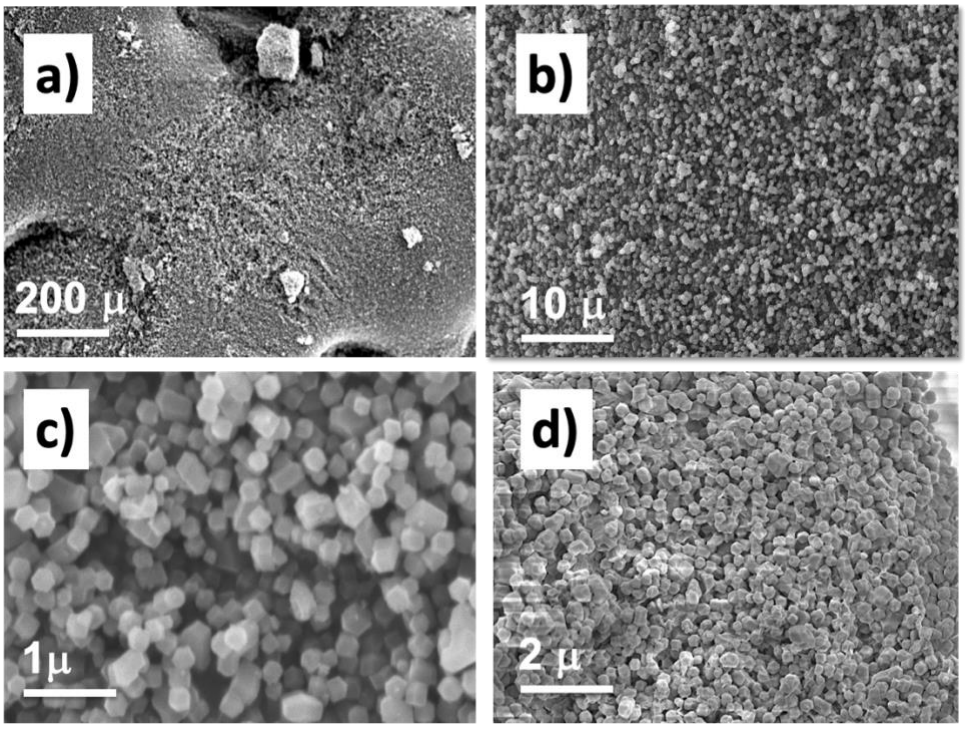

Figure S1 Different magnification scanning electron microscopy (SEM) images of (a-d) ZIF-8 nanoparticles.

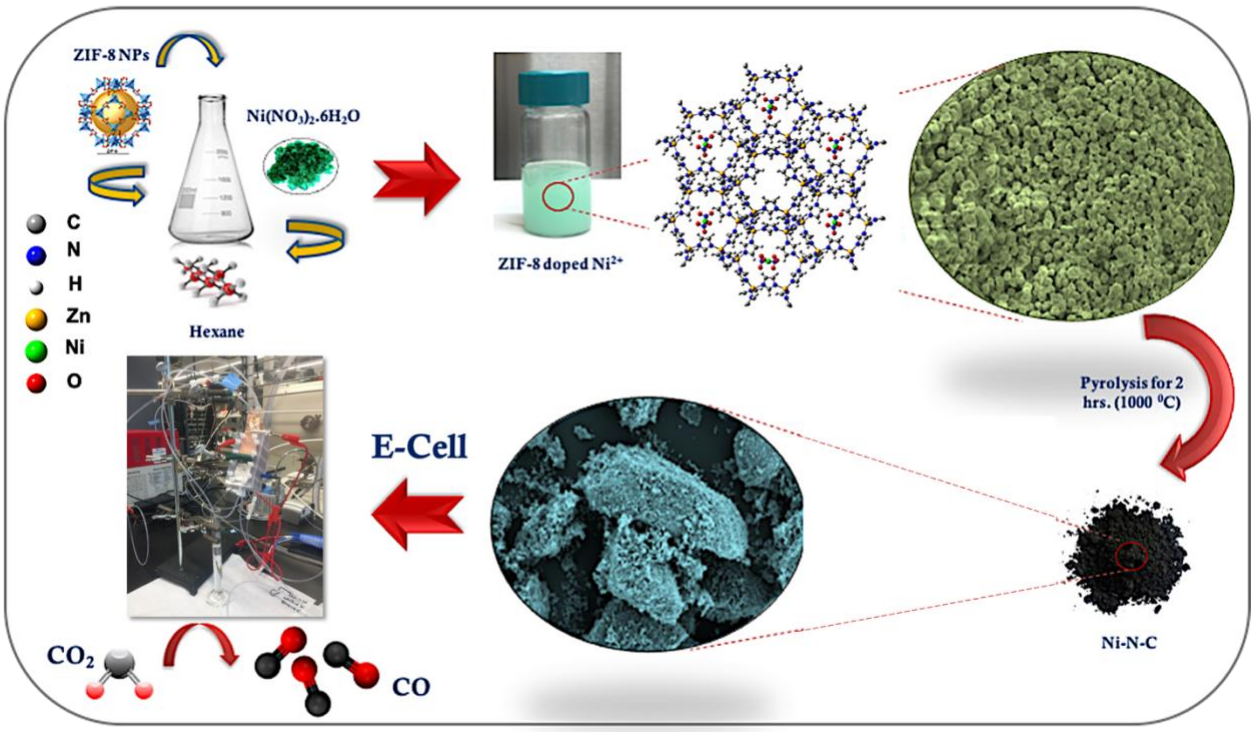

Figure S2. Schematic diagram elaborating the synthesis approach of the produced Ni-N-C single atoms.

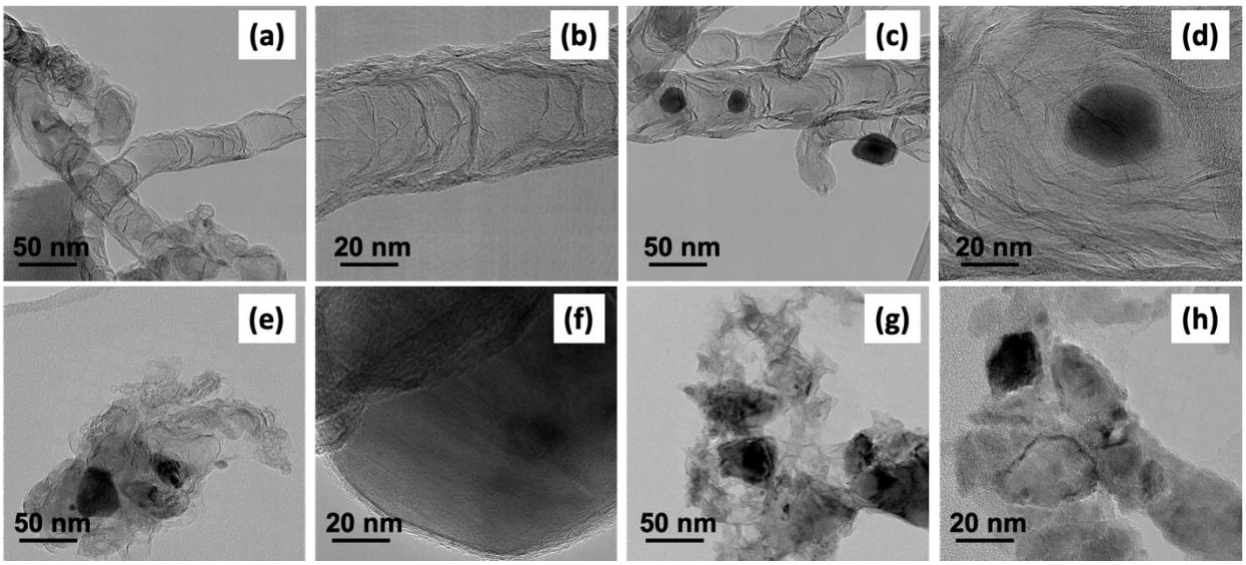

Figure S3. Different magnification TEM/HRTEM images of Ni:Zn different atomic ratios; (a,b) a-Ni-N-C, (c,d) b-Ni-N-C, (e,f) c-Ni-N-C, (g,h) d-Ni-N-C.

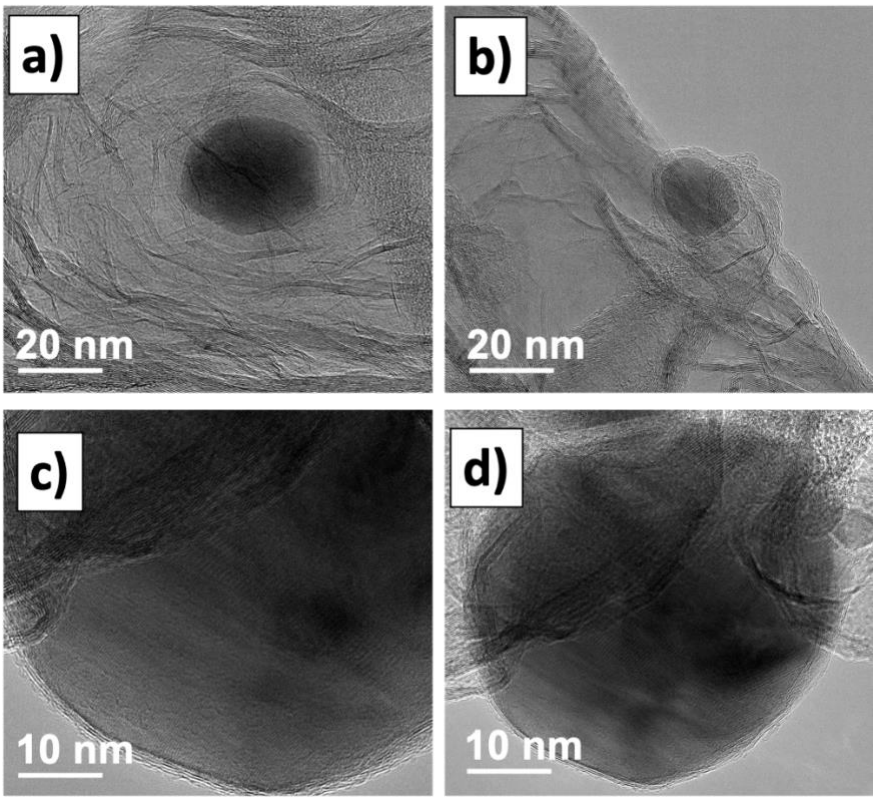

Figure S4. HRTEM images of the Ni nanoparticles present in (a,b) b-Ni-N-C, (c,d) c-Ni-N-C

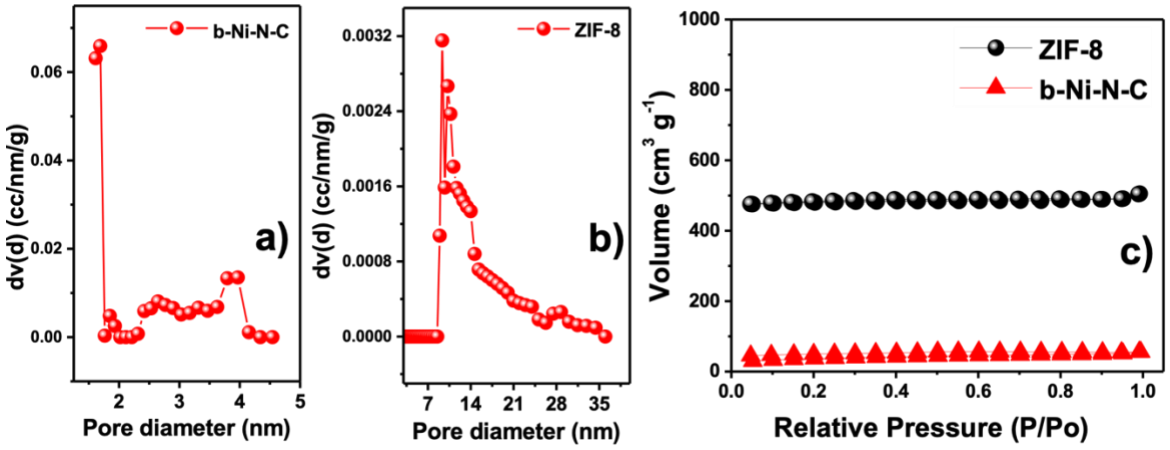

Figure S5. BET measurement results, showing pore diameter distributions for (a) b-Ni-N-C and (b) ZIF-8. (c) BET adsorption isotherm measurements for ZIF-8 and b-Ni-N-C.

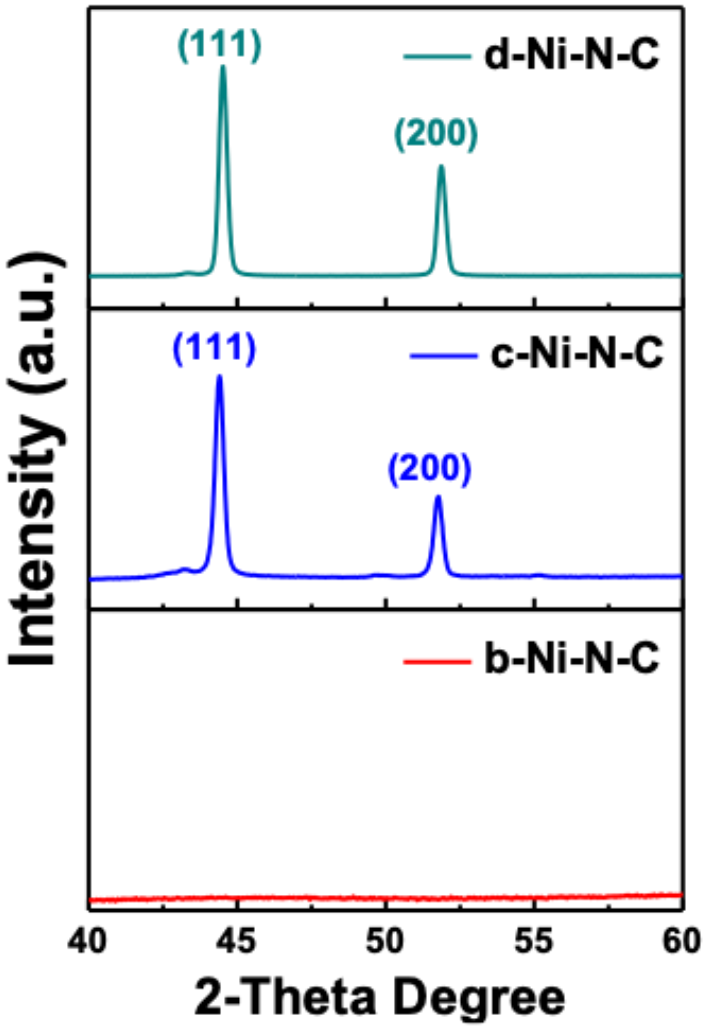

Figure S6: High resolution PXRD spectra of b-Ni-N-C, c-Ni-N-C, d-Ni-N-C catalysts, illustrating no peak shifts due to Ni-Zn alloying.

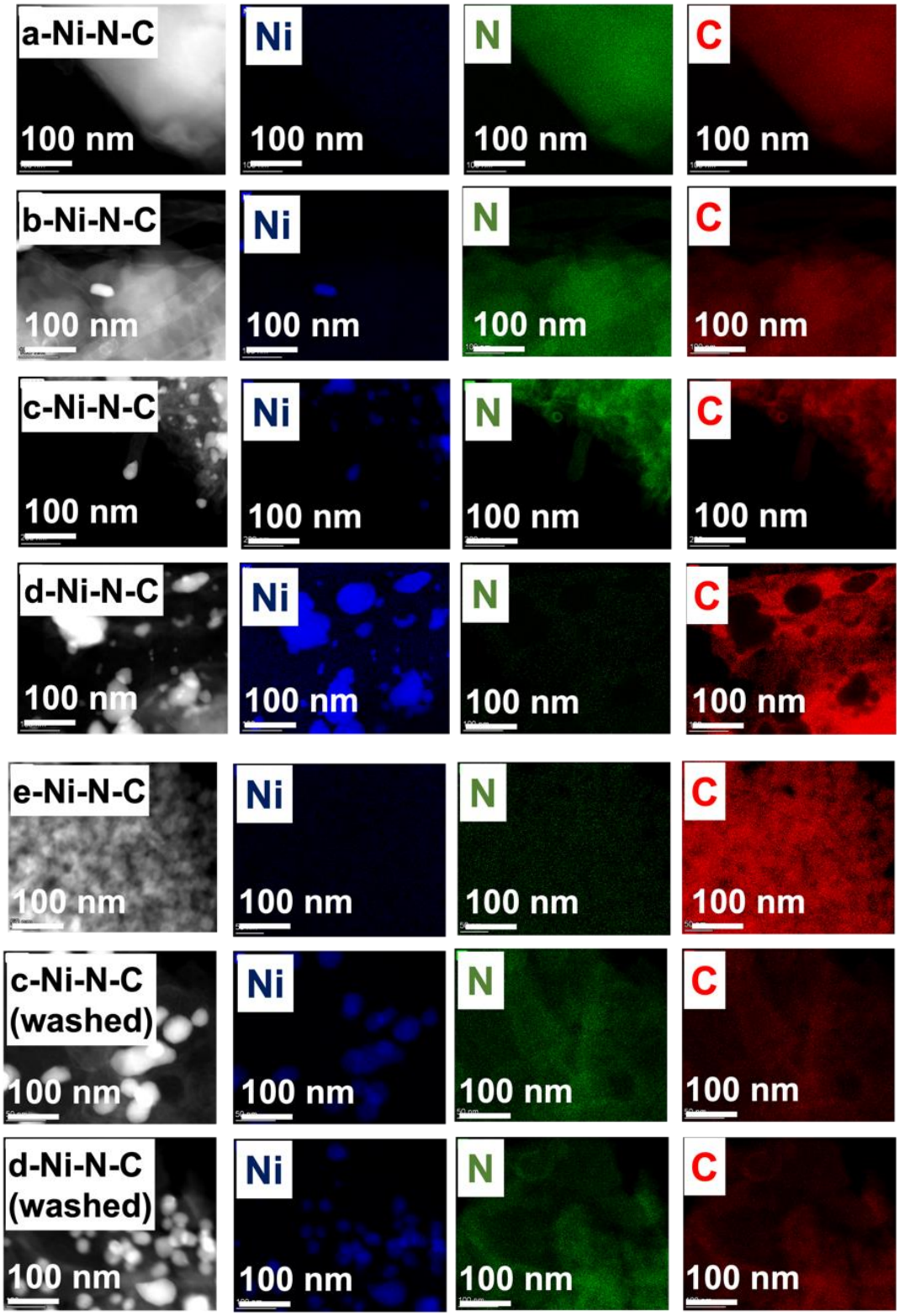

Figure S7. EDS mapping of all Ni-N-C catalysts developed for CO_2R before and after acid wash.

Table S1 Compositional distribution of nickel, nitrogen, and carbon processed by EDS mapping for all Ni-N-C catalysts before and after acid wash.

Catalyst	Nickel (wt.%)	Nitrogen (wt.%)	Carbon (wt.%)
a-Ni-N-C	1.7	5.8	88
b-Ni-N-C	6.7	4.9	89
c-Ni-N-C	34	3.2	60
d-Ni-N-C	76	1.2	20
e-Ni-N-C	0.9	6.2	89
c-Ni-N-C acid washed	35	4.1	55
d-Ni-N-C acid washed	40	3.2	49

Table S2 ICP-AES measurements of the developed Ni-N-C catalysts with different Ni:Zn atomic ratios.

Catalyst	Nickel (%)
a-Ni-N-C	6.8
b-Ni-N-C	10
c-Ni-N-C	16
d-Ni-N-C	60
e-Ni-N-C	0.5
c-Ni-N-C acid washed	4.5
d-Ni-N-C acid washed	5.2

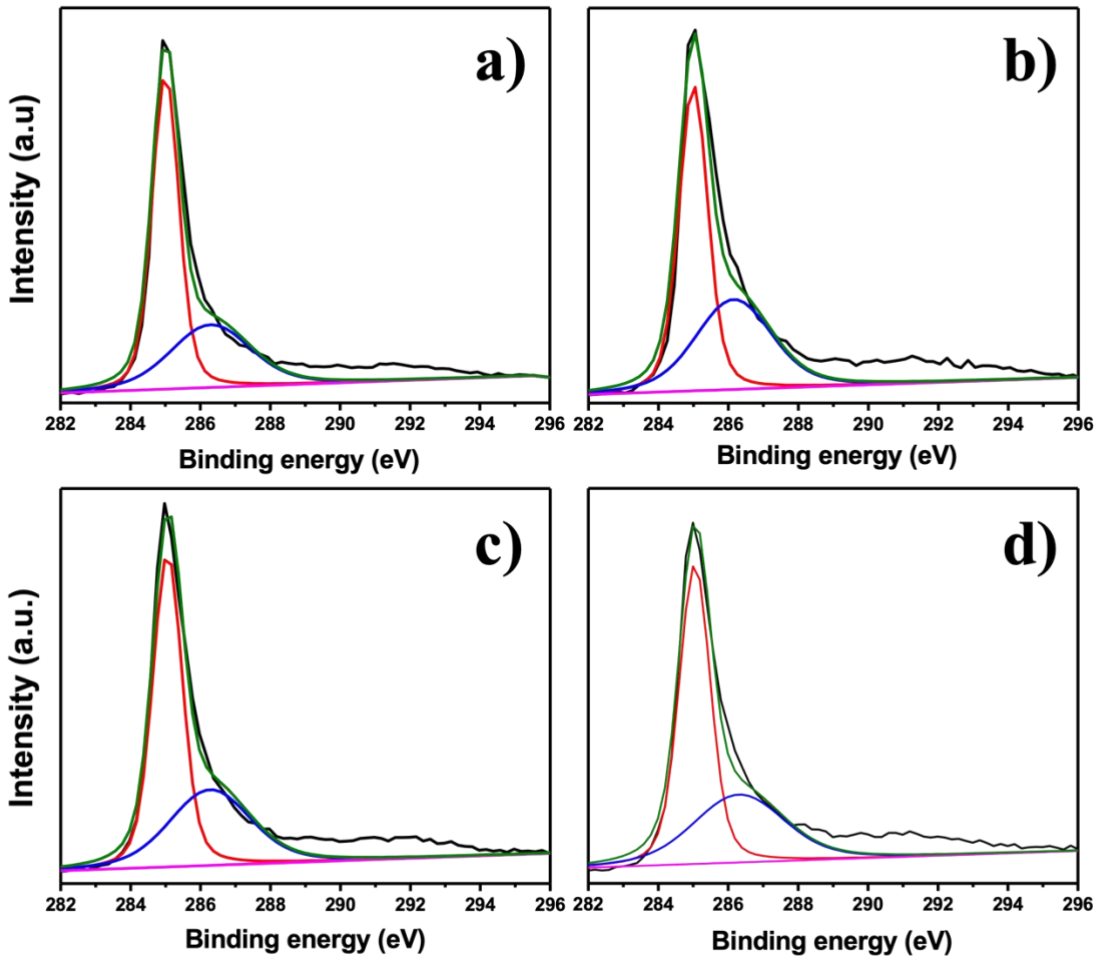

Figure S8: C 1s XPS spectra of a) a-Ni-N-C b) b-Ni-N-C c) c-Ni-N-C d) d-Ni-N-C catalysts.

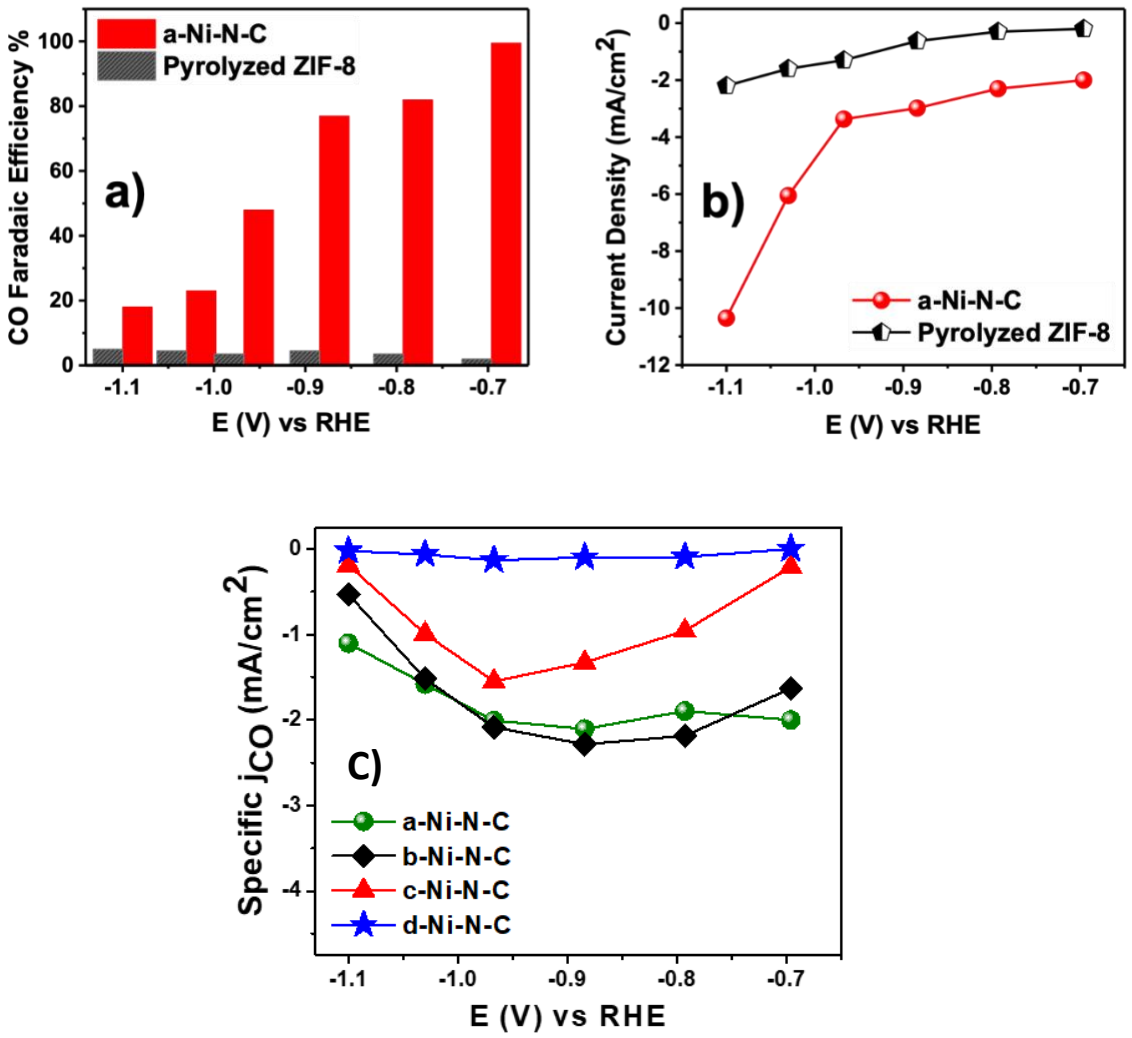

Figure S9. (a) CO Faradaic efficiencies, (b) total current densities for a-Ni-N-C catalyst and Ni-free pyrolyzed ZIF-8 catalyst at different electrode potentials, and (c) CO partial current densities for all Ni-N-C electrocatalysts.

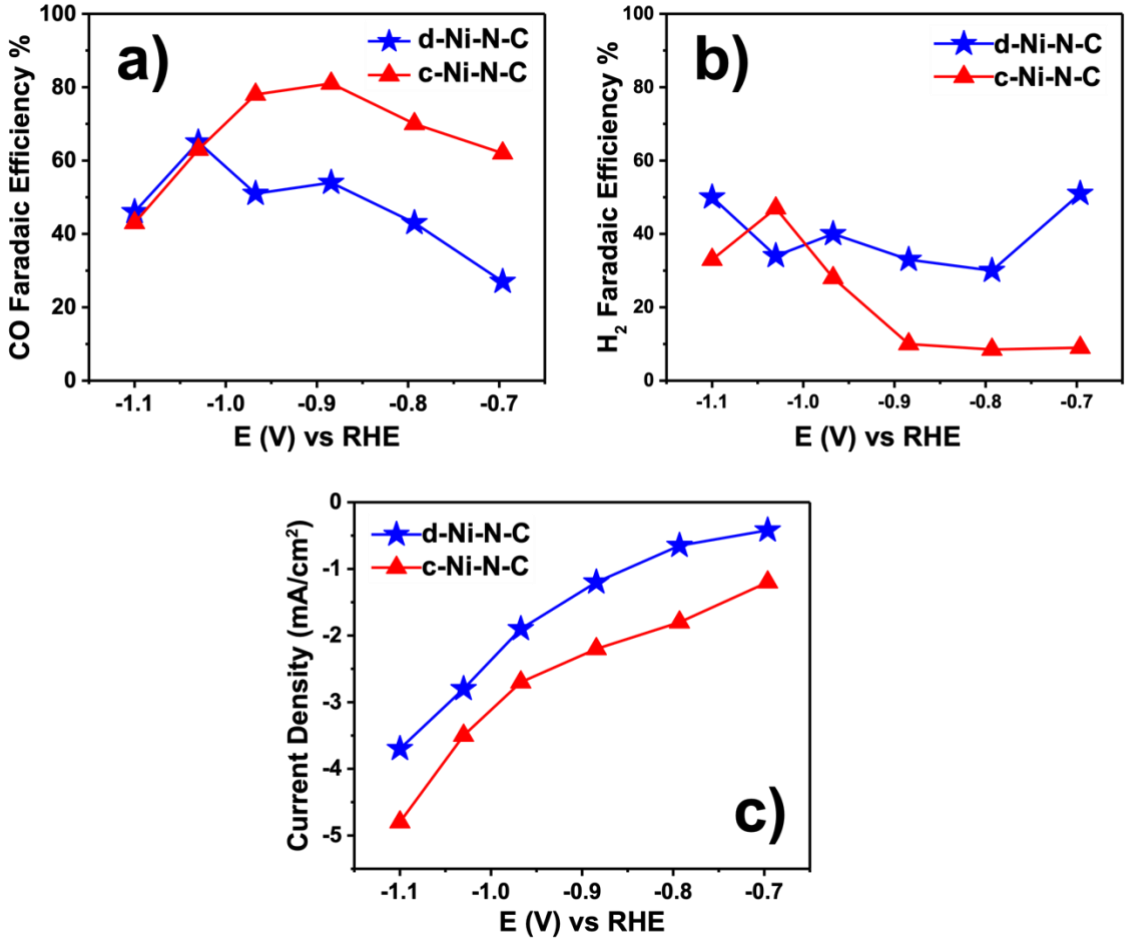

Figure S10. (a) CO Faradaic efficiencies, (b) H_2 Faradaic efficiencies, and (c) total current densities of both c-Ni-N-C and d-Ni-N-C catalysts after acid wash.

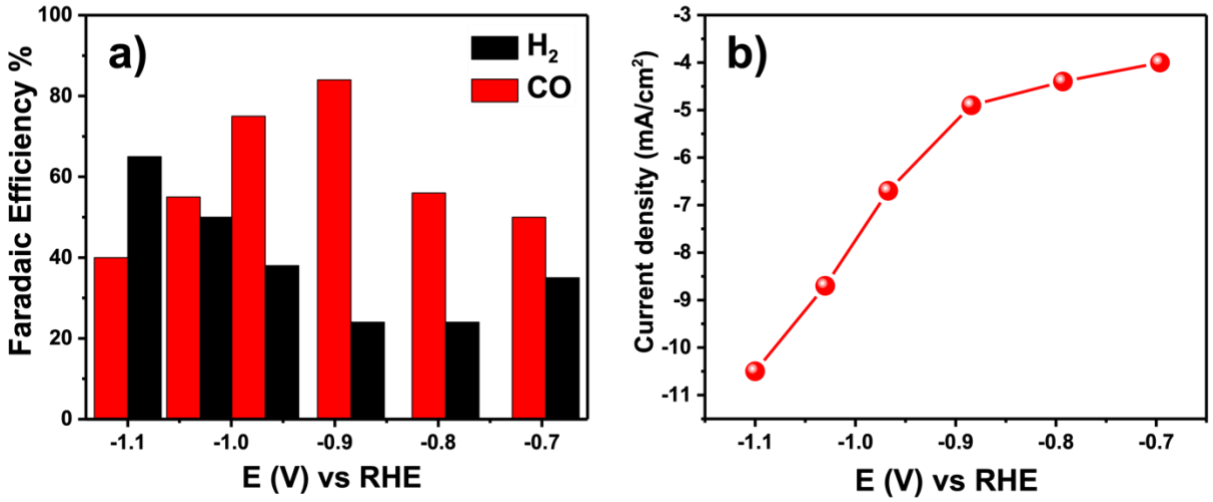

Figure S11. (a) CO and H_2 Faradaic efficiencies (b) total current density of 0.25:1 Ni:Zn atomic ratio (e-Ni-N-C).

Calculating Faradaic Efficiencies:

$$Faradaic\ Efficiency\ \% = \frac{Moles\ of\ the\ product * e - per\ mole * F\ constant}{Average\ I * \frac{60}{Flow\ rate}}$$

Where:

F: Farad constant 96485 C mol^{-1}.

I: Average current.

e^-: Number of electrons transferred per mole, "2 electrons" in case of CO.

4. Chapter| Atomically Isolated Ni–N–C Electrocatalysts Derived by the Utilization of Mg^{2+} ions as Spacers in Bimetallic Ni/ Mg−MOF Precursors for Boosting the Electroreduction of CO_2

In this chapter, a non-nitrogen-based MOF has been employed to derive atomically dispersed Ni–N–C catalysts to impart a new class of MOFs –that build from non-nitrogen-based organic ligands– to prepare Ni–N–C catalysts. However, maintaining the isolation of the transition metal species, achieving high surface concentrations of active sites, and imparting porosity during the high-temperature heat treatment of MOFs used during synthesis remains a challenge. In this report, Mg^{2+} ions have been employed as spacers in a bi-metallic metal-organic framework (NiMg-MOF-74) to assist in preventing the coalescence of the Ni atoms into Ni-based particles during heat treatment, which combined with the use of urea as a nitrogen source resulted in the formation of isolated Ni-N_x/C active sites. Our findings demonstrated that Mg^{2+} ions play a crucial role in extending the distance between the adjacent Ni sites in the precursor structure and generating atomically isolated Ni sites. On the contrary, the utilization of Mg-free Ni-MOF-74 led to the formation of metallic Ni particles embedded in carbon nanotubes-based structures. Furthermore, we investigated the impact of pyrolysis temperature on the produced catalyst morphology. The generation of isolated Ni-N_x/C sites was promoted at higher pyrolysis temperatures (900°C), while Ni-based particles were predominantly formed at a lower temperature (700°C). The optimized atomically dispersed Ni-N-C catalyst exhibited excellent selectivity towards CO with a Faradaic efficiency of ~90% and a current density of -4.2 mA/cm^2 at -0.76 V vs a reversible hydrogen electrode.

Atomically Isolated Nickel-Nitrogen-Carbon Electrocatalysts Derived by the Utilization of Mg^{2+} ions as Spacers in Bimetallic Ni/Mg-Metal Organic Framework Precursors for Boosting the Electroreduction of CO_2

Fatma Ismail[a], Ahmed Abdellah[b], Ning Chen[c], Veeranmaril Sudheeshkumar[d]
Amirhossein Rakhsha[e], Drew C. Higgins[f*]

Department of Chemical Engineering, McMaster University, Hamilton, Ontario L8S 4L7, Canada

[a]ismaif1@mcmaster.ca, [b]abdellaa@mcmaster.ca, [c]ning.chen@lightsource.ca
[d]sudheeshkumar.v@gmail.com, [e]a.h.rakhsha@gmail.com [f]higgid2@mcmaster.ca

4.1 Abstract

Electrochemical CO_2 reduction (CO_2R) is a promising avenue for the conversion of CO_2 into fuels and beneficial chemicals. Significant efforts have been devoted to the development of active and selective electrocatalysts for CO_2R. Atomically dispersed transition metal electrocatalysts have recently attracted consideration for CO_2R due to their unique electronic and structural properties that can impart good catalytic performance and high active metal utilization. Among different precursors used for preparing these catalysts, metal organic frameworks (MOFs) have been utilized as templates for generating atomically dispersed transition metal active sites as they provide well-defined structures that contain transition metals isolated from each other by organic ligands, along with high surface areas. However, maintaining the isolation of the transition metal species, achieving high surface concentrations of active sites, and imparting porosity during the high temperature heat treatment of MOFs used during synthesis remains a challenge. In this report, Mg^{2+} ions have been employed as spacers in a bi-metallic metal organic framework (NiMg-MOF-

74) to assist on preventing the coalescence of the Ni atoms into Ni-based particles during heat treatment, which combined with the use of urea as a nitrogen source resulted in the formation of isolated Ni-N_x/C active sites. Our findings demonstrated that Mg^{2+} ions play a crucial role in extending the distance between the adjacent Ni sites in the precursor structure and generating atomically isolated Ni sites. On the contrary, the utilization of Mg-free Ni-MOF-74 led to the formation of metallic Ni particles embedded in carbon nanotubes-based structure. Furthermore, we investigated the impact of pyrolysis temperature on the produced catalyst morphology. The generation of isolated Ni-N_x/C sites was promoted at higher pyrolysis temperatures (900°C), while Ni-based particles were predominantly formed at a lower temperature (700°C). The optimized atomically dispersed Ni-N-C catalyst exhibited excellent selectivity towards CO with a Faradaic efficiency of ~90% and a current density of -4.2 mA/cm^2 at -0.76 V vs a reversible hydrogen electrode.

Keywords: MOF-derived electrocatalyst; CO_2 electrolysis; Ni single atoms; metal-nitrogen-carbon, Atomically dispersed nickel-nitrogen-carbon.

4.2 Introduction

The drastic increase of global carbon emissions resulting in increased atmospheric CO_2 concentration is attributed to the intensive dependence on fossil fuels as the main energy resource, that has resulted in serious temperature variations along with disturbances in agricultural lands and habitats. Scholars are devoting tremendous efforts towards the development of sustainable energy technologies to mitigate our reliance on fossil fuels or their associated emissions. The electrochemical CO_2 reduction (CO_2R) into chemicals and fuels is one promising approach under investigation.[1, 2, 3] Through the CO_2R, renewable energy resources such as solar, wind, or hydro could be utilized to generate the required electricity for driving the reduction reaction. CO_2R can

be carried out at near-ambient conditions, restraining the need for high temperature and/or high-pressure operation.[4-15]

The development of inexpensive and high-performance catalysts and their integration into electrode structures is the main gateway towards efficient CO_2R technologies. In the context of catalyst development, researchers have pursued efforts to produce high performance electrocatalysts that can overcome the CO_2R related challenges.[16-19] Atomically dispersed metal-nitrogen-doped carbon (M-N-C) catalysts, featured with an atomic level dispersion of the metal atoms, exhibited a remarkable electrocatalytic performance in various energy-related applications, particularly, CO_2R, due to maximum utilization of metal sites and good electronic conductivity of the carbon-based supports.[20-27] M-N-C materials are solid materials that combine the merits of both homogenous and heterogenous catalysts.[28-32] The stabilization of isolated metal active sites in M-N-C catalysts is achieved by coordination with nitrogen-dopant species to reduce their surface energy and prevent metal atom coalescence, whereby the local coordination environment has a significant influence on the electrocatalytic selectivity and activity of M-N-C in CO_2R.[33] Despite its importance, precise control of the local coordination environment of the active site structures in M-N-C catalysts during synthesis remains challenging.[33-36]

Metal-organic frameworks (MOFs), a class of materials with diverse compositions and highly porous architectures have been shown useful in several applications,[37-41] including for use as well-defined precursors for the synthesis of materials for catalysis and energy applications.[40, 42-45] MOFs are considered an ideal platform to generate atomically dispersed M-N-C catalysts due to the rational and spatial separation of metal atoms at an atomic level.[46-52] More specifically, it is possible to control the local coordination environment and structure of the atomically dispersed metal species in MOFs owing to the ability to precisely tailor their structures. Although efforts

have been devoted in this regard, most of the synthetic approaches using MOFs for generating M-N-C catalysts are confined to the nitrogen-containing MOFs, for instance, zeolitic imidazole frameworks (ZIFs)[46, 47, 53] and porphyrin-based MOFs.[54-57] Since the nitrogen-containing MOFs account for only a small portion of the various MOFs in existence, developing a general strategy for producing atomically dispersed M-N-C catalysts based on other types of MOFs can provide additional levers of control during catalyst synthesis. As an example, MOF-74 is constructed by the coordination of 2,5-dioxido-1,4- benzenedicarboxylate ligand and various divalent M^{2+} ions such as Ni^{2+}, Mg^{2+}, Co^{2+}, etc, via facile approaches.[58, 59] The utilization of MOF-74 as a precursor for creating atomically dispersed M-N_x/C sites provides an opportunity to optimize the concentration and dispersion of the metal species integrated into the structure, as well as tunability in terms of the identity of the metals and the ability to explore a mixed-metal approach.[60-62]

In our previous study, a series of atomically dispersed Ni-N-C catalysts were derived from ZIF-8 as a nitrogenous platform, whereby the impact of Ni content on the structure and electrochemical performance in each catalyst has been investigated.[63] Moving forward, in this report, newly developed atomically dispersed Ni-N-C catalysts have been prepared through a host-guest synthetic strategy where a bimetallic NiMg-MOF-74 was utilized as a platform as a non-nitrogenous template to host urea molecules as the nitrogen-containing guests into its 1D channels, yielding a urea@NiMg-MOF-74. During the synthesis of bimetallic NiMg-MOF-74, the content of Mg^{2+} ions was optimized to surpass the Ni^{2+} concentration to ensure the successful isolation of the adjacent Ni atoms, which enabled us to achieve spatial isolation of the Ni sites in the MOF structure. Upon pyrolysis of the urea@NiMg-MOF-74 compound, a porous carbon structure is derived from the decomposition of the MOF skeleton while nitrogen atoms from urea were incorporated as dopants into the carbon that act as stabilizers to generate atomically dispersed M-

N_x/C sites. The pyrolysis temperature utilized was demonstrated as a key parameter to control the formation of atomically dispersed Ni-N_x/C sites. Using a higher pyrolysis temperature (900 °C) resulted in the successful formation of atomically dispersed Ni-N_x/C sites which are favourable for CO_2R, while at a lower pyrolysis temperature (700 °C), metallic Ni nano/microparticles were also produced resulting in a switch in selectivity towards the competing hydrogen evolution reaction (HER). The optimized atomically dispersed Ni-N-C catalysts exhibited an excellent selectivity towards CO in CO_2R with a Faradaic efficiency of ~90% at -0.76 V vs the reversible hydrogen electrode (RHE) at a current density of -4.2 mA/cm^2.

4.3 Materials & Methods

4.3.1 Materials

Nickel nitrate hexahydrate ($Ni(NO_3)_2.6H_2O$), magnesium nitrate hexahydrate ($Mg(NO_3)_2.6H_2O$), 2,5-dioxido-1,4-benzenedicarboxylate (H_4dobdc), potassium bicarbonate ($KHCO_3$), nitric acid, n-hexane, urea, ethanol (EtOH), Nafion solution 5%, isopropanol (IPA), dimethyl formamide (DMF), graphite foil, and Millipore water (H_2O) were used in this work. All chemicals have been obtained from Sigma Aldrich and used without further purification.

4.3.2 Synthesis of bi-metallic NiMg-MOF-74

In a typical procedure, a mixed solvent of 1mL EtOH, 1mL H_2O, and 15 mL DMF was used to dissolve (0.001 g) of $Ni(NO_3)_2.6H_2O$, (0.14 g) of $Mg(NO_3)_2.6H_2O$, and (0.04 g) of 2,5-dioxido-1,4-benzenedicarboxylate. After a complete dissolution, the mixture was kept for 24 hours at 120 °C. Then, the yellow NiMg-MOF-74 precipitate was collected by centrifugation and washed three times with acetone.

4.3.3 Synthesis of Ni-MOF-74

0.16 g of $Ni(NO_3)_2.6H_2O$ and 0.04 g of H_4dobdc was ultrasonically dissolved in 1mL EtOH, 1mL H_2O, and 15 mL DMF mixed solvent, and kept at 120 °C for 24 hours. The product was collected by centrifugation and washed three times with acetone.

4.3.4 Synthesis of Mg-MOF-74

0.14 g of $Mg(NO_3)_2.6H_2O$ and 0.04 g of H_4dobdc was ultrasonically dissolved in 1mL EtOH, 1mL H_2O, and 15 mL DMF mixed solvent, and kept at 120 °C for 24 hours. The product was collected by centrifugation and washed three times with acetone.

4.3.5 Synthesis of urea@bi-metallic NiMg-MOF-74, urea@Ni-MOF-74, and urea@Mg-MOF-74

The as-prepared MOF products were immersed in acetone for 24 hours for solvent exchange. Then, to evacuate MOF channels from the solvent, 200 mg of each MOF sample was heated at 135 °C for 24 hours in an oven. Subsequently, the activated MOF samples were mixed with 1 g of urea and dissolved in 100 mL Millipore H_2O. The mixture was placed in a 150 mL Teflon-lined autoclave, sealed and kept at 140 °C for 24 hours. The final products were centrifuged and rinsed with Millipore H_2O after cooling down at room temperature.

4.3.6 Synthesis of atomically dispersed Ni-N-C catalysts

To synthesize Ni-N-C catalysts, 200 mg of urea@bi-metallic NiMg-MOF-74 sample was transferred to a ceramic boat and pyrolyzed in a tube furnace for 2 hours under Ar flow using a heating rate of 5 degree/minute at 900 °C and 700 °C to produce Ni-N-C@900 °C and Ni-N-C@700 °C catalysts, respectively. Additionally, 200 mg of urea@Ni-MOF-74 and urea@Mg-MOF-74 were pyrolyzed under the same conditions at 900 °C to produce NiNP-N-C and Ni free-

N-C, respectively. After cooling down at room temperature, the solid products were collected and washed with 1M nitric acid three times to remove any formed MgO or labile Ni-based particles in the final Ni-N-C catalysts. Subsequently, the acid washed Ni-N-C catalysts were rinsed repeatedly with Millipore H_2O until neutralization and kept at 70 °C for 12 hours for drying.

4.3.7 Material Characterization

Various characterization techniques were employed to investigate the morphology and compositions of the newly developed Ni-N-C catalysts. The crystallinity of the synthesized materials was identified by the utilization of powder X-ray diffraction (PXRD) analysis conducted at McMaster Analytical X-Ray Diffraction Facility (MAX) using Cu Kα radiation. The near-surface chemical compositions and coordination environments were investigated by X-ray photoelectron spectroscopy (XPS) measurements performed at Biointerfaces Institute at McMaster University using a PHI Quantera II Scanning XPS Microprobe. High resolution transmission electron microscopy (HRTEM), and high-angle annular dark-field scanning transmission electron microscopy (HAADF-STEM) imaging along with energy dispersive spectroscopy (EDS) mapping were carried out in the Canadian Centre for Electron Microscopy (CCEM) using a FEI Titan operating at 300 keV to investigate the morphology of the different Ni-N-C catalysts.

4.3.8 EXAFS Characterization

X-ray Absorption Spectroscopy (XAS) analysis was performed on the HXMA beamline 061D-1 (energy range 5-30 keV, resolution $1x10^{-4}$ $\Delta E/E$) at the Canadian Light Source. All data were collected in transmission mode using Ionization chambers filled with He gas. The energy of the Ni-K edge (8333 eV) was done using a Si(220) double-crystal Si monochromator, with a Pt-coated water-cooled collimating KB mirror. The Higher harmonics of the beam were removed by

the double crystal monochromator. Demeter software packages were used for data analysis and Extended X-ray Absorption Fine Structure (EXAFS) fitting.1 An amplitude reduction factor of 0.74 was obtained from the first shell fitting of Ni foil. The EXAFS fitting parameters of samples were determined by keeping this amplitude reduction factor fixed. Black and red lines represent the experimental data and simulated EXAFS fit, respectively.

4.3.9 Electrode preparation

10 mg of the black pyrolyzed Ni-N-C catalyst powder were grounded and dispersed in 2 mL of a mixed solvent of (3:1) IPA:H_2O and 120 µL of Nafion solution was added. Afterwards, the as-prepared homogenous ink was drop-casted onto a graphite foil substrate and dried at 70 °C for 2 hours.

4.3.10 Electrochemical Characterization

A previously reported customized electrochemical cell containing two compartments was employed in this research to investigate the electrocatalytic CO_2R performance of the developed Ni-N-C catalysts.[17]The catholyte and anolyte chambers were separated by a Selemion anion exchange membrane (Selemion AMV, AGC Inc.) and 9 mL of 0.1 M $KHCO_3$ was used to fill each chamber. To control the CO_2 gas flow rate, a mass flow control (MKS Instrument) was employed and a flow rate of 20 sccm was fed through the catholyte chamber during the CO_2 electroreduction. An Ag/AgCl reference electrode was connected to the cell (catholyte chamber) by a Luggin capillary, while a Pt foil was employed as the counter electrode. All electrochemical measurements were performed by a Biologic VSP-300 potentiostat, and all applied potentials vs Ag/AgCl were converted to RHE using the following equation: V vs RHE = V measured vs. Ag/AgCl + 0.197 + 0.059*6.8 (pH of electrolyte). The effluent from the catholyte chamber was connected with an on-

line gas chromatography unit (GC, supplier: SRI, model: 8610C in the Multi-Gas configuration #5), to quantify the gas phase products.

4.4 Results & Discussion

The preparation of atomically dispersed Ni-N-C catalysts were carried out using the protocol illustrated in **Figure 4.1**, where the synthesis of bi-metallic MOF-74 was conducted according to previous reports.[59, 64, 65]. During the synthesis of Ni/Mg-MOF-74, a large content of Mg^{2+} was embedded into the structure to assist on the separation of adjacent Ni^{2+} species coordinated with the M-oxo chains. **Figure S1a** reveals the EDS mapping of the pristine bi-metallic Ni/Mg-MOF-74 and shows the elemental distribution of Ni, Mg, N, C in the entire structure. **Figure 4.2** illustrates TEM images at different magnification of the prepared Ni-N-C catalysts using different pyrolysis temperatures, and **Figure S2** shows images of the NiNP-N-C and Ni-free N-C catalyst for comparison. **Figure 4.3a and b** and **Figure S1** provide EDS mapping of the same electrocatalysts. As revealed in **Figure 4.2a-c**, Ni-N-C@900°C catalyst demonstrated a homogenous porous structure with no observations of the formation of metallic Ni nano/microparticles, which could likely be attributed to the successful formation of atomically dispersed Ni-N_x/C sites. At a high pyrolysis temperature, the MOF host molecule is decomposed, and a porous graphitized structure is formed, the graphitized carbon structure is doped with nitrogen species resulting from urea decomposition which likely act as stabilizing sites for the Ni atoms. After pyrolysis, an acid wash strategy assisted in removing any formed MgO or exposed labile Ni-based particles, leaving a structure of atomically dispersed Ni-N_X/C sites, where x could be 1, 2, 3 or 4 as shown in **Figure 4.1**. On the contrary, at a lower pyrolysis temperature (700°C), Ni-N-C@700°C electrocatalyst exhibits a clear formation of metallic Ni particles embedded into the graphitic structure as shown in **Figure 4.2d-f**, emphasizing the impact of the employed

pyrolysis temperature on the obtained morphology of the prepared Ni-N-C catalysts. The formation of Ni-based particle at lower pyrolysis temperature (700°C) indicates that the coalescence of Ni atoms becomes more intense compared to higher pyrolysis temperatures (900°C). Optimizing the ratio of the activated MOF to urea is one of the parameters that could be investigated later in this research to assess the influence of the doped nitrogen concentration on the structure and electrochemical CO_2R performance of the resulted Ni-N-C catalysts. Ni-N-C catalyst prepared by pyrolyzing urea@Ni-MOF-74 (i.e., no Mg^{2+} in the structure) exhibits the formation of a heterogenous structure consisting of a high portion of metallic Ni particles integrated with carbon nanotubes (CNTs) as shown in **Figure S2a-b**, illustrating the role of Mg^{2+} ions on isolating neighboring Ni sites to prevent the formation of Ni nano/microparticles during pyrolysis. As Ni is well-known to catalyze the formation of CNTs,[66-69] the reason CNTs are produced in the NiNP-N-C catalyst and not in the Ni-N-C@900°C and Ni-N-C@700°C catalysts could likely be ascribed to the Ni content inside each catalyst,[66-69]the higher Ni content in NiNP-N-C has likely enhanced the formation of CNTs. Ni-free N-C catalyst images exhibit a porous N-rich graphitic structure as shown in **Figure S1** and Figure **S2c-d. EDS** mapping was carried out to identify the compositional distributions of Ni, N and C within the as-synthesized catalyst structures **(Figure 4.3a-b, and Figure S1)**, whereby a homogeneous dispersion of all three elements was demonstrated in all developed Ni-N-C materials.

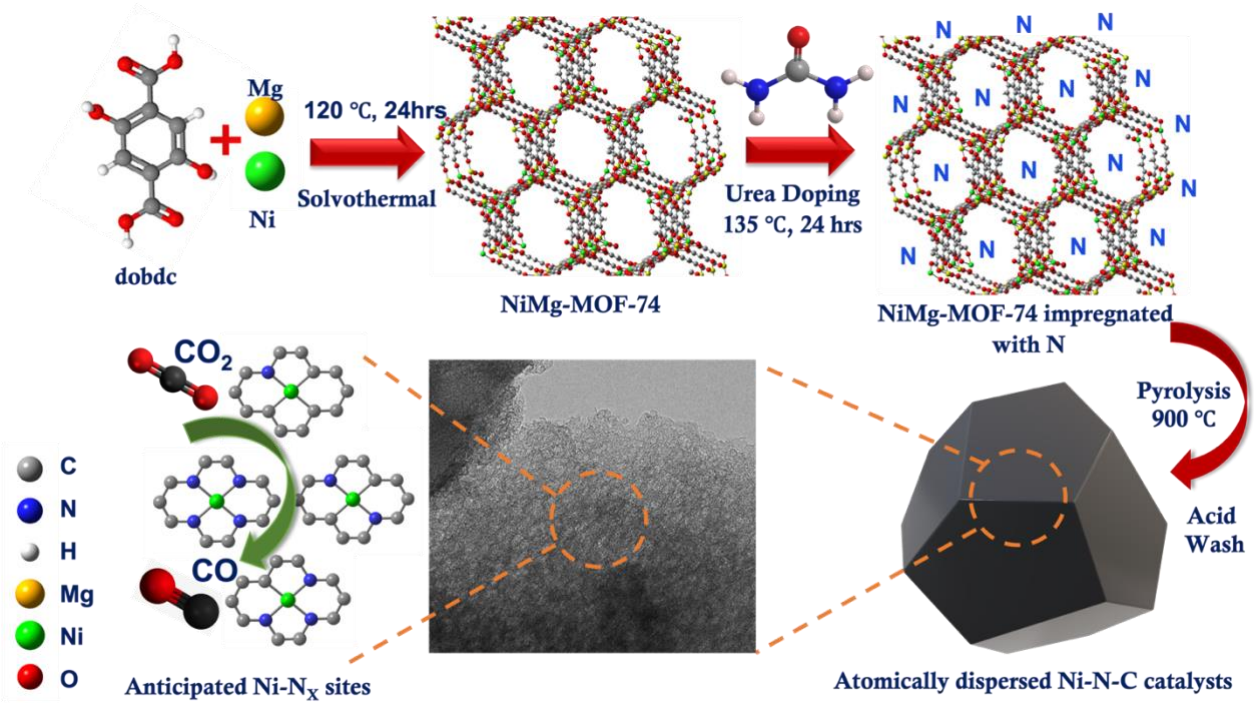

Figure 4-1 Schematic diagram illustrates the formation of the atomically dispersed Ni-N-C catalysts.

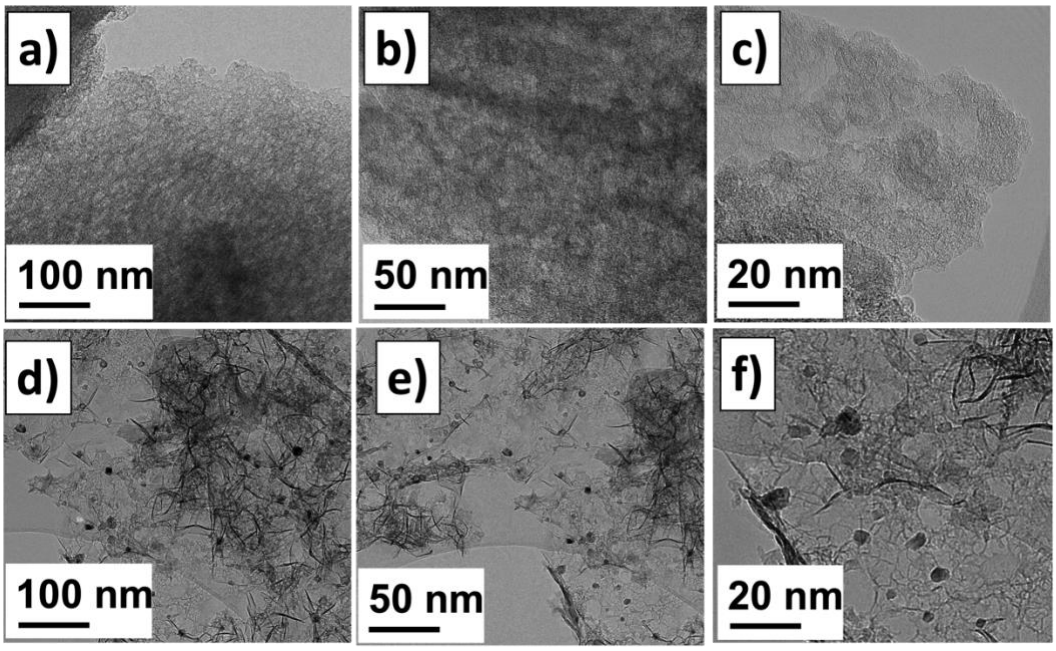

Figure 4-2 TEM images of atomically dispersed Ni-N-C catalysts prepared at different pyrolysis temperatures ; (a-c) Ni-N-C@900°C, and (d-f) Ni-N-C@700°C.

To investigate the crystalline characteristics of all MOF-precursors and Ni-N-C catalysts, PXRD measurements were performed as illustrated in **Figure 4.3c**. The PXRD spectra of the Ni-MOF-74, Mg-MOF-74, and NiMg-MOF-74 precursors exhibited the same spectral patterns that were previously reported for the same MOF structures.[65] No additional peaks were observed after urea impregnation, indicating that NH_4^+ ions were incorporated into the MOF architecture without resulting in any structural modifications. For the developed Ni-N-C catalysts prepared at different pyrolysis temperature and synthetic conditions, Ni-N-C@900°C didn't show any noticeable diffraction peaks, indicating that the Ni species inside the obtained catalyst likely formed atomically dispersed Ni-N_x/C rather than coalescing into crystalline structures that would be observed by PXRD. On the contrary, Ni-N-C@700°C and NiNP-N-C catalysts demonstrated clear crystalline diffraction peaks at 45.1°, 54.6°, and 75.3°, which are assigned to metallic Ni(111), Ni(200), and Ni(220), respectively. These observations obtained from the PXRD spectral patterns are consistent with the TEM imaging and EDS mapping that showed the formation Ni-based particles in both Ni-N-C@700°C and NiNP-N-C. The Ni-free N-C catalyst revealed only a broad diffraction peak in the range of 20-30° assigned to the graphitic (002) plane.

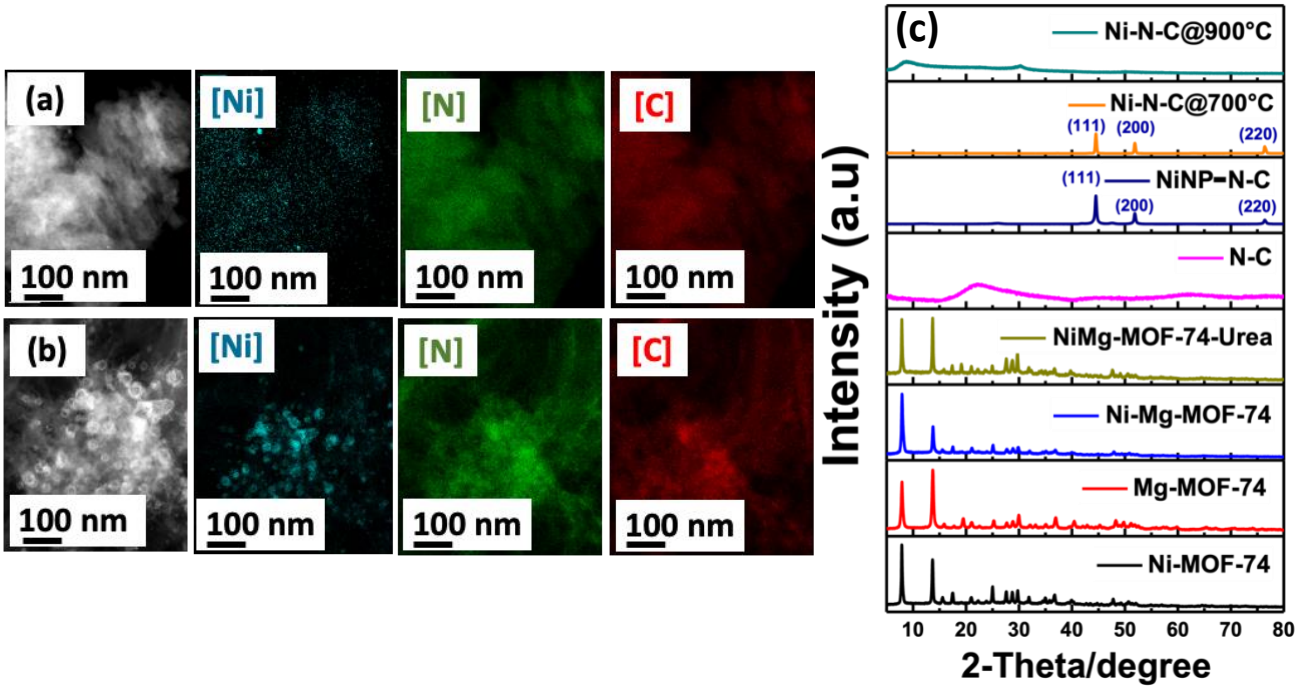

Figure 4-3 EDS mapping of the developed atomically dispersed Ni-N-C catalysts prepared at different pyrolysis temperatures; (a) Ni-N-C@900°C and (b) Ni-N-C@700°C. (c) XRD spectra of all MOF precursors along with the synthesized Ni-N-C catalysts.

X-ray photoelectron spectroscopy (XPS) analysis was carried out on Ni-N-C@900°C as presented in **Figure 4.4**. The near surface composition of the this catalyst was identified to be ca. 87.0 at.% carbon, 4.5 at.% nitrogen, and less than 1.0 at.% Ni **(Figure 4.4a)**. The N 1s spectra **(Figure 4.4b)** illustrates five different peaks including pyrrolic-N at 400.2 eV, pyridinic-N at 398.7 eV, graphitic-N at 401.5 eV, oxidized-N at 403.2 and 407.1 eV, and Ni–N at 399.1 eV.[70, 71] Various studies have investigated the impact of N-configuration on the obtained selectivity and activity of the electroreduction of CO_2, emphasizing that N-coordination has a significant influence on the overall performance of CO_2R.[72, 73] In the present work, it is hard to deconvolute what nitrogen configurations are influencing the activity due to the ambiguity in fitting XPS peaks. Hence, extended X-ray absorption fine structure (EXAFS) analysis were performed of Ni-N-C@700°C

and Ni-N-C@900°C to obtain a better identification of the local coordination environment surrounded the atomically dispersed Ni-N_x/C sites. The C 1s spectra **(Figure 4.4c)** reveals two different peaks at 285.0 eV and 286.2 eV, which correspond to C-C sp^2 and C-N/O respectively. The Ni 2p XPS spectra shown in Figure 4d illustrates a major peak at 855 eV which could be likely attributed to Ni species in a low valent energy level.

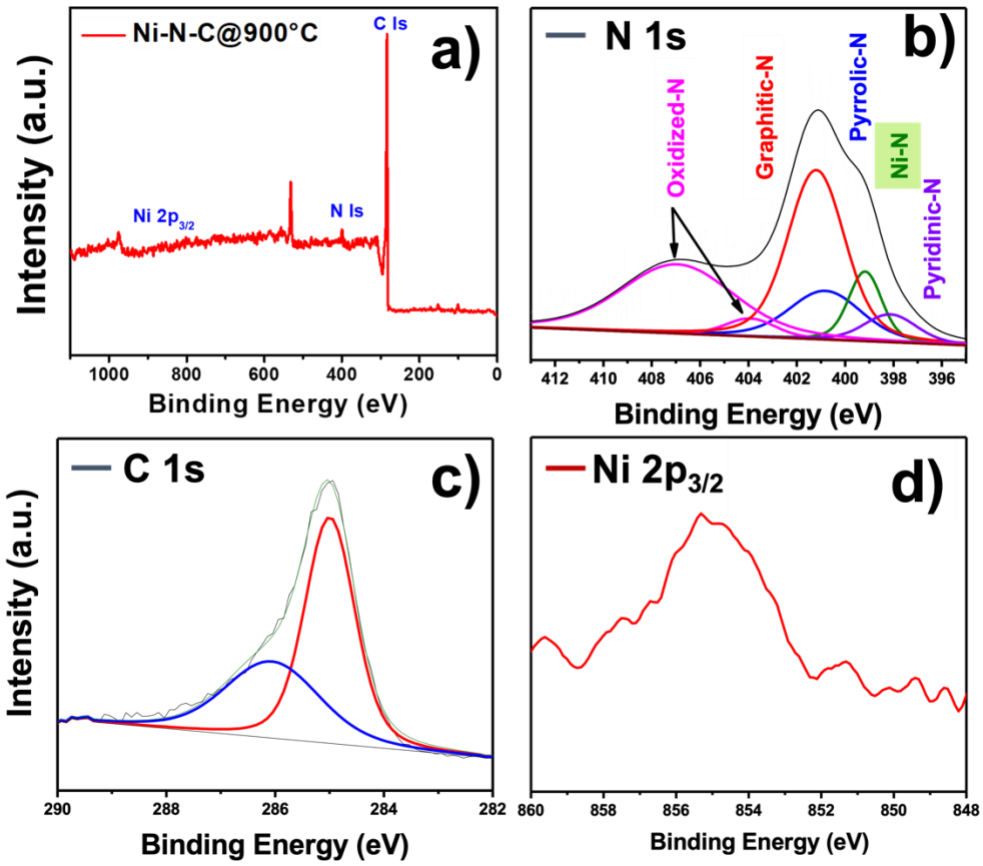

Figure 4-4 XPS spectra of the synthesized Ni-N-C@900°C, (a) Elemental survey, (b) N 1s, (c) C 1s, and (d) Ni 2p3/2 spectra.

To explore the Ni coordination environment, the catalysts pyrolyzed at two different temperatures (Ni-N-C@700ºC and Ni-N-C@900ºC) were investigated by X-ray absorption

spectroscopy. For reference, the spectra of standard materials- Ni foil, NiO, and Ni-TPP were also collected. EXAFS oscillation in k-space and R-space spectra for Ni catalysts and the reference samples are shown in **Figure 4.5**. The EXAFS oscillation of Ni-N-C@700 ºC is almost close to the Ni reference, which suggests a large population of Ni nanoparticles exists in the catalyst. Since the EXAFS spectra of Ni-N-C@700 ºC were nearly the same as that of metallic Ni, the Ni-Ni scattering path was used to fit the data. The peak at 2.490(4)Å is due to the scattering of the first shell of metallic Ni atoms.[73] **Figures 4.5a and b** show both k-space and R-space EXAFS spectra at the Ni K edge of the samples and obtained fitting parameters are presented in **Table 4.1**. The estimated coordination number (CN) 11.7(8) of Ni-Ni suggests the formation of Ni nanoparticles. **Figures 4.5c and d** illustrate no significant Ni-N contribution at 1.88 Å, demonstrating Ni-N environments are minority species in Ni-N-C 700ºC sample. The EXAFS of Ni-N-C@900 ºC shows the first shell peak at 1.83(2) Å which almost matches the Ni-N bonding location in Ni-TPP.[72] In addition, another peak at 2.478(9)Å indicates the presence of Ni–Ni bonding from smaller Ni clusters, which is consistent with HRTEM and STEM observations **(Figure 4.2 and 4.3)**. Since the sample has two prominent peaks, a combination of Ni-N and Ni-Ni fcc models was adopted to fit the data **(Figures 4.5e and f)** resulting in a coordination number of 3.1(9) and 7.5(4) respectively. A combination of EXAFS and STEM-HAADF studies supports the existence of atomically dispersed Ni atoms in the Ni-N-C@900ºC catalyst. Also, inductively coupled plasma (ICP) has been performed on the Ni-N-C@900°C to identify the Ni concentration of this catalyst, the obtained results reveal a Ni concentration of 0.5 at.%.

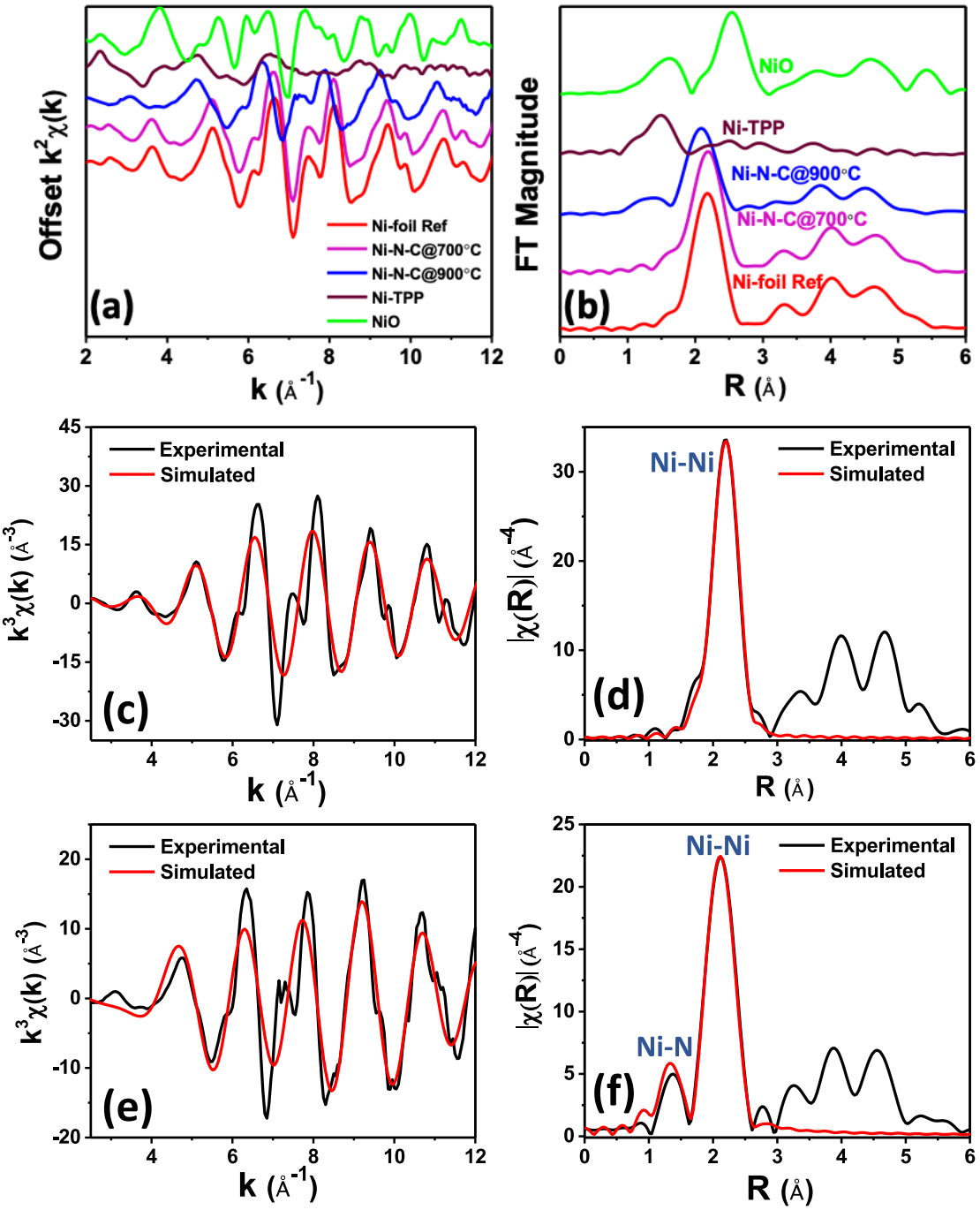
Offset k²χ(k)
k (Å⁻¹)
(a)
Ni-foil Ref
Ni-N-C@700°C
Ni-N-C@900°C
Ni-TPP
NiO
FT Magnitude
R (Å)
(b)
NiO
Ni-TPP
Ni-N-C@900°C
Ni-N-C@700°C
Ni-foil Ref
k³χ(k) (Å⁻³)
Experimental
Simulated
(c)
|χ(R)| (Å⁻⁴)
Ni-Ni
(d)
(e)
Ni-N
(f)

Figure 4-5 a) k space and b) R space (phase shift not corrected) EXAFS spectra at the Ni K edge of the catalysts of NiN-C@700 ºC, Ni-N-C@900 ºC and references, EXAFS data in k space (k3-weighted) and R space c) and d) Ni-N-C@700ºC e) and f) Ni-N-C@900 ºC.

Table 4.1 EXAFS fitting results of catalysts of NiN-C@700 ºC, Ni-N-C@900 ºC.

Catalysts	Type	CN	R/Å	σ^2 /Å^2	E_o Shift (eV)	R factor
Ni-N-C@700ºC	Ni-Ni	11.7(8)	2.490(4)	0.006(1)	7.0(7)	0.4%
Ni-N-C@900ºC	Ni-N	3.1(9)	1.83(2)	0.003(2)	-8.9(7)	0.9%
	Ni-Ni	7.5(4)	2.478(9)	0.005(1)	-8.9(7)	

The electrochemical CO_2R behavior of the developed atomically dispersed Ni-N-C catalysts prepared at different pyrolysis temperatures and conditions was investigated at different applied potentials in 0.1M $KHCO_3$ saturated with CO_2. Generally, CO_2R measurements revealed that the selectivity of the Ni-N-C electrocatalysts is towards producing CO and H_2. A potential window range of -0.68 V vs RHE to -1.1 V vs RHE was employed as the most proper potential range for the prepared catalysts. The Faradaic efficiencies of all synthesized Ni-N-C catalysts towards CO are illustrated in **Figure 4.6a**. Ni-N-C@900°C demonstrated an excellent selectivity towards CO production at -0.76 V vs RHE and a current density of -4.2 mA/cm^2, while Ni-N-C@700°C revealed a relatively lower CO FE (62%) at the same applied potential. We postulate that the higher selectivity of CO in Ni-N-C@900°C could be attributed to the successful formation of atomically dispersed Ni-N_x/C sites. In contrast, as indicated by TEM imaging and EDS mapping, Ni-N-C@700°C exhibits the formation of metallic Ni-based particles along with atomically dispersed Ni-N_x/C sites **(Figure 4.2d-f and Figure 4.3b)**. These Ni nano/microparticles have likely switched the selectivity towards the competing hydrogen evolution reaction which

consequently reduces the selectivity towards CO production. The NiNP-N-C catalyst showed a maximum FE of only 35% for CO production at -0.85 V vs RHE, whereby we postulate that this significant decrease in CO selectivity is likely ascribed to the formation of mainly metallic Ni-based particles **(Figure S2a-b and Figure S1b)** which are known to favor HER rather than CO_2R.[14] The Ni-free N-C catalyst shows the predominant production of H_2 with less than 10% CO FE at all applied potentials, emphasizing the crucial role of Ni-based species in catalyzing the CO_2R reaction. At more negative applied potentials, the selectivity towards CO steadily decreases **(Figure 4.6a)** while H_2 selectivity increases **(Figure 4.6b)**. These trends are in agreement with a previously reported study indicated that the selectivity of CO for Ni-N-C catalysts showed a maximum at ca. -0.7 V vs RHE,[74] emphasizing that this difference in selectivity is likely resulted from shifting reaction energetics between the CO_2R and HER. All electrochemical measurements have been repeated for all samples and demonstrated the same performance. Liquid product analysis was not performed as the Faradaic efficiencies of the formed gas-phase products were close to 100% at all applied potentials, indicating that the developed atomically dispersed Ni-N-C catalysts are very selective towards the formation of gaseous products. Density functional theory (DFT) measurements will be performed in the next stage of this research to identify the key intermediates and predict the Gibbs free energy changes during the CO_2R. In addition to their metal abundance, the produced atomically dispersed Ni-N-C catalysts, particularly Ni-N-C@900°C, demonstrates higher selectivity and activity towards CO compared to state-of-the-art. For instance, Toru Hatsukade[75], have investigated the activity and selectivity of the metallic silver in CO_2R, their finding shows lower activity of (-1.9 mA/cm^2) at -0.98 V vs RHE compared to the developed Ni-N-C@900°C which exhibits -4.2 mA/cm^2 at -0.76 V vs RHE. With the excellent CO_2R selectivity revealed in this work for the atomically dispersed Ni-N-C catalysts, the

employment of these efficient electrocatalysts into high current density electrochemical devices such as membrane electrode assembly (MEA) will be conducted in the next stages of this work for developing competitive electrochemical CO_2R configurations.

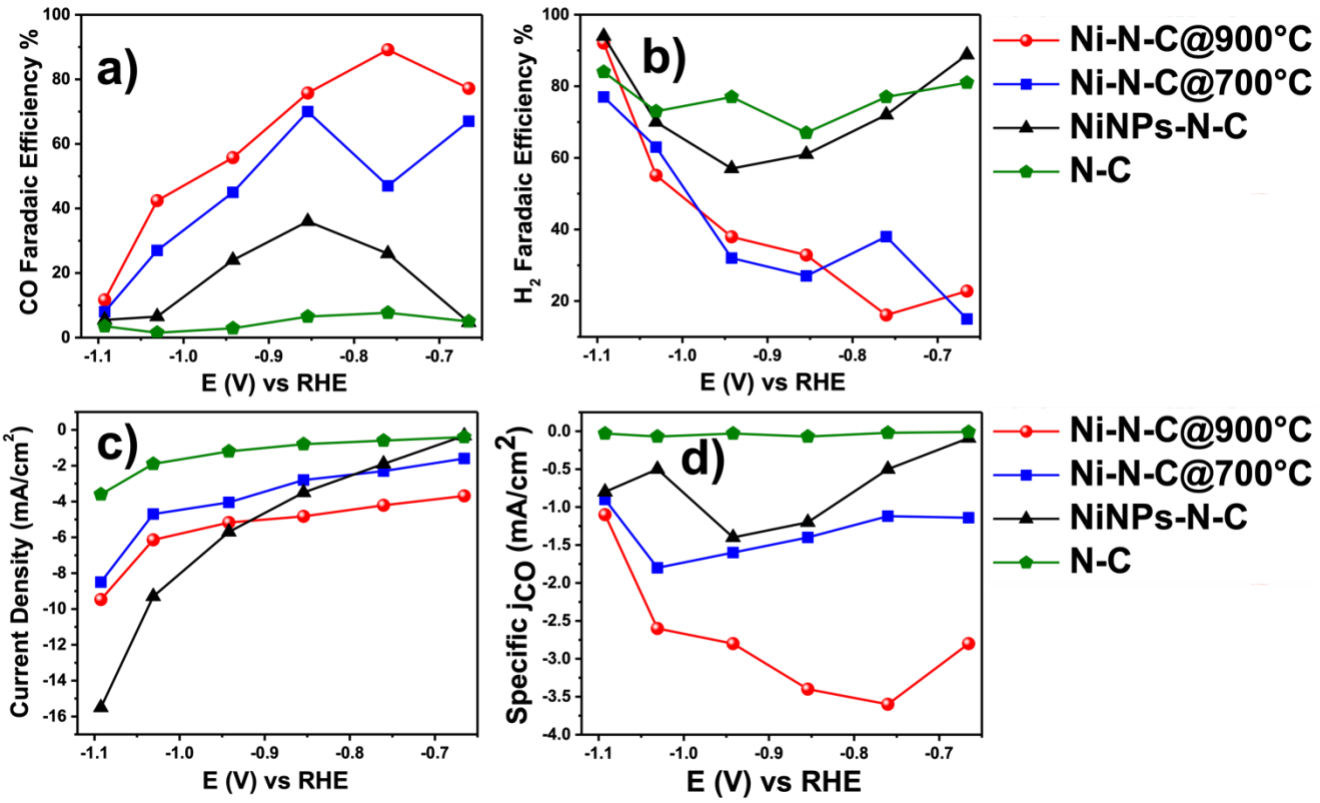

Figure 4-6 The electrochemical behavior of the developed Ni-N-C catalysts, a) the obtained CO FE %, b) the obtained H_2 FE %, c) current density (mA/cm^2), d) partial current density towards the CO production (mA/cm^2) at different potentials.

4.5 Conclusion

In summary, a host-guest synthetic approach has been followed to generate atomically dispersed Ni-N-C catalysts. This strategy has been conducted by urea impregnation into a bi-metallic NiMg-MOF-74 structure where Mg^{2+} ions were utilized as spacer to increase the distance between Ni atoms in the MOF precursor structure with the goal of preventing agglomeration of

the Ni atoms during pyrolysis to preferentially form atomically dispersed Ni-N_x/C sites. Our findings demonstrated that using a pyrolysis temperature 900°C resulted in the formation of atomically dispersed Ni-Nx/C sites, while a pyrolysis temperature of 700°C resulted in the formation of a significant portion of metallic Ni particles. This difference in the obtained morphology impacted the CO_2 electroreduction performance of both catalysts, where Ni-N-C@900°C catalyst exhibited high CO selectivity with a Faradaic efficiency of 90% at -0.76 V vs RHE and a current density of -4.2 mA/cm^2. On the contrary, Ni-N-C@700°C showed 62% CO selectivity at the same applied potential, indicating the crucial role of the employed pyrolysis temperature during the synthesis. In addition, to investigate the beneficial role of Mg^{2+} ions, urea@Ni-MOF-74 prepared in the absence of Mg^{2+} was pyrolyzed at 900°C. The obtained catalyst demonstrated a heterogenous structure consisting of predominantly metallic Ni particles along with CNTs and exhibited a Faradaic efficiency towards CO of only 35% at -0.85 V vs RHE at a current density of -3.5 mA/cm^2. These findings show Mg^{2+} ions in the MOF-74 precursor structure were beneficial in avoiding Ni atom coalescence, and instead preferentially form atomically dispersed Ni-N_X sites. Ni free N-C catalyst were also prepared and found to provide negligible selectivity towards CO, emphasizing that Ni sites are essential for driving the CO_2 electroreduction reaction.

Supporting Information

TEM images and EDS mapping are included in the supporting information file.

Acknowledgments

This work was supported by the Department of Chemical Engineering at McMaster University and the National Research Council of Canada (NRC) Materials for Clean Fuels Challenge Program. Electron microscopy measurements were carried out at the Canadian Centre for Electron

Microscopy (CCEM). X-ray photoelectron spectroscopy analysis was performed at the Biointerfaces Institute (BI), while X-ray diffraction measurements were conducted at McMaster Analytical X-ray Diffraction Facility (MAX). X-ray absorption spectroscopy (XAS) analysis has been carried out at HXMA beamtime at the Canadian Light Source (CLS).

4.6 References

Atomically Isolated Nickel-Nitrogen-Carbon Electrocatalysts Derived by the Utilization of Mg^{2+} ions as Spacers in Bimetallic Ni/Mg-Metal Organic Framework Precursors for Boosting the Electroreduction of CO_2

Fatma Ismail[a], Ahmed Abdellah[b], Veeranmaril Sudheeshkumar[c] Amirhossein Rakhsha[d,] Weifang Chen[e], Ning Chen[f], Drew C. Higgins[g*]

Department of Chemical Engineering, McMaster University, Hamilton, Ontario L8S 4L7, Canada

[a]ismaif1@mcmaster.ca, [b]abdellaa@mcmaster.ca, [c]sudheeshkumar.v@gmail.com, [d]a.h.rakhsha@gmail.com, [e]weifeng.chen@lightsource.ca, [f]ning.chen@lightsource.ca [g]higgid2@mcmaster.ca

4.7 Supporting Information

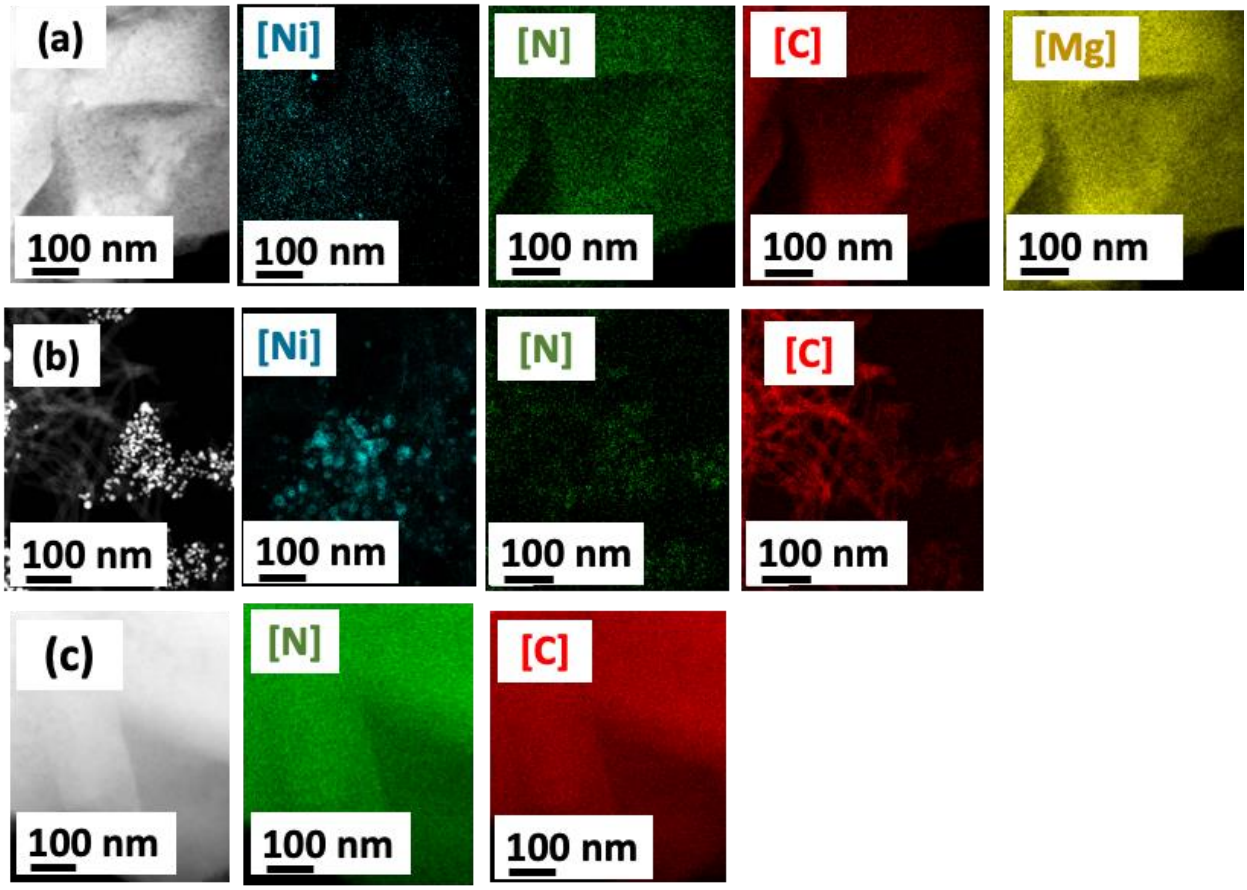

Figure S1. EDS mapping of a) pristine NiMg-MOF-74 b) NiNP-N-C, and c) Ni-free N-C catalysts

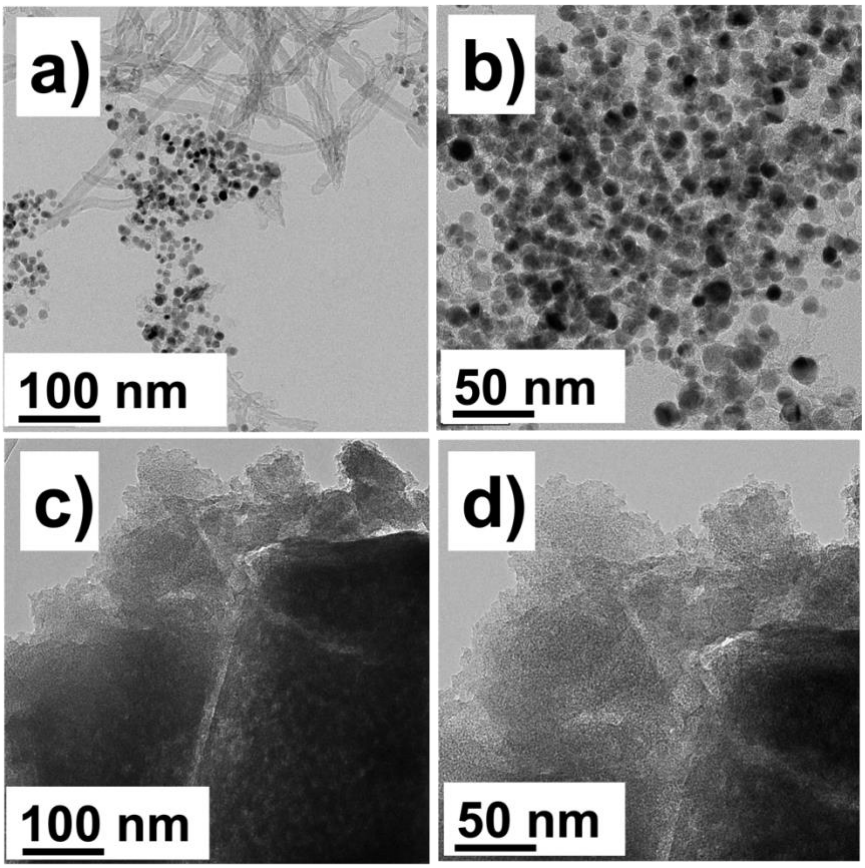

Figure S2. TEM images of (a and b) NiNPs-N-C, (c and d) Ni-free-N-C catalysts

Intrinsic Electrochemical Surface Area (ECSA):

Electrochemical Surface Area (ECSA) measurements have been conducted to investigate the intrinsic activity of the synthesized Ni-N-C@900°C and Ni-N-C@700°C materials. Using different scan rates from 50 to 130 mV/s, double-layer capacitance (C_{dl}) was calculated from the slope of the of the current (the difference between anodic and cathodic currents for each cycle) versus the scan rate. By dividing (C_{dl}) over the specific capacitance (C_s) of Ni (40µF/cm^2)[76], ECSA were calculated for both samples using the following formula:

$$\mathbf{A_{ECSA}} = \frac{\mathbf{C_{dl}\ of\ the\ catalyst}\ \left(\frac{\mathbf{mF}}{\mathbf{cm^2}}\right)}{\mathbf{C_s\ (Specific\ Capacitance\ of\ NF)}\ \mathbf{0.04}\ \left(\frac{\mathbf{mF}}{\mathbf{cm^2}}\right)\mathbf{/\ ECSA\ cm^2}}$$

A_{ECSA} of Ni-N-C@900°C was calculated accordingly:

$$\mathbf{A_{ECSA}} = \frac{\mathbf{23.4}\ \left(\frac{\mathbf{mF}}{\mathbf{cm^2}}\right)}{\mathbf{0.04}\ \left(\frac{\mathbf{mF}}{\mathbf{cm^2}}\right)\mathbf{/\ ECSA\ cm^2}} = \mathbf{585\ cm^2}$$

A_{ECSA} of Ni-N-C@700°C was calculated as the following:

$$\mathbf{A_{ECSA}} = \frac{\mathbf{19.1}\ \left(\frac{\mathbf{mF}}{\mathbf{cm^2}}\right)}{\mathbf{0.04}\ \left(\frac{\mathbf{mF}}{\mathbf{cm^2}}\right)\mathbf{/\ ECSA\ cm^2}} = \mathbf{477.5\ cm^2}$$

The difference in the activity and selectivity between Ni-N-C@900°C and Ni-N-C@700°C under CO_2R conditions could be likely attributed to the higher ECSA value of Ni-N-C@900°C (585 cm^2) compared to Ni-N-C@700°C (477.5 cm^2).

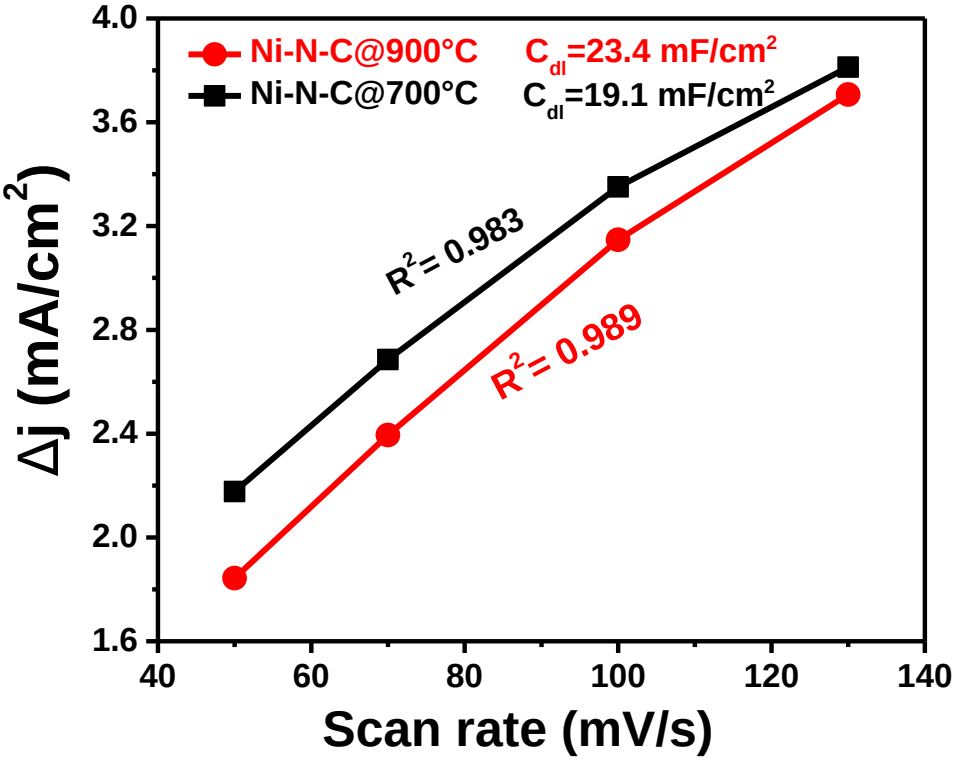

Figure S3. Current density difference vs. scan rate for calculating the double layer capacitance (c_{dl}) layer to determine ECSA for Ni-N-C@900°C and Ni-N-C@700°C

Calculating Faradaic Efficiencies:

$$\boldsymbol{Faradaic\ Efficiency}\ \% = \frac{\boldsymbol{Moles\ of\ the\ product} * \boldsymbol{e-per\ mole} * \boldsymbol{F\ constant}}{\boldsymbol{Average\ I} * \frac{\boldsymbol{60}}{\boldsymbol{Flow\ rate}}}$$

Where:

F: Faraday's constant of 96485 C mol^{-1}.

I: Average current.

e^-: Number of electrons transferred per mole, which is 2 in the case of CO.

References

1. Seh, Z. W.; Kibsgaard, J.; Dickens, C. F.; Chorkendorff, I.; Nørskov, J. K.; Jaramillo, T. F., Combining theory and experiment in electrocatalysis: Insights into materials design. Science 2017, 355 (6321).

2. Zhang, H.; Xu, H.; Li, Y.; Su, Y., Octahedral core–shell bimetallic catalysts M@ UIO-67 (M= Pt–Pd nanoparticles, Pt–Pd nanocages): metallic nanocages that enhanced CO_2 conversion. Applied Materials Today 2020, 19, 100609.

3. Cárdenas-Arenas, A.; Quindimil, A.; Davó-Quiñonero, A.; Bailón-García, E.; Lozano-Castello, D.; De-La-Torre, U.; Pereda-Ayo, B.; González-Marcos, J. A.; González-Velasco, J. R.; Bueno-López, A., Design of active sites in Ni/CeO_2 catalysts for the methanation of CO_2: tailoring the Ni-CeO2 contact. Applied Materials Today 2020, 19, 100591.

4. Chen, Z.; Jaramillo, T. F.; Deutsch, T. G.; Kleiman-Shwarsctein, A.; Forman, A. J.; Gaillard, N.; Garland, R.; Takanabe, K.; Heske, C.; Sunkara, M., Accelerating materials development for photoelectrochemical hydrogen production: Standards for methods, definitions, and reporting protocols. Journal of Materials Research 2010, 25 (1), 3-16.

5. De Klerk, A., Fischer–Tropsch facilities at a glance. Fischer–Tropsch Refining 2011, 1-20.

6. De Luna, P.; Hahn, C.; Higgins, D.; Jaffer, S. A.; Jaramillo, T. F.; Sargent, E. H., What would it take for renewably powered electrosynthesis to displace petrochemical processes? Science 2019, 364 (6438).

7. Back, S.; Kim, J.-H.; Kim, Y.-T.; Jung, Y., Bifunctional interface of Au and Cu for improved CO_2 electroreduction. ACS applied materials & interfaces 2016, 8 (35), 23022-23027.

8. Zhao, K.; Liu, Y.; Quan, X.; Chen, S.; Yu, H., CO_2 electroreduction at low overpotential on oxide-derived Cu/carbons fabricated from metal organic framework. ACS applied materials & interfaces 2017, 9 (6), 5302-5311.

9. Chen, H.; Handoko, A. D.; Xiao, J.; Feng, X.; Fan, Y.; Wang, T.; Legut, D.; Seh, Z. W.; Zhang, Q., Catalytic effect on CO_2 electroreduction by hydroxyl-terminated two-dimensional MXenes. ACS applied materials & interfaces 2019, 11 (40), 36571-36579.

10. Daiyan, R.; Chen, R.; Kumar, P.; Bedford, N. M.; Qu, J.; Cairney, J. M.; Lu, X.; Amal, R., Tunable syngas production through CO_2 electroreduction on cobalt–carbon composite electrocatalyst. ACS applied materials & interfaces 2020, 12 (8), 9307-9315.

11. Mascaretti, L.; Niorettini, A.; Bricchi, B. R.; Ghidelli, M.; Naldoni, A.; Caramori, S.; Li Bassi, A.; Berardi, S., Syngas evolution from CO_2 electroreduction by porous au nanostructures. ACS applied energy materials 2020, 3 (5), 4658-4668.

12. He, B.; Jia, L.; Cui, Y.; Zhou, W.; Sun, J.; Xu, J.; Wang, Q.; Zhao, L., $SnSe_2$ nanorods on carbon cloth as a highly selective, active, and flexible electrocatalyst for electrochemical reduction of CO_2 into formate. ACS Applied Energy Materials 2019, 2 (10), 7655-7662.

13. Gattrell, M.; Gupta, N.; Co, A., Electrochemical reduction of CO_2 to hydrocarbons to store renewable electrical energy and upgrade biogas. Energy conversion and Management 2007, 48 (4), 1255-1265.

14. Kuhl, K. P.; Hatsukade, T.; Cave, E. R.; Abram, D. N.; Kibsgaard, J.; Jaramillo, T. F., Electrocatalytic conversion of carbon dioxide to methane and methanol on transition metal surfaces. Journal of the American Chemical Society 2014, 136 (40), 14107-14113.

15. Kou, Z.; Li, X.; Wang, T.; Ma, Y.; Zang, W.; Nie, G.; Wang, J., Fundamentals, On-Going Advances and Challenges of Electrochemical Carbon Dioxide Reduction. Electrochemical Energy Reviews 2021, 1-30.

16. Hori, Y. i., Electrochemical CO_2 reduction on metal electrodes. In Modern aspects of electrochemistry, Springer: 2008; pp 89-189.

17. Kuhl, K. P.; Cave, E. R.; Abram, D. N.; Jaramillo, T. F., New insights into the electrochemical reduction of carbon dioxide on metallic copper surfaces. Energy & Environmental Science 2012, 5 (5), 7050-7059.

18. Higgins, D.; Landers, A. T.; Ji, Y.; Nitopi, S.; Morales-Guio, C. G.; Wang, L.; Chan, K.; Hahn, C.; Jaramillo, T. F., Guiding electrochemical carbon dioxide reduction toward carbonyls using copper silver thin films with interphase miscibility. ACS Energy Letters 2018, 3 (12), 2947-2955.

19. Higgins, D.; Hahn, C.; Xiang, C.; Jaramillo, T. F.; Weber, A. Z., Gas-diffusion electrodes for carbon dioxide reduction: A new paradigm. ACS Energy Letters 2018, 4 (1), 317-324.

20. Shi, Q.; Hwang, S.; Yang, H.; Ismail, F.; Su, D.; Higgins, D.; Wu, G., Supported and coordinated single metal site electrocatalysts. Materials Today 2020.

21. Su, X.; Yang, X.-F.; Huang, Y.; Liu, B.; Zhang, T., Single-atom catalysis toward efficient CO_2 conversion to CO and formate products. Accounts of chemical research 2018, 52 (3), 656-664.

22. Liu, P.; Zhao, Y.; Qin, R.; Mo, S.; Chen, G.; Gu, L.; Chevrier, D. M.; Zhang, P.; Guo, Q.; Zang, D., Photochemical route for synthesizing atomically dispersed palladium catalysts. Science 2016, 352 (6287), 797-800.

23. Fei, H.; Dong, J.; Feng, Y.; Allen, C. S.; Wan, C.; Volosskiy, B.; Li, M.; Zhao, Z.; Wang, Y.; Sun, H., General synthesis and definitive structural identification of MN 4 C 4 single-atom catalysts with tunable electrocatalytic activities. Nature Catalysis 2018, 1 (1), 63-72.

24. Han, Y.; Wang, Z.; Xu, R.; Zhang, W.; Chen, W.; Zheng, L.; Zhang, J.; Luo, J.; Wu, K.; Zhu, Y., Ordered Porous Nitrogen-Doped Carbon Matrix with Atomically Dispersed Cobalt Sites as an Efficient Catalyst for Dehydrogenation and Transfer Hydrogenation of N-Heterocycles. Angewandte Chemie International Edition 2018, 57 (35), 11262-11266.

25. Shahcheraghi, L.; Zhang, C.; Lee, H.-J.; Cusack-Striepe, M.; Ismail, F.; Abdellah, A.; Higgins, D. C., Identifying Activity and Selectivity Trends for the Electrosynthesis of Hydrogen Peroxide via Oxygen Reduction on Nickel–Nitrogen–Carbon Catalysts. The Journal of Physical Chemistry C 2021, 125 (29), 15830-15840.

26. Koshy, D. M.; Chen, S.; Lee, D. U.; Stevens, M. B.; Abdellah, A. M.; Dull, S. M.; Chen, G.; Nordlund, D.; Gallo, A.; Hahn, C., Understanding the origin of highly selective CO_2 electroreduction to CO on Ni, N-doped carbon catalysts. Angewandte Chemie 2020, 132 (10), 4072-4079.

27. Koshy, D.; Nathan, S.; Asundi, A.; Abdellah, A.; Dull, S.; Cullen, D.; Higgins, D.; Bao, Z.; Bent, S.; Jaramillo, T., Bridging thermal catalysis and electrocatalysis: Catalyzing CO_2 conversion with carbon-based materials. Angewandte Chemie International Edition 2021.

28. Chen, Z.; Higgins, D.; Yu, A.; Zhang, L.; Zhang, J., A review on non-precious metal electrocatalysts for PEM fuel cells. Energy & Environmental Science 2011, 4 (9), 3167-3192.

29. Koshy, D. M.; Landers, A. T.; Cullen, D. A.; Ievlev, A. V.; Meyer III, H. M.; Hahn, C.; Bao, Z.; Jaramillo, T. F., Direct Characterization of Atomically Dispersed Catalysts: Nitrogen-Coordinated Ni Sites in Carbon-Based Materials for CO_2 Electroreduction. Advanced Energy Materials 2020, 10 (39), 2001836.

30. Fan, L.; Liu, P. F.; Yan, X.; Gu, L.; Yang, Z. Z.; Yang, H. G.; Qiu, S.; Yao, X., Atomically isolated nickel species anchored on graphitized carbon for efficient hydrogen evolution electrocatalysis. Nature communications 2016, 7 (1), 1-7.

31. Gu, J.; Hsu, C.-S.; Bai, L.; Chen, H. M.; Hu, X., Atomically dispersed Fe3+ sites catalyze efficient CO2 electroreduction to CO. Science 2019, 364 (6445), 1091-1094.

32. Möller, T.; Ju, W.; Bagger, A.; Wang, X.; Luo, F.; Thanh, T. N.; Varela, A. S.; Rossmeisl, J.; Strasser, P., Efficient CO_2 to CO electrolysis on solid Ni–N–C catalysts at industrial current densities. Energy & Environmental Science 2019, 12 (2), 640-647.

33. Wang, X.; Chen, Z.; Zhao, X.; Yao, T.; Chen, W.; You, R.; Zhao, C.; Wu, G.; Wang, J.; Huang, W., Regulation of coordination number over single Co sites: triggering the efficient electroreduction of CO_2. Angewandte Chemie 2018, 130 (7), 1962-1966.

34. Liu, W.; Zhang, L.; Liu, X.; Liu, X.; Yang, X.; Miao, S.; Wang, W.; Wang, A.; Zhang, T., Discriminating catalytically active FeN x species of atomically dispersed Fe–N–C catalyst for selective oxidation of the C–H bond. Journal of the American Chemical Society 2017, 139 (31), 10790-10798.

35. Yan, C.; Li, H.; Ye, Y.; Wu, H.; Cai, F.; Si, R.; Xiao, J.; Miao, S.; Xie, S.; Yang, F., Coordinatively unsaturated nickel–nitrogen sites towards selective and high-rate CO_2 electroreduction. Energy & Environmental Science 2018, 11 (5), 1204-1210.

36. Pan, Y.; Chen, Y.; Wu, K.; Chen, Z.; Liu, S.; Cao, X.; Cheong, W.-C.; Meng, T.; Luo, J.; Zheng, L., Regulating the coordination structure of single-atom Fe-N x C y catalytic sites for benzene oxidation. Nature communications 2019, 10 (1), 1-11.

37. Mukhopadhyay, S.; Das, A.; Jana, T.; Das, S. K., Fabricating a MOF material with polybenzimidazole into an efficient proton exchange membrane. ACS Applied Energy Materials 2020, 3 (8), 7964-7977.

38. Ferhi, N.; Desalegn Assresahegn, B.; Ardila-Suarez, C.; Dissem, N.; Guay, D.; Duong, A., Defective Metal–Organic Framework-808@ Polyaniline Composite Materials for High Capacitance Retention Supercapacitor Electrodes. ACS Applied Energy Materials 2022.

39. Abdelkader-Fernandez, V. K.; Fernandes, D. M.; Balula, S. S.; Cunha-Silva, L.; Pérez-Mendoza, M. J.; Lopez-Garzon, F. J.; Pereira, M. F.; Freire, C., Noble-metal-free MOF-74-derived nanocarbons: insights on metal composition and doping effects on the electrocatalytic activity toward oxygen reactions. ACS Applied Energy Materials 2019, 2 (3), 1854-1867.

40. Kitagawa, S., Metal–organic frameworks (MOFs). Chemical Society Reviews 2014, 43 (16), 5415-5418.

41. Canivet, J.; Fateeva, A.; Guo, Y.; Coasne, B.; Farrusseng, D., Water adsorption in MOFs: fundamentals and applications. Chemical Society Reviews 2014, 43 (16), 5594-5617.

42. Zhao, M.; Yuan, K.; Wang, Y.; Li, G.; Guo, J.; Gu, L.; Hu, W.; Zhao, H.; Tang, Z., Metal–organic frameworks as selectivity regulators for hydrogenation reactions. Nature 2016, 539 (7627), 76-80.

43. Islamoglu, T.; Goswami, S.; Li, Z.; Howarth, A. J.; Farha, O. K.; Hupp, J. T., Postsynthetic tuning of metal–organic frameworks for targeted applications. Accounts of chemical research 2017, 50 (4), 805-813.

44. Huang, Y.-B.; Liang, J.; Wang, X.-S.; Cao, R., Multifunctional metal–organic framework catalysts: synergistic catalysis and tandem reactions. Chemical Society Reviews 2017, 46 (1), 126-157.

45. Luo, Y.-H.; Dong, L.-Z.; Liu, J.; Li, S.-L.; Lan, Y.-Q., From molecular metal complex to metal-organic framework: The CO2 reduction photocatalysts with clear and tunable structure. Coordination Chemistry Reviews 2019, 390, 86-126.

46. Zhao, C.; Dai, X.; Yao, T.; Chen, W.; Wang, X.; Wang, J.; Yang, J.; Wei, S.; Wu, Y.; Li, Y., Ionic exchange of metal–organic frameworks to access single nickel sites for efficient electroreduction of CO_2. Journal of the American Chemical Society 2017, 139 (24), 8078-8081.

47. Ma, Z.; Wu, D.; Han, X.; Wang, H.; Zhang, L.; Gao, Z.; Xu, F.; Jiang, K., Ultrasonic assisted synthesis of Zn-Ni bi-metal MOFs for interconnected Ni-NC materials with enhanced electrochemical reduction of CO_2. Journal of CO_2 Utilization 2019, 32, 251-258.

48. Zheng, Y.; Qiao, S.-Z., Metal-organic framework assisted synthesis of single-atom catalysts for energy applications. National Science Review 2018, 5 (5), 626-627.

49. Jiao, L.; Jiang, H.-L., Metal-organic-framework-based single-atom catalysts for energy applications. Chem 2019, 5 (4), 786-804.

50. Han, X.; Ling, X.; Wang, Y.; Ma, T.; Zhong, C.; Hu, W.; Deng, Y., Spatial isolation of zeolitic imidazole frameworks-derived cobalt catalysts: from nanoparticle, atomic cluster to single atom. Angew. Chem. Int. Ed 2019, 58, 5359-5364.

51. Zhang, H.; Hwang, S.; Wang, M.; Feng, Z.; Karakalos, S.; Luo, L.; Qiao, Z.; Xie, X.; Wang, C.; Su, D., Single atomic iron catalysts for oxygen reduction in acidic media: particle size control and thermal activation. Journal of the American Chemical Society 2017, 139 (40), 14143-14149.

52. Zhang, M.; Dai, Q.; Zheng, H.; Chen, M.; Dai, L., Novel MOF-derived Co@ N-C bifunctional catalysts for highly efficient Zn–air batteries and water splitting. Advanced Materials 2018, 30 (10), 1705431.

53. Lu, P.; Yang, Y.; Yao, J.; Wang, M.; Dipazir, S.; Yuan, M.; Zhang, J.; Wang, X.; Xie, Z.; Zhang, G., Facile synthesis of single-nickel-atomic dispersed N-doped carbon framework for efficient electrochemical CO2 reduction. Applied Catalysis B: Environmental 2019, 241, 113-119.

54. Chen, X.; Xiao, S.; Wang, H.; Wang, W.; Cai, Y.; Li, G.; Qiao, M.; Zhu, J.; Li, H.; Zhang, D., MOFs Conferred with Transient Metal Centers for Enhanced Photocatalytic Activity. Angewandte Chemie International Edition 2020, 59 (39), 17182-17186.

55. Jiao, L.; Yang, W.; Wan, G.; Zhang, R.; Zheng, X.; Zhou, H.; Yu, S. H.; Jiang, H. L., Single-Atom Electrocatalysts from Multivariate Metal–Organic Frameworks for Highly Selective Reduction of CO2 at Low Pressures. Angewandte Chemie 2020, 132 (46), 20770-20776.

56. Fang, X.; Shang, Q.; Wang, Y.; Jiao, L.; Yao, T.; Li, Y.; Zhang, Q.; Luo, Y.; Jiang, H. L., Single Pt atoms confined into a metal–organic framework for efficient photocatalysis. Advanced Materials 2018, 30 (7), 1705112.

57. Sun, K.; Liu, M.; Pei, J.; Li, D.; Ding, C.; Wu, K.; Jiang, H. L., Incorporating Transition-Metal Phosphides Into Metal-Organic Frameworks for Enhanced Photocatalysis. Angewandte Chemie International Edition 2020, 59 (50), 22749-22755.

58. Millward, A. R.; Yaghi, O. M., Metal− organic frameworks with exceptionally high capacity for storage of carbon dioxide at room temperature. Journal of the American Chemical Society 2005, 127 (51), 17998-17999.

59. Caskey, S. R.; Wong-Foy, A. G.; Matzger, A. J., Dramatic tuning of carbon dioxide uptake via metal substitution in a coordination polymer with cylindrical pores. Journal of the American Chemical Society 2008, 130 (33), 10870-10871.

60. Jiao, Y.; Morelock, C. R.; Burtch, N. C.; Mounfield III, W. P.; Hungerford, J. T.; Walton, K. S., Tuning the kinetic water stability and adsorption interactions of Mg-MOF-74 by partial substitution with Co or Ni. Industrial & Engineering Chemistry Research 2015, 54 (49), 12408-12414.

61. Masoomi, M. Y.; Morsali, A.; Dhakshinamoorthy, A.; Garcia, H., Mixed-metal MOFs: unique opportunities in metal–organic framework (MOF) functionality and design. Angewandte Chemie 2019, 131 (43), 15330-15347.

62. Chen, Y. Z.; Wang, C.; Wu, Z. Y.; Xiong, Y.; Xu, Q.; Yu, S. H.; Jiang, H. L., From bimetallic metal-organic framework to porous carbon: high surface area and multicomponent active dopants for excellent electrocatalysis. Advanced Materials 2015, 27 (34), 5010-5016.

63. Ismail, F.; Abdellah, A.; Lee, H.-J.; Sudheeshkumar, V.; Alnoush, W.; Higgins, D. C., Impact of Nickel Content on the Structure and Electrochemical CO2 Reduction Performance of Nickel–Nitrogen–Carbon Catalysts Derived from Zeolitic Imidazolate Frameworks. ACS Applied Energy Materials 2021.

64. Rosi, N. L.; Kim, J.; Eddaoudi, M.; Chen, B.; O'Keeffe, M.; Yaghi, O. M., Rod packings and metal− organic frameworks constructed from rod-shaped secondary building units. Journal of the American Chemical Society 2005, 127 (5), 1504-1518.

65. Wang, L. J.; Deng, H.; Furukawa, H.; Gándara, F.; Cordova, K. E.; Peri, D.; Yaghi, O. M., Synthesis and characterization of metal–organic framework-74 containing 2, 4, 6, 8, and 10 different metals. Inorganic chemistry 2014, 53 (12), 5881-5883.

66. Sengupta, J.; Jacob, C., The effect of Fe and Ni catalysts on the growth of multiwalled carbon nanotubes using chemical vapor deposition. Journal of Nanoparticle Research 2010, 12 (2), 457-465.

67. Dupuis, A.-C., The catalyst in the CCVD of carbon nanotubes—a review. Progress in materials science 2005, 50 (8), 929-961.

68. Rao, R.; Sharma, R.; Abild-Pedersen, F.; Nørskov, J. K.; Harutyunyan, A. R., Insights into carbon nanotube nucleation: Cap formation governed by catalyst interfacial step flow. Scientific reports 2014, 4 (1), 1-6.

69. Chen, M.; Zhao, G.; Shao, L.-L.; Yuan, Z.-Y.; Jing, Q.-S.; Huang, K.-J.; Huang, Z.-Y.; Zhao, X.-H.; Zou, G.-D., Controlled synthesis of nickel encapsulated into nitrogen-doped carbon nanotubes with covalent bonded interfaces: the structural and electronic modulation strategy for an efficient electrocatalyst in dye-sensitized solar cells. Chemistry of Materials 2017, 29 (22), 9680-9694.

70. Sun, C.; Zhang, Y.; Wang, P.; Yang, Y.; Wang, Y.; Xu, J.; Wang, Y.; William, W. Y., Synthesis of nitrogen and sulfur co-doped carbon dots from garlic for selective detection of Fe 3+. Nanoscale research letters 2016, 11 (1), 1-9.

71. Yang, H. B.; Hung, S.-F.; Liu, S.; Yuan, K.; Miao, S.; Zhang, L.; Huang, X.; Wang, H.-Y.; Cai, W.; Chen, R., Atomically dispersed Ni (I) as the active site for electrochemical CO 2 reduction. Nature energy 2018, 3 (2), 140-147.

72. Li, X.; Bi, W.; Chen, M.; Sun, Y.; Ju, H.; Yan, W.; Zhu, J.; Wu, X.; Chu, W.; Wu, C., Exclusive Ni–N4 sites realize near-unity CO selectivity for electrochemical CO2 reduction. Journal of the American Chemical Society 2017, 139 (42), 14889-14892.

73. Yang, J.; Qiu, Z.; Zhao, C.; Wei, W.; Chen, W.; Li, Z.; Qu, Y.; Dong, J.; Luo, J.; Li, Z., In situ thermal atomization to convert supported nickel nanoparticles into surface-bound nickel single-atom catalysts. Angewandte Chemie International Edition 2018, 57 (43), 14095-14100.

74. Ju, W.; Bagger, A.; Hao, G.-P.; Varela, A. S.; Sinev, I.; Bon, V.; Cuenya, B. R.; Kaskel, S.; Rossmeisl, J.; Strasser, P., Understanding activity and selectivity of metal-nitrogen-doped carbon catalysts for electrochemical reduction of CO 2. Nature communications 2017, 8 (1), 1-9.

75. Hatsukade, T.; Kuhl, K. P.; Cave, E. R.; Abram, D. N.; Jaramillo, T. F., Insights into the electrocatalytic reduction of CO 2 on metallic silver surfaces. Physical Chemistry Chemical Physics 2014, 16 (27), 13814-13819.

76. Zhang, H.; Zheng, J.; Chao, Y.; Zhang, K.; Zhu, Z., Surface engineering of FeCo-based electrocatalysts supported on carbon paper by incorporating non-noble metals for water oxidation. New Journal of Chemistry 2018, 42 (9), 7254-7261.

5 Chapter | Unravelling the Nature of Active Sites in Metal-Organic Framework-derived Heterogenous Electrocatalysts for Boosting the Electroreduction of CO_2 to CO at Industrially Relevant Current Densities

In this chapter, zeolitic imidazole framework (ZIF-8) –a subclass of MOFs– has been doped with Ni^{2+} to develop an efficient heterogeneous electrocatalyst structure for CO_2R. Our findings demonstrated that, under thermal treatment, the atomic ratio of Ni^{2+}: Zn^{2+} ions and the metal content have significantly influenced the structure-property relationship of the developed catalysts. With the excess of Zn^{2+} atomic ratio over Ni^{2+} along with the utilization of low metal (Ni and Zn) concentrations, a homogenous structure of atomically dispersed dual Ni-Zn-N_X/C sites is formed. Meanwhile, using high metal loadings under similar synthetic conditions has led to the formation of a heterogeneous structure of atomically dispersed dual Ni-Zn-N_X/C sites along with Ni_3ZnC-based particles. Both catalyst designs have been investigated for CO_2 electroreduction using a membrane electrode assembly (MEA)-type electrolyzer and exhibited over 90% CO Faradaic efficiency at different current densities/reaction rates. The latter catalyst design revealed higher activity towards CO production under CO_2R conditions, attaining a current density of 448mA/cm^2 at 3.1V, emphasizing the role of Ni_3ZnC particles in enhancing the reaction rate compared to the homogenous structure of atomically dispersed Ni-Zn-N_X/C sites. To unravel the nature of the evolved active sites under CO_2R conditions, *in-situ* and *ex-situ* X-ray absorption spectroscopy measurements were performed. Our results demonstrated that both atomically dispersed dual Ni-Zn-N_X/C sites and Ni_3ZnC particles are contributing to the overall activity during CO_2R.

Unravelling the Nature of Active Sites in Metal-Organic Framework-derived Heterogenous Electrocatalysts for Boosting the Electroreduction of CO_2 to CO at Industrially Relevant Current Densities

Fatma Ismail[a], Wajdi Alnoush[b], Ahmed Abdellah[c], Shunquan Tan[d], Kholoud Abousalem[e], Amirhossein Rakhsha[f], Ning Chen [g*], Drew C. Higgins[h*]

[a]ismaif1@mcmaster.ca, [b]alnoushw@mcmaster.ca, [c]abdellaa@mcmaster.ca,

[d]tans49@mcmaster.ca, [e]abousalk@mcmaster.ca, [f]rakhsha@mcmaster,

[g]ning.chen@lightsource.ca, [h]higgid2@mcmaster.ca

Keywords: CO_2 electrolysis; membrane electrode assembly, nickel zinc carbide, metal-nitrogen-carbon; Ni single atoms; Zn single atoms; MOF-based electrocatalyst; ionic exchange.

5.1 Abstract

The electrochemical reduction of CO_2 (CO_2R) to value-added chemicals and fuels is a promising approach to mitigate the devastating impact of greenhouse emissions on climate change. In recent years, numerous efforts have been dedicated to the development of efficient and selective electrocatalysts for CO_2R. Metal-organic frameworks (MOFs) with well-defined structures and high surface areas have attracted intensive attention as a promising precursor for deriving several catalyst designs such as atomically isolated metal sites and dual-metal alloys. However, identifying the active sites employed of MOF-derived catalysts during CO_2R remains a grand challenge due to the heterogeneous nature of the produced electrocatalysts that comprise various active sites. Herein, zeolitic imidazole framework (ZIF-8) –a subclass of MOFs– has been doped with Ni^{2+} to develop an efficient heterogeneous electrocatalyst structure for CO_2R. Our findings demonstrated that, under thermal treatment, the atomic ratio of Ni^{2+}: Zn^{2+} ions and the metal content have significantly influenced the structure-property relationship of the developed catalysts. With the

excess of Zn^{2+} atomic ratio over Ni^{2+} along with the utilization of low metal (Ni and Zn) concentrations, a homogenous structure of atomically dispersed dual Ni-Zn-N_X/C sites is formed. Meanwhile, using high metal loadings under similar synthetic conditions has led to the formation of a heterogeneous structure of atomically dispersed Ni-Zn-N_X/C along with Ni_3ZnC-based particles. Both catalyst designs have been investigated for CO_2R using membrane electrode assembly (MEA) and exhibited over 90% CO Faradaic efficiency (FE) at different current densities/reaction rates. The latter catalyst design revealed higher activity towards CO production, attaining a current density of 448mA/cm^2 at 3.1V, emphasizing the role of Ni_3ZnC particles in enhancing the reaction rate compared to the homogenous structure of atomically dispersed Ni-Zn-N_X/C sites. To unravel the nature of the evolved active sites under CO_2R conditions, *in-situ* and *ex-situ* X-ray absorption spectroscopy measurements were performed. Our results demonstrated that both atomically dispersed dual Ni-Zn-N_X/C sites and Ni_3ZnC particles contribute to the overall activity and selectivity of the developed catalysts during CO_2R.

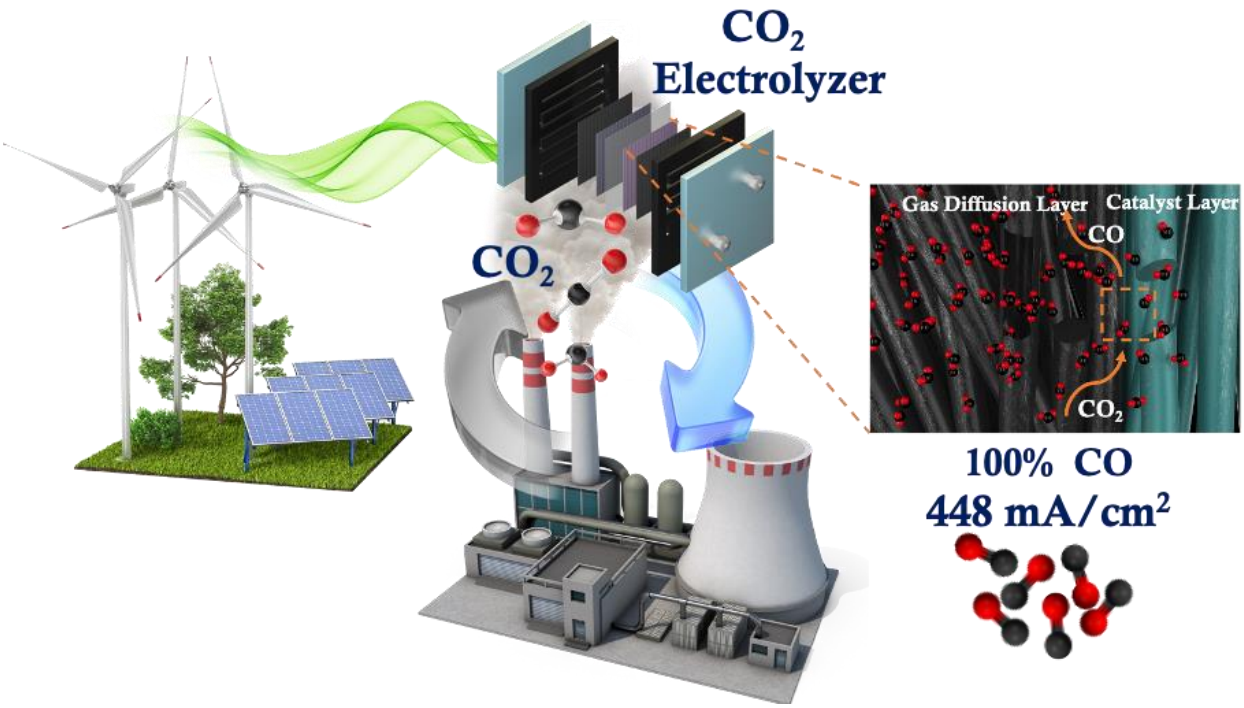

A graphical abstract illustrates the practical implementation of CO_2 conversion technology using renewable energy resources and an MEA-based electrolyzer to produce chemical feedstocks (CO) at industrially relevant reaction rates

5.2 Introduction

The development of sustainable energy technologies that rely largely on renewable energy sources became a rising demand over the last few decades in order to lessen the dependence on limited fossil fuel reserves and diminish anthropogenic climate change.[1] One of the promising approaches is the employment of renewable electricity for deriving chemical reaction for the production of fuels and value-added chemicals using naturally profuse resources.[2] The increased generation of electricity via renewable resources such as wind and solar has facilitated electrifying the chemical industry through electro-synthetic processes and enabled the sustainable production of hydrocarbons and chemicals to become more viable.[3] Among various strategies, intensive efforts have been devoted to the electro-conversion of CO_2 (CO_2R) to value-added products such

as alcohols and chemical feedstocks, given the fact that carrying the CO_2R reaction industrially is not energy intensive and can be carried out using ambient reaction conditions.[4] CO_2 molecules could be reduced to several products such as carbon monoxide (CO), methane (CH_4), ethylene (C_2H_4), and ethanol (C_2H_5OH).[5-7] Particularly, CO is one of the most valuable chemical feedstocks for numerous industries and could be employed in crucial technologies such as Fischer–Tropsch process.[8, 9] CO_2R to CO technologies are limited by the large energy barrier of the reaction which increases the demand for developing efficient and in-expensive electrocatalysts.

Initially, various catalyst designs including molecular complexes,[10-12] heterogeneous metal and metal oxides,[13-17] and carbon-based materials[18-20] were designed and investigated for CO_2 conversion to CO. Despite the well-defined structure and high surface areas of molecular catalysts such as metalophthalocyanine and metalloporphyrin, however, their further utilization in CO_2R is hindered by the instability and poor electronic conductivity.[21-23] On the other hand, the high cost of metal catalysts such as Pd, Au, and Ag impede their commercial applications although they can afford very promising selectivity towards CO production.[13, 24] Electrocatalysts of non-metal atoms doped in carbon skeletons have been evaluated for CO_2R, but their properties and electrocatalytic performance need further improvement to compete with the other developed catalysts. Hence, designing highly efficient electrocatalysts with commercial qualifications is still under investigation.

Atomically dispersed metal−nitrogen−doped carbon (M−N−C) class of materials have recently emerged for CO_2R and exhibited high activity and selectivity towards generating CO.[25-27] In M–N–C electrocatalysts, metal ions are coordinated to graphitic carbon structures containing N-dopants to generate atomically dispersed active sites ($M\text{-}N_X/C$).[28-31] Developing M-N-C catalysts has imparted a new opportunity to couple the advantages of heterogenous and molecular

catalysts, which enabled achieving high electrocatalytic performance during CO_2R.[32] Scientists have attributed the enhanced performance of M-N-C-based catalysts during CO_2R to several factors including the unique local coordination environment, maximum atomic utilization of metal centers, and facile electron transport through the graphitic support.[33, 34] The fabrication of atomically dispersed M-N-C catalysts is commonly carried out through the co-pyrolysis of carbon-, nitrogen-, and earth-abundant metal salt-containing mixture. A variety of M-N-C electrocatalysts have been synthesized where M could be Co, Fe, Mn, Cu, and Ni. In particular, atomically dispersed Ni–N–C catalysts with the active site configuration of $Ni–N_X$ (X=1, 2, 3, or 4) immobilized in a graphitic architecture, demonstrated high selectivity of CO production while suppressing the competing hydrogen evolution reaction (HER). Various precursors are being employed to produce Ni–N–C catalysts; however, researchers have recently focused on the utilization of metal-organic frameworks (MOFs) due to their well-defined crystalline structures, superior surface area, and porosity.[35-39] It is postulated that MOF's structural characteristics, particularly, its high surface area, would be inherited into the derived Ni–N–C catalyst structure, leading to producing a configuration with a high concentration of atomically dispersed $Ni\text{-}N_X/C$ sites.

Generally, atomically dispersed $Ni\text{-}N_X/C$ sites are integrated into carbon-based structures such as N-doped carbon nanotubes[40, 41] and N-doped nanosheets,[42, 43] however, achieving high selectivity of CO at high current densities/reaction rates remains challenging for most of the developed Ni–N–C catalysts. Various attempts have been made on improving their intrinsic (e.g., local geometric/chemical configurations, and atomic coordination environment)[14, 44] and extrinsic (e.g., porosities, surface area and morphologies) characteristics.[45] Incorporating an additional transition metal site adjacent to the main site is one of the promising approaches to promote the

overall reaction rate and introduce different mechanistic pathways of CO_2R.[46, 47] The local coordination environment, more specifically the N-coordination of a single-metal site varies significantly from a dual-metal site.[48, 49] Therefore, the intrinsic activity of dual-metal catalyst could be enhanced by modulating the geometric and electronic configuration, resulting in improved electrocatalytic activity under CO_2 electrolysis.[50] Very recently, Yi Li et al have developed a series of atomically dispersed dual-metal sites for CO_2R such as Ni-Co and Ni-Fe, their findings demonstrated that atomically dispersed Ni-Fe catalyst showed higher electrocatalytic activity and selectivity compared to other atomically dispersed dual-metal catalysts.[47] Further, their theoretical predictions revealed that the synergetic effect of the dual-metal site (NiFe) has enhanced the intrinsic catalytic activity and selectivity by enabling more optimal *CO desorption and *COOH adsorption compared to single-metal sites ($Ni–N_4$/$Fe–N_4$). Another study reported by Youzhi Li et al[51] performed DFT measurements on atomically dispersed dual Ni-Zn catalyst, their results showed the influence of the heteronuclear coordination on the metal atom d-states, whereby the gap between Fermi energy level (E_F) and d-band (εd) of the Ni (3d) orbitals is narrowed, leading to enhancing the electronic interactions, and lowering both free energy barrier (ΔG) and activation energy (E_a). These electronic modifications have impacted the intrinsic activity of the atomically dispersed Ni-Zn dual catalyst and enabled achieving >90% of CO selectivity at a wide potential window. However, this research is in the early stages and further investigation on the influence of the adjacent metal atom on the coordination environment and electrocatalytic activity is still required.

On the other hand, electrocatalysts of intermetallic carbide embedded in a structure of porous carbon-containing nitrogen dopants have been investigated for different electrocatalytic applications due to their atomic arrangement, controlled crystal structure, and the well-defined

stoichiometry, providing various desired chemical and physical characteristics.[52, 53] Qi et al have used the co-pyrolysis procedure of M@ZIF-8 whereby M=Au, Rh, Pd Pt, and Ru to develop a series of Zn-intermetallic nanoparticles (iNPs) impregnated in an N-doped carbon structure.[54] Whereas Xue et al. has reported an enhanced oxygen reduction reaction (ORR) of intermetallic PtZn@N-doped carbon electrocatalyst with multi-functional order compared to the commercially available Pt/C.[55] In the context of CO_2 conversion, Nágila E. C. Maluf et al. have designed Ni–Zn carbide (Ni_3ZnC) supported in N-doped porous carbon, under the reverse water gas shift reaction, their developed catalyst exhibited selective hydrogenation of CO_2 into CO at atmosphere pressure (CO_2:H_2 = 1:4 GHSV = 30000 mL/g_{cat} h) and 450 °C.[56]

Herein, a synthetic procedure has been developed and optimized to prepare different catalyst designs that comprise both atomically dispersed dual sites and intermetallic particles to investigate the influence of the coexistence of these species on the obtained CO_2R performance. In which, one design has a structure of atomically dispersed dual Ni-Zn-N_X sites embedded in a carbonaceous architecture. Whereas the other catalyst design comprised a heterogenous structure of Ni–Zn/C intermetallic particles and atomically dispersed dual Ni-Zn sites impregnated in N-doped carbon support. Zeolitic imidazole framework (ZIF-8) – a subclass of MOFs with the analogous structure of zeolites – built from the coordination of tetrahedral Zn^{2+} to 2-methyl imidazole organic ligand to form 3-D solidate (SOD) topology – has been used as a precursor. ZIF-8 couples the features of both MOF and zeolites such as porosity, enthralling crystallinity, and thermal stability.[57] In this work, (ZIF-8) was embedded with Ni^{2+} at different Ni^{2+}: Zn^{2+} atomic ratios and metal concentrations. Our findings exhibited that the co-pyrolysis of ZIF-8 impregnated with Ni^{2+} using low metal concentrations and excess content of Zn^{2+} ions over Ni^{2+} ions has resulted in the successful formation of homogenous atomically dispersed dual Ni-Zn-N_X/C sites.

Whilst the utilization of high metal content under similar conditions has generated a heterogeneous catalyst structure of atomically dispersed dual Ni-Zn-N_X/C sites adjacent to Ni_3ZnC-based particles. Following synthesis, both designs were evaluated for CO_2R using an industrial competitive membrane electrode assembly (MEA)–based electrolyzer. The developed electrocatalysts with homogenous and heterogenous structures revealed >90% of CO Faradaic efficiencies at different applied voltages, however, the heterogenous catalyst design displayed an improved selectivity of CO_2 reduction to CO at a high current density (~100% CO FE and 448mA/cm^2 at 3.1V) compared to the homogenous structure. This difference in the electrocatalytic activities between both designs suggests that introducing Ni_3ZnC-based particles to the homogenous atomically dispersed dual Ni-Zn-N_X/C sites has likely induced a synergetic effect on the intrinsic catalytic activity which consequently enhanced the reaction rate towards CO formation. Further, *in-situ* and *ex-situ* X-ray absorption spectroscopy measurements were carried out to assist in unveiling the nature of the active sites evolved in both catalyst designs under CO_2R conditions.

5.3 Materials and Methodologies

5.3.1 Materials

$Zn(NO_3)_2.6H_2O$, 2-methylimidazole, ($Ni(NO_3)_2.6H_2O$), $KHCO_3$, ethanol, isopropanol (IPA), a 5 wt % Nafion solution in isopropanol, methanol, n-hexane, nitric acid, hydrochloric acid and graphite foil were purchased from Sigma Aldrich and used without further purification. Type 1 ultrapure water (< 10 ppb TOC; > 18 MΩ-cm) was used for all conducted experiments.

5.3.2 Methods

5.3.3 Synthesis of Zeolitic Imidazolate Frameworks (ZIF-8)

Initially, 0.616g of 2-methyl imidazole (organic linker) was dissolved in 25 mL of methanol, followed by dissolving 0.558g of zinc nitrate hexahydrate (metal salt) in a separate 15 mL of methanol. Subsequently, the organic linker-containing solution was added to the metal salt-containing solution and kept at 35 °C under vigorous stirring for 12 hours. Then, a centrifuge with 12,000 rpm was utilized to wash and separate the formed white precipitate, followed by keeping the obtained white paste at 70°C for 12 hours to dry.

5.3.4 Synthesis of Ni_3ZnC-based particles@atomically dispersed dual Ni-Zn-N-C structure (The heterogenous catalyst design)

To prepare this heterogenous catalyst, a complete suspension of 1gm ZIF-8 in 50 mL n-hexane has been performed. The homogenous ZIF-8-containing solution has been impregnated with an aqueous solution of $Ni(NO_3)_2.6H_2O$ (100 mg/1 mL), this sample is denoted as [a-Ni_3ZnC@Ni-Zn-N-C]. This mixed solution was stirred vigorously for 4 hours. A filtration procedure has been followed to separate the formed green precipitate, and the obtained light green paste was kept for 12 hours at 70 °C to dry. Afterwards, the collected greenish powder was pyrolyzed under inert gas conditions (Ar) in a tube furnace using a ramp of 5°C/minute. An additional sample was prepared using different atomic ratios by injecting (300 mg/3 mL) of $Ni(NO_3)_2.6H_2O$, this sample is represented here as [b-Ni_3ZnC@Ni-Zn-N-C].

5.3.5 Synthesis of atomically dispersed dual Ni-Zn-N-C catalysts (The homogenous catalyst design)

Atomically dispersed dual Ni-Zn-N-C catalysts were fabricated by the suspension of 100 mg of as-prepared ZIF-8 in 10 mL of n-hexane. The suspended solution was doped with Ni-containing solution of $Ni(NO_3)_2.6H_2O$ (10 mg/1 mL), this catalyst is referred here as [a-Ni-Zn-N-

C]. This mixed solution was stirred continuously for 4 hours, followed by filtering, and separating the formed green precipitate, the light green paste was kept at 70 °C for 12 hours to dry. The collected powder was pyrolyzed in a tube furnace at 1000 °C using inert gas conditions (Ar) with of 5°C/minute temperature ramp for 2 hours. Another atomic ratio has been prepared by injecting (30 mg/1 mL) of $Ni(NO_3)_2.6H_2O$ which is denoted here as [b-Ni-Zn-N-C].

5.3.6 Material Characterization

The morphology of the developed catalyst designs was investigated using high-resolution transmission electron microscopy (HR-TEM). While the crystallinity and near-surface composition were assessed using powder X-ray diffraction (PXRD) and X-ray photoelectron microscopy (XPS), respectively. The elemental distribution of the produced catalysts was obtained using energy dispersive spectroscopy (EDS) measurements. All these characterization techniques are available at McMaster X-ray Facility (MAX), Bioinformatics Institute (BI), and Canada Center of Electron Microscopy (CCEM).

5.3.7 *In-situ* and *Ex-situ* X-ray Absorption Spectroscopy (XAS) Measurements

In-situ and ex-situ XAS characterizations including extended X-ray absorption fine structure (EXAFS) and X-ray absorption near-edge structure (XANES) were conducted in a synchrotron-based facility (HXMA beamline 061D-1) at the Canadian Light Source (CLS) capable of a 1×10^{-4} $\Delta E/E$ resolution in the energy range of 5−30 keV. To collect Ni K–edge and Zn K–edge measurements, He-filled ionization chambers were used to measure incident and transmitted x-rays in the transmission mode while fluorescent X-rays were detected by a multi-element silicon drift detector. A double-crystal Si monochromator (Si 220) was used for both Ni K–edge (8333 eV) and Zn K–edge (9660 eV), where the second monochromator crystal was 50% detuned at the end of the scan to remove higher harmonics. Further, *in-situ* XAS measurements of Ni K–edge

were carried out under CO_2R conditions employing a custom-designed MEA cell that mimics laboratory MEA system with adaption to XAS measurement requirements and the end in HXMA beamline. The employed MEA reactor utilized a catalyst-loaded gas diffusion layer (GDL) with an active area of $1cm^2$ and catalyst loading of 2.5 mg/cm^2. A mass flow controller (MFC) unit was used to regulate the CO_2 gas to a flow rate of 60 sccm during the *in-situ* measurements, and a peristaltic pump was utilized to circulate 0.1M $KHCO_3$ electrolyte in the MEA anodic side. Data analysis and EXAFS fitting were performed using Demeter software packages. Ni foil's first shell has resulted in a 0.74 amplitude reduction factor which was used to determine other EXAFS fitting parameters.

5.3.8 Electrode Preparation for CO_2 Electrolysis

15 mg of each catalyst powder was dispersed in a 3:1 mix solvent of IPA:H_2O and 50 µL of Nafion solution (5%) was added, the mixture was sonicated for 1 hour until the complete suspension. Gas diffusion electrodes were prepared by drop-casting the previous ink on a microporous carbon paper layer (SGL 34BC) as a substrate and kept at room temperature for 12 hours before CO_2R measurements.

5.3.9 Electrode Engineering in MEA-based CO_2 Electrolyzer

MEA-based electrolyzer was purchased from Dioxide Materials Inc. and validated for CO production using Dioxide Materials standard electrode. Prior validation, MEA was constructed by the mechanical pressure of both cathodic and anodic GDEs whereby a standard catalyst layer (2 cm*2.5 cm) and IrO_2 layer (2.5 cm* 2.5 cm) were used, respectively. Subsequently, the developed catalyst-based GDEs with an active area of (1.9 cm*1.9 cm) were integrated into the validated MEA electrolyzer to evaluate them for CO_2R. Both anodic and cathodic GDEs were separated by

an anion exchange membrane (Dioxide Materials; Sustainion X37-50). A humidified CO_2 gas was fed to the cathodic catalyst side with a mass flow control unit using 80 sccm flow rate while 1M $KHCO_3$ electrolyte was supplied to the anodic side using a 50 mL/min flow rate. The overall reaction was held at ambient conditions and controlled using a Biologic VSP-300 potentiostat. To investigate the influence of different reaction factors such as GDE active area, catalyst loading, and catalyst deposition method, a homogenous catalyst structure of Ni–N–C developed in our previous work[38] was selected for the optimization study and evaluated using four different GDE configurations (a $5cm^2$ square-based configuration, $1cm^2$ square-based configuration, $1cm^2$ rectangle-based configuration, and $1cm^2$ catalyst active area integrated into a $5cm^2$ GDE). Also, three catalyst loading (1, 2, and 4 mg/cm^2) and two deposition methods (spray coating and drop-casting) were investigated. A gas chromatography (GC) unit was employed to quantify the obtained gas products, more specifically CO and H_2. GC instrument SRI, model: 8610C, multi-Gas configuration #5 provided with both flame ionization detector (FID) and thermal conductivity detector (TCD) was used, in which the sample loop in the GC is linked directly to effluent from the MEA.

5.4 Results and discussions

5.4.1 Structure and Morphology

Synthesis of ZIF-8 nanoparticles has been performed in previous reports[58], and a uniform rhombododecahedral crystal shape was obtained. The synthetic methods and hypothesized structural transformations of both catalyst designs are illustrated in **Figure 5.1**. To investigate the morphology and elemental distribution of the developed catalysts at different Ni^{2+}: Zn^{2+}atomic ratios and metal content, TEM imaging at different magnifications **(Figures 5.2a−h and S1a−d)** and HAADF-STEM coupled with EDS mapping **(Figures 5.3a–d and S1e,f)** have been

performed. Both [a-Ni_3ZnC@Ni-Zn-N-C] and [b-Ni_3ZnC@Ni-Zn-N-C] catalysts **(Figure 5.2a–d)** exhibited a heterogeneous distribution of different species comprising large carbon particles, carbon nanotubes (CNTs), and dark metallic particles of different sizes varying from few nanometers to ca. 150 nm. **Figure 5.2e–h** reveals that a ZIF-8-like graphitic structure has been generated in [a-Ni-Zn-N-C] and [b-Ni-Zn-N-C] catalysts along with the formation of a small portion of CNTs in the b-Ni-Zn-N-C catalyst. Initially, the pre-impregnation procedure of Ni salt into the ZIF-8 structure has assisted in the physical adsorption of Ni^{2+} ions on its pores and surface. The co-pyrolysis of ZIF-8 embedded with $Ni(NO_3)_2$ at elevated temperatures (~1000°C) has likely led to the evaporation of Zn^{2+} sites (their boiling point is ca. 910°C) and the formation of an N-doped graphitic structure resulting from the decomposition of ZIF-8 building blocks (2-methyl imidazole). These N-doped carbonaceous sites are postulated to act as coordination sites for the pre-adsorbed Ni^{2+} ions to create atomically isolated Ni-N_X/C sites. The atomic ratio between the impregnated Ni^{2+} ions and the existing Zn^{2+} was demonstrated previously to play a significant role in the obtained catalyst morphology, for example, 0.5:1 Ni^{2+}:Zn^{2+} atomic ratio was found to produce a homogenous structure of atomically dispersed Ni-N_X/C sites, whereas 2:1 Ni^{2+}: Zn^{2+} atomic ratio led to the formation of metallic Ni-based particles[38]. However, our findings demonstrated that varying the atomic ratio along with metal concentrations has resulted in generating different active sites. During pyrolysis, introducing an excess Zn^{2+} atomic ratio (ca. Ni^{2+}: Zn^{2+}1:5 and 1:14) has likely suppressed the ionic exchange process and assisted in forming atomically dispersed dual Ni-Zn-N_X sites immobilized in a graphitic structure as revealed in [a-Ni-Zn-N-C] and [b-Ni-Zn-N-C] catalysts. This could be observed in EDS mapping of the same catalysts, **Figure 5.3c,d illustrates** a homogenous distribution of Zn, Ni, N, and C elements in both catalysts with no observation of metallic-based particles in [a-Ni-Zn-N-C] catalyst and only

few Ni particles in [b-Ni-Zn-N-C] catalyst. This suggests that Ni and Zn species were largely dispersed in the N-C matrix to create atomically dispersed dual Ni-Zn-N_X/C sites. On the contrary, the progressive increase of metal content at the same atomic ratios in [a-Ni_3ZnC@Ni-Zn-N-C] and [b-Ni_3ZnC@Ni-Zn-N-C] catalysts has produced a heterogenous structure of different species. EDS mapping of these catalysts **(Figure 5.3a,b)** shows the presence of metallic Ni-based particles, intermetallic particles that contain Ni, Zn, and C, and homogenously distributed Ni, Zn, N, and C species. This could be likely speculated to the formation of Ni_3ZnC particles along with metallic Ni and atomically dispersed dual Ni-Zn-N_X/C sites. The formation of metallic Ni_3ZnC along with Ni-based particles could be likely because the formation of atomically dispersed dual Ni-Zn-N_X/C sites has achieved a saturation point where Ni-Zn pairs started to agglomerate and form metallic Ni_3ZnC and Ni-based particles. Further, the reason that CNTs were not observed in the [a-Ni-Zn-N-C] catalyst compared to the other prepared catalysts is likely the very low Ni content in this catalyst. Generally, CNT nucleation through Ni sites is governed by several factors, for instance, Ni content, synthetic procedures, Ni crystal facets, composition, and morphology of the Ni catalyst.[59] The progressive increase of Ni content in the different catalysts has resulted in the enhancement of CNT formation accordingly, whereby [a-Ni_3ZnC@Ni-Zn-N-C] and [b-Ni_3ZnC@Ni-Zn-N-C] catalysts show a relatively large portion of CNTs compared to [b-Ni-Zn-N-C] catalyst. An acid wash strategy has been employed by nitric acid (1M) and hydrochloric acid (4M) for one of the developed catalysts [b-Ni_3ZnC@Ni-Zn-N-C] as illustrated in **Figure S1a−f**. Unlike the impact of HNO_3 acid wash, it could be observed that concentrated HCl acid has likely succeeded to leach out all metallic particles, leaving a structure of homogenous atomically dispersed dual Ni-Zn-N_X/C sites through the catalyst. While the catalyst yield is a key parameter for the practical employment of these catalysts, it is worth mentioning that the developed catalysts

with heterogenous features have produced ~450mg/batch, which is almost 10-fold the homogenous catalyst yield (~50mg/batch).

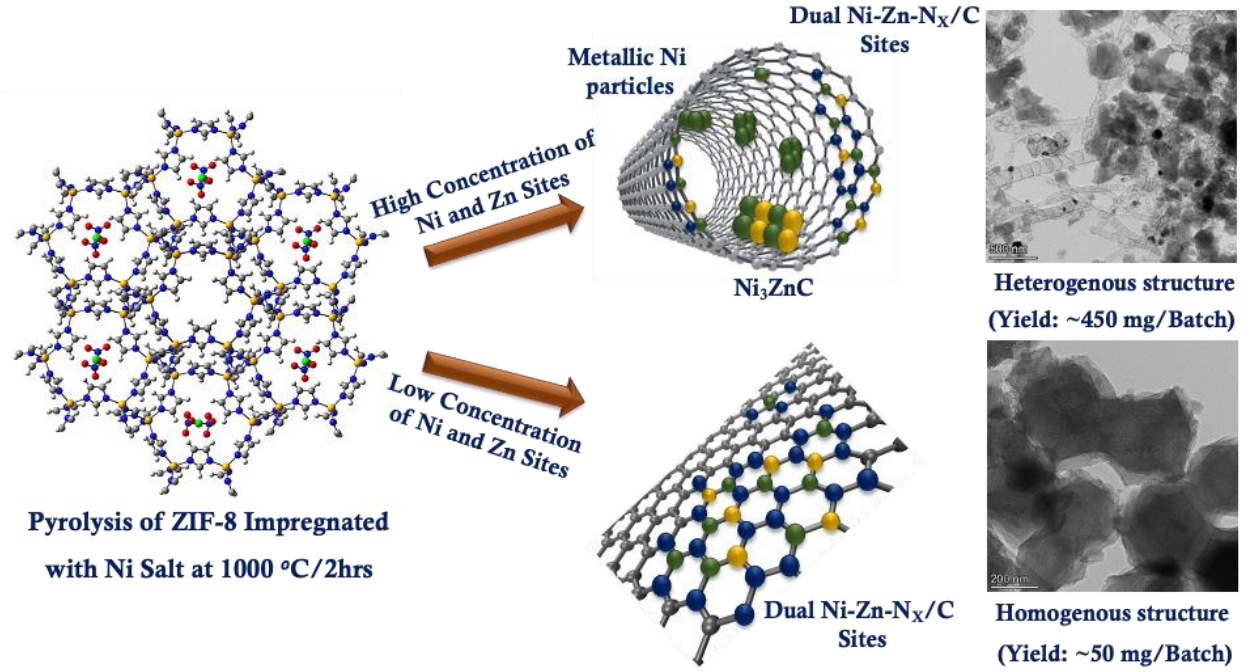

Figure 5-1 A schematic diagram illustrates the synthetic approaches and anticipated active sites

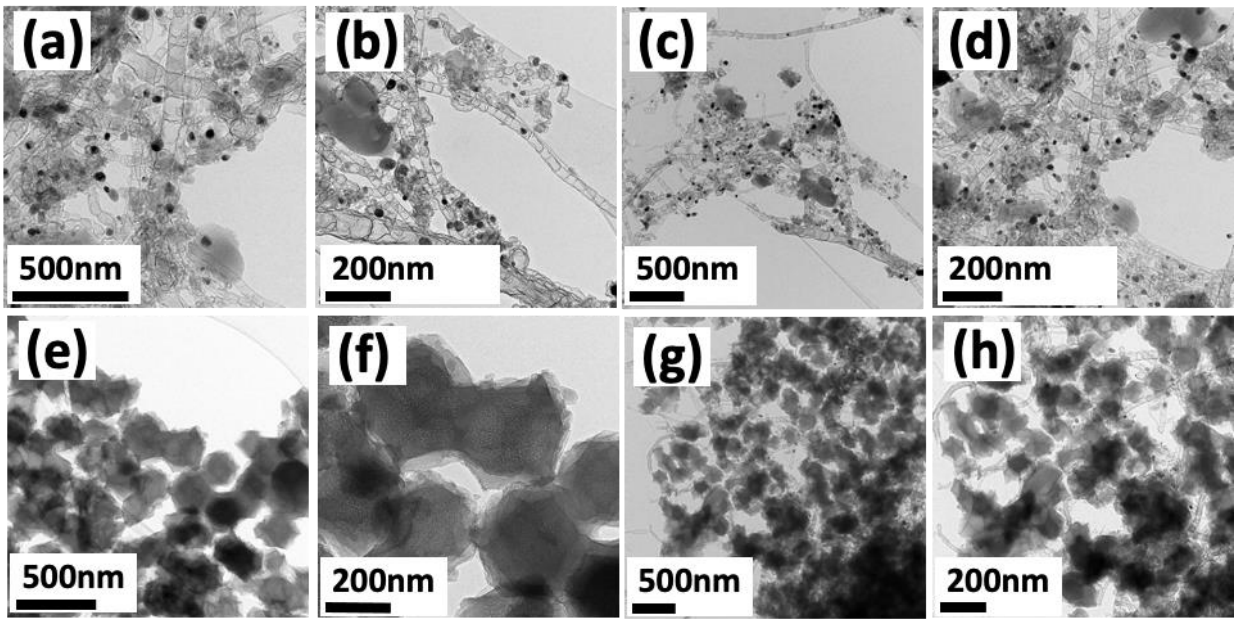

Figure 5-2 TEM images of all developed catalysts with different $Ni^{2+:}$ Zn^{2+} atomic ratios and metal loadings. (a,b) [a-Ni_3ZnC@Ni-Zn-N-C], (c,d) [b-Ni_3ZnC@Ni-Zn-N-C], (e,f) [a-Ni-Zn-N-C], and (g,h) [b-Ni-Zn-N-C].

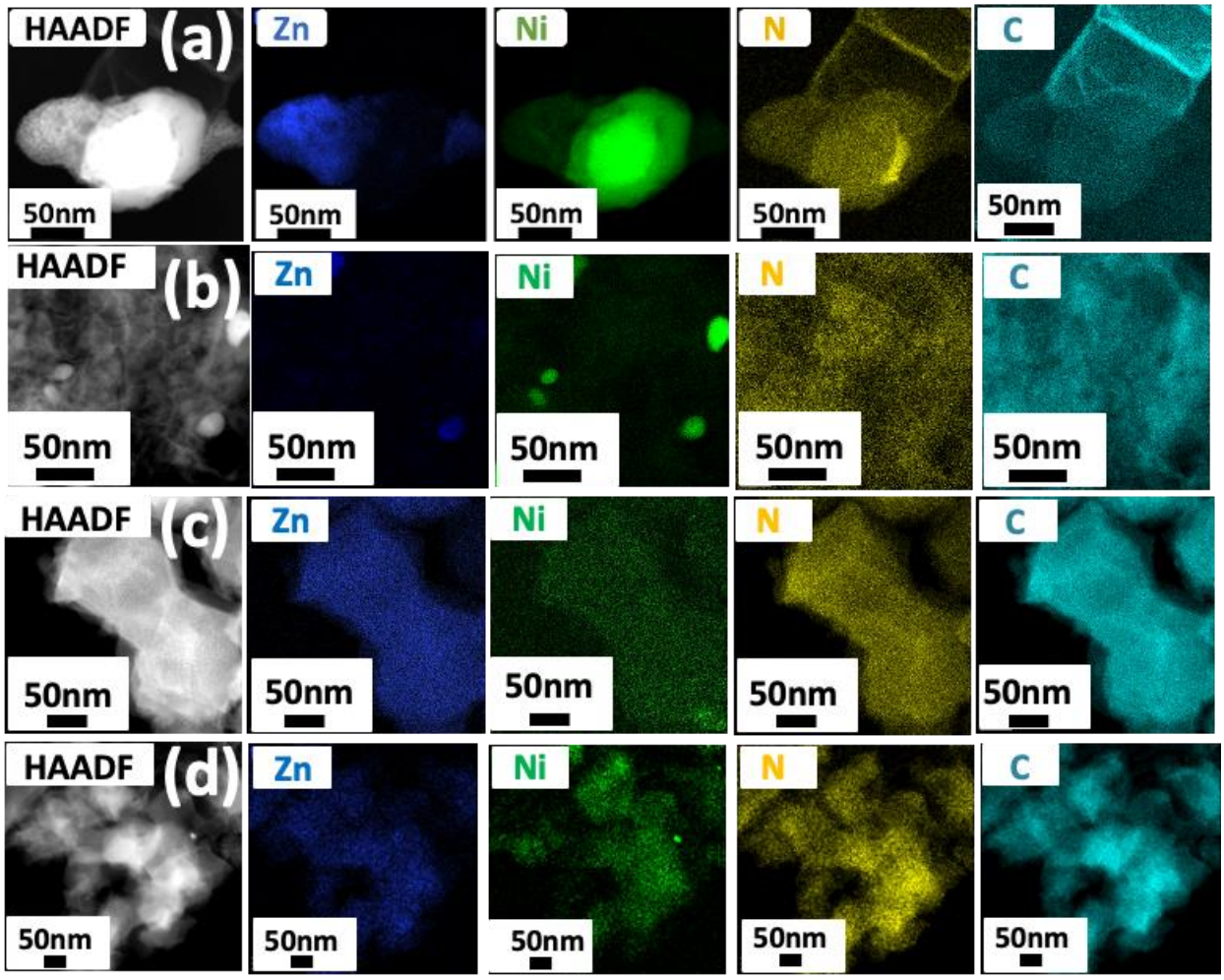

Figure 5-3 HAADF coupled with EDS elemental mapping of all developed catalysts with different Ni^{2+}: Zn^{2+} atomic ratios and metal loadings. (a) [a-Ni_3ZnC@Ni-Zn-N-C], (b) [b-Ni_3ZnC@Ni-Zn-N-C], (c) [a-Ni-Zn-N-C], and (d) [b-Ni-Zn-N-C].

To obtain detailed insights into the crystalline structure of the developed catalyst designs, PXRD measurements have been performed of heterogenous, homogenous and acid-washed catalysts **(Figure 5.4)**. The PXRD spectra of [a-Ni_3ZnC@Ni-Zn-N-C] and [b-Ni_3ZnC@Ni-Zn-N-C] reveal similar diffraction peaks at 42.7°, 49.7°, 73.3° which could be assigned to Ni_3ZnC (111),

(200), and (220), respectively, **(Figure 5.4a,b)**. It could be observed that these crystalline characteristic peaks have higher intensity in [b-Ni_3ZnC@Ni-Zn-N-C] compared to [a-Ni_3ZnC@Ni-Zn-N-C] which could be due to the lower Ni content in the latter catalyst. NiO (202) and (220) diffraction peaks at 43.6°, 62.9° were observed in [a-Ni_3ZnC@Ni-Zn-N-C] which is an indication of the formation of some NiO species in this catalyst. Both [a-Ni_3ZnC@Ni-Zn-N-C] and [b-Ni_3ZnC@Ni-Zn-N-C] catalysts shared similar features of Ni (111), (200), (220) at 44.4°, 51.7°, 76.2°, respectively. These observations are consistent with the TEM and EDS insights that demonstrated the formation of a heterogeneous structure of Ni_3ZnC and metallic Ni. On the contrary, [a-Ni-Zn-N-C] demonstrated almost an amorphous structure with no significant diffraction peaks which implies that both Ni and Zn species were not in a crystalline structure for PXRD detection and likely have created atomically dispersed dual Ni-Zn moieties immobilized in N-doped carbon structure instead of the formation of either metallic Ni or Ni_3ZnC-based particles. Similar features were obtained for [b-Ni-Zn-N-C] except for the presence of very small peaks at 44.4° and 51.7° that could be assigned to Ni (111) and (200), respectively. By combining the obtained insights from TEM, EDS and XRD, it could be proven that metal content plays a significant role in controlling the morphology and crystalline structure of the prepared catalysts. PXRD spectra in **Figure 5.4c,d** illustrates the impact of acid wash on [b-Ni_3ZnC@Ni-Zn-N-C] catalyst using HNO_3 and HCl. It could be observed that, unlike HNO_3 acid, HCl acid has leached out all metallic Ni and Ni_3ZnC particles, leaving an amorphous structure of atomically dispersed dual Ni-Zn-N_X/C sites.

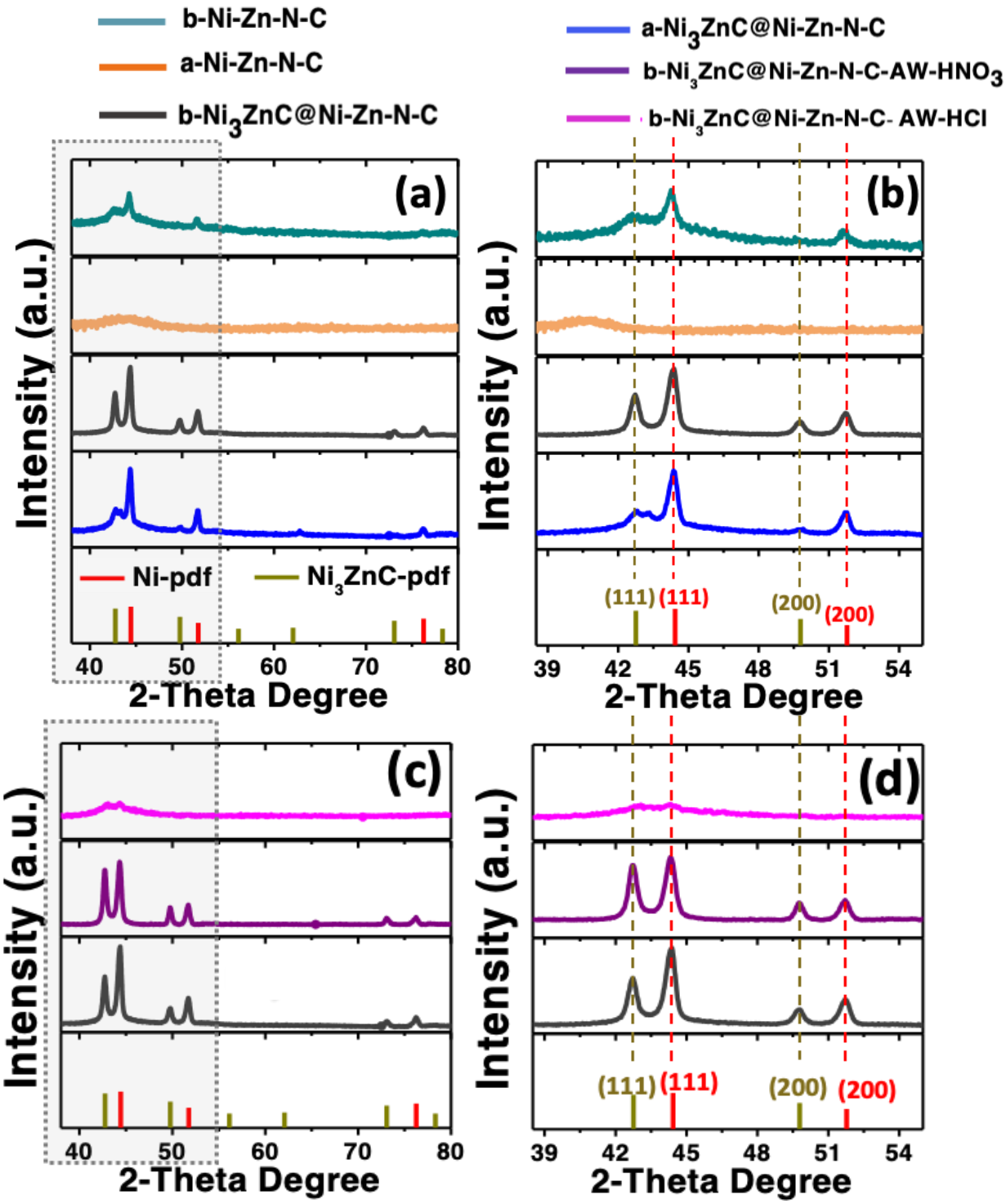

Figure 5-4 PXRD spectra of all developed catalysts at different Ni^{2+}: Zn^{2+} atomic ratios and metal loadings. (a) spectra of the different catalyst designs, (b) a magnified spectra indicate the matching of the assigned peaks and pdf cards (c) spectra of [b-Ni_3ZnC@Ni-Zn-N-C] catalyst before and after acid wash using different acids, and (d) a magnified spectra assign the different peaks to the pdf cards.

Among the developed catalysts, the heterogenous design of [a-Ni_3ZnC@Ni-Zn-N-C] and [b-Ni_3ZnC@Ni-Zn-N-C] have been selected for further characterization using X-ray photoelectron spectroscopy (XPS). The employment of XPS measurements has revealed that the near-surface composition of both catalysts is ca. 80.0 at. % carbon, 7.5 at. % nitrogen, 8.0 at. % oxygen, 3.5 at. % Ni, and less than 1.0 at. % Zn. N 1s high-resolution spectra of [a-Ni_3ZnC@Ni-Zn-N-C] is illustrated in **Figure 5.5a**, whereby four different peak positions are observed, that includes, pyridinic-N, graphitic-N, quaternary-N, and N-oxidized at 399.1, 401.2, 402.7, 404.9 eV, respectively. Previously, N-configurations have been proven to significantly influence the electrocatalytic performance of different catalysts. However, the precise identification of the local coordination environment by XPS is a challenge due to the ambiguity of XPS data fitting, therefore, *in-situ* and *ex-situ* extended X-ray absorption fine structure (EXAFS) measurements were performed for the developed catalysts. **Figure 5.5b** shows the Ni 2p spectra of the same catalyst, two main peaks are centered at 854.4 and 856.17 eV, the major peak at 854.4 eV demonstrates higher binding energy than the metallic Ni^0 (852.9 eV) and lower than that for Ni^{2+} (856.17 eV), suggesting that Ni moieties are mostly in a state with low-valent than Ni^{2+} and higher than metallic Ni^0. Zn 2p spectra **(Figure 5.5c)** indicate two XPS peaks at 1021.3 and 1022.4 eV, these peaks could be assigned to the presence of metallic Zn^0 and Zn^{2+}, respectively. For C 1s spectra illustrated in **Figure S3**, three different peaks were deconvoluted into 284.7, 286, and 287.4 eV, these are characteristic peaks of C=C/C–C, O/C–N, and C=O, respectively. Similarly, [b-Ni_3ZnC@Ni-Zn-N-C] catalyst shared most of the XPS characteristics of [a-Ni_3ZnC@Ni-Zn-N-C], where N 1s spectra exhibit four peaks deconvoluted into 398.87, 400.91, 401.89, and 404.03 eV which could be ascribed to pyridinic-N, pyrrolic-N, graphitic-N, and N-oxidized as shown in **Figure 5.5d.** Ni 2p spectra reveal two peaks at 854.15 and 855.56 eV which could be attributed to

Ni^{d+} and Ni^{2+}, respectively. Zn 2p spectra show a major metallic Zn^0 peak at 1021.8 eV, while C 1s spectra represent three main peaks at 284.7, 285.6, and 287.6 eV, these peaks are assigned to C=C/C–C, O/C–N, and C=O, respectively **(Figure S2)**.

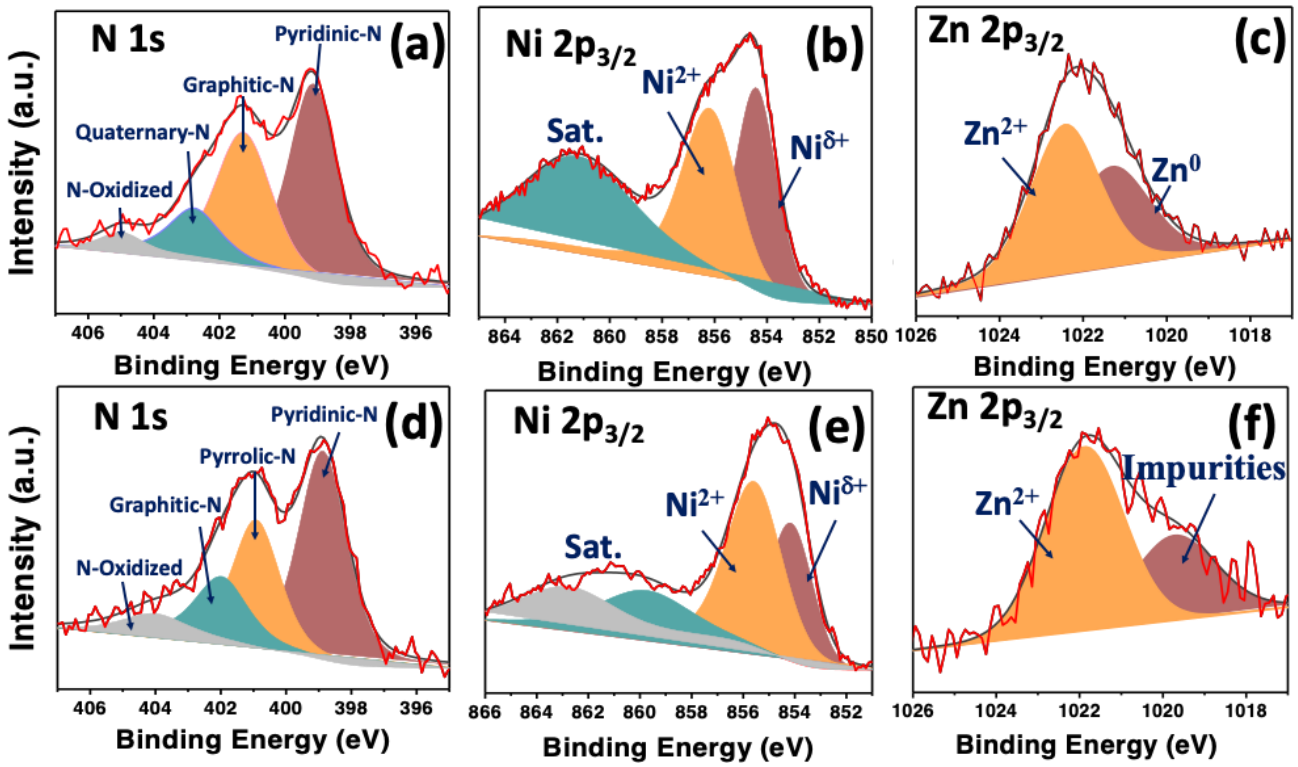

Figure 5-5 XPS spectra of [a-Ni_3ZnC@Ni-Zn-N-C]: (a) N 1s, (b) Ni $2p_{3/2}$, and (c) Zn $2p_{3/2}$, and [b-Ni_3ZnC@Ni-Zn-N-C]: (d) N 1s, (e) Ni $2p_{3/2}$, and (f) Zn $2p_{3/2}$.

5.4.2 Electrochemical Measurements and Electrode Engineering

The electrocatalytic performance of the synthesized catalyst designs has been investigated in CO_2R at industrially relevant reaction rates, all synthesized catalysts were integrated into gas diffusion electrodes (GDEs) and evaluated for CO_2R using a membrane electrode assembly (MEA) electrolyzer. GDE-driven CO_2R, whereby CO_2 molecules transfer through the GDE/catalyst interface and get reduced, is one of the most reliable and efficient CO_2R technologies that enable

higher electrocatalytic activity and selectivity compared to planar electrodes. As illustrated in **Figure 5.6a**, gas diffusion electrodes predominantly comprise a gas diffusion layer (GDL) which plays a significant role in gas permeability, the local environment around the catalyst, and the mass transport of products, reactants, and water from and to the catalyst layer.[60] GDEs are integrated into a membrane electrode assembly (MEA) electrolyzer with a zero-gap configuration **(Figure 5.6b)** to lower the ohmic resistance and enhance the reaction rates under CO_2R conditions. The ultimate electrocatalytic performance of GDEs during CO_2 electrolysis is governed by the catalyst structure/design, integration strategies, and local microenvironment that surrounds the catalytic interface. The microenvironment of the integrated GDE regulates most of the physical and electronic properties and GDE-driven CO_2R could be significantly enhanced by altering these properties.[60]

5.4.2.1 MEA Optimization and Validation for CO_2R

A systematic study has been carried out to optimize and validate the MEA electrolyzer before evaluating the prepared catalyst designs including the catalyst/GDL active area, loading, and deposition procedures. A homogenous catalyst design of atomically dispersed Ni–N–C catalyst developed and reported in our previous work[38] has been selected for this systematic study. Initially, the impact of altering the catalyst/GDE active area has been evaluated by the employment of different GDE configurations, whereby Ni–N–C catalyst ink was prepared and drop-casted on four different GDE active areas using a catalyst loading of $2mg/cm^2$. The selected active areas were a $5cm^2$ square-based configuration, $1cm^2$ square-based configuration, $1cm^2$ rectangle-based configuration, and $1cm^2$ catalyst active area integrated into a $5cm^2$ GDE, these configurations are denoted here as GDE–1, GDE–2, GDE–3, and GDE–4, respectively, and illustrated in **Figure 5.6c–f**. All developed GDE configurations have exhibited high selectivity towards CO production

at different reaction rates and certain limitations (**Figure S4a–c**). GDE–1 with a large active area has demonstrated 86% of CO FE and 150mA/cm^2 at 2.9V, and the MEA electrolyzer was stable during the course of the reaction. On the contrary, GDE–2 and –3 configurations with smaller active areas revealed lower activities compared to GDE–1, while the difference in geometry has not induced remarkable changes in the obtained activity. GDE–4 with a large GDE active area (5 cm^2) and smaller deposited catalyst area (1 cm^2) showed better electrocatalytic activity compared to the other configurations where ca. 90% CO FE was obtained and 210 mA/cm^2 at 2.7V. The improved electrocatalytic activities of GDE–1 could be speculated to the increased CO_2 mass transport through the carbon support, leading to achieving high conversion rates compared to smaller active areas with limited CO_2 mass transport. However, the higher catalytic activity of GDE–4 could be likely postulated to the elimination of the CO_2 mass transfer factor in which a large number of CO_2 molecules achieved the diffused active sites inside the 3-D carbon fibre-based GDE. Therefore, this configuration does not provide reliable and reflective insights into the real intrinsic activity of the integrated catalyst.

One of the common challenges of employing MEA technology in CO_2R is cathode flooding. At high current densities, water molecules penetrate the deposited catalyst layer on the GDE and consequently hinder the transfer of CO_2 molecules to the active sites. There are several factors that influence cathodic floodings such as the decomposition of GDL and the back diffusion of water molecules along with cations to the cathode. Further, we found that the active area employed has an indirect effect on the possibility of cathode flooding during CO_2R. GDEs with large active areas (GDE–1 and –4) have demonstrated a fairly stable system with no flooding observation, however, GDE–2 and –3 have experienced flooding, especially at high applied voltages. Using small active areas has affected the homogenous diffusion of the catalyst ink inside

the GDE and formed a non-homogenous catalyst layer which was detached from the GDL surface after a short time, leading to the decomposition of the GDE, also the agglomeration of a large number of the active sites has likely blocked many of them and decreased CO_2 mass transport during the reaction.

Another factor has been investigated by varying the catalyst loading (**Figure S4d–f**). GDE–2 configuration was selected to deposit three different catalyst loadings, that includes 1mg, 2mg, and 4mg/cm^2. Our findings revealed that increasing the catalyst loading would enhance the reaction rates towards CO production by introducing a high concentration of active sites. However, it was found that 2mg and 4mg/cm^2 catalyst loadings have resulted in cathode flooding at 2.9V and 2.5V, indicated by red and blue arrows, respectively, (**Figure S4e).** This could be likely attributed to the same observation of the aggregation of catalyst particles on the small active area, resulting in fast detachment of the catalyst layer. This consequently has hampered the further increase of catalyst loading using this GDE configuration. Therefore, varying the catalyst loading has revealed that GDE configurations with large active areas were found to provide a practical implementation of CO_2 electrolysis using MEA by affording a stable system with limited cathode floodings.

Further, the influence of the catalyst deposition method was evaluated by using drop-casting and spray gun methods. Our results showed that the deposition method has impacted the electrocatalytic activity. Using the spray gun method has led to a significant decrease in the electrocatalytic activity, suggesting that an amount of the catalyst ink has not been sprayed properly and got restricted inside the gun needles. As the gaseous phase products of CO and H_2 are being identified and quantified using a GC unit, it is very crucial to consider the GC capabilities and detection limits for both products. Although the utilization of GDE configurations with large

active areas has been proven in this study to provide an efficient and stable MEA system for CO_2 conversion to CO at high reaction rates. However, the GC capabilities could be challenging while producing high gaseous concentrations that exceed the GC detection limit. This could result in the imprecise quantification of these products along with limiting the further increase of catalyst loading and GDE active area.

5.4.2.2 CO_2 Electrolysis of the Developed Catalyst Designs

Following the optimization methods, a GDE configuration of 3.61 cm^2 and a catalyst loading of 4mg/cm^2 were selected to evaluate the newly developed catalysts using an MEA electrolyzer with 1M $KHCO_3$ anolyte circulation. The electrocatalytic performance of all materials prepared at different Ni^{2+}: Zn^{2+} atomic ratios and metal content is summarized in **Figure 5.7**. Initially, all developed materials exhibited the production of CO and H_2 under CO_2 electrolysis conditions, whereby a variety of different voltages in the range of 2.5V to 3.2V was applied. The obtained CO Faradaic efficiencies of each electrocatalyst are illustrated in **Figure 5.7a**, which reveals that [a-Ni_3ZnC@Ni-Zn-N-C] catalyst exhibited CO selectivity of 92% and 344 mA/cm^2 at 2.9V. While [b-Ni_3ZnC@Ni-Zn-N-C] catalyst showed CO FE of ca.100% and 448 mA/cm^2 at 3.1V. These activities are relatively higher than those resulted from the homogenous design of [a-Ni-Zn-N-C] and [b-Ni-Zn-N-C] catalysts which showed maximum CO FE of 88% and 66mA/cm^2 at 2.8V, and 90% CO FE and 165mA/cm^2 at 2.8V, respectively.

The improved electrocatalytic activity of the heterogenous design compared to the homogenous one could be speculated to the presence of Ni_3ZnC-based particles in the heterogenous design as confirmed by the PXRD (**Figure 5.4a,b**) and TEM/EDS measurements (**Figure 5.2a–d and Figure 5.3a, b**). The ability of Ni_3ZnC particles to catalyze CO_2 hydrogenation to CO has been recently discussed by Nagila et al who achieved 100% of CO

selectivity.[56] Therefore, we postulate that the presence of Ni_3ZnC particles in the structure has likely resulted in enhancing the reaction rates under CO_2 electrolysis conditions. To ensure this contribution of both Ni_3ZnC particles and the atomically dispersed Ni-Zn-N_X/C sites in the overall CO_2R performance, the best-performance sample [b-Ni_3ZnC@Ni-Zn-N-C] has been acid washed using (1M) HNO_3 and (4M) HCl. According to PXRD spectra in **Figure 5.4c,d**, the crystalline features of Ni_3ZnC remained after HNO_3 acid wash procedure, however, it could be observed that electrocatalytic performance of the same sample showed a substantial decrease in the activity and selectivity during CO_2R, achieving a maximum CO FE of 78% and 110 mA/cm^2 at 2.5V, suggesting that the acid treatment has leached out a large amount of the atomically dispersed dual Ni-Zn-N_X/C sites that contribute to the overall CO_2R performance. Similar performance observations were obtained when using HCl for acid washing – which has been proven to leach out the Ni_3ZnC particles as illustrated by PXRD spectra in **Figure 5.4c,d** – that showed a maximum CO selectivity of 87% at 280mA/cm^2 and 3V. These findings illustrate that the presence of both Ni_3ZnC sites and the atomically dispersed dual Ni-Zn-N_X/C sites has likely improved the electrocatalytic performance of this catalyst design. Further electrochemical impedance spectroscopy (EIS) Nyquist plot shown in **Figure 5.7d** illustrates that [b-Ni_3ZnC@Ni-Zn-N-C] catalyst exhibited smaller interfacial charge-transfer resistance (R_{CT}) with the value of 17.99Ω compared to [b-Ni-Zn-N-C] catalyst that has R_{CT} value of 53.45Ω. This suggests that the electron transfer kinetics of [b-Ni-Zn-N-C] catalyst design is relatively sluggish compared to [b-Ni_3ZnC@Ni-Zn-N-C] catalyst under CO_2R conditions. The electrochemical active surface area (ECSA) has been assessed on selected catalysts as shown in **Figure 5.7e**. The obtained results indicated that [b-Ni-Zn-N-C] catalyst has half value of [b-Ni_3ZnC@Ni-Zn-N-C], suggesting that the heterogeneous structure affords a higher number of active sites than the homogenous structure.

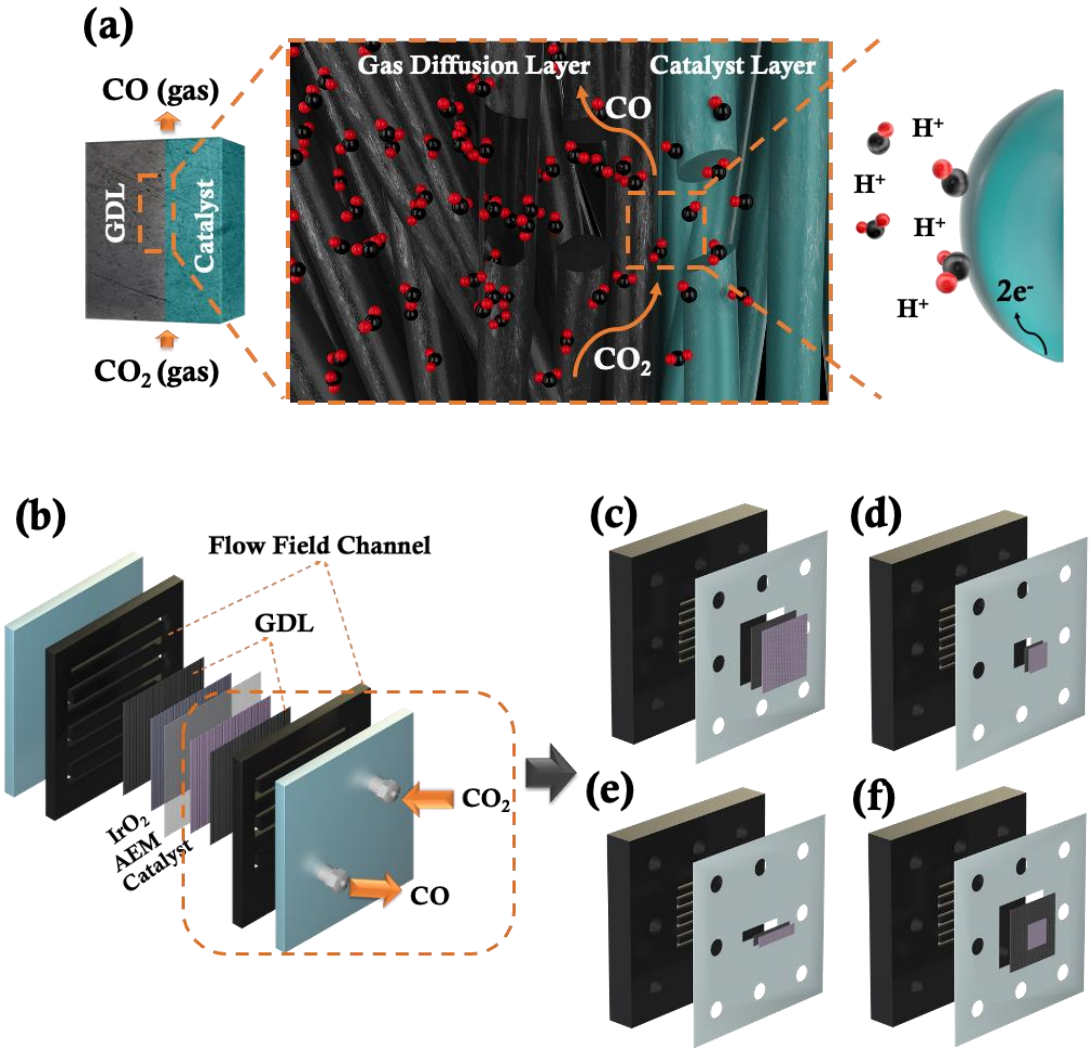

Figure 5-6 (a) a schematic diagram illustrates the GDE configuration with the integrated catalyst layer, (b) a schematic diagram shows the MEA cell components, (c–f) different GDE configurations: (c) GDE-1, (d) GDE-2, (e) GDE-3, and (f) GDE-4.

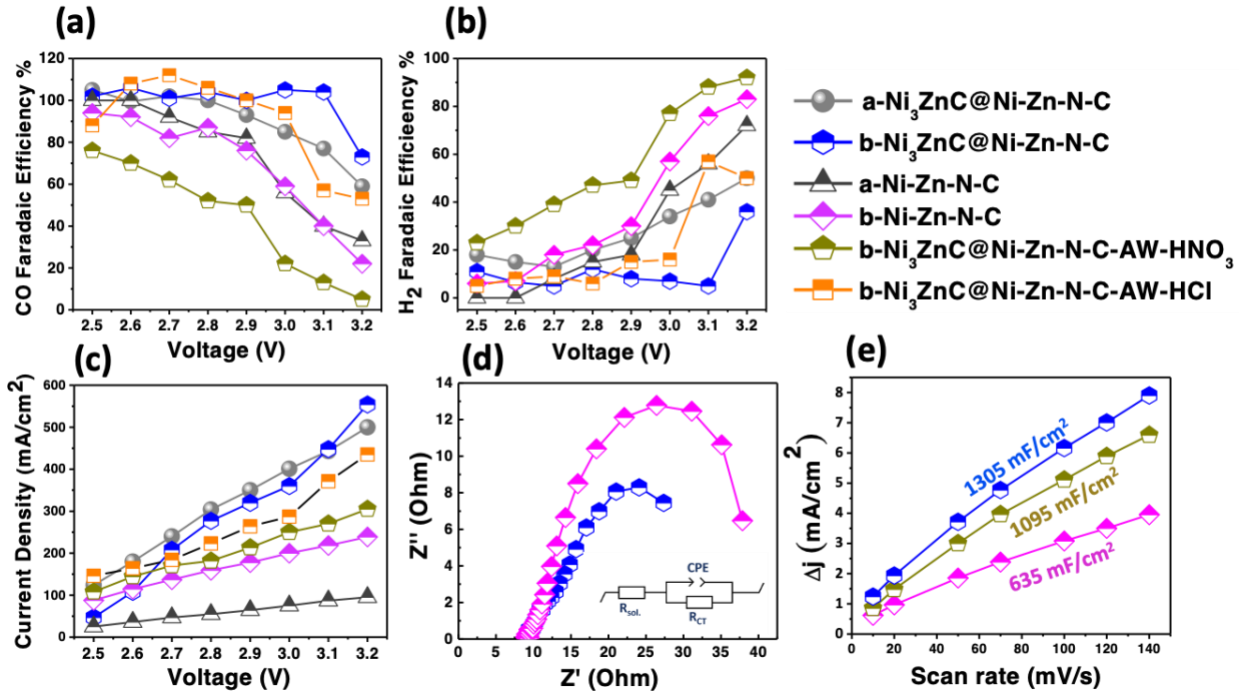

Figure 5-7 The electrochemical performance of the prepared catalysts; (a) and (b) show the Faradaic efficiency of CO and H_2, respectively, (c) the obtained total current densities of all catalysts, (d) EIS measurements of [b-Ni_3ZnC@Ni-Zn-N-C] and [b-Ni-Zn-N-C] catalysts., and (e) ECSA measurements of [b-Ni_3ZnC@Ni-Zn-N-C], [b-Ni_3ZnC@Ni-Zn-N-C-AW-HNO_3], and [b-Ni-Zn-N-C]

5.4.3 *Ex-situ* and *In-situ* XAS Measurements

In-situ and *ex-situ* XAS (EXAFS and XANES) measurements have been carried out to identify the local environment, coordination, and existing species in the developed catalyst designs. **Figure 5.8a,b** illustrates *ex-situ* XANES spectra of Ni K-edge of all developed catalysts along with different reference spectra of such as NiO, Ni–TPP and Ni foil. The obtained spectra revealed that the rising edges of all prepared catalysts (homogenous and heterogenous designs) are positioned between NiO and Ni foil, suggesting an intermediate valence state between +2 and +1 and presence of Ni moieties. The observations were also similar for Zn through Zn K-edge XANES **(Figure 5.8c and d)**, whereby the Zn K-edges of all catalysts are at an intermediate between ZnO and Zn foil references, emphasizing that Zn species with an oxidation state between +2 and +1 were

formed. Furthermore, e*x-situ* Ni K-edge FT-EXAFS spectra are shown in **Figure 5.8e**, a major peak at 1.72°A was observed in the four catalysts including the homogenous and heterogeneous catalyst structures; this peak could be likely attributed to the Ni–N coordination, while another characteristic peak is located at 2.2°A is appeared in all prepared catalysts is indicative of the presence of metallic Ni particles were generated along with Ni–N_X species. In the *ex-situ* Zn K-edge FT-EXAFS spectra, the presence of a peak positioned at 1.46°A of [a-Ni_3ZnC@Ni-Zn-N-C], [a-Ni-Zn-N-C], and [b-Ni-Zn-N-C] catalysts could be assigned to the Zn–N coordination. However, the peak intensity in [b-Ni_3ZnC@Ni-Zn-N-C] catalyst is lower than the other prepared catalysts, indicating that other Zn species are more dominant in this catalyst structure. Also, a sharp peak located at 2.3°A in the FT-EXAFS spectra of [b-Ni_3ZnC@Ni-Zn-N-C] catalyst spectra indicates that metallic Zn particles were formed in addition to Zn–N_X moieties. XANES Modelling and Linear combination fitting (LCF) on Ni K-edge XANES have been performed for all developed catalysts to identify the existing species and approximate their ratios in each catalyst structure. Five different models have been employed for LCF fitting, including metallic Ni, Ni-TPP(N_4), Ni_3ZnC, Ni-TPP(N_3), and Ni–Zn-TPP (**Figures S6a–e** and **S7a–e)**. LCF fitting parameters and weight distribution are included in **Table S1** where the presence of metallic Ni, Ni-TPP(N_3), Ni_3ZnC, and Ni–Zn-TPP species were identified in the four samples. The approximate concentration via LCF of these species was found to be varied in each catalyst composition. In the heterogeneous catalyst structures, Ni-Zn-TPP was dominating the [a-Ni_3ZnC@Ni-Zn-N-C] catalyst structure with 67.7 wt %, whereas metallic Ni was identified as a major component in [b-Ni_3ZnC@Ni-Zn-N-C] catalyst with 68 wt%. Ni–TPP(N_3) was identified as a minor component for both catalysts within the range of 8 wt% to 23 wt%. In the homogenous catalyst structures, Ni-Zn-TPP formed ~41 and 43 wt% in [a-Ni-Zn-N-C] and [b-Ni-Zn-N-C]

catalysts, respectively. While metallic Ni and Ni_3ZnC also co-existe with ~ 52 and 54 wt %, respectively. To obtain detailed information of the nature of the active sites, *in-situ* XANES and EXAFS measurements were performed on Ni K-edge of [a-Ni_3ZnC@Ni-Zn-N-C] catalyst under CO_2R conditions. Four different spectra were collected at different applied potentials including OCV, 2.5V, 2.7V, and 2.9V. *In-situ* XANES ,is illustrated in **Figure 11a**, for the Ni K-edge. XANES spectra at OCV reveal the absence of a pre-edge peak at 3338.7 eV which is characteristic for the symmetry of square planar D_{4th} of Ni sites. Also, a weak rising peak around ~8333.2 eV was observed which is postulated to be as a result of the transition of 1*s* to 3*d* transition. This dipole transition reveals that the geometry of the Ni sites is not centrosymmetric, and the Ni coordination of all developed catalysts is different from the Ni-TPP (Ni-N_4) fingerprint. Under CO_2 electrolysis and at 2.5V, the rising edge of OCV was shifted to a lower energy value, demonstrating that some of the Ni^{2+} species were reduced to lower valency such as Ni^{1+} which is active towards CO_2R. This shift was further increased by applying 2.7V indicating that Ni^{1+} moieties were continuously generated along the course of the reaction. However, at 2.9V the shift to lower energy has reached a point where metallic Ni rising edge could be observed, indicating that the Ni^{1+} species is further reduced to metallic Ni sites – which favors HER – at higher voltages. These observations are consistent and well-correlated with the obtained electrochemical CO_2R insights presented in **Figure 5.7** whereby a max CO FE was achieved at 2.9V and 344mA/cm^2, in which the Ni^{1+} species were active towards CO_2R. Ni K-edge FT-EXAFS spectra at OCV show two main peaks at 1.72°A and 2.3 °A, which could be likely assigned to Ni–N and Ni-Ni coordination.

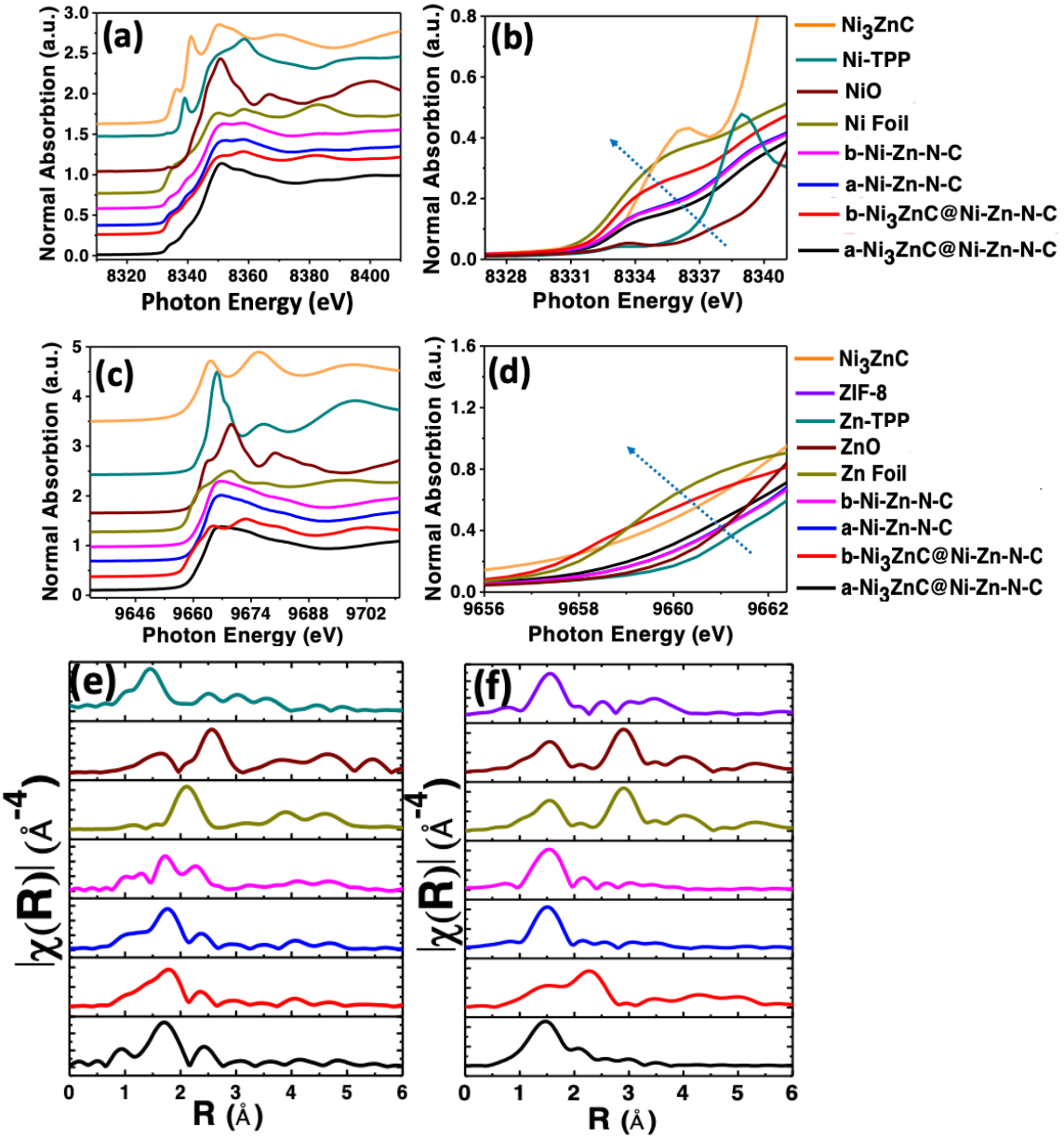

Figure 5-8 *Ex-situ* XAS measurements; (a,b) Ni K-edge XANES spectra, (c,d) Zn K-edge XANES spectra, (e) Ni, (f) Zn, k^3-weighted FT of EXAFS spectra of all prepared catalysts and references.

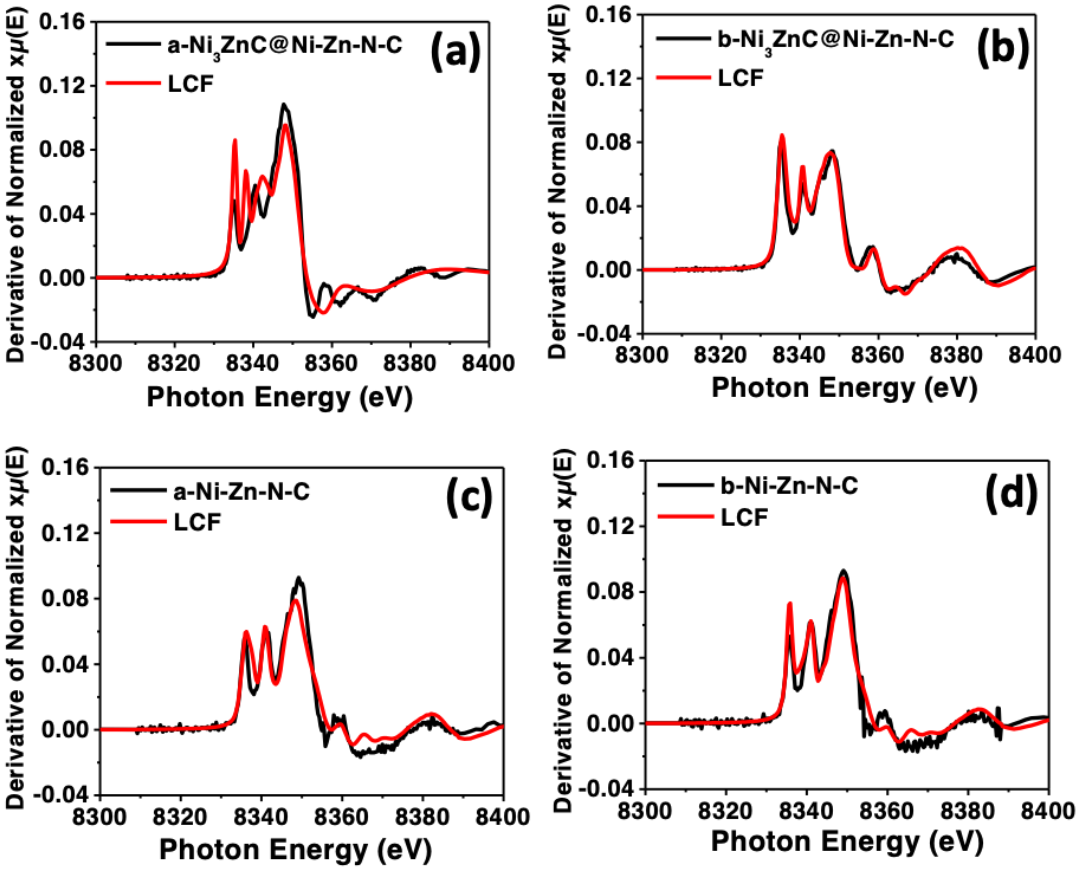

Figure 5-9 XANES 1st derivative modelling guided Ni K-edge LCF comparison between the experimental data of (a) [a-Ni_3ZnC@Ni-Zn-N-C], (b) [b-Ni_3ZnC@Ni-Zn-N-C], (c) [a-Ni-Zn-N-C], and (d) [b-Ni-Zn-N-C] and N_3-Ni-Zn-N_3 model.

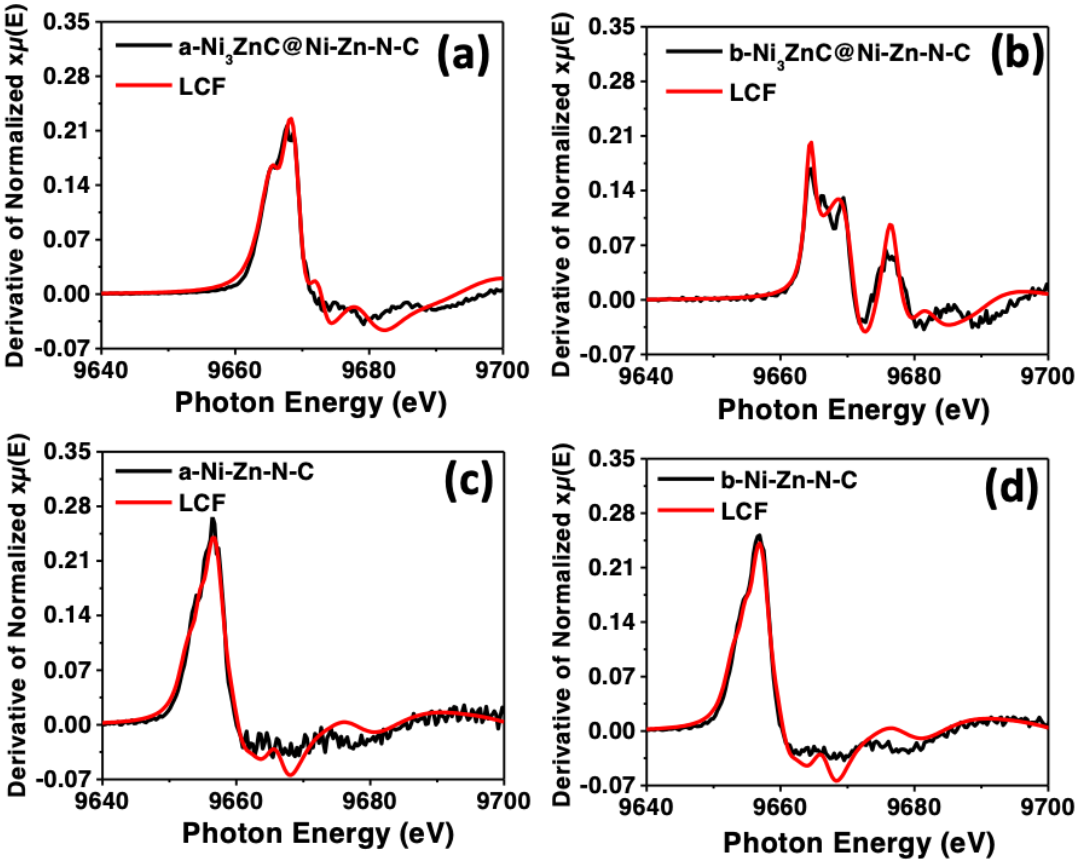

Figure 5-10 XANES 1st derivative modelling guided Zn K-edge LCF comparison between the experimental data of (a) [a-Ni_3ZnC@Ni-Zn-N-C], (b) [b-Ni_3ZnC@Ni-Zn-N-C], (c) [a-Ni-Zn-N-C], and (d) [b-Ni-Zn-N-C] and N_3-Ni-Zn-N_3 model.

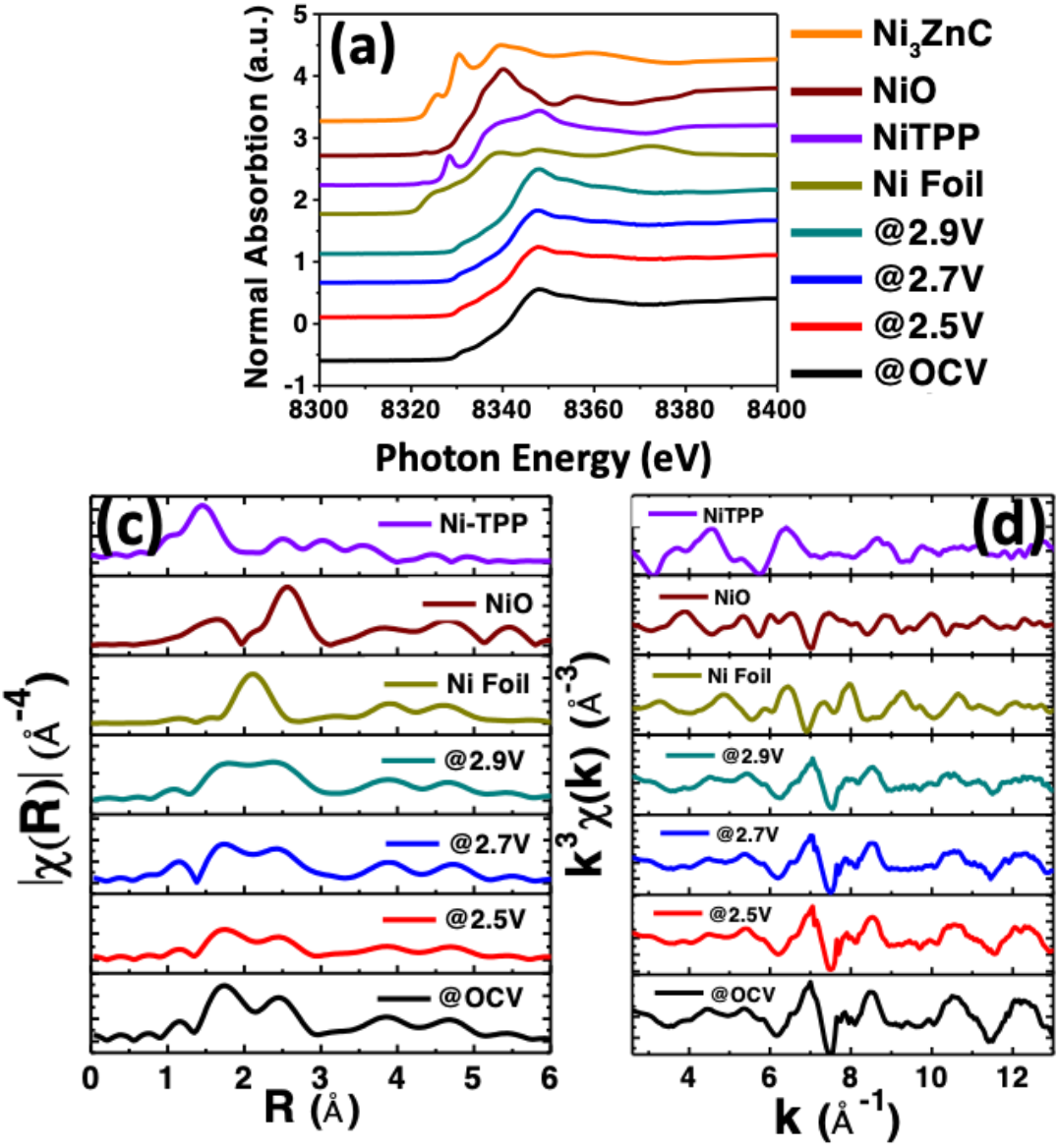

Figure 5-11 *In-situ* XAS measurements; (a,b) Ni K-edge XANES spectra, (c) Ni k^3-weighted FT of EXAFS spectra, and (d) *k*-space of [a-Ni_3ZnC@Ni-Zn-N-C] catalyst at different applied voltages and references under CO_2R conditions.

5.5 Conclusion

In conclusion, ZIF-8 nanoparticles were utilized to develop designs of electrocatalysts by introducing different synthetic conditions. This has resulted in generating various active site moieties that are able to produce CO during CO_2R. One developed design consists of homogenously distributed atomically dispersed dual Ni–Zn–N_X/C sites. Whereas the other catalyst design demonstrated a heterogenous structure of Ni_3ZnC-based particles and atomically dispersed dual Ni–Zn–N_X/C sites. Both electrocatalyst designs were integrated into a gas diffusion electrode (GDE) and evaluated for CO_2R using an MEA-based electrolyzer. Our findings exhibited that the co-existence of Ni_3ZnC and atomically dispersed dual Ni–Zn–N_X/C active sites in a heterogenous structure has boosted the electrocatalytic activity towards CO production, achieving 100% CO FE and 448 mA/cm^2 by using 3.1 cell voltage. Aside from the unique electrocatalytic performance, unveiling the nature of the active sites in the developed catalyst designs has been explored using *in-situ* and *ex-situ* X-ray absorption spectroscopy.

Supporting Information:

TEM images and EDS mapping, MEA configuration, XPS spectra, XAS spectra, and LCF spectra are included in the SI documents.

Acknowledgments

This research has been supported by Suncor Inc, the National Research Council of Canada (NRC) Materials for Clean Fuels Challenge Program and the Chemical Engineering Department at McMaster University. Electron microscopy analysis (TEM and EDS) has been performed at the Canadian Centre for Electron Microscopy (CCEM). Biointerfaces Institute (BI) at McMaster University has facilitated performing X-ray photoelectron spectroscopy analysis, while McMaster Analytical X-ray Diffraction center (MAX) has facilitated conducting X-ray diffraction measurements. Also, XAS measurements have been carried out in HXMA beamline at the Canadian Light Source, Saskatoon.

References

1. Chu, S.; Majumdar, A., Opportunities and challenges for a sustainable energy future. nature 2012, 488 (7411), 294-303.

2. Weber, R. S., Effective use of renewable electricity for making renewable fuels and chemicals. ACS Publications: 2018; Vol. 9, pp 946-950.

3. De Luna, P.; Hahn, C.; Higgins, D.; Jaffer, S. A.; Jaramillo, T. F.; Sargent, E. H., What would it take for renewably powered electrosynthesis to displace petrochemical processes? Science 2019, 364 (6438), eaav3506.

4. Hori, Y. i., Electrochemical CO_2 reduction on metal electrodes. Modern aspects of electrochemistry 2008, 89-189.

5. Gattrell, M.; Gupta, N.; Co, A., Electrochemical reduction of CO_2 to hydrocarbons to store renewable electrical energy and upgrade biogas. Energy conversion and Management 2007, 48 (4), 1255-1265.

6. Seh, Z. W.; Kibsgaard, J.; Dickens, C. F.; Chorkendorff, I.; Nørskov, J. K.; Jaramillo, T. F., Combining theory and experiment in electrocatalysis: Insights into materials design. Science 2017, 355 (6321), eaad4998.

7. Zhang, H.; Xu, H.; Li, Y.; Su, Y., Octahedral core–shell bimetallic catalysts M@ UIO-67 (M= Pt–Pd nanoparticles, Pt–Pd nanocages): metallic nanocages that enhanced CO_2 conversion. Applied Materials Today 2020, 19, 100609.

8. Ren, S.; Joulié, D.; Salvatore, D.; Torbensen, K.; Wang, M.; Robert, M.; Berlinguette, C. P., Molecular electrocatalysts can mediate fast, selective CO_2 reduction in a flow cell. Science 2019, 365 (6451), 367-369.

9. Gao, D.; Arán-Ais, R. M.; Jeon, H. S.; Roldan Cuenya, B., Rational catalyst and electrolyte design for CO_2 electroreduction towards multicarbon products. Nature Catalysis 2019, 2 (3), 198-210.

10. Peng, Y.; Wang, L.; Luo, Q.; Cao, Y.; Dai, Y.; Li, Z.; Li, H.; Zheng, X.; Yan, W.; Yang, J., Molecular-level insight into how hydroxyl groups boost catalytic activity in CO_2 hydrogenation into methanol. Chem 2018, 4 (3), 613-625.

11. Sheberla, D.; Bachman, J. C.; Elias, J. S.; Sun, C.-J.; Shao-Horn, Y.; Dincă, M., Conductive MOF electrodes for stable supercapacitors with high areal capacitance. Nature materials 2017, 16 (2), 220-224.

12. Meng, D. L.; Zhang, M. D.; Si, D. H.; Mao, M. J.; Hou, Y.; Huang, Y. B.; Cao, R., Highly selective tandem electroreduction of CO_2 to ethylene over atomically isolated nickel–nitrogen site/copper nanoparticle catalysts. Angewandte Chemie 2021, 133 (48), 25689-25696.

13. Mun, Y.; Lee, S.; Cho, A.; Kim, S.; Han, J. W.; Lee, J., Cu-Pd alloy nanoparticles as highly selective catalysts for efficient electrochemical reduction of CO_2 to CO. Applied Catalysis B: Environmental 2019, 246, 82-88.

14. Feng, J.; Gao, H.; Zheng, L.; Chen, Z.; Zeng, S.; Jiang, C.; Dong, H.; Liu, L.; Zhang, S.; Zhang, X., A Mn-N3 single-atom catalyst embedded in graphitic carbon nitride for efficient CO_2 electroreduction. Nature communications 2020, 11 (1), 4341.

15. Zhao, C.; Luo, G.; Liu, X.; Zhang, W.; Li, Z.; Xu, Q.; Zhang, Q.; Wang, H.; Li, D.; Zhou, F., In situ topotactic transformation of an interstitial alloy for CO electroreduction. Advanced materials 2020, 32 (39), 2002382.

16. Sun, X.; Lu, L.; Zhu, Q.; Wu, C.; Yang, D.; Chen, C.; Han, B., MoP nanoparticles supported on indium-doped porous carbon: outstanding catalysts for highly efficient CO_2 electroreduction. Angewandte Chemie International Edition 2018, 57 (9), 2427-2431.

17. Karapinar, D.; Creissen, C. E.; Rivera de la Cruz, J. G.; Schreiber, M. W.; Fontecave, M., Electrochemical CO_2 reduction to ethanol with copper-based catalysts. ACS Energy Letters 2021, 6 (2), 694-706.

18. Zheng, T.; Jiang, K.; Ta, N.; Hu, Y.; Zeng, J.; Liu, J.; Wang, H., Large-scale and highly selective CO_2 electrocatalytic reduction on nickel single-atom catalyst. Joule 2019, 3 (1), 265-278.

19. Zhao, C.; Wang, Y.; Li, Z.; Chen, W.; Xu, Q.; He, D.; Xi, D.; Zhang, Q.; Yuan, T.; Qu, Y., Solid-diffusion synthesis of single-atom catalysts directly from bulk metal for efficient CO2 reduction. Joule 2019, 3 (2), 584-594.

20. Jiao, L.; Zhu, J.; Zhang, Y.; Yang, W.; Zhou, S.; Li, A.; Xie, C.; Zheng, X.; Zhou, W.; Yu, S.-H., Non-bonding interaction of neighboring Fe and Ni single-atom pairs on MOF-derived N-doped carbon for enhanced CO_2 electroreduction. Journal of the American Chemical Society 2021, 143 (46), 19417-19424.

21. Yi, J. D.; Xie, R.; Xie, Z. L.; Chai, G. L.; Liu, T. F.; Chen, R. P.; Huang, Y. B.; Cao, R., Highly Selective CO_2 Electroreduction to CH_4 by In Situ Generated Cu_2O Single-Type Sites on a Conductive MOF: Stabilizing Key Intermediates with Hydrogen Bonding. Angewandte Chemie International Edition 2020, 59 (52), 23641-23648.

22. Zhang, M.-D.; Si, D.-H.; Yi, J.-D.; Yin, Q.; Huang, Y.-B.; Cao, R., Conductive phthalocyanine-based metal-organic framework as a highly efficient electrocatalyst for carbon dioxide reduction reaction. Science China Chemistry 2021, 64, 1332-1339.

23. Wei, S.; Zou, H.; Rong, W.; Zhang, F.; Ji, Y.; Duan, L., Conjugated nickel phthalocyanine polymer selectively catalyzes CO_2-to-CO conversion in a wide operating potential window. Applied Catalysis B: Environmental 2021, 284, 119739.

24. Zhu, W.; Kattel, S.; Jiao, F.; Chen, J. G., Shape-controlled CO_2 electrochemical reduction on nanosized Pd hydride cubes and octahedra. Advanced Energy Materials 2019, 9 (9), 1802840.

25. Wu, G.; More, K. L.; Johnston, C. M.; Zelenay, P., High-performance electrocatalysts for oxygen reduction derived from polyaniline, iron, and cobalt. Science 2011, 332 (6028), 443-447.

26. Choi, J.-Y.; Hsu, R. S.; Chen, Z., Highly active porous carbon-supported nonprecious metal− N electrocatalyst for oxygen reduction reaction in PEM fuel cells. The Journal of Physical Chemistry C 2010, 114 (17), 8048-8053.

27. Johnson, D.; Qiao, Z.; Djire, A., Progress and challenges of carbon dioxide reduction reaction on transition metal based electrocatalysts. ACS Applied Energy Materials 2021, 4 (9), 8661-8684.

28. Tylus, U.; Jia, Q.; Strickland, K.; Ramaswamy, N.; Serov, A.; Atanassov, P.; Mukerjee, S., Elucidating oxygen reduction active sites in pyrolyzed metal–nitrogen coordinated non-precious-metal electrocatalyst systems. The Journal of Physical Chemistry C 2014, 118 (17), 8999-9008.

29. Lefèvre, M.; Dodelet, J.; Bertrand, P., Molecular oxygen reduction in PEM fuel cells: evidence for the simultaneous presence of two active sites in Fe-based catalysts. The Journal of Physical Chemistry B 2002, 106 (34), 8705-8713.

30. Lefevre, M.; Dodelet, J.; Bertrand, P., Molecular oxygen reduction in PEM fuel cell conditions: ToF-SIMS analysis of Co-based electrocatalysts. The Journal of Physical Chemistry B 2005, 109 (35), 16718-16724.

31. Li, J.; Sougrati, M. T.; Zitolo, A.; Ablett, J. M.; Oğuz, I. C.; Mineva, T.; Matanovic, I.; Atanassov, P.; Huang, Y.; Zenyuk, I., Identification of durable and non-durable FeN x sites in Fe–N–C materials for proton exchange membrane fuel cells. Nature Catalysis 2021, 4 (1), 10-19.

32. Shi, Q.; Hwang, S.; Yang, H.; Ismail, F.; Su, D.; Higgins, D.; Wu, G., Supported and coordinated single metal site electrocatalysts. Materials Today 2020, 37, 93-111.

33. Chen, Z.; Higgins, D.; Yu, A.; Zhang, L.; Zhang, J., A review on non-precious metal electrocatalysts for PEM fuel cells. Energy & Environmental Science 2011, 4 (9), 3167-3192.

34. Koshy, D. M.; Landers, A. T.; Cullen, D. A.; Ievlev, A. V.; Meyer III, H. M.; Hahn, C.; Bao, Z.; Jaramillo, T. F., Direct characterization of atomically dispersed catalysts: nitrogen-coordinated Ni sites in carbon-based materials for CO2 electroreduction. Advanced Energy Materials 2020, 10 (39), 2001836.

35. Yang, R.-X.; Wang, Y.-R.; Gao, G.-K.; Chen, L.; Chen, Y.; Li, S.-L.; Lan, Y.-Q., Self-Assembly of Hydroxyl Metal–Organic Polyhedra and Polymer into Cu-Based Hollow Spheres for Product-Selective CO_2 Electroreduction. Small Structures 2021, 2 (7), 2100012.

36. Cai, G.; Yan, P.; Zhang, L.; Zhou, H.-C.; Jiang, H.-L., Metal–organic framework-based hierarchically porous materials: synthesis and applications. Chemical Reviews 2021, 121 (20), 12278-12326.

37. Wang, G.; Chen, J.; Ding, Y.; Cai, P.; Yi, L.; Li, Y.; Tu, C.; Hou, Y.; Wen, Z.; Dai, L., Electrocatalysis for CO_2 conversion: from fundamentals to value-added products. Chemical Society Reviews 2021, 50 (8), 4993-5061.

38. Ismail, F.; Abdellah, A.; Lee, H.-J.; Sudheeshkumar, V.; Alnoush, W.; Higgins, D. C., Impact of Nickel Content on the Structure and Electrochemical CO_2 Reduction Performance of Nickel–Nitrogen–Carbon Catalysts Derived from Zeolitic Imidazolate Frameworks. ACS Applied Energy Materials 2022, 5 (1), 430-439.

39. Ismail, F.; Abdellah, A.; Sudheeshkumar, V.; Rakhsha, A.; Chen, W.; Chen, N.; Higgins, D. C., Atomically Isolated Nickel–Nitrogen–Carbon Electrocatalysts Derived by the Utilization of Mg^{2+} ions as Spacers in Bimetallic Ni/Mg–Metal–Organic Framework Precursors for Boosting the Electroreduction of CO2. ACS Applied Energy Materials 2022, 5 (8), 9408-9417.

40. Hou, Y.; Liang, Y.-L.; Shi, P.-C.; Huang, Y.-B.; Cao, R., Atomically dispersed Ni species on N-doped carbon nanotubes for electroreduction of CO_2 with nearly 100% CO selectivity. Applied Catalysis B: Environmental 2020, 271, 118929.

41. Fan, Q.; Hou, P.; Choi, C.; Wu, T. S.; Hong, S.; Li, F.; Soo, Y. L.; Kang, P.; Jung, Y.; Sun, Z., Activation of Ni particles into single Ni–N atoms for efficient electrochemical reduction of CO_2. Advanced Energy Materials 2020, 10 (5), 1903068.

42. Kuang, M.; Guan, A.; Gu, Z.; Han, P.; Qian, L.; Zheng, G., Enhanced N-doping in mesoporous carbon for efficient electrocatalytic CO_2 conversion. Nano Research 2019, 12, 2324-2329.

43. Tang, S.-F.; Lu, X.-L.; Zhang, C.; Wei, Z.-W.; Si, R.; Lu, T.-B., Decorating graphdiyne on ultrathin bismuth subcarbonate nanosheets to promote CO_2 electroreduction to formate. Science Bulletin 2021, 66 (15), 1533-1541.

44. Zhao, C.; Dai, X.; Yao, T.; Chen, W.; Wang, X.; Wang, J.; Yang, J.; Wei, S.; Wu, Y.; Li, Y., Ionic exchange of metal–organic frameworks to access single nickel sites for efficient electroreduction of CO_2. Journal of the American Chemical Society 2017, 139 (24), 8078-8081.

45. Li, Y.; Adli, N. M.; Shan, W.; Wang, M.; Zachman, M. J.; Hwang, S.; Tabassum, H.; Karakalos, S.; Feng, Z.; Wang, G., Atomically dispersed single Ni site catalysts for high-efficiency CO_2 electroreduction at industrial-level current densities. Energy & Environmental Science 2022, 15 (5), 2108-2119.

46. Pei, J.; Wang, T.; Sui, R.; Zhang, X.; Zhou, D.; Qin, F.; Zhao, X.; Liu, Q.; Yan, W.; Dong, J., N-Bridged Co–N–Ni: new bimetallic sites for promoting electrochemical CO_2 reduction. Energy & Environmental Science 2021, 14 (5), 3019-3028.

47. Li, Y.; Shan, W.; Zachman, M. J.; Wang, M.; Hwang, S.; Tabassum, H.; Yang, J.; Yang, X.; Karakalos, S.; Feng, Z., Atomically dispersed dual-metal site catalysts for enhanced CO_2 reduction: mechanistic insight into active site structures. Angewandte Chemie International Edition 2022, 61 (28), e202205632.

48. Qiao, Z.; Wang, C.; Li, C.; Zeng, Y.; Hwang, S.; Li, B.; Karakalos, S.; Park, J.; Kropf, A. J.; Wegener, E. C., Atomically dispersed single iron sites for promoting Pt and Pt_3 Co fuel cell catalysts: performance and durability improvements. Energy & Environmental Science 2021, 14 (9), 4948-4960

49. Li, X.; He, Y.; Cheng, S.; Li, B.; Zeng, Y.; Xie, Z.; Meng, Q.; Ma, L.; Kisslinger, K.; Tong, X., Atomic Structure Evolution of Pt–Co Binary Catalysts: Single Metal Sites versus Intermetallic Nanocrystals. Advanced Materials 2021, 33 (48), 2106371.

50. Chen, Z.; Liao, X.; Sun, C.; Zhao, K.; Ye, D.; Li, J.; Wu, G.; Fang, J.; Zhao, H.; Zhang, J., Enhanced performance of atomically dispersed dual-site Fe-Mn electrocatalysts through cascade reaction mechanism. Applied Catalysis B: Environmental 2021, 288, 120021.

51. Li, Y.; Wei, B.; Zhu, M.; Chen, J.; Jiang, Q.; Yang, B.; Hou, Y.; Lei, L.; Li, Z.; Zhang, R., Synergistic effect of atomically dispersed Ni–Zn pair sites for enhanced CO_2 electroreduction. Advanced Materials 2021, 33 (41), 2102212.

52. Cable, R. E.; Schaak, R. E., Solution synthesis of nanocrystalline M− Zn (M= Pd, Au, Cu) intermetallic compounds via chemical conversion of metal nanoparticle precursors. Chemistry of materials 2007, 19 (16), 4098-4104.

53. Yang, Y.; Wei, M., Intermetallic compound catalysts: Synthetic scheme, structure characterization and catalytic application. Journal of Materials Chemistry A 2020, 8 (5), 2207-2221.

54. Qi, Z.; Pei, Y.; Goh, T. W.; Wang, Z.; Li, X.; Lowe, M.; Maligal-Ganesh, R. V.; Huang, W., Conversion of confined metal@ ZIF-8 structures to intermetallic nanoparticles supported on nitrogen-doped carbon for electrocatalysis. Nano Research 2018, 11, 3469-3479.

55. Xue, Y.; Li, H.; Ye, X.; Yang, S.; Zheng, Z.; Han, X.; Zhang, X.; Chen, L.; Xie, Z.; Kuang, Q., N-doped carbon shell encapsulated PtZn intermetallic nanoparticles as highly efficient catalysts for fuel cells. Nano Research 2019, 12, 2490-2497.

56. Maluf, N. E.; Braga, A. H.; Gothe, M. L.; Borges, L. R.; Alves, G. A.; Gonçalves, R. V.; Szanyi, J.; Vidinha, P.; Rossi, L. M., Zeolitic-Imidazolate Framework Derived Intermetallic Nickel Zinc Carbide Material as a Selective Catalyst for CO_2 to CO Reduction at High Pressure. European Journal of Inorganic Chemistry 2021, 2021 (44), 4521-4529.

57. Chen, B.; Yang, Z.; Zhu, Y.; Xia, Y., Zeolitic imidazolate framework materials: recent progress in synthesis and applications. Journal of Materials Chemistry A 2014, 2 (40), 16811-16831.

58. Huang, X. C.; Lin, Y. Y.; Zhang, J. P.; Chen, X. M., Ligand-directed strategy for zeolite-type metal–organic frameworks: zinc (II) imidazolates with unusual zeolitic topologies. Angewandte Chemie International Edition 2006, 45 (10), 1557-1559.

59. Sengupta, J.; Jacob, C., The effect of Fe and Ni catalysts on the growth of multiwalled carbon nanotubes using chemical vapor deposition. Journal of Nanoparticle Research 2010, 12, 457-465.

60. Wakerley, D.; Lamaison, S.; Wicks, J.; Clemens, A.; Feaster, J.; Corral, D.; Jaffer, S. A.; Sarkar, A.; Fontecave, M.; Duoss, E. B., Gas diffusion electrodes, reactor designs and key metrics of low-temperature CO_2 electrolysers. Nature Energy 2022, 7 (2), 130-143.

Unravelling the Nature of Active Sites in Metal-Organic Framework-derived Heterogenous Electrocatalysts for Boosting the Electroreduction of CO_2 to CO at Industrially Relevant Current Densities

Fatma Ismail[a], Ahmed Abdellah[b], Wajdi Alnoush[c], Shunquan Tan, Kholoud Abousalem, Amirhossein Rakhsha[d], Ning Chen[e*], Drew C. Higgins[h*]

5.6 Supporting Information

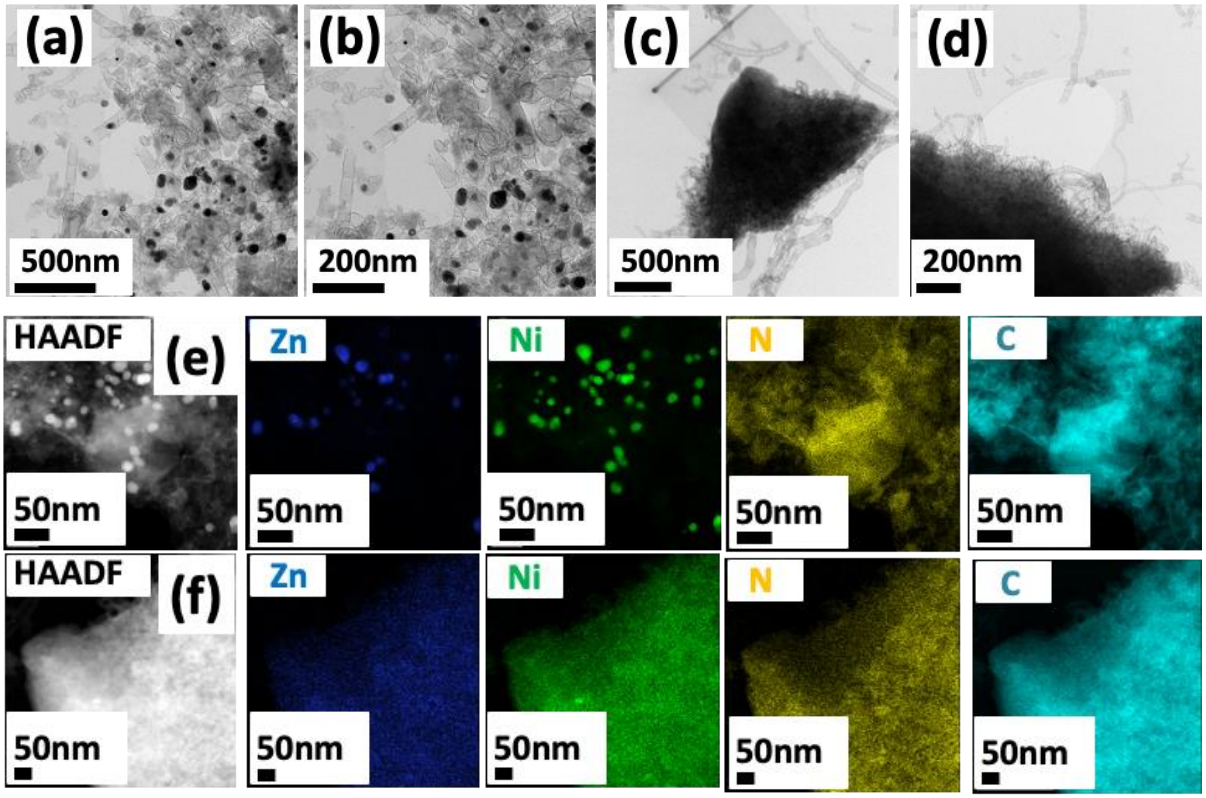

Figure S1. TEM images and EDS elemental mapping of [b Ni_3ZnC@Ni-Zn-N-C] after acid wash using (a, b, and e) nitric acid and (c, d, and f) hydrochloric acid

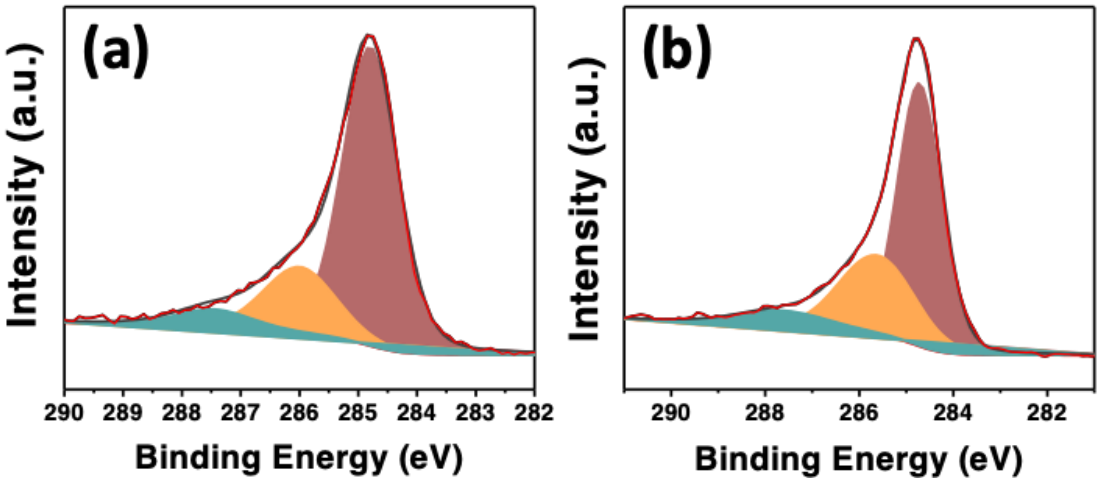

Figure S2. XPS spectra of C 1s of (a) [a-Ni_3ZnC@Ni-Zn-N-C] and (b) [b-Ni_3ZnC@Ni-Zn-N-C]

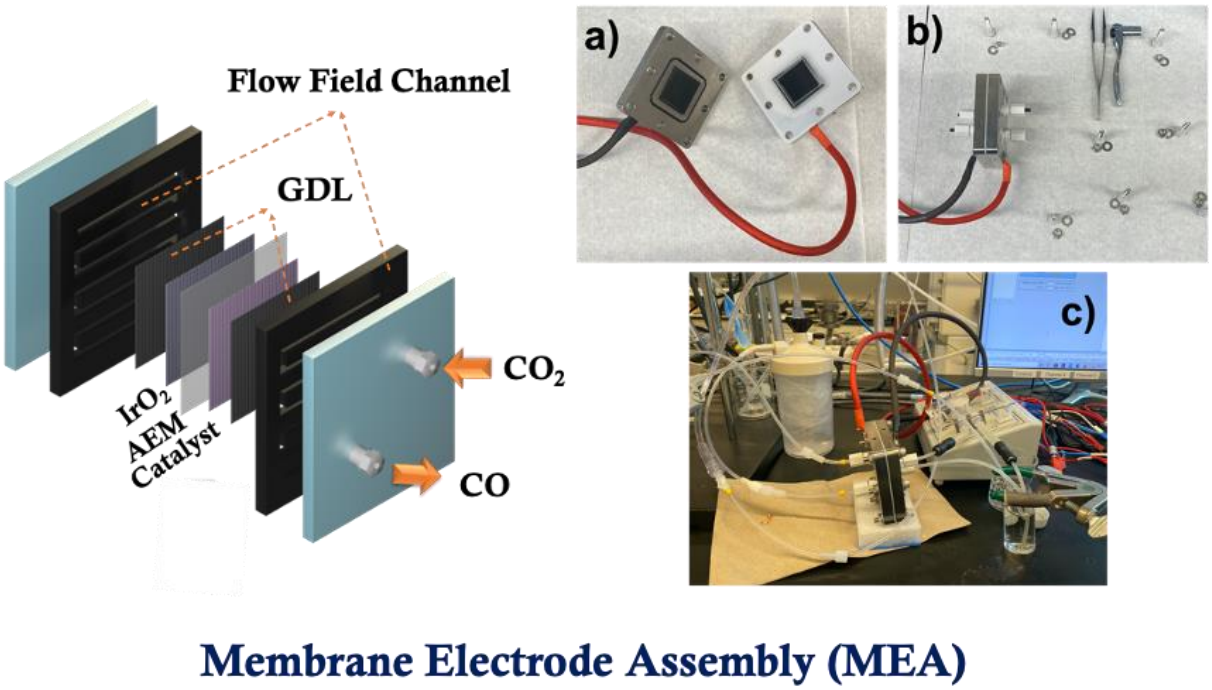

Figure S3. Membrane electrode assembly (MEA) electrolyzer: the left schematic illustrates the MEA configuration, and the right images show the lab-based MEA setup used in CO_2 electrolysis.

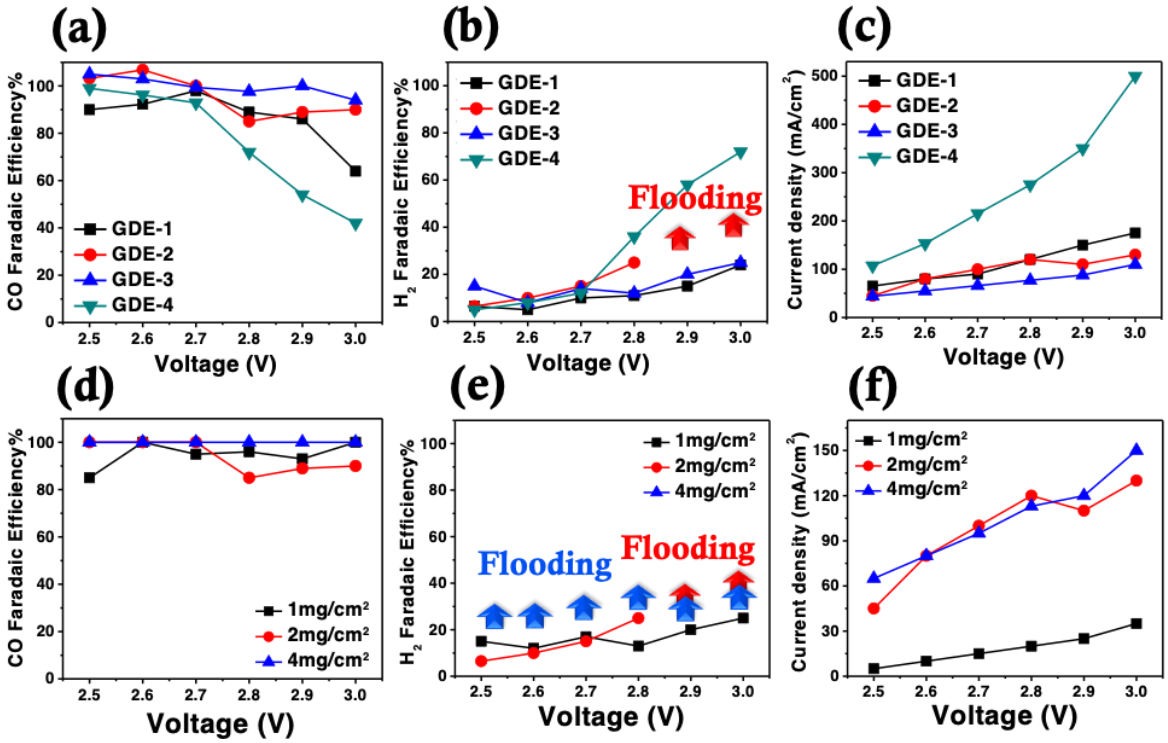

Figure S4. Electrochemical performance during CO_2R using different reaction factors for optimizing MEA setup: (a) CO FE %, (b) H_2 FE %, (c) current density (mA/cm^2) at different applied voltages of various GDE configurations using 2mg/cm^2 catalyst loading. (d) CO FE %, (e) H_2 FE %, (f) current density (mA/cm^2) at different applied voltages of different catalyst loading using GDE-2 configuration.

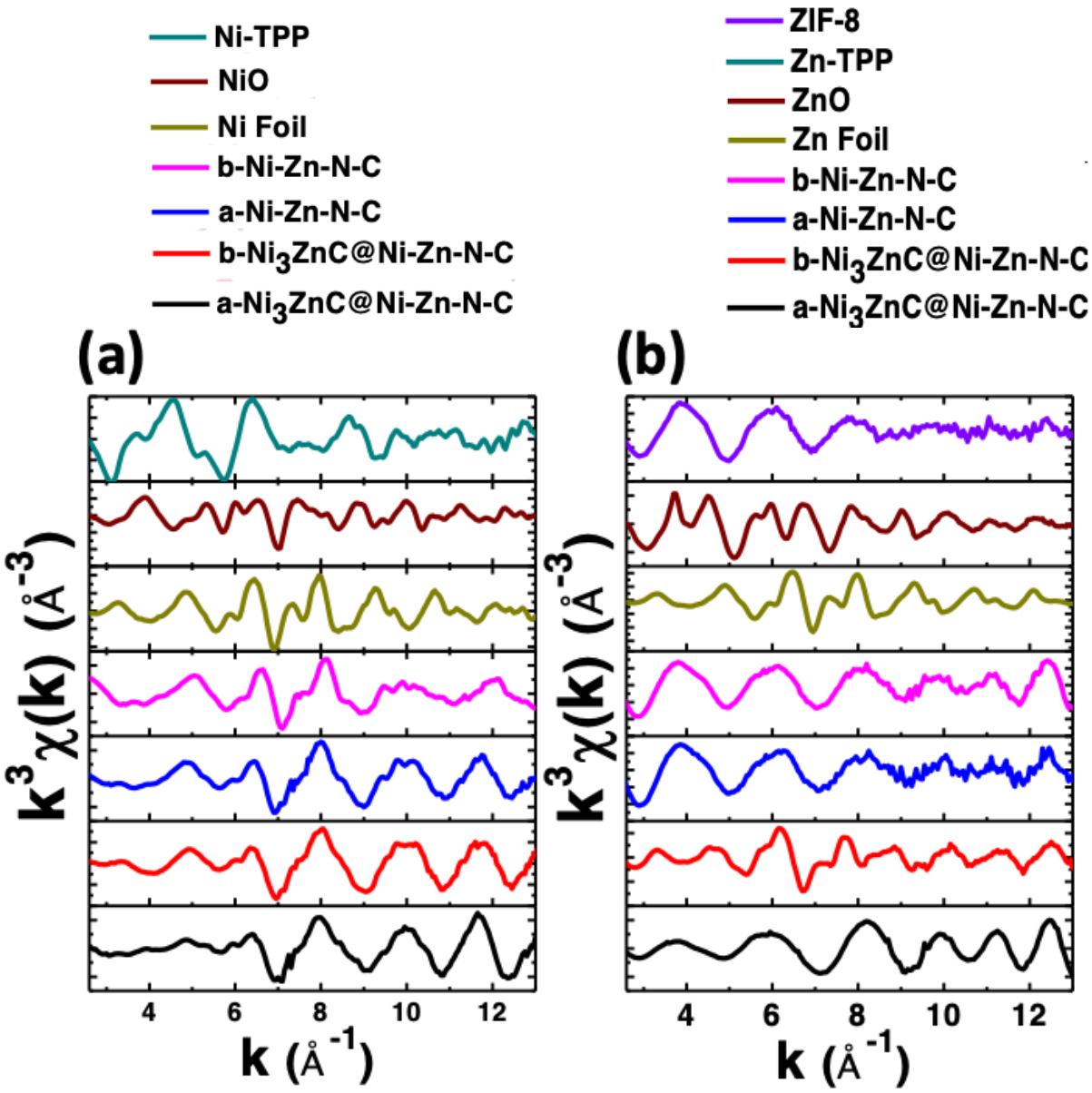

Figure S5. (a) Ni, (b) Zn *k*-space (k^3-weighted) of all developed catalysts and references.

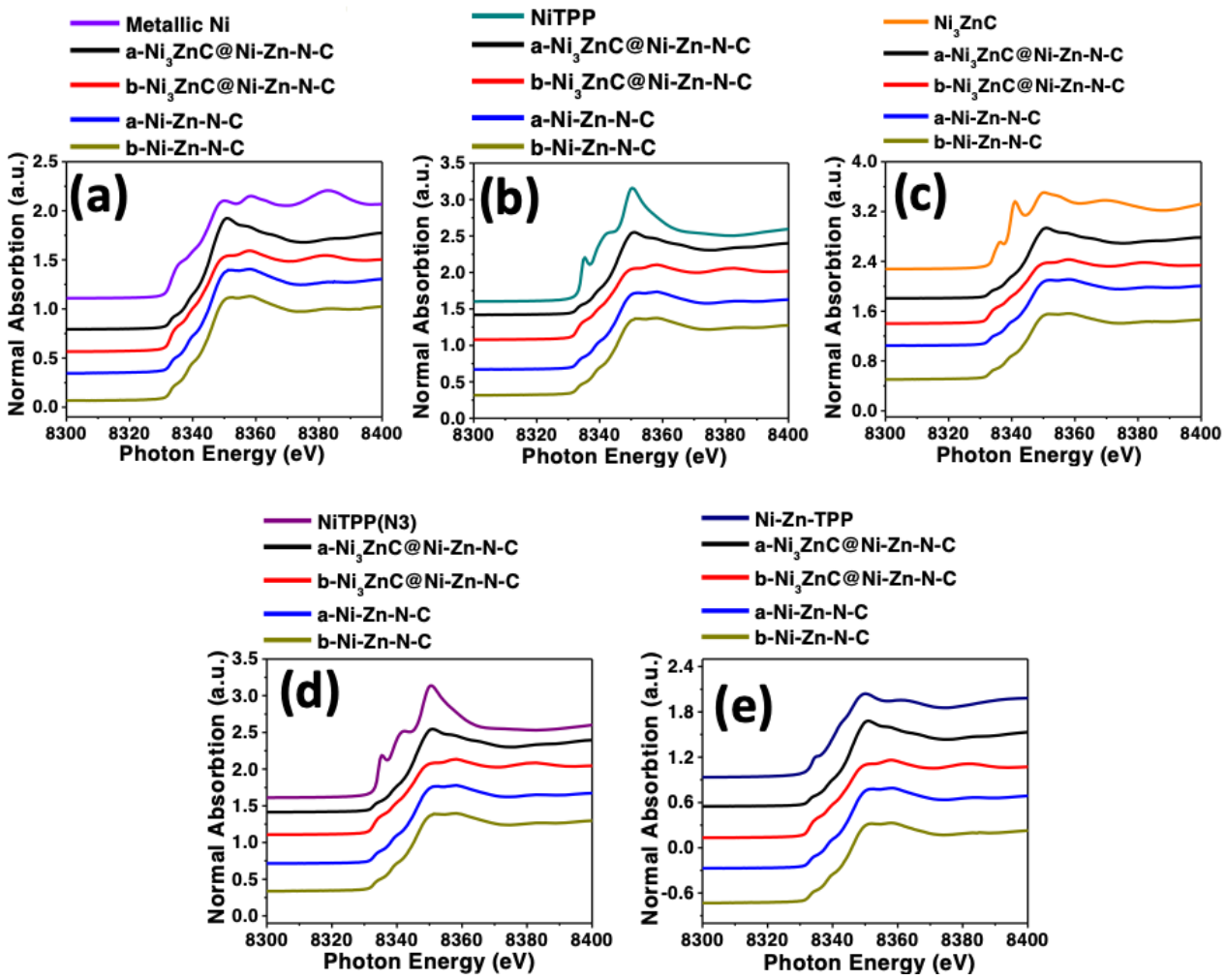

Figure S6 XANES modelling guided Ni K-edge LCF analysis of (a) metallic Ni, (b) Ni-TPP(N_4), (c) Ni_3ZNC, (d) Ni-TPP(N_3), and (e) Ni-Zn-TPP with the developed catalyst structures

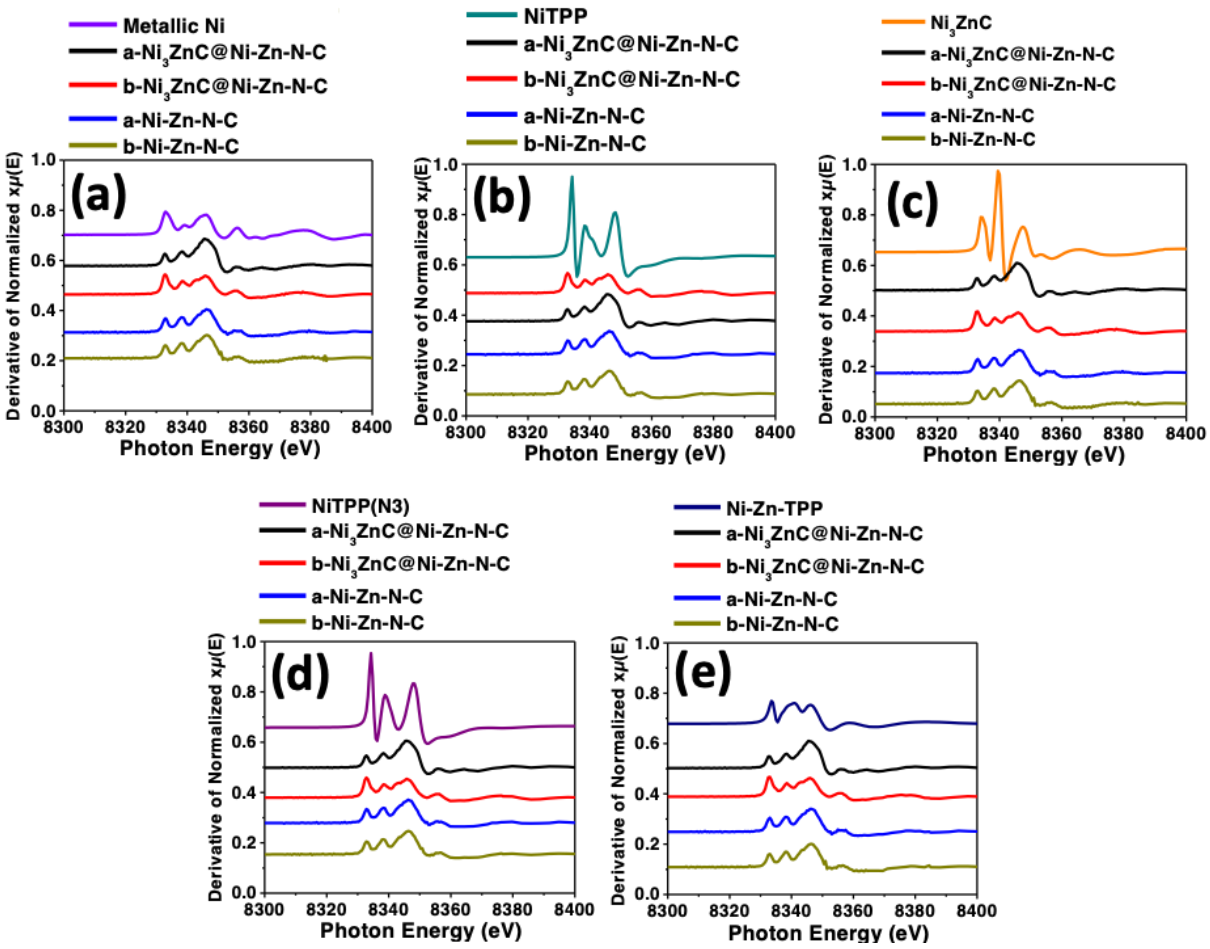

Figure S7 XANES 1st derivative modelling guided Ni K-edge LCF analysis of (a) metallic Ni, (b) Ni-TPP(N4), (c) Ni_3ZNC, (d) Ni-TPP(N_3), and (e) Ni-Zn-TPP with the developed catalyst structures.

Table 5.1 XANES 1st derivative modelling guided Ni K-edge LCF parameters

	a-Ni_3ZnC@Ni-Zn-N-C		**b-Ni_3ZnC@Ni-Zn-N-C**		**a-Ni-Zn-N-C**		**b-Ni-Zn-N-C**	
Standards	Weight	E0	Weight	E0	Weight	E0	Weight	E0
Ni Metal			0.684	0.0	0.536	0.2	0.541	0.7
Ni-TPP								
NiTPP (N_3)	0.237	-1.3	0.087	3.9				
Ni_3ZnC	0.085	5.8			0.054	-0.9		
N_3-Ni-Zn-N_3	0.677	2.0	0.229	-0.5	0.410	4.0	0.436	4.6
R-factor	0.1		0.03		0.06		0.05	

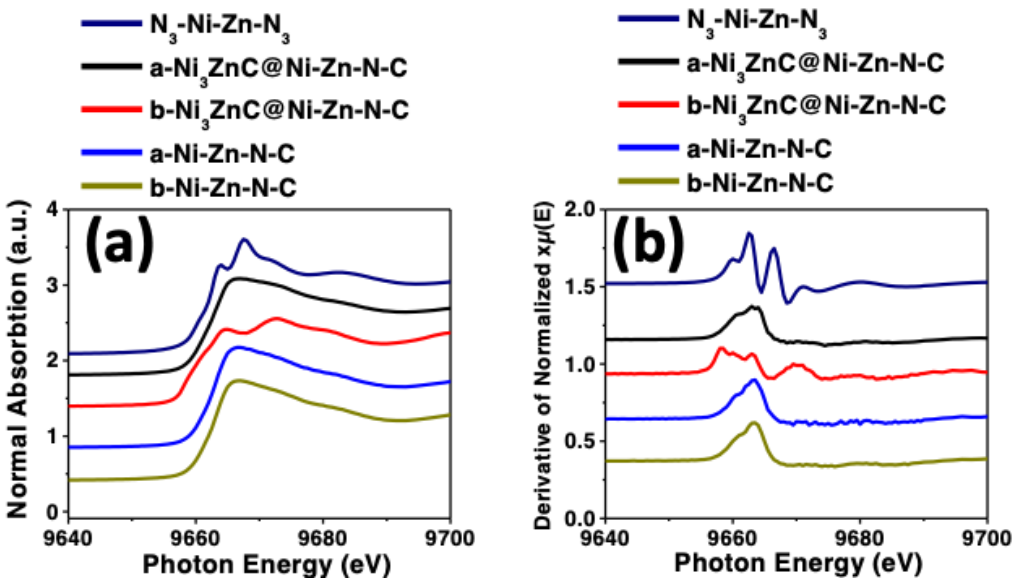

Figure S8 (a) XANES, (b) XANES1st derivative modelling guided Zn K-edge LCF analysis of all prepared catalysts and Ni-Zn-TPP model.

Table S 5.2 XANES 1st derivative modelling guided Zn K-edge LCF parameters.

	a-Ni_3ZnC@Ni-Zn-N-C		**b-Ni_3ZnC@Ni-Zn-N-C**		**a-Ni-Zn-N-C**		**b-Ni-Zn-N-C**	
Standards	Weight	E0	Weight	E0	Weight	E0	Weight	E0
Zn Metal			0.503	-2.8	0.27	0.2	0.25	0.2
Zn-TPP								
Zn-TPP (N_3)	0.541	-0.1			0.600	-0.9		
Ni_3ZnC	0.336	-0.3	0.293	0.9	0.144	9.5	0.145	9.7
N_3-Ni-Zn-N_3	0.123	1.2	0.204	6.4				
R-factor	0.05		0.09		0.05		0.04	

6 Chapter | Conclusions and Outlook

In this PhD thesis, our research goals focused on developing new catalyst designs for the efficient CO_2 electroreduction along with integrating them into an industrially competitive system such as MEA. M–N–C, more specifically, Ni–N–C catalysts and intermetallic carbides were prepared by the employment of MOF structures as a platform. The main findings of this thesis have been divided into three chapters starting with Chapter 3.

In chapter 3, the utilization of N-based MOF structure (ZIF-8) to produce atomically dispersed Ni–N_X sites has been investigated, the main obtained insights are concluded as follows:

- The co-pyrolysis of ZIF-8 impregnated with Ni salt at elevated temperatures has generated a catalyst structure of atomically isolated Ni-N_X sites through an ionic exchange process.
- A series of Ni–N–C catalysts have been prepared by varying the Ni^{2+}: Zn^{2+} atomic ratios, which include 0.5:1, 1:1, 2:1, and 3:1.
- The lower Ni contents in 0.5:1 and 1:1 Ni^{2+}: Zn^{2+} atomic ratios were demonstrated to assist in generating atomically isolated Ni–N_X sites, whilst higher Ni contents have produced Ni-based nano/microparticles.
- Under CO_2R conditions, the developed atomically dispersed Ni–N–C catalysts exhibited excellent CO selectivity (ca.99% FE) at low applied potential –0.68 V vs RHE. On the contrary, catalysts that contain a large portion of metallic Ni particles have directed the selectivity towards the competing HER.

In Chapter 4, another MOF topology (MOF-74) was used to prepare Ni–N–C catalysts. This MOF structure is constructed from non-N-based building blocks coordinated directly to Ni clusters. Our findings are concluded as follows:

- MOF-74 precursor has been successfully used to produce atomically dispersed Ni–N_X sites by urea impregnation as a N source and using Mg^{2+} ions as spacers.
- The direct pyrolysis of Ni-MOF-74 impregnated with urea has resulted in the formation of metallic Ni particles which favors the competing HER.
- The utilization of another metal ion (Mg^{2+}) as a spacer has increased the distance between the neighbouring Ni sites and assisted in the formation of Ni–N_X sites.
- The influence of the pyrolysis temperature has been also investigated, higher temperatures (e.g., 900°C) have enhanced the generation of Ni–N_X sites while using lower temperatures (e.g., 700°C) has formed Ni-based particles.
- The developed Ni–N–C catalyst demonstrated high CO selectivity during CO_2R, which achieved 90% FE at –0.76 V vs RHE.

In Chapter 5, ZIF-8 nanoparticles impregnated with Ni have been further employed to develop other catalyst designs, the main resulted insights are concluded in the following points:

- At high pyrolysis temperatures, during synthesis, the atomic ratio of Ni^{2+}: Zn^{2+} ions and the metal content have significantly influenced the structure-property relationship of the developed catalysts.
- During synthesis, introducing excess of Zn^{2+} atomic ratio over Ni^{2+} along with the utilization of low metal (Ni and Zn) concentrations has generated a homogenous structure of atomically dispersed dual Ni-Zn-N_X/C sites.
- Using high metal loadings under similar synthetic conditions has led to the formation of a heterogeneous structure of atomically dispersed dual Ni-Zn-N_X/C sites along with Ni_3ZnC-based particles.

- Both catalyst designs have been investigated for CO_2 electroreduction using a membrane electrode assembly (MEA)-type electrolyzer and exhibited over 90% CO Faradaic efficiency at different current densities/reaction rates.
- The heterogeneous catalyst design revealed higher activity towards CO production under CO_2R conditions, attaining a current density of 448mA/cm^2 at 3.1V.
- *In-situ* and *ex-situ* X-ray absorption spectroscopy measurements were performed to unravel the nature of the evolved active sites under CO_2R conditions
- XAS measurements demonstrated that both atomically dispersed dual Ni-Zn-N_X/C sites and Ni_3ZnC particles are contributing to the overall activity during CO_2R.

While the focus of this thesis is developing efficient electrocatalysts for converting CO_2 to CO, the further employment of the produced CO to generate C_{2+} products could be outlined in the next steps of this research. Cu-based electrocatalysts are still the main ones that can reduce CO_2 at high Faradaic efficiency into C^{2+} chemicals despite all previous investigations. Various methodologies have been followed to increase the selectivity of the Cu-based catalyst towards C_{2+} products, that includes, modulating the composition of the Cu surface, exposing the preferred facets, inducing grain boundaries by the crystal structure modifications and finally, developing Cu-based alloys with other metals. Compared to the commercial Cu electrocatalyst such as Cu nanoparticles, most of the previously mentioned efforts have developed catalysts with low selectivity toward some C_{2+} chemicals including ethanol and ethylene. To achieve the industrial level of selectivity of these products and maintain high energy efficiency values, developing novel designs for electrodes and catalysts is required. Therefore, various attempts could be performed in the next steps of this PhD research, which includes the following stages:

Stage 1: Catalyst design and MEA integration:

Using the outcomes of this PhD thesis, the developed Ni-based catalysts with different structures and active sites could be utilized to design a tandem catalyst structure that couples Ni-based active sites (either Ni_3ZnC or Ni-Zn-N-C) and Cu-based active sites. To initiate, the following experimental steps could be performed:

- Prepare both homogenous and heterogeneous Ni-based catalysts, and validate the prepared structure for producing CO during CO_2 electrolysis using an MEA-based electrolyzer.
- Prepare ink solutions using the homogenous or heterogenous catalyst structures using the methods mentioned in this thesis.
- Spray-coat the prepared ink on a pure Cu-based substrate.
- Vary the Ni-catalyst loading on the Cu electrode surface starting from a low loading (0.1 mg/cm^2) to a high loading ($1mg/cm^2$).
- Prepare other ink solutions that comprise both Ni-catalyst and Cu nanoparticles with different Ni: Cu weight ratios.
- Spray-coat the mixture ink with different Ni: Cu rations on a carbon fiber electrode.
- Evaluate the prepared electrodes with different methods for CO_2 electrolysis using MEA configuration.
- Optimize the catalyst integration until obtaining high selectivity toward C_{2+} products.

Following this optimization and validation procedures, a catalyst design could be developed by the integration of Cu sites during the synthesis of the different Ni-catalysts, this could be performed by the thermal treatment of a precursor that contains both Ni and Cu sites, for example, H-KUST-1 MOF impregnated with Ni salts.

Stage 2: Operando measurements of the developed tandem catalysts using X-ray absorption spectroscopy:

Unveiling the nature of active sites and mechanistic pathways under operational conditions would enable producing a performance descriptor of catalyst design, which could facilitate the development of stable and efficient CO_2R technology. To investigate the mechanistic pathways of CO_2 electrolysis of the developed tandem catalysts under reaction conditions, XAS technique is a powerful tool that can provide detailed insights on the electronic configuration of the evolved active sites and the local coordination environment during CO_2 electrolysis. These measurements could be carried out in a synchrotron-based facility (e.g., Canadian Light Source). This experiment would require an MEA electrolyzer that enables the absorption of X-ray beams, therefore, a modification of the commercially available MEA electrolyzer components should be done by replacing the stainless-steel plates with graphite ones. To perform these measurements, the following experimental steps should be carried out in a synchrotron facility:

- Prepare fresh GDE substrates that comprise the developed tandem catalyst.
- Integrate the prepared GDEs in the modified MEA electrolyzer.
- Start CO_2 electrolysis with applying different voltages using a reliable power supply.
- Control the CO_2 gas flow using a mass flow control unit.
- Circulate 0.1M $KHCO_3$ electrolyte to the anode side to keep the hydration of the membrane.
- Record XANES and EXAFS spectra at each applied voltage starting from the lower voltage (e.g., 2.5V) to the higher voltage (e.g., 3.5V).

We postulate that following the proposed experimental plans would result in a clear enhancement of C_{2+} products (mostly ethylene and ethanol) at industrially competitive current densities/reaction rates. Additionally, performance descriptors of catalyst design and the nature of active sites under operational CO_2R conditions would be provided to the catalysis community to assist in constructing more reliable CO_2R technology.